HEAT EXTRACTION AND DENDRITIC GROWTH DURING DIRECTIONAL SOLIDIFICATION OF SINGLE-CRYSTAL NICKEL-BASE SUPERALLOYS

by

Jonathan D. Miller

A dissertation submitted in partial fulfillment
of the requirements for the degree of
Doctor of Philosophy
(Materials Science and Engineering)
in the University of Michigan
2011

Doctoral Committee:

Professor Tresa M. Pollock, Co-Chair
Professor J. Wayne Jones, Co-Chair
Professor Jyotirmoy Mazumder
S. Lee Semiatin, Air Force Research Laboratory

DEDICATION

This thesis is dedicated to my family, especially my wife and our children. Without your love, support and encouragement none of this would have been possible.

ACKNOWLEDGEMENTS

The author would like to sincerely express his gratitude to everyone who has contributed to this work. The guidance of T.M. Pollock has been exceptional. The support of P.D. Lee is much appreciated. The mentorship of S.L. Semiatin over the past ten years is gratefully acknowledged. Further recognition is due to the members of the dissertation committee. The assistance of C.J. Torbet has been outstanding. Thanks to the students and alumni of the Pollock research group, especially those who have either contributed to or distracted me from this research, especially K.M. Gallup and C.L. Brundidge. Further appreciation is due to the students of Imperial College for their overwhelming acceptance and technical assistance, especially L. Yuan, S. Abolghasemi, F. Tariq and P. Ramirez. The support, guidance and suggestions from those of the Metals Branch at the Air Force Research Laboratory are also recognized. The efforts of M.J. Eisman are gratefully acknowledged. The support from the administrative staff in the Materials Science and Engineering Department deserves mention as well. Finally, I would like to thank my friends and family for their overwhelming support throughout this journey.

TABLE OF CONTENTS

LIST OF FIGURES

LIST OF TABLES

ABSTRACT

HEAT EXTRACTION AND DENDRITIC GROWTH DURING DIRECTIONAL SOLIDIFICATION OF SINGLE-CRYSTAL NICKEL-BASE SUPERALLOYS

by

Jonathan D. Miller

Co-Chairs: J. Wayne Jones and Tresa M. Pollock

Single crystal (SX) growth requires directional solidification (DS) with a sustained thermal gradient in the withdrawal direction. By increasing the thermal gradient, the dendrite structure in nickel-base superalloys is refined resulting in a mechanically-superior SX with reduced defect occurrence. One method to achieve higher thermal gradients is the utilization of the Liquid Metal Cooling (LMC) process. Optimization of the process has been limited by a lack of the fundamental understanding of the various heat transfer processes associated with the technique.

Solidification experiments of nickel-base superalloys have been conducted in a DS furnace capable of Bridgman or LMC modes. The degree of structure refinement has

been investigated in castings with varying cross-sectional areas. The feasibility of a mono-crystalline ring comprised of multiply-seeded, SX segments has been investigated.

Three-dimensional, finite-element (FE) solidification modeling has been used to investigate the thermal characteristics of the Bridgman and LMC DS processes. The dominant heat-transfer step during solidification is radiation from the mold for the Bridgman process and conduction through the mold for the LMC process. In the LMC process, the primary role of the floating baffle is to provide a thermal barrier between the furnace environment and the coolant. Relationships between dendritic structure and the local thermal field are presented. The preferred process conditions occur when the solidification-front position is just above the baffle for both the Bridgman and LMC processes.

The stability of unidirectional dendritic growth is dependent on the curvature of the solid-liquid interface. Some processing conditions cause substantial lateral heat extraction that leads to a change in dendrite morphology, resulting in grain nucleation or *lateral growth* – the formation of long secondary dendrite arms overgrowing favorably aligned primary dendrites. The conditions under which lateral growth occurs have been studied experimentally and via solidification modeling using FE and diffusional dendrite growth modeling. Lateral growth of dendrites occurs at interface inclination angles as low as 25 deg., and grain nucleation and breakdown of the solidification front occur when the interface inclination reaches 45 deg. The misorientation of the [001] SX orientation from the withdrawal axis significantly contributed to the onset of lateral growth.

CHAPTER 1

INTRODUCTION

The application of single crystal (SX) materials has provided significant advancement in material performance in engineering systems compared to equiaxed or columnar-grained materials. Increased system requirements within the aerospace and energy communities have provided a driving force for SX- and columnar-grained directionally-solidified (DS) components with improved high-temperature creep and fatigue resistance along with reduced scrap rates, in order to achieve increased efficiency of gas turbines while maintaining system affordability. These requirements necessitate the use of components possessing large cross-sections or complex geometries made from refractory-rich, defect-prone alloys. In order to achieve the desired performance, utilization of novel processing techniques is required. One solution that addresses these enhanced requirements and can provide a considerable increase in the capability of these materials is the Liquid-Metal-Cooling (LMC) process. LMC is a high-gradient, directional-solidification process that provides enhanced heat extraction as compared to the conventional Bridgman technique. Due to the improved heat extraction, the stability of dendrite growth can break down, which may degrade material performance [1]. The directional-solidification experiments of Elliott demonstrated that for a fixed alloy and cooling rate, two different dendritic structures formed due to a change in process conditions [1]. Therefore, there is a need to understand the detailed heat transfer mechanisms during directional solidification and

their effect on dendrite growth, specifically in the presence of a non-axial thermal field or the presence of non-ideal processing conditions.

The development and application of solidification models has provided significant advancement in the understanding of directional-solidification processes. A detailed understanding of the model assumptions, boundary conditions, and limitations is necessary for each modeling approach employed. Coupling models at different length scales provides accurate predictions of solidification behavior through large domains and long time scales, while minimizing computational expense. Concurrently, careful experimentation is utilized to provide critical input parameters and validate model predictions.

This research integrates micro- and meso-scale process models with careful experimentation, utilizing novel characterization tools to provide significant advances in the understanding of directional-solidification processing. Continuum-scale process simulations are coupled to microstructure-scale modeling tools to establish a connection between macroscopic heat transfer processes and microscopic solute redistribution and dendritic growth processes. Predictive criteria that can be employed within the computationally-fast macro models have been extracted from computationally-intensive microstructure models to predict the formation of defects and the resultant structure. A comprehensive description of the formation of microstructure under a broad range of processing conditions has been established. Overall, this effort aims to improve the fundamental understanding of dendritic growth during directional solidification and

enable the evaluation of production-relevant casting configurations over a broad range of processing conditions.

In this chapter, the literature relevant to SX solidification and the LMC process are discussed, including a background of conventional SX Ni-base superalloys, their processing and a complete history and description of the LMC process. Continuum-based and microstructure-modeling capabilities are discussed and current gaps in knowledge summarized.

Single Crystal Nickel-base Superalloys

Single-crystal nickel-base superalloys have been studied extensively over the past few decades, and the science of these materials has been summarized [2,3]. In this section, a review of the evolution of SX superalloys, the conventional processing techniques for SX superalloys and the structure that forms during solidification is provided.

Alloy Chemistry

Ni-base superalloys are a class of structural materials that are utilized at higher temperatures, relative to their melting point, than any other material system [2]. In general, these alloys are based on the Ni-Al binary system. The unique high-temperature capability is largely attributed to precipitation strengthening via the ordered $L1_2$ γ' precipitates [2]. This thesis focuses on single-crystal Ni-base superalloys. A list of commonly investigated alloys and their compositions is provided in Table 1.1.

Table 1.1 – Common SX Ni-base superalloys and their compositions (in wt pct).

Alloy	Cr	Co	Mo	W	Ta	Re	Al	Ti	Hf	C	B	Other	Ni
René N4	9.8	7.5	1.5	6	4.8		4.2	3.5	0.15	0.05	0	0.5 Nb	bal
René N5	7	7.5	1.5	5	6.5	3	6.2		0.15	0.05	0	0.01 Y	bal
PWA 1484	5	10	2	6	9	3	5.6		0.1				bal
CMSX-4	6.5	9.6	0.6	6.4	6.5	3	5.6	1.0	0.1				bal
CMSX-486	5	9.3	0.7	8.6	4.5	3	5.7	0.7	1.2	0.07	0.015	0.005 Zr	bal
CM 186 LC	6	9.3	0.5	8.4	3.4	3	5.7	0.7	1.4	0.07	0.015	0.005 Zr	bal

The first alloys cast via the directional solidification process possessed chemical compositions similar to conventionally-cast superalloys due to the fact that columnar-grained DS alloys still have grain boundaries and thus require grain boundary strengthening elements [4]. These alloys contained chromium for environmental resistance and solid-solution strengthening and boron and carbon to strengthen grain boundaries [4]. Refractory elements were also utilized for solid-solution strengthening [2,3]. The presence of high-angle grain boundaries within the columnar-grained structure can result in grain boundary cracking during directional solidification [5]. However, hafnium additions in alloy compositions were found to further strengthen grain boundaries and improve the resistance to grain boundary cracking [4,5]. The relationship between alloy composition and tendency for grain boundary cracking and the fundamental role of hafnium are not well understood. In any case, the mechanical benefit of DS alloys was attributed to the absence of grain boundaries transverse to the axis in which stresses are the highest for turbine components [4-7]. Conversely, SX alloys are absent of all grain boundaries. Thus, early compositions did not contain grain-boundary strengthening elements [4,8]. The absence of grain-boundary strengthening elements enabled more solution-treatable alloys, providing an improvement in mechanical

behavior over DS alloys and establishing the typical first-generation SX superalloy compositions [4,8-10]. Second and third generation SX alloys contained increased quantities of solid-solution strengthening elements (W, Ta, Re) to further improve creep rupture strength and fatigue resistance [9,11,12]. However, the segregation of heavy alloying elements caused convective instabilities at the solidification front that induced the formation of freckle-type defects [9,13]. The use of multi-component alloys for engineering components inevitably results in low-angle boundaries within the complex geometry [14]. Thus, additional quantities of grain-boundary strengthening elements were added to alloy compositions [4,15-18]. With the utilization of boron, carbon and hafnium to increase low-angle grain-boundary strength, the resistance to grain boundary cracking also improved [4,9,15-17,19,20]. However, boron and carbon reduce incipient melting temperature and limit solution-treatment capability, such that alloys are being developed that are designed to be used without solution treatment [15-17].

Phase stability and enhanced creep-rupture capability provided a driving force for the development of fourth-generation single-crystal superalloys [21]. Increased refractory element content and the application of ruthenium provided the targeted improvements [21]. Due to the expense of the alloying elements used in state-of-the-art SX alloys, affordability has recently inspired continued alloy development to strike a balance among performance, castability and affordability [22].

Investment Casting and Directional Solidification

A comprehensive description of directional solidification has been given in several publications [6,7,23-25]. The directional solidification process was originally developed in the 1960's and has matured significantly over the past five decades [26,27]. Currently, DS Ni-base superalloy components for air- and land-based applications, such as turbine blades, are manufactured on a routine basis using a specialized investment-casting process, commonly referred to as the Bridgman technique [6]. Investment casting is a technique used to manufacture metal components, typically with intricate geometries, to near net-shape without the need for additional processing steps (Figure 1.1) [25]. This casting process has extensive flexibility and capability, but the expense associated with cost of patterns, molds, cores, and labor required restrict its applications to high value-added components.

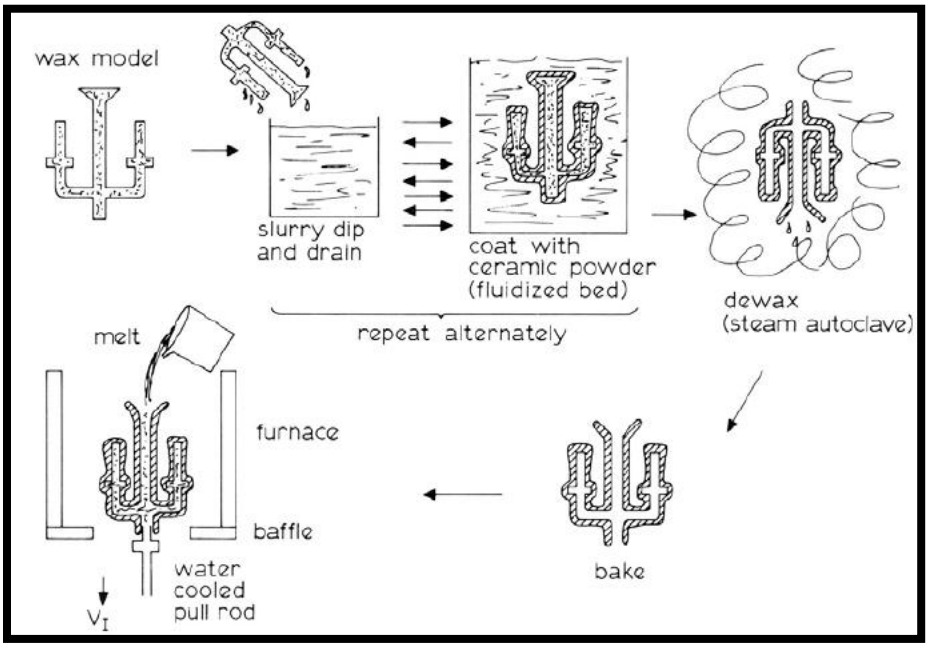

Figure 1.1 – Schematic of the investment casting process [6].

The Bridgman technique is the conventional processing method for directionally-solidfying Ni-base superalloys (Figure 1.2a) [6]. In this approach, a water-cooled chill supports an investment mold prior to alloy melting. The investment mold is positioned in a mold heater in which the temperature is maintained above the melting temperature of the alloy. Molten alloy is deposited into the ceramic investment mold, and the chill and casting are then withdrawn from a mold heater through a cavity to a "cold zone" in the furnace. The mold is cooled by radiation heat transfer to water-cooled walls of the furnace. The heat-transfer processes generate a high thermal gradient upon withdrawal from the mold heater, thereby promoting the growth of an array of dendrites parallel to the withdrawal direction. The crystallographic texture of the resulting grains is determined by the thermal-gradient direction and the initial crystallographic orientation, occurring from epitaxial growth from a seed or dendritic growth directly from the chill. In many cases, a starter containing a seed crystal is used in which the array of dendrites compete in a geometrically-constrained configuration such that a single orientation grows from the starter to the component.

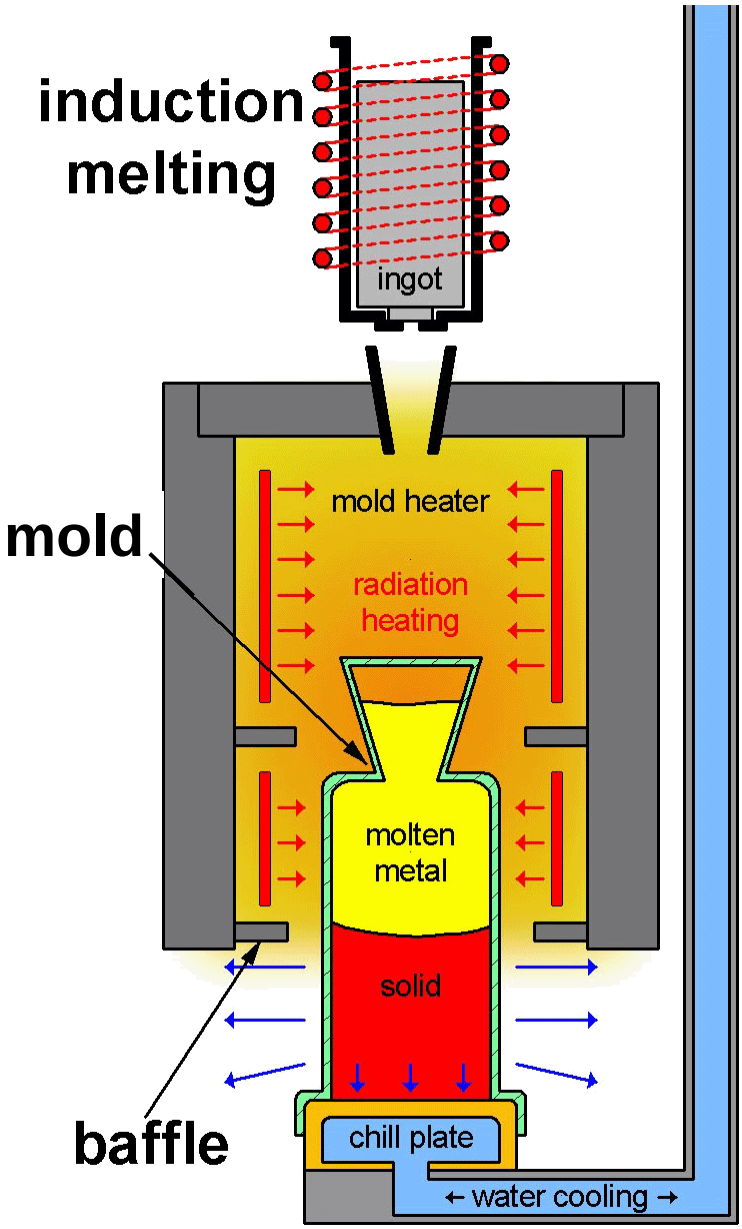
induction
melting
ingot
mold
mold heater
radiation
heating
molten
metal
solid
baffle
chill plate
water cooling

(a)

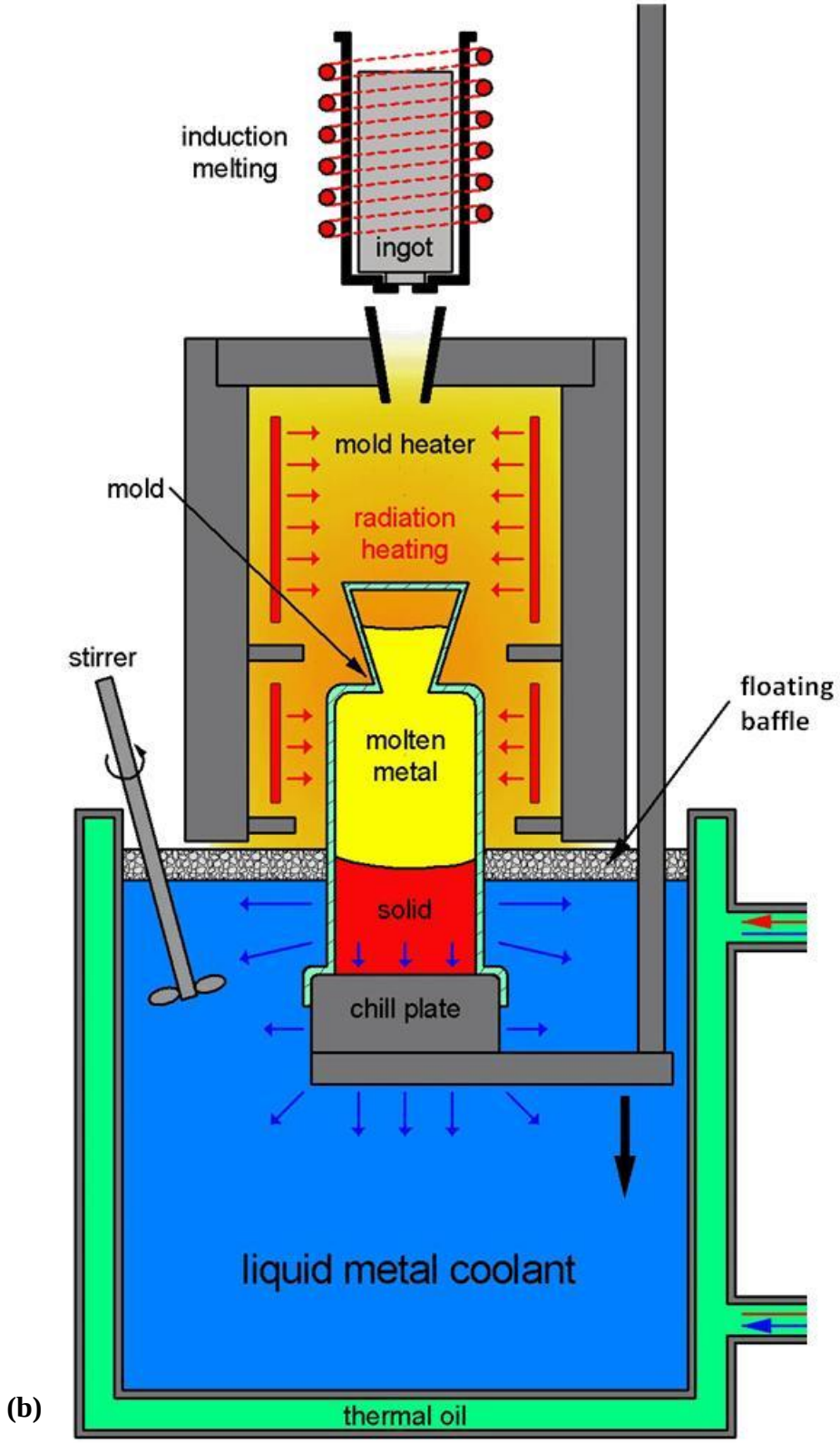

(b)

Figure 1.2 – Schematics of the (a) Bridgman and (b) LMC processes [28].

The typical geometry of DS and SX blades comprises a relatively long axial dimension with a small cross-sectional area transverse to the withdrawal direction. Ideally, the geometry of a given cross-section is simple to prevent any loss in the axial temperature gradient developed by the process. Any abrupt change in geometry can have a dramatic effect on the desired unidirectional thermal gradient, which can alter the morphology of the dendritic structure [28-35].

Solidification Structure

The microstructure that forms during SX casting comprises an array of dendrites that preferentially grow in the direction of the thermal gradient (Figure 1.3). Dendrites can be characterized according to their crystallographic orientation, primary dendrite-arm spacing (PDAS), and secondary dendrite-arm spacing (SDAS). In cubic materials, dendrites grow preferentially along the <001> crystallographic axes. This is beneficial to mechanical performance as the <001> is the low-modulus orientation of Ni-base superalloys and thus provides thermal fatigue resistance [9]. In general, the primary dendrites grow parallel to the thermal gradient. For ideal cases, the thermal gradient is aligned with the orientation of the dendrites and a particular dimension of a cast component (e.g., the axis of an airfoil).

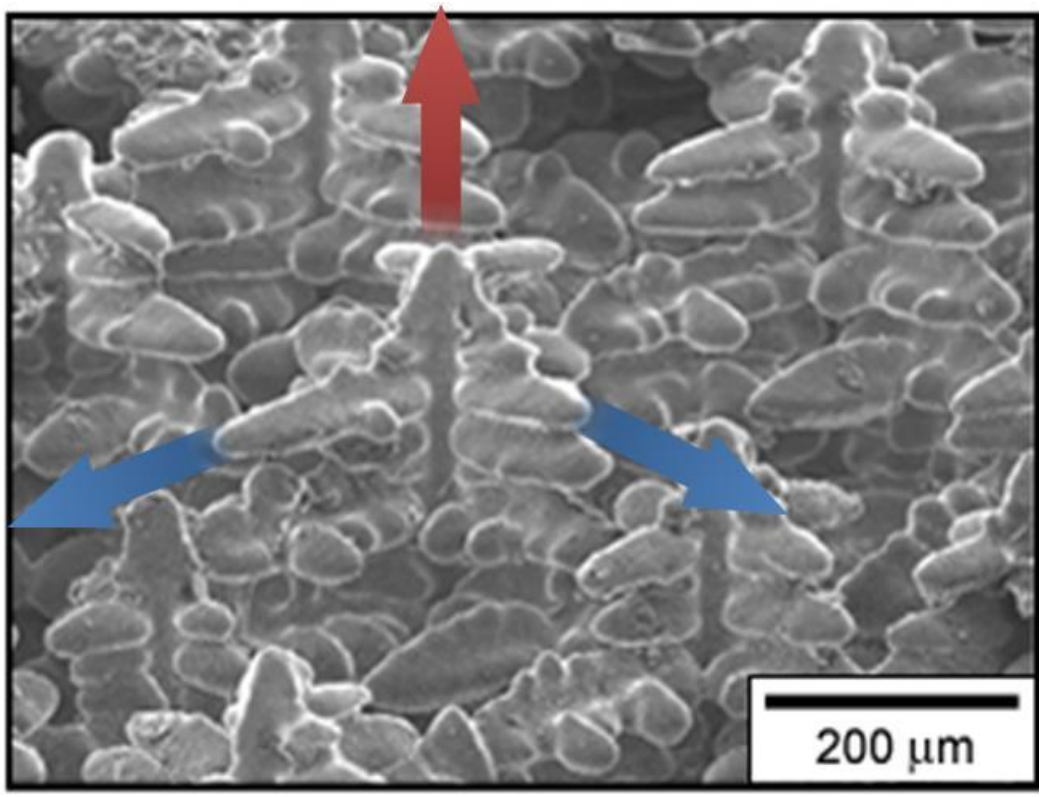

Figure 1.3 – Image of 3D dendritic growth depicting primary (red) and secondary (blue) orientations [36].

The dependence of dendrite morphology and scale on thermal conditions has been studied experimentally [9,13,37-62]. From this research, the dendrite morphology has been associated to thermal conditions at the solidification front: thermal gradient, solidification rate and cooling rate. Regions of plane-front, cellular, dendritic and equiaxed growth have been established based on these thermal conditions (Figure 1.4a) [24]. Similar processing maps have been developed that are specific to dendritic solidification and include regions of increased defect propensity (Figure 1.4b) [13]. In general, the dendritic structure is refined with increased cooling rate [37-39]. Solidification conditions near the transitions between the different solidification

morphologies are not well understood. Each of the dendrite-growth regimes is described in this section.

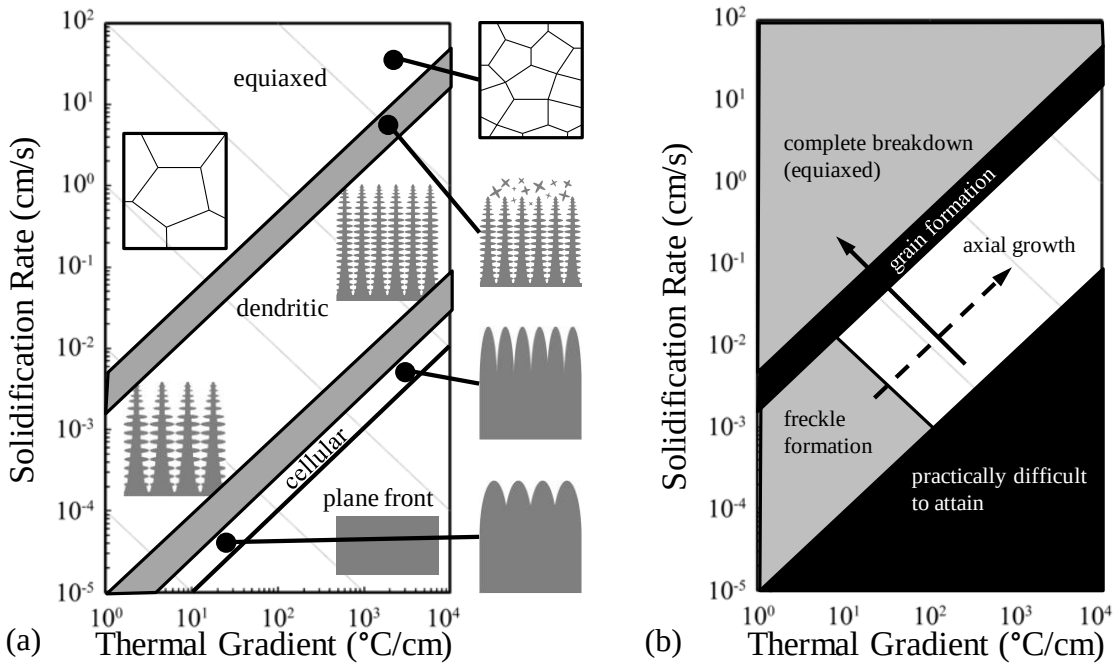

Figure 1.4 – Maps of (a) solidification morphologies and (b) dendritic morphologies and defects based on thermal conditions at the solidification front. Note: The dashed arrow indicates a direction of structure refinement, while the solid arrow indicates constant cooling rate.

When the thermal gradient is high and the solidification front planar, the desired axial dendritic structure is formed, and defects tend to be suppressed (Figure 1.5a) [28-35]. However, sharp changes in cross section, thick sections, or complex geometrical features within the casting perturb the local thermal gradient, thus promoting the formation of solidification-induced defects [28-35].

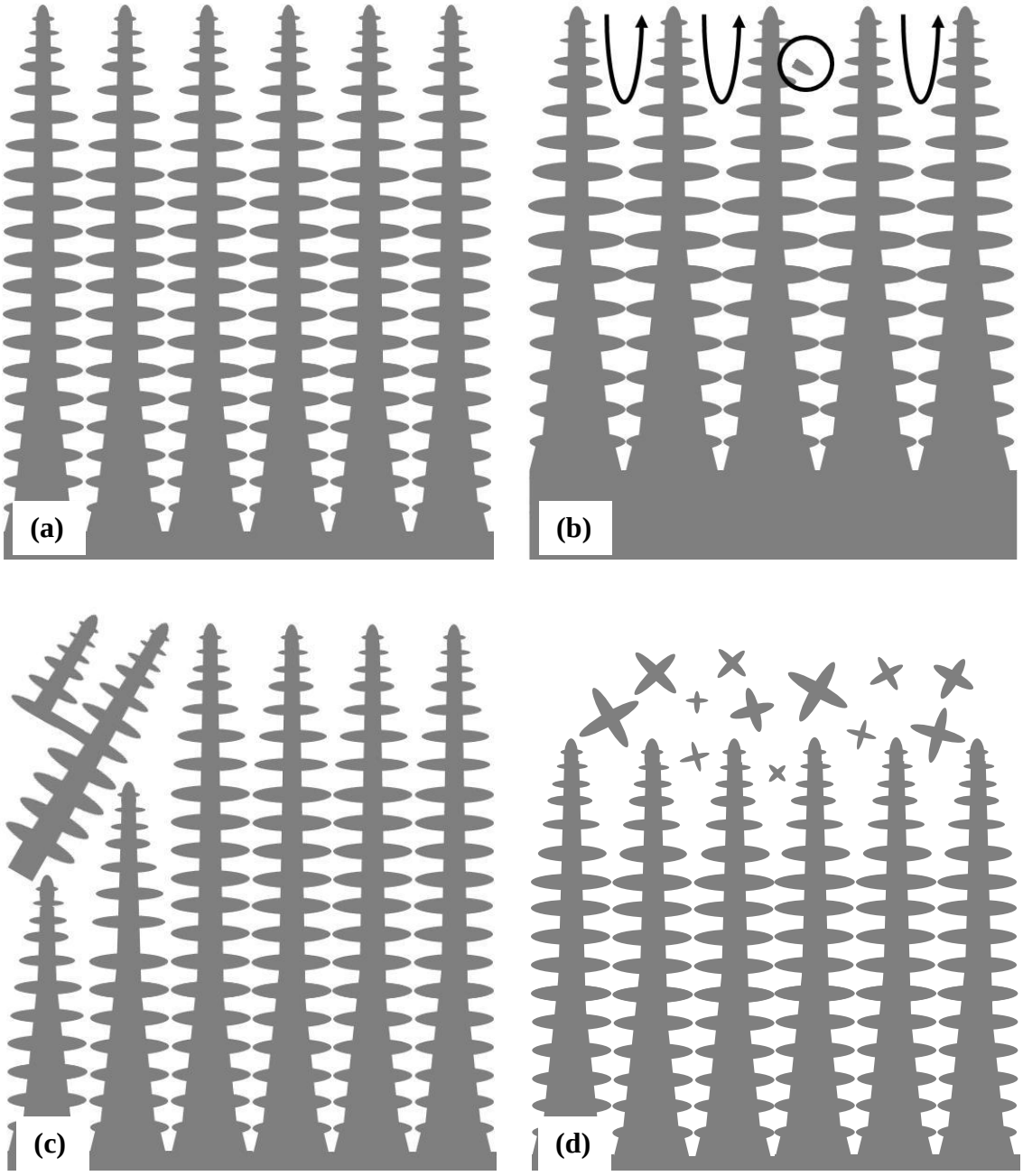

Figure 1.5 – Schematic depiction of (a) well-aligned dendritic growth, (b) freckle formation (c) stray grain formation and (d) complete breakdown of directional solidification.

The formation of defects, such as freckles or nucleated grains, degrades mechanical properties due to the high-angle boundary formed between the defect and single crystal. Significant research has been devoted to understanding the thermal and solutal conditions

under which freckle formation occurs [13,59,63-70]. A freckle is a chain of equiaxed grains solidified in a melt of columnar or single-crystal alloy (Figure 1.5b) [59]. Experimental findings from dendrite growth of transparent compounds and nickel-base superalloys attributed the onset of freckling to convective instabilities near the tips of growing dendrites [13,63-67]. The convective instability is caused by the segregation of light alloy elements to the melt causing density inversion and convective flow in the form of channels. Solidification conditions with a low thermal gradient and solidification rate are especially prone to freckle formation due to the increased mushy-zone length, further increasing the segregation instability. This leads to dendrite tip melt- or break-off as the dendrite front interacts with the flow field, thus forming freckles. A criterion utilizing the Rayleigh number has been developed for prediction of the onset of freckling [59,68-70]. On the other hand, the formation of nucleated grains occurs via a different mechanism that can be associated to the interaction of the thermal and solutal fields ahead of the dendrite-growth front and is discussed further.

The formation of nucleated grains occurs when the thermal gradient is too low or the solidification rate is too high, identified in Figure 1.4b as a band between dendritic and equiaxed growth (Figure 1.5c). Grain nucleation occurs when the undercooling ahead of the solidification front is too large and a nucleus is present in the melt [34]. Typically, nucleated grains are present at the surface of a casting initially, due to the presence of a cold mold wall and increased curvature of the solidification front, which increases the undercooling along the mold wall ahead of the solidification front [28-35]. The interaction of the local thermal conditions and the solidification-front curvature is not

well understood. For solidification conditions with a higher solidification rate or lower thermal gradient (proceeding further to the upper left in Figure 1.4b), the thermal gradient is insufficient to maintain directional solidification, resulting in widespread nucleation ahead of the solidification front (Figure 1.5d) [13,56-60].

Once an orientation defect forms, the interaction of the misoriented dendrites with [001] dendrites has been studied extensively and is termed *competitive dendrite growth* [46-51]. Walton and Chalmers studied the interaction of misaligned dendrites and developed a competitive-dendrite growth model [46]. According to the model, the dendrite whose orientation is more closely aligned with the thermal gradient grows faster than the less favorably aligned dendrite since the growth velocity is related to the thermal gradient in the growth direction [46]. Over time, the favorably dendrite may overgrow the unfavorably aligned dendrite, as was later confirmed by observation from dendrite-growth experiments on transparent compunds [47]. In the case of converging dendrites, Figure 1.6a, well aligned primary arms grow ahead of unaligned primaries, thus forming a stable vertical boundary between grains. In addition, diverging dendrites are overgrown by secondary arms of well-aligned dendrites (Figure 1.6b). Competitve dendrite growth in the presence of a curved solidification front is less understood. However, competition under this condition is most relevant since grain nucleation tends to occur at the surface of a casting where the solidification front may not be planar. While there have been detailed studies of dendrite growth under unidirectional thermal conditions, an understanding of the morphology of dendrites in the presence of a non-axial thermal field is lacking and is discussed in this research.

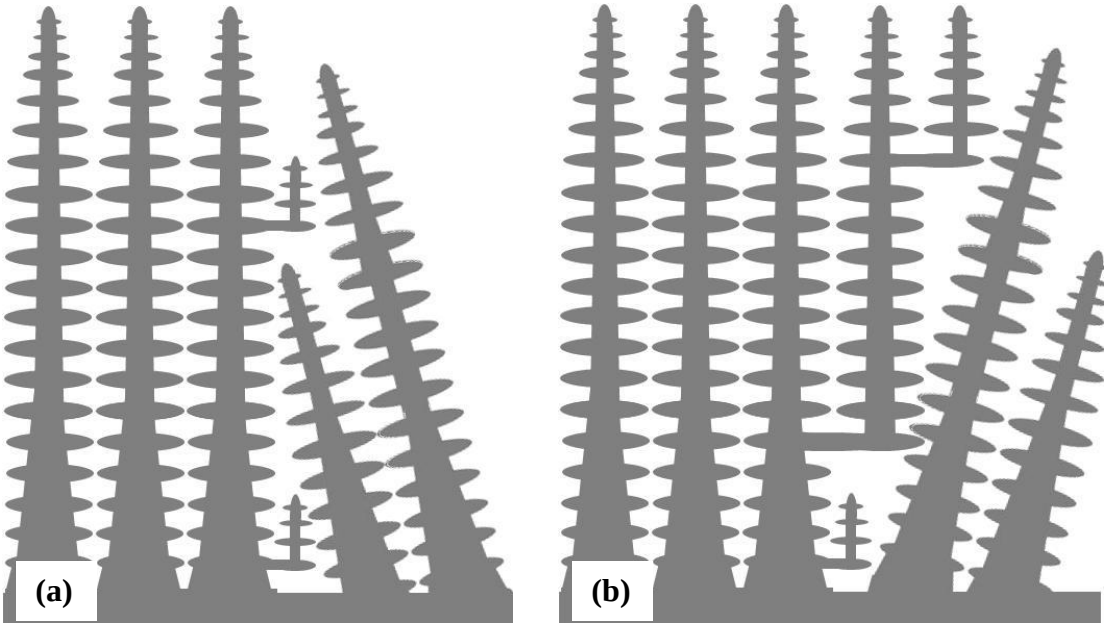

Figure 1.6 – Competitive dendrite growth of (a) converging and (b) diverging dendrites.

Experiments have also been conducted in which the primary orientation of the dendrites is misaligned with the thermal gradient. These dendrite-growth experiments utilized a transparent compound and a thermal rig in which the thermal gradient direction could be controlled along a 90 degree rotation about the [010] of the dendrites [45]. Grugel and Zhou found that when the solidification-front angle reached 45 degrees relative to the primary <001> orientation there was strong propensity for lateral growth of secondary dendrites [45]. For angles greater than 45 degrees, the secondary arms effectively grew as primaries along the lateral thermal gradient [45].

The propensity for secondary arms to propagate tertiary arms and overgrow well-aligned primary arms has not been studied extensively. Herein, this phenomenon is referred to as *lateral growth* (Figure 1.7). Studies have been conducted to evaluate solidification

morphologies over a range of thermal gradients and solidification rates [9,39,41-44]. Under these conditions, lateral growth has been attributed to an increase in the curvature of the solid-liquid interface in conjunction with high pulling velocities (50 mm-min^{-1}) [39]. Because high curvatures are associated with the breakdown of single-crystal solidification, process conditions are selected in order to minimize curvature [39,41].

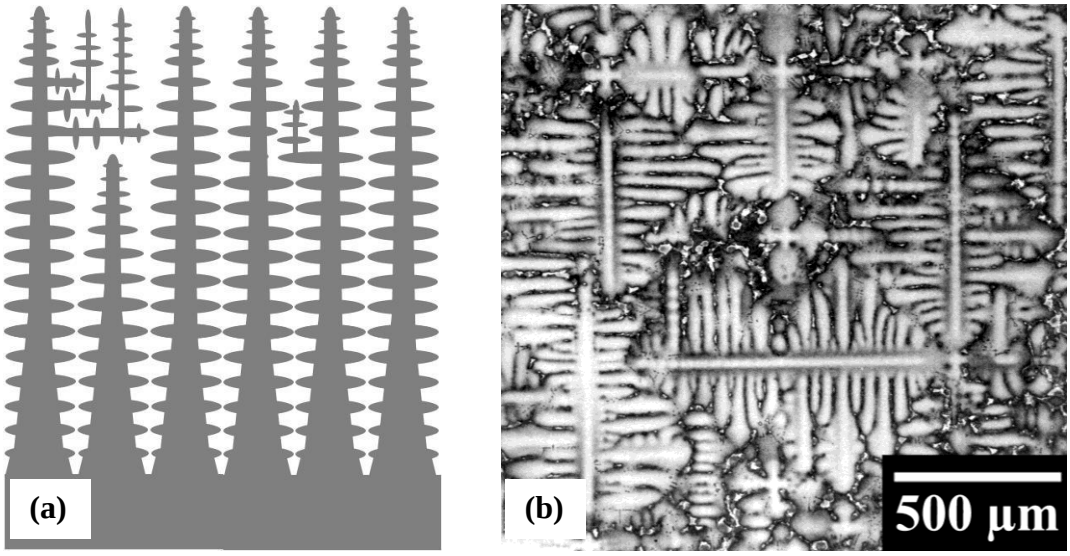

Figure 1.7 – (a) Schematic depicting lateral growth and (b) micrograph transverse to the growth direction of a region of lateral growth [1,77].

To summarize, transitions in solidification morphology and the formation of defects have been associated to thermal conditions during solidification (Figure 1.4) and are depicted schematically (Figure 1.5). The thermal conditions that promote the formation of lateral growth are not well understood, but lateral growth occurs in the presence of increased curvature of the solidification front. In general, orientation defects can be suppressed by maintaining proper alignment of the solid-liquid interface with the primary orientation of the dendrites and a strong, unidirectional thermal gradient.

The Liquid Metal Cooling Directional Solidification Process

A novel process that utilizes Liquid Metal Cooling (LMC) of the mold as it is withdrawn from the furnace has been developed [41,71]. Initial research has shown that this technique is capable of enhanced heat extraction resulting in fine dendritic structure within complex and/or thick-section geometries [28]. Applications directly benefiting from the LMC process include cooled turbine blades and industrial gas-turbine buckets [22]. Other high gradient solidification processes have been evaluated, including Gas Cooling Casting (GCC) and utilization of a fluidized bed, but are not discussed [72,73].

Process Description

The LMC process is similar to the Bridgman method, in that the mold is axially withdrawn from a furnace. The main difference in the LMC process compared to the Bridgman process relates to the fact that the mold is withdrawn into a molten bath of a low-melting point, low vapor pressure metal, thus increasing the heat extraction from the mold surface by changing the heat transfer mechanism at the surface of the mold from radiation to conduction and convection (Figure 1.2b). The selection of the material for the cooling medium is discussed in the next section. In order to prevent heating of the molten bath by the mold heater above, a floating baffle is utilized on the surface of the tin. The floating baffle is composed of ceramic beads that float on the surface of the tin and are free to flow during the process. Ultimately, the improvement in heat extraction provides increased thermal gradient and solidification rate, thus reducing the dendrite spacing, defect formation and microsegregation [28,74,75]. This process is thus ideal for

thick and/or complex geometries because the enhanced heat extraction dominates solidification irregularities arising from geometry changes along the length of the component [28].

Process Development

The LMC process was originally developed in the 1970's on an experimental scale [71], but was not utilized on a commercial scale due to the relative ease of the Bridgman technique for alloys and components being developed at that time [74]. Because of increased complexity and thickness of SX and DS components and the high refractory content of 2nd and 3rd generation superalloy single crystals, the process has been re-evaluated in recent years [28,72,75-79]. At the same time, a better understanding of the LMC process and the potential benefits to properties has been established [28,72,74-79].

One process variable evaluated during the development of LMC was the cooling medium. Because nickel-base superalloys are cast in vacuum, the candidate materials were limited to low melting point, low vapor pressure metals [41]. Tin and aluminum have been used as the low-melting point metal, but tin has been preferred in recent investigations due to its lower melting point and reduced reactivity with the casting alloy and coolant container [74,77]. In order to evaluate the dissolution of alloy due to inadvertent contact of the cooling medium with the casting, direct immersion experiments have been conducted [78]. The melting point of aluminum (660°C) is higher than tin (232°C). Due to the higher melting point, significant dissolution of the alloy PWA1483 was reported with aluminum as the cooling medium [78]. However, no dissolution was

observed for tin as the cooling medium [78]. In addition, trace levels of tin were intentionally incorporated into SX alloys for evaluation of the sensitivity of low-cycle fatigue and creep resistance to tin concentration [78-82]. Depending on the alloy system, no degradation of mechanical behavior was observed for up to a concentration of 4150 ppm [78-82].

The baffling conditions between the hot and cold sections of the furnace have also been identified as an important process parameter [28,75]. The thickness of the floating baffle and presence of a fixed baffle and floating baffle were evaluated in order to identify which features of the baffle positively influenced the conditions at the solidification front [75]. It was concluded that the presence of a floating baffle provided an enhanced thermal gradient [75]. However, the baffle thickness did not greatly impact the thermal gradient [75]. Recently, the presence of the floating baffle was again demonstrated to be critical to establishing a strong thermal gradient [1,28].

Advantages and Limitations of the LMC Process

Because the LMC process provides enhanced heat extraction compared to the Bridgman process, the thermal gradient at the solidification interface is significantly increased, as described previously [83]. A finer dendritic structure is thus formed, resulting in a finer γ' precipitate structure and defect structure – finely distributed porosity and γ/γ' eutectic - with improved mechanical performance (Figure 1.8) [28,39,52,79-89]. With regard to mechanical properties, application of the LMC process can result in crystals with improved fatigue life [77,1-85]. In addition, increased thermal gradient and solidification

rate have been shown to lead to improved creep rupture life [39,86-89]. Because the dendritic scale is refined, the diffusion distances required to homogenize the material are lower, thus reducing the solution treatment times or enabling full solutioning during heat treatment for highly alloyed materials [74]. In addition, the γ' precipitates and carbides produced during LMC were found to be more finely and homogeneously distributed, thus more beneficial than the respective Bridgman morphologies [74]. Ultimately, these process changes produce an economic benefit as well, because the processing time for both the solidification process and other downstream processing steps is reduced.

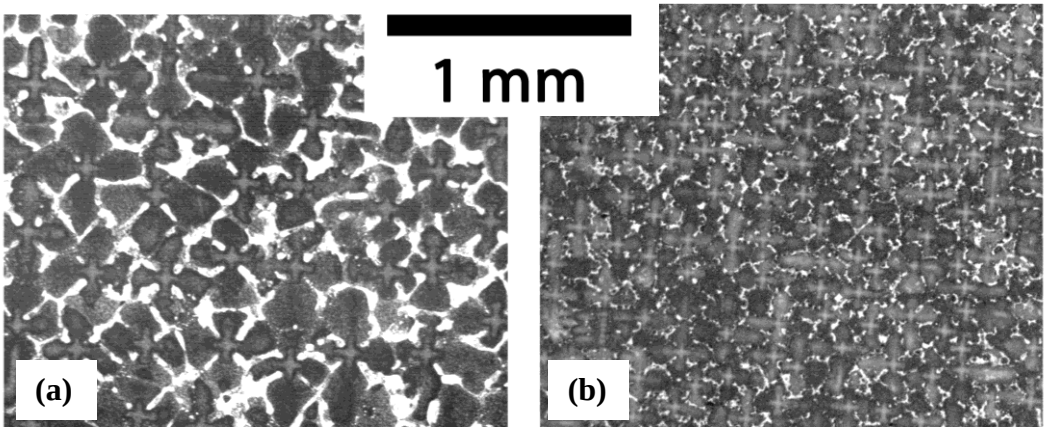

Figure 1.8 – Micrographs transverse to withdrawal direction of same alloy and casting configuration, processed via the (a) Bridgman and (b) LMC techniques [52].

Unfortunately, the increase in the magnitude of the thermal gradient during LMC is often accompanied by a change in the axiality of the temperature gradient and curvature of the solidification front [41]. That is to say, heat is extracted so efficiently that the thermal gradient becomes non-axial for LMC casting [28,41]. Under some growth conditions, the complex thermal field results in the formation of an irregular dendritic microstructure formed due to substantial lateral growth, thus giving rise to a microstructure containing

what appears to be primary arms *transverse* to the withdrawal direction (Figure 1.9) [39,41,77]. Lateral growth is observed during conventional processing when the solidification front is lowered into the cooling zone of the furnace due to high pulling velocities or drastic changes in geometry as described previously [9,39,41,43]. However, the presence of such irregularity is greatly increased during LMC compared to the conventional Bridgman process [41,72,77]. Such microstructure irregularities which do not necessarily introduce high-angle boundaries are not well understood, although they appear in typical LMC castings and may impact the resulting mechanical and service behavior.

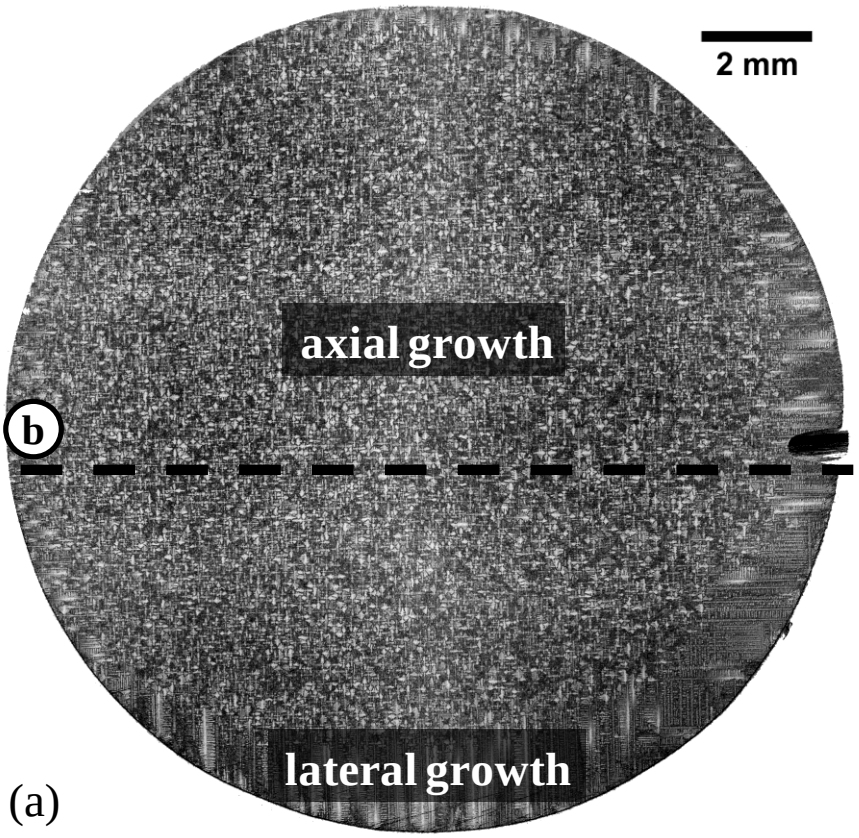

(a)

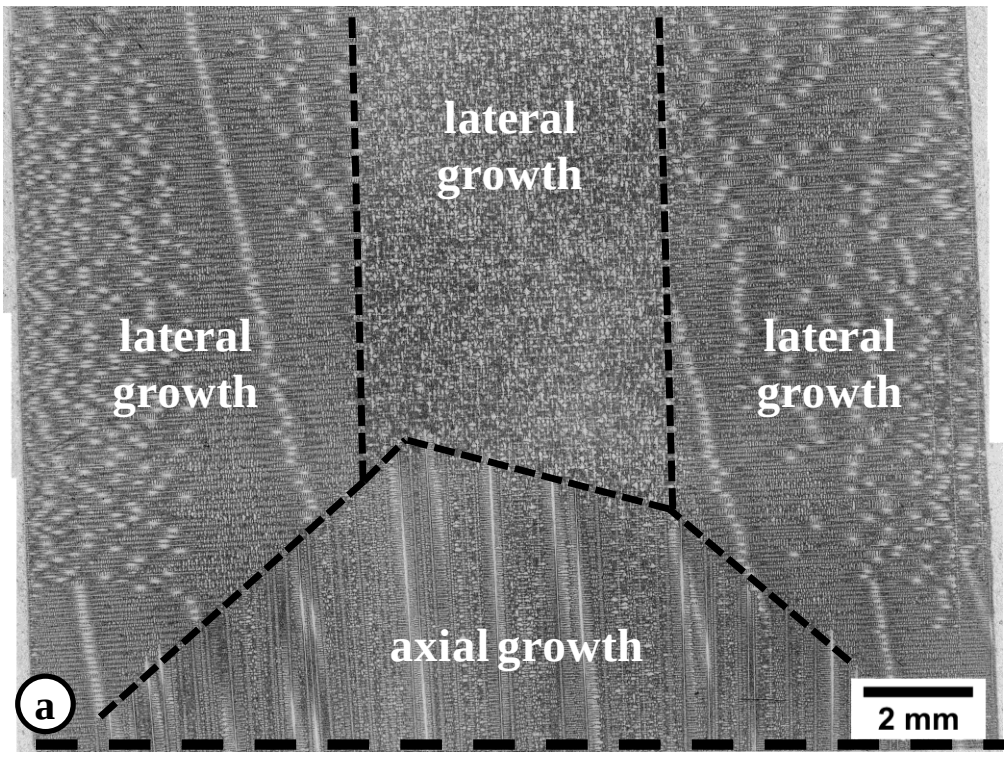

(b)

Figure 1.9 – Macrographs (a) transverse and (b) parallel to the growth direction depicting lateral growth at the surface of the casting.

Modeling and Simulation of Directional Solidification

Computational capabilities for evaluating the evolution of microstructure during solidification have been developed. Early modeling approaches focused on macroscopic fluid flow and heat transfer. Thereafter, modeling capabilities were extended to the microstructure level and consisted of phenomenological models that correlated thermal conditions, such as thermal gradient and solidification rate, to microstructure features such as primary dendrite arm spacing [37,38]. Current state-of-the-art microstructure models consider heat and mass transfer, specifically the local thermal, convective and solutal variations in order to more accurately predict microstructure evolution. Several

reviews of microstructure modeling, including the evolution of dendritic growth at the scale of the dendrites have been published [90-92]. In order to understand how these micro- and meso-scale, computational models have evolved, the development and application of macro-scale models are discussed briefly. Following this, a description of the development of microstructure models for dendritic solidification is provided. Finally, the application of the microstructure models to the component scale is discussed.

Macro-scale Model Development

Models of fluid flow, heat transfer and phase transformation have been used to predict the thermal conditions during directional solidification. Original models were analytical in nature and capable of evaluating only simple casting configurations. Models of this type were developed for the evaluation of the LMC process [41,75,76]. Parametric studies independently evaluating the effect of specific processing conditions on thermal conditions at the solidification front were performed [41,75,76]. However, because of the assumptions required to formulate analytical solutions, improved simulation methodologies were required.

A framework for numerical simulation, specifically finite element modeling (FEM), of the directional solidification process was subsequently developed [93]. One example of commercially-available solidification modeling software is ProCAST^{TM}, developed by ESI Group [ProCAST^{TM} is a trademark of ESI Group]. ProCAST^{TM} is a continuum-based, finite-element model (FEM) specifically designed for fluid flow, heat transfer, stress and microstructure calculations relevant to solidification problems. Fluid flow is

calculated based on the equation of motion for either Newtonian or non-Newtonian fluids. Heat transfer calculations consider conduction, convection, radiation and phase transformation. Thermo-mechanical stresses may be calculated for materials defined by constitutive laws for elasticity, plasticity and viscosity. Phenomenological microstructure predictions are then developed by correlation of macroscopic heat flow calculations by analytically mapping microstructural models to thermal parameters. Other microstructure calculations are based on cellular automata and other micro-scale techniques [93].

Commonly, only fluid flow and heat transfer (with phase transformation) are considered for Newtonian fluids. In this configuration, heat conduction within each domain is modeled considering Fourier's law (Equation 1.1) resulting in the equation of energy (Equation 2) including enthalpy-based, latent-heat release during phase transformation.

$$q = -k\nabla T \tag{1.1}$$

Fourier's law relates the heat flux to the thermal conductivity, *k*, and the gradient of the temperature, *T*. An energy balance gives Equation 1.2.

$$\rho c_p \left[\frac{\partial T}{\partial t} + (v \cdot \nabla T)\right] = k\nabla^2 \mathrm{T} + \mu\Phi_\mathrm{v} + \rho L(1 - f_s) \tag{1.2}$$

This form of the equation of energy is based on the assumption that material properties - including density, specific heat, thermal conductivity and viscosity - are constant. Numerically, it is reasonable to assume constant thermophysical parameters because these properties do not vary strongly across the small spatial and temporal steps in simulations. In Equation 1.2, ρ, c_p, k and μ are density, specific heat, thermal conductivity and viscosity, respectively, and are the material properties. Other parameters include time *t*, velocity v and dissipation function Φ_v that is only significant

when velocity gradients are high. The final term accounts for latent heat of fusion, where L is the latent heat and f_s is the fraction of solid. Material properties are applied by dividing the model into a set of domains in which each domain represents a different material in the process. At the surfaces of domains, either a free surface or an interface between domains, calculations are based on a defined boundary condition (Equation 1.3).

$$q = q_0 + h(T - T_a) + \sigma\varepsilon F(T^4 - T_a^4) \tag{1.3}$$

The heat flux (q) across the surface of a domain can be described by a pre-defined flux (q_0), Newton's law of cooling and the Stefan-Boltzmann law. For each parameter, a time- or temperature-dependent parameter can be used. The heat transfer coefficient, h, is dependent on geometry, material and the local flow field. Other parameters include the ambient temperature T_a, the Stefan-Boltzmann constant σ and the emissivity of the surface ε. Shadowing effects are accounted for by the radiation view factor F. Fluid flow is governed by the Navier-Stokes equation (Equation 1.4), which is derived from the equation of motion and Newton's law of viscosity, assuming constant density and viscosity.

$$\rho\left[\frac{\partial v}{\partial t} + (v \cdot \nabla v)\right] = -\nabla P + \mu\nabla^2 v + \rho g \tag{1.4}$$

In this equation, P is the pressure and g is the acceleration due to gravity.

Once the framework for fluid flow and heat transfer modeling of the directional solidification process was established, commercialization and widespread application of the approach continued [93]. Recently, a thermal stress model was incorporated into the FEM during solidification [80]. As the FEM model matured, correlations to

microstructure scale, defect formation and mechanical behavior were applied [37,38,52,59,67,94].

Modeling the evolution of the microstructure can be challenging at the macro-scale. At this scale, the thermal environment is predicted, thus allowing for predictions of dendrite growth limited by thermal diffusion. Equations can be developed for the prediction of microstructure scale based on the local thermal conditions at the solidification front. The first well-accepted analytical model for association of microstructure scale and thermal conditions was developed by Hunt [37]. In this model, the growth of a dendrite was analyzed by considering diffusion of the solute at an ellipsoidal dendrite tip. The key assumption for this model is that growth occurs at the minimum undercooling for a given velocity [37]. Other assumptions made for this analysis are the following: temperature varied in only the primary growth direction of the dendrite, latent heat and convective flow were ignored, the dendrite near the tip was a smooth steady-state shape with radial symmetry in a binary alloy with a spherical tip, and the thermal field was at steady state. For dendrite growth in a thermal condition far from the constitutional undercooling limit, i.e. $dT_L/dx >> dT/dx$, the following relationship is given in Equation 1.5:

$$\lambda_1 = \left[\frac{64\gamma D_L m_L (1-k) C_0}{\Delta S}\right]^{1/4} G^{-1/2} V^{-1/4} \tag{1.5}$$

In this equation, λ_1 is the primary dendrite arm spacing, γ is the solid-liquid interface energy, D_L is the diffusion coefficient in the liquid, m_L is the slope of the liquidus line on the phase diagram, k is the partition coefficient, C_0 is the initial composition of the solute, ΔS is the entropy of fusion per unit volume, G is the thermal gradient in the liquid and V is the velocity of the interface.

A similar model was proposed by Kurz and Fisher [38]. Their analytical model was based on heat-diffusion-limited growth proposed by Langer and Muller-Krumbharr [95-98] and the stability criterion of Mullins and Sekerka [99] applied to the dendrite tip [38]. This assumes that the tip radius is equal to the minimum radius required to cause an instability [99]. Other assumptions of the analytical model are as follows: planar solid-liquid interface in the primary growth direction, no latent heat during solidification, equal solid and liquid thermal conductivities, a small distribution coefficient, ellipsoidal dendrite shapes, and a hexagonal arrangement of dendrites [38]. Based on these assumptions, the average primary dendrite arm spacing for the condition of high solidification rate is calculated according to Equation 1.6 [38].

$$\lambda_1 = 4.3\Delta T'^{1/2}\left(\frac{D\Gamma}{\Delta T_0 k}\right)^{1/4} G^{-1/2}V^{-1/4} \tag{1.6}$$

In this equation, ΔT_0 and $\Delta T'$ are the equilibrium and non-equilibrium melting ranges and Γ is the Gibbs-Thompson coefficient (= $\gamma/\Delta S$ in the preceding equation). By lumping the alloy-dependent properties, the relationship between average primary dendrite arm spacing and thermal conditions is given (Equation 1.7), where A_1 is a parameter dependent on alloy composition only.

$$\lambda_1 = A_1 G^{-1/2}V^{-1/4} \tag{1.7}$$

Despite the significant assumptions employed in the above two models, reasonable agreement with experimental measurement is observed [28-38,47,52,53,64-107]. More recently, other models have been developed that attempt to describe a more general growth condition [100,104,108,109]. Inevitably, the more recent models become more

complex and more difficult to validate, limiting their widespread use. On the other hand, new theories related to the history dependence of primary dendrite arm spacing for a given thermal condition have been proposed, suggesting a stable *range* of PDAS for a given thermal condition [110-114].

Predictions of secondary dendrite arm spacing take the form of similar analytical expressions (Equation 1.8) which are based on coarsening kinetics through the melting range [23,24].

$$\lambda_2 = A_2 L^{-1/3} \text{or } \lambda_2 = A_3 t_s^{1/3} \tag{1.8}$$

In this equation, λ_2 is the secondary dendrite arm spacing (SDAS), A_2 is parameter dependent on alloy composition only, L is the cooling rate through the melting range, and t_s is the solidification time. The expression has been represented both ways in the literature since the solidification time and melting-range cooling rate can be related via the melting range. Thus, the faster the cooling rate through the melting range, the less time available to coarsen, and the finer the resulting secondary dendrite arm spacing.

One assumption that is of particular interest to this work is the assumption of a planar solidification interface normal to the primary orientation direction. Engineering-components and industrially-relevant process conditions inherently violate this assumption, which has been shown for experiments of off-axis heat flow [45,109] and experiments evaluating abrupt changes in geometry [28,31,32,77]. As a more fundamental understanding of dendrite growth is obtained by improved experimental techniques and computational capabilities, the prediction of dendrite structure via

microstructure modeling and the consideration of thermal and solutal fields during solidification becomes feasible.

Further refining model scale, dendritic structure has been tracked during solidification by using cellular automata techniques on the scale of a few dendrites that account for probability of grain nucleation and growth [40,115-122] based on thermal diffusion considerations. A probability distribution of nucleation propensity over a range of thermal undercooling is applied locally to determine the presence of a nucleated grain [115]. Growth is calculated according to the Kurz-Giovanola-Trivedi (KGT) model for growth velocity in an undercooled melt [123]. From this approach, stray grain nucleation has been predicted at the component scale. However, the details of competitive growth required consideration of the interaction between solidifying dendrites. This approach necessitates a model at the length scale of the solidifying dendrites in order to account for diffusion-limited growth, which is the most physically appropriate calculation. Therefore, despite the ability for continuum-based models to qualitatively predict microstructure development during ideal solidification processes, there is a need to model at smaller length scales in order to capture the physics of solidification, specifically the effect of solute diffusion.

Micro-scale Model Development

Phenomenological models have been used in the evaluation of solidification behavior but have limitations due to assumptions employed, as discussed previously. Thus, more physically-realistic models of microstructure formation during solidification that account

for solute redistribution in the solidifying melt and the associated dendritic growth have also been developed. Generally, these microstructure models of dendritic solidification are capable of two-dimensional simulations of simplified alloy compositions and highly simplified solidification conditions (flat solidification front and axial thermal gradient) in order to investigate the formation and growth of hypothetical microstructures. In the case of complex and/or thick geometries, or in the presence of a non-axial thermal field, these model assumptions do not apply.

The framework for models capable of handling more complex processing conditions has been developed recently. Dendrite growth has been modeled via coupled cellular-automata (CA) and finite difference (FD) methods [56,112,120,34-137]. The benefit of this modeling approach is that large domains can be evaluated with moderate computation times. CA is used to model growth and nucleation, while the FD method is used to evaluate solute diffusion. Other techniques have been applied to dendritic solidification, including CA-FV (finite volume) [138], phase field [139,140], dendrite grain envelope [141,142] and level set [143-148] techniques. Nucleation has also been analyzed via a Monte Carlo technique [149]. The CA-FV technique is a similar approach to the CA-FD approach employed with this research. The dendrite grain envelope technique does not provide a complete morphological representation of the dendritic structure while the Monte Carlo technique does not consider the surface-energy anisotropy of dendritic growth. The phase field model is a technique that requires small time and spatial steps, thus requiring unrealistic computational requirements for modeling of domains on the scale of multiple dendrites growing in three dimensions. In addition,

this approach utilizes fitting parameters to simulate the local kinetics and thermodynamics. The level set technique is also promising and does not require a pre-defined length scale. The diffusion-limited, dendrite-growth model based on a CA-FD technique is most relevant to this research and is discussed in the remainder of this section.

There have been continued advances in the CA-FD modeling capabilities, including the extension to three dimensions, the inclusion of stochastic heterogeneous nucleation, the consideration of liquid convection, the extension to multi-component alloys or the application of non-uni-directional heat flow – including angled or curved time-dependent solid-liquid interfaces (Figure 1.10) [34-125]. These extensions enable the prediction of the scale of the microstructure as well as the propensity to form defects, such as the formation of stray grains via nucleation or freckles via thermosolutal convection for more applicable processing conditions [34,124]. Unfortunately, many of these extensions are applied selectively to small spatial domains due to computational limitations, thus restricting evaluation to a limited range of microstructure evolution under specific processing conditions.

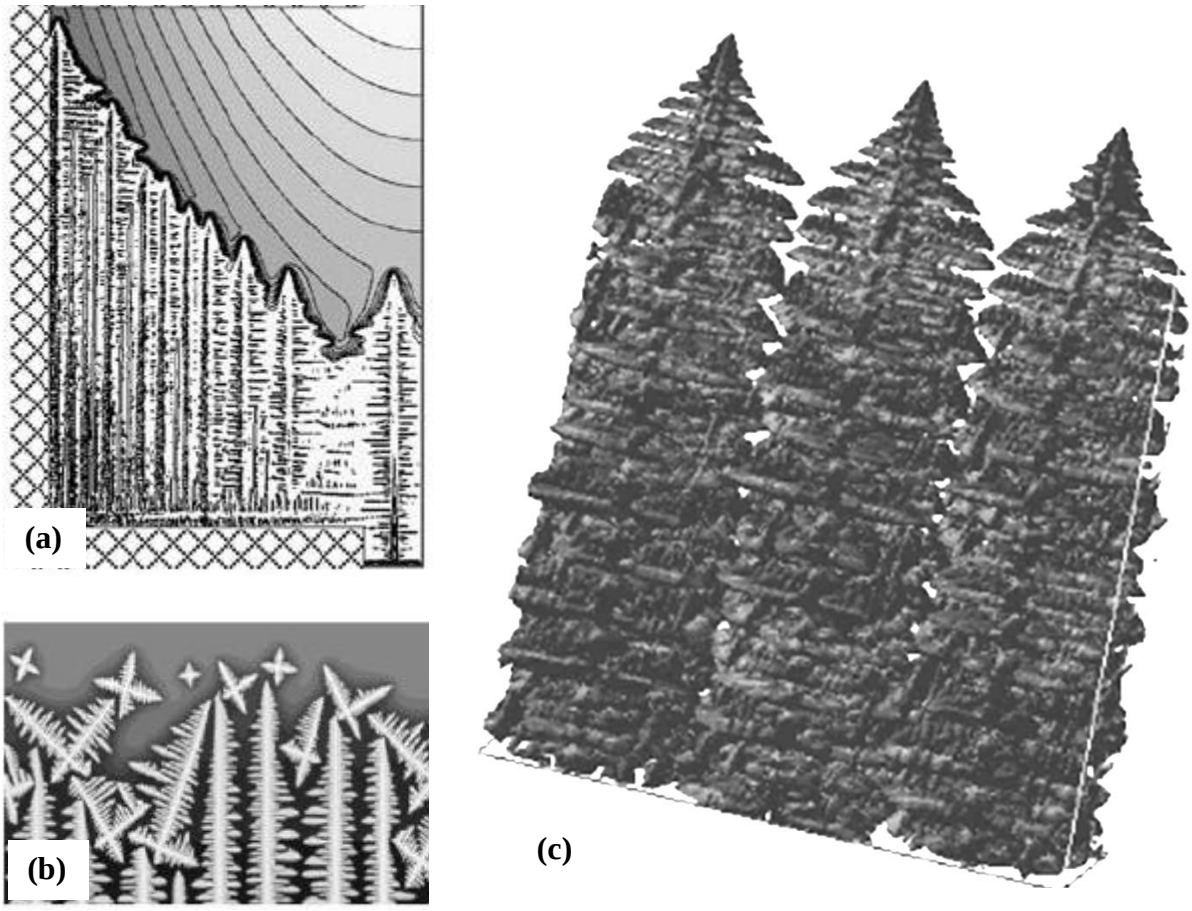

Figure 1.10 – Simulation results of advanced microstructure models, extending the capability of the model to (a) non-uni-directional thermal fields [31], (b) stochastic nucleation [56] and (c) three dimensions [112].

Application of Models to Solidification Problems

With the advent of mature models and efficient computational systems, the application of solidification models to process-relevant thermal conditions and component scales has been realized. Carefully validated FEM simulations demonstrated the sensitivity of the thermal field during solidification and predicted dendrite scale to withdrawal rate and utilization of the LMC process for a fixed geometry with a large cross-sectional area [83].

Airfoil geometries and thermal conditions have been simulated with FEM models for the Bridgman process and were validated with experimental observation [31,33,34,126]. The sensitivity of dendritic structure to thermal conditions during solidification was modeled to successfully predict the columnar-to-equiaxed transition (CET) [57-60,115]. Freckle formation during ingot solidification has also been predicted by consideration of thermosolutal convection ahead of the dendrite-growth front [124]. CA models used in conjunction with continuum-based, FEM models have been developed to predict the dendritic macrostructure, including nucleation and growth of columnar grains during directional solidification [33,40,115,116,119,122]. Finally, CA-FE models were used to predict grain selection in order to optimize the geometry of single-crystal selectors [121]. These CA-FE models were capable of predicting the formation of nucleated grains based on a probability distribution as a function of the local undercooling but did not resolve the dendritic microstructure [115].

Other microstructure-scale models have also been applied to solidification problems at the scale of the dendritic microstructure. CA-FD models have been used to predict the evolution of dendritic growth based on local thermal and solutal conditions [56,34-127,150]. Accurate thermal conditions, required as input data, were obtained using commercially-available FEM techniques. Competitive dendrite growth hypotheses were evaluated with this model and validated with experiment [126,128]. Stochastic nucleation based on solute-adjusted undercooling with distributions for both heterogeneous and homogeneous nucleation was applied to airfoil geometries and also validated [31,56,34,125,129,130]. Seed melt-back was evaluated by considering the re-

melting and subsequent growth of dendrite structure from a seed to infer grain nucleation from maximum undercooling in the liquid [35,125,127]. Ultimately, the CET based on thermal gradient and solidification rate was demonstrated [56,130]. However, because the models are only capable of simulating simplified alloy compositions, their ability to predict microstructures characteristic of the multi-component, commercially-relevant alloys is limited.

Summary

While there has been substantial progress in controlling and predicting the features of dendritic growth during directional solidification, a number of significant questions remain.

- What are the critical process parameters for LMC?
    - Initial analysis on heat transfer mechanisms has been completed and suggests a change in the dominant heat-transfer step with the LMC process, thus limiting the applicability of critical Bridgman-process conditions for the LMC process.
    - Changes in withdrawal rate and furnace temperature have been studied for a given geometry, but other critical process parameters that are fixed during the process have not been defined or optimized.
    - The effects of the floating baffle and cooling-medium conditions on solidification have not yet been studied in detail.

- An incomplete description of the detailed thermal conditions and the use of non-standardized process conditions limit the ability to extrapolate previous experimental investigations to new alloys or casting conditions.
- At the same time, continuum-scale computational models have not been well validated. Combined, these factors resulted in a discussion of observations without a fundamental understanding of the thermal process.
- Establishing an improved understanding of the solidification process and determining the critical processing parameters are needed. From this new knowledge, insights to solidification behavior can be developed, independent of casting geometry or specific process conditions

- Can the fundamental understanding of heat transfer be applied to a more complex geometry to provide useful insight to microstructure evolution as it relates to thermal conditions during solidification?
  - Transverse growth has been shown to occur in materials during LMC.
  - Avoidance of processing conditions that give rise to lateral growth is preferred since breakdown of solidification can occur. Due to geometrical complexity, however, lateral growth at the surface of a casting is not always avoidable.
  - A detailed characterization of the dendritic structure in regions of lateral growth and at the interface between regions of axial and lateral growth has not been completed.
  - There is a need to establish a mechanism and understand the conditions that promote the formation of lateral growth, as well as identify differences in the associated defect structure.

- Can state-of-the-art, microstructure models of solidification be applied to more complex thermal environments to predict the formation of lateral growth and nucleated grains observed experimentally?
    - Application of micro-scale models to the thermal environments present during LMC has not been completed. It is anticipated that faster solidification rates and high solidification-front curvatures may violate model assumptions.
    - More research is needed to determine their applicability.
- What are the critical process variables (thermal gradient, solidification rate, solidification-front inclination angle, microstructure scale, or thermal perturbation) that drive the formation of lateral growth and the breakdown of single-crystal solidification?
    - Once the morphology of the dendritic structure is determined under a range of processing conditions, the presence of lateral growth can be associated to specific thermal conditions that can be used as an input to dendritic-growth models to better understand the onset of lateral growth.
    - This integration of experiments with multi-scale modeling has not been attempted for the LMC process for investigating the morphology of dendritic growth. Such an effort would provide useful insight to understanding solidification behavior with 3D heat extraction.
- Are there macroscopic analytical criteria, such as the inclination angle of the solidification front, that can be utilized to predict instability of microstructure and defect formation, in order to reduce the reliance on computationally-expensive microstructure models?

- Analytical criteria developed on the basis of detailed computational models have been successfully implemented for other microstructural features, such as microstructure scale, freckle formation and porosity.
- Determination of a macroscopic criterion for lateral growth could enable a simulated process design for avoidance of this disturbance in the growth process.

References

1. A.J. Elliott, G.B. Karney, M.F.X. Gigliotti and T.M. Pollock, *Superalloys 2004*, eds. K.A. Green, T.M. Pollock, H. Harada, T.E. Howson, R.C. Reed, J.J. Schirra and S. Walston (The Minerals, Metals & Materials Society, 2004) 421-430.
2. C.T. Sims, N.S. Stoloff and W.C. Hagel, *Superalloys II*, New York: John Wiley & Sons, 1987.
3. R.C. Reed, *The Superalloys: Fundamentals and Applications*, Cambridge University Press, 2006.
4. E.W. Ross and K.S. O'Hara, *Superalloys 1996*, eds. R.D. Kissinger, D.J. Dye, D.L. Anton, A.D. Cetel, M.V. Nathal, T.M. Pollock and D.A. Woodford (The Minerals, Metals & Materials Society, 1996) 19-25.
5. J. Zhang and R.F. Singer, *Metall and Mater Trans A*, 35 (3) (2004) 939-946.
6. M. McLean, *Directionally Solidified Materials for High Temperature Service*, London: The Metal Society, 1983.
7. D.N. Duhl, "Directionally Solidified Superalloys," *Superalloys II*, ed. C.T. Sims, N.S. Stoloff and W.C. Hagel, New York: John Wiley & Sons, 1987, 189-214.
8. E.W. Ross and C.T. Sims, "Nickel-Base Alloys," *Superalloys II*, ed. C.T. Sims, N.S. Stoloff and W.C. Hagel, New York: John Wiley & Sons, 1987, 97-134.
9. A. Wagner, B.A. Shollock and M. McLean, *Mat Sci Eng A*, 374 (2004) 270-279.
10. M. Gell, D.N. Duhl and A.F. Giamei, *Superalloys 1980*, eds. J.K. Tien, S.T. Wlodek, H. Morrow, M. Gell and G.E. Maurer (The Metallurgical Society, 1980) 205-214.
11. A.D. Cetel and D.N. Duhl, *Superalloys 1988*, eds. S. Reichman, D.N. Duhl, G. Maurer, S. Antolovich and C. Lund (The Metallurgical Society, 1988) 235-244.

12. K. Harris, G.L. Erikson, S.L. Sikkenga, W.D. Brentnall, J.M. Aurrecoechea and K.G. Kubarych, *Superalloys 1992*, eds. S.D. Antolovich, R.W. Stusrud, R.A. MacKay, D.L. Anton, T. Khan, R.D. Kissinger and D.L. Klarstrom (The Minerals, Metals & Materials Society, 1992) 297-306.

13. T.M. Pollock and W.H. Murphy, *Metall Trans A*, 27 (1996) 1081-1094.

14. M.G. Ardakani, N. D'Souza, A. Wagner, B.A. Shollock and M. McLean, *Superalloys 2000*, eds. T.M. Pollock, R.D. Kissinger, R.R. Bowman, K.A. Green, M. McLean, S. Olson and J.J. Schirra (The Mineral, Metals & Materials Society, 2000) 219-228.

15. K. Harris and J.B. Wahl, *Superalloys 2004*, eds. K.A. Green, T.M. Pollock, H. Harada, T.E. Howson, R.C. Reed, J.J. Schirra and S. Walston (The Minerals, Metals & Materials Society, 2004) 45-52.

16. J.B. Wahl, K.Harris and T.L. Moore, *Advanced Materials and Processes for Gas Turbines*, ed. G. Fuchs, A. James, T. Gabb, M. McLean and K. Harada (The Minerals, Metals and Materials Society, 2003) 129-135.

17. J.B. Wahl and K. Harris, *Proceedings of Turbine Expo* (ASME, 2006) GT2006-90267.

18. C.Y. Jo, D.H. Kim, Y.S. Yoo, D.H. Ye and J.H. Lee, *Mat Sci Forum*, 486-487 (2005) 460-463.

19. S. Tin, T.M. Pollock and W.T. King, *Superalloys 2000*, eds. T.M. Pollock, R.D. Kissinger, R.R. Bowman, K.A. Green, M. McLean, S. Olson and J.J. Schirra (The Mineral, Metals & Materials Society, 2000) 201-210.

20. G.W. Meetham, *Metals Technol*, 11 (1984) 414-418.

21. S. Walston, A. Cetel, R. MacKay, K. O'Hara, D. Duhl and R. Dreshfield, *Joint Development of a Fourth Generation Single Crystal Superalloy*, NASA Report (2004) 213062.

22. M. Konter and M. Thumann *Journal of Materials Processing Technology*, 117 (2001) 386-390.

23. M.C. Flemings, *Solidification Processing*, New York, NY: McGraw-Hill, 1974.

24. W. Kurz and D.J. Fisher, *Fundamentals of Solidification*, 4th rev. ed., Enfield, NH: Trans Tech Publications, 1998.

25. W.R. Freeman, Jr, "Investment Casting," *Superalloys II*, ed. C.T. Sims, N.S. Stoloff and W.C. Hagel, New York: John Wiley & Sons, 1987, p. 411-439.

26. F.L. Versnyder and R.W. Guard, *Trans ASM*, 52 (1960) 485.

27. F.L. Versnyder and M.E. Shank, *Mat Sci Eng*, 6 (1970) 213.

28. A.J. Elliott, S. Tin, W.T. King, S.-C. Huang, M.F.X. Gigliotti and T.M. Pollock, *Metall and Mater Trans A*, 35 (2004) 3221-3231.

29. M. Meyer ter Vehn, D. Dedecke, U. Paul and P.R. Sahm, *Superalloys 1996*, eds. R.D. Kissinger, D.J. Dye, D.L. Anton, A.D. Cetel, M.V. Nathal, T.M. Pollock and D.A. Woodford (The Minerals, Metals & Materials Society, 1996) 471-479.

30. B.B. Seth, *Superalloys 2000*, eds. T.M. Pollock, R.D. Kissinger, R.R. Bowman, K.A. Green, M. McLean, S. Olson and J.J. Schirra (The Mineral, Metals & Materials Society, 2000) 3-16.

31. W. Wang, A. Kermanpur, P.D. Lee and M. McLean, *J Mater Sci*, 38 (2003) 4385-4391.

32. U. Paul and P.R. Sahm, *Mat Sci Eng A*, 173 (1993) 49-54.

33. A. Kermanpur, N. Varahram, P. Davami and M. Rappaz, *Metall and Mater Trans B*, 31 (2000) 1293-1304.

34. X.L. Yang, H.B. Dong, W. Wang and P.D. Lee, *Mat Sci Eng A*, 386 (2004) 129-139.

35. N. D'Souza, P.A. Jennings, X.L. Yang, H.B. Dong, P.D. Lee and M. McLean, *Metall Trans B*, 36 (2005) 657-666.

36. J. Madison, "Investigating Solidification Defect Formation by Three Dimensional Reconstruction of Dendritic Structure," (Ph.D. thesis, University of Michigan, 2010).

37. J.D. Hunt, *Solidification and Casting of Metals*, ed. J.D. Hunt (London: The Metals Society, 1979), 3-9.

38. W. Kurz and D.J. Fisher, *Acta Metall*, 29 (1) (1981) 11-20.

39. P.N. Quested and M. McLean, *Mat Sci Eng*, 65 (1984) 171-180.

40. M. Newell, K. Devendra, P.A. Jennings and N. D'Souza, *Mater Sci EngA*, 412 (2005) 307-315.

41. A.F. Giamei and J.G Tschinkel, *Metall and Mater Trans A*, 7 (1976) 1427-1434.

42. V.A. Willis and D.G. McCartney, *Mat Sci Eng A*, 145 (1991) 223-232.

43. H.S. Whitesell and R.A. Overfelt, *Mat Sci Eng A*, A318 (2001) 264-276.

44. L. Liu, T. Hang, M. Zou, W. Zhang, J. Zhang and H. Fu, *Superalloys 2008*, ed. R.C. Reed, K.A. Green, P. Caron, T.P. Gabb, M.G. Fahrmann, E.S. Huron and S.R. Woodard (Warrendale, PA: TMS, 2008) 287-294.

45. R.N. Grugel and Y. Zhou, *Metall Mater Trans A*, 20 (1989) 969-973.

46. D. Walton and B. Chalmers, *Trans Metall Soc*, AIME 215 (1959) 447.

47. S-C. Huang and M.E. Glicksman, *Acta Metall*, 29 (1981) 717-734.

48. N. D'Souza, M.G. Ardakani, M. McLean and B.A. Shollock, *Metall Mater Trans A*, 31 (2000) 2877-2886.

49. N. D'Souza, M.G. Ardakani, A. Wagner, B.A. Shollock and M. McLean, *J Mat Sci*, 37 (2002) 481-487.

50. Y. Zhou and N.R. Green, *Superalloys 2008*, ed. R.C. Reed, K.A. Green, P. Caron, T.P. Gabb, M.G. Fahrmann, E.S. Huron and S.R. Woodard (Warrendale, PA: TMS, 2008) 317-324.

51. Y.Z. Zhou, A. Volek and N.R. Green, *Acta Mat*, 56 (2008) 2631-2637.

52. J.D. Miller and T.M. Pollock, *Proceedings of the 2009 International Symposium on Liquid Metal Processing and Casting*, ed. P.D. Lee, A. Mitchell and R. Williamson (The Minerals, Metals & Materials Society, 2009) 119-126.

53. L. Li, R.A. Overfelt, *J Mat Sci*, 37 (2002) 3521-3532.

54. J.D. Hunt, Solidification Cast Met., *Proc. Int. Conf. Solidification*, (Met. Society, 1979) 3.

55. X. Wan, Q. Han and J.D. Hunt, *Acta Mater*, 45 (10) (1997) 3975-3979.

56. H.B. Dong, X.L. Yang, P.D. Lee and W. Wang, *J Mater Sci*, 39 (2004) 7207-7212.

57. C.Y. Wang and C. Beckermann, *Metall and Mater Trans A*, 25 (1994) 1081-1093.

58. C.Y. Wang and C. Beckermann, *Metall and Mater Trans A*, 27 (1996) 2754-2764.

59. C. Beckermann, J.P. Gu, W.J. Boettinger, *Metall Trans A*, 31 (2000) 2545-2557.

60. J.D. Hunt, *Mat Sci Eng*, 65 (1984) 75-83.

61. W.A. Tiller, K.A. Jackson, J.W. Rutter and B. Chalmers, *Acta Metall*, 1 (1953) 428-437.

62. N. D'Souza, M. Newell, K. Devendra, P.A. Jennings, M.G. Ardakani and B.A. Shollock, *Mat Sci Eng A*, 413-414 (2005) 567-570.

63. R.J. McDonald and J.D. Hunt, *Trans Metall Soc AIME*, 245 (1969) 1993-1997.

64. A.F. Giamei and B.H. Kear, *Metall Trans*, 1 (1970) 2185.

65. S.M. Copley, A.F. Giamei, S.M. Johnson and M.F. Hornbecker, *Metall Trans*, 1 (1970) 2193-2204.

66. S. Tin and T.M. Pollock, *Metall and Mater Trans A*, 21 (7) (2001) 1743-1753.

67. S. Tin and T.M. Pollock, *J Mat Sci*, 39 (2004) 7199-7205.

68. J.R. Sarazin and A. Hellawell, *Metall Trans A*, 19 (1988) 1861-71.

69. M.I. Bergman, D.R. Fearn, J. Bloxham and M.C. Shannon, *Metall Trans A*, 28 (1997) 859-66.

70. S. Tin and T.M. Pollock, *Metall and Mater Trans A*, 34 (9) (2003) 1953-1967.

71. J.G. Tschinkel, A.F. Giamei and B.H. Kearn, "Apparatus for Casting of Directionally Solidified Articles," (U.S. Patent No 3,763,926), 1973.

72. M. Konter, E. Kats and N. Hofmann, *Superalloys 2000*, eds. T.M. Pollock, R.D. Kissinger, R.R. Bowman, K.A. Green, M. McLean, S. Olson and J.J. Schirra (The Mineral, Metals & Materials Society, 2000) 189-200.

73. L.D. Graham and B.L. Rauguth, "Method and device for casting a metal article using a fluidized bed," (European Patent EP1153681) 16 JAN 2008.

74. J. Grossmann, J. Preuhs, W. Esser and R.F. Singer, *Proceedings of the 1999 International Symposium on Liquid Metal Processing and Casting*, eds. A. Mitchell, L. Ridgway and M. Baldwin (The Minerals, Metals & Materials Society, 1999) 31-40.

75. F. Hugo, U. Betz and J. Ren, *Proceedings of the 1999 International Symposium on Liquid Metal Processing and Casting*, eds. A. Mitchell, L. Ridgway and M. Baldwin (The Minerals, Metals and Materials Society, 1999) 16-30.

76. T.J. Fitzgerald and R.F. Singer, *Metall Trans A*, 28 (1997) 1377-1383.

77. A.J. Elliott, "Directional Solidification of Large Cross-Section Ni-Base Superalloy Castings via Liquid Metal Cooling," (Ph.D. thesis, University of Michigan, 2005).

78. A. Lohmüller, W. Esser, J. Grossman, M. Hördler, J. Preuhs and R.F. Singer, *Superalloys 2000*, ed. T.M. Pollock, R.D. Kissinger, R.R. Bowman, K.A. Green, M. McLean, S.L. Olson, and J.J. Schirra (Warrendale, PA: TMS, 2000) 181-188.

79. M. Lamm and R.F. Singer, *Metall and Mater Trans A*, 38 (2007) 1177.

80. D.R. Wood and R.M. Cook, *Metallurgia*, 67 (1963) 109-117.

81. R.L. Dreshfield, W.A. Johnson and G.A. Maurer, "Effects of Tin on Microstructure and Mechanical Behavior of Inconel 718" (Report No. TM-86866, NASA, 1984).

82. R.T. Holt and W. Wallace, *Int Met Rev*, 21 (1976) 1-24.

83. A.J. Elliott and T.M. Pollock, *Metall and Mater Trans A*, 38 (2007) 871-882.

84. C. Brundidge, D. VanDrasek, B. Wang and T.M. Pollock, *Proceedings of the 2009 International Symposium on Liquid Metal Processing and Casting*, ed. P.D. Lee, A. Mitchell and R. Williamson (The Minerals, Metals & Materials Society, 2009) 107-117.

85. S. Balsone, G. Feng, L. Peterson and J. Schaeffer, *Solidification Processes and Microstructures: A Symposium in Honor of Wilfried Kurz*, ed. M. Rappaz, C. Beckermann and R. Trivedi (The Minerals, Metals & Materials Society, 2004) 77-83.

86. A. Kermanpur, N. Varahraam, E. Engilehei, M. Mohammadzadeh and P. Davami, *Mat Sci Technol*, 16 (5) (2000) 579-586.

87. L. Liu, T.W. Huang, J. Zhang and H.Z. Fu, *Material Letters*, 61 (2007) 227-230.

88. C. Liu, J. Shen, J. Zhang and L. Lou, *J Mater Sci Technol*, 26 (4) (2010) 306-310.

89. J. Zhang and L.H. Lou, *J Mater Sci Technol*, 23 (2007) 289-300.

90. M. Rappaz and M Rettenmayr, *Curr Opinion Solid State Mater Sci*, 3 (1998) 275-282.

91. L. Nastac, *Modeling and Simulation of Microstructure Evolution in Solidifying Alloys*, Kluwer Academic Publishers, 2004.

92. M. Asta, C. Beckermann, A. Karma, W. Kurz, R. Napolitano, M. Plapp, G. Purdy, M. Rappaz and R. Trivedi, *Acta Mater*, 57 (2009) 941-971.

93. *ProCAST User Manual Version 2009.1* (Paris, France: ESI Group, 2009).

94. X. Xue and L. Xu, *Mat Sci Eng A*, 499 (2009) 69-73.

95. J.S. Langer and H. Müller-Krumbhaar, *J Cryst Growth*, 42 (1977) 11.

96. J.S. Langer and H. Müller-Krumbhaar, *Acta Metall*, 26 (1978) 1681.

97. J.S. Langer and H. Müller-Krumbhaar, *Acta Metall*, 26 (1978) 1689.

98. H. Müller-Krumbhaar and J.S. Langer, *Acta Metall*, 26 (1978) 1697.

99. W.W. Mullins and R.F. Sekerka, *J Appl Phys*, 35 (1964) 444.

100. J.D. Hunt and S-Z. Lu, *Metall Trans A*, 27 (3) (1996), 611-623.

101. K. Somboonsuk, J.T. Mason and R. Trivedi, *Metall Trans A*, 15 (6) (1984), 967-975.

102. R. Trivedi, *Metall Trans A*, 15 (6) (1984) 977-982.

103. H. Weidong, G. Xingguo and Z. Yaohe, *J Cryst Growth*, 134 (1993) 105-115.

104. D. Ma and P.R. Sahm, *Metall Trans A*, 29 (3) (1998) 1113-1119.

105. K.A. Jackson, J.D. Hunt, D.R. Uhlmann and T.P. Seward III, *Trans AIME*, 236 (1966) 149.

106. J. Lipton, M.E. Glicksman and W. Kurz, *Mat Sci and Eng*, 65 (1) (1984) 57-63.

107. M.A. Chopra, M.E. Glicksman and N.B. Singh, *Metall and Mater Trans A*, 19 (12) (1988) 3087-3096.

108. S.-Z. Lu and J.D. Hunt, *J Cryst Growth*, 123 (1-2) (1992) 17-34.

109. Ch.-A. Gandin, M. Eshelman and R. Trivedi, *Metall and Mater Trans A*, 27 (9) (1996) 2727-2737.

110. G. Ding, W. Huang, X. Lin and Y. Zhou, *J Cryst Growth*, 177 (1997) 281-288.

111. H.B. Dong, W. Wang and P.D. Lee, *Superalloys 2004*, ed. K.A. Green, T.M. Pollock, H. Harada, T.E. Howson, R.C. Reed, J.J. Schirra and S. Walston (The Mineral, Metals & Materials Society, 2004) 925-931.

112. W. Wang, P.D. Lee and M. McLean, *Acta Metall*, 51 (2003) 2971-2987.

113. J.A. Warren and J.S. Langer, *Phys Rev A*, 42 (6) (1990) 3518-3525.

114. J.A. Warren and J.S. Langer, *Phys Rev E*, 47 (4) (1993) 2702-2712.

115. M. Rappaz and Ch.-A. Gandin, *Acta Metall Mater*, 41 (2) (1993) 345-360.

116. S.-M. Seo, I.-S. Kim, C.-Y. Jo and K. Ogi, *Mat Sci Eng A*, 449-451 (2007) 713-716.

117. Ch.-A. Gandin and M. Rappaz, *Acta Metall Mater*, 42 (7) (1994) 2233-2246.

118. M. Rappaz, Ch.-A. Gandin, J.-L. Desbiolles and Ph. Thevoz, *Metall and Mater Trans A*, 27 (1996) 695-705.

119. Ch.-A. Gandin, J.-L. Desbiolles, M. Rappaz and Ph. Thevoz, *Metall and Mater Trans A*, 30 (1999) 3153-3165.

120. Ch.-A. Gandin and M. Rappaz, *Acta Mater*,45 (5) (1997) 2187-2195.

121. H.J. Dai, J-C. Gebelin, M. Newell, R.C. Reed, N. D'Souza, P.D. Brown and H.B. Dong, *Superalloys 2008*, ed. R.C. Reed, K.A. Green, P. Caron, T.P. Gabb, M.G. Fahrmann, E.S. Huron and S.R. Woodard (Warrendale, PA: TMS, 2008) 367-376.

122. P. Carter, D.C. Cox, C.A. Gandin and R.C. Reed, *Mat Sci Eng A*, 280 (2000) 233-246.

123. W. Kurz, B. Giovanola and R. Trivedi, *Acta Metall*, 34 (5) (1986) 823-830.

124. L. Yuan, P.D. Lee, G. Djambazov and K. Pericleous, *Proceedings of the 2009 International Symposium on Liquid Metal Processing and Casting*, ed. P.D. Lee, A. Mitchell and R. Williamson (The Minerals, Metals & Materials Society, 2009) 31-46.

125. X.L. Yang, P.D. Lee and N.D'Souza, *JOM*, (May 2005) 40-44.

126. W. Wang, "A Mathematical Model of Dendritic Microstructures in Nickel-Based Superalloys," (Ph.D. thesis, University of London, 2003).

127. X.L. Yang, D. Ness, P.D. Lee and N. D'Souza, *Mat Sci Eng A*, 413-414 (2005) 571-577.

128. P.D. Lee, A. Chirazi, R.C. Atwood and W. Wang, *Mat Sci Eng A*, 365 (2004) 57-65.

129. R.C. Atwood and P.D. Lee, *Metall and Mater Trans B*, 33 (2002) 209-221.

130. H.B. Dong and P.D. Lee, *Acta Mater*, 53 (2005) 659-668.

131. P.D. Lee and J.D. Hunt, *Acta Mater*, 49 (2001) 1383-1398.

132. P.D. Lee, R.C. Atwood, R.J. Dashwood and H. Nagaumi, *Mat Sci Eng A*, 328 (2002) 213-222.

133. R.C Atwood and P.D. Lee, *Acta Mater*, 51 (2003) 5447-5466.

134. D. See, R.C. Atwood and P.D. Lee, *J Mat Sci*, 36 (2001) 3423-3435.

135. X.L. Yang, P.D. Lee, R.F. Brooks and R. Wunderlich, *Superalloys 2004*, ed. K.A. Green, T.M. Pollock, H. Harada, T.E. Howson, R.C. Reed, J.J. Schirra and S. Walston (The Minerals, Metals & Materials Society, 2004) 951-958.

136. M. Ganesan, D. Dye and P.D. Lee, *Metall and Mater Trans A*, 36 (2005) 2191-2204.

137. L. Beltran-Sanchez and D.M. Stefanescu, *Metall Trans A*, 34 (2) (2003) 367-382.

138. R. Shao, "Numerical and Experimental Study of Constrained Solidification," (Ph.D. thesis, Purdue University, 2007).

139. W.J. Boettinger and J.A. Warren, *Metall Trans A*, 27 (3) (1996) 657-669.

140. N. Warnken, A. Drevermann, D. Ma, S.G. Fries and I. Steinbach, *Superalloys 2008*, ed. R.C. Reed, K.A. Green, P. Caron, T.P. Gabb, M.G. Fahrmann, E.S. Huron and S.R. Woodard (Warrendale, PA: TMS, 2008) 951-960.

141. Ch.-A. Gandin, R.J. Schaefer and M. Rappaz, *Acta Mater*, 44 (8) (1996) 3339-3347.

142. T.-M. Wang, Y.-Q. Su, J.-J. Guo, I. Ohnaka and H. Yusada, *Trans Nonferrous Met Soc China*, 16 (2006) 753-759.

143. S. Chen, B. Merriman, S. Osher and P. Smereka, *J Computational Phys*, 135 (1997) 8-29.

144. F. Gibou, R. Fedkiw, R. Caflisch and S. Osher, *J Sci Computing*, 19 (1-3) (2003) 183-199.

145. L. Tan and N. Zabaras, *J Computational Physics*, 211 (2006) 36-63.

146. N. Zabaras, B. Ganapathysubramanian and L. Tan, *J Computational Physics*, 218 (2006) 200-227.

147. L. Tan and N. Zabaras, *J Computational Physics*, 221 (2007) 9-40.

148. L. Tan and N. Zabaras, *J Computational Physics*, 226 (2007) 131-155.

149. J.A. Spittle and S.G.R. Brown, *Acta Metall*, 37 (1989) 1803-1810.

150. S. Tin, P.D. Lee, A. Kermanpur, M. Rist and M. McLean, *Metall and Mater Trans A*, 36 (2005) 2493-2504.

CHAPTER 2

OBJECTIVES, EQUIPMENT, EXPERIMENTAL TECHNIQUES AND MODELING METHODS

The objective of this research is to determine the effect of three-dimensional heat extraction on dendritic growth and defect formation during directional solidification with non-conventional processing conditions such as encountered in the LMC process. In this effort, computational and experimental evaluations of solidification behavior during directional solidification are presented. The specific objectives for this work are the following:

- Improve understanding of non-ideal directional solidification.
- Establish the sensitivity of thermal predictions to variations in process conditions.
- Apply fundamental heat transfer knowledge to a novel casting concept and validate simulation predictions.
- Design a casting geometry to evaluate three-dimensional heat extraction conditions resulting in a change in dendritic morphology.
- Determine a mechanism for lateral growth and examine the competition between axial and lateral dendrite-growth fronts.
- Generate a means to predict lateral-growth formation using process simulations.
- Obtain the sensitivity of dendrite-growth predictions to thermal and solutal conditions at the solidification front.

In this section, a complete description of the equipment and materials used for this effort is provided. In particular, preparation of materials for directional solidification, the furnace in which the materials were cast and the methods in which the microstructure was evaluated and modeled is detailed. The methods discussed in this section are common to all solidification experiments described in this thesis. More specific information, such as alloys and geometries investigated, is discussed in subsequent chapters, as relevant.

Preparation of Materials for Directional Solidification

Ceramic investment molds utilized during this effort were fabricated by a casting vendor. The dimensions of the mold were limited by the furnace and included a maximum diameter of 152 mm and a maximum height of 305 mm. Several different casting geometries were investigated, and the details are discussed in the respective chapters. The nominal shell thickness was 8 mm. Compressed air was blown through the mold cavity prior to casting to remove any debris. If applicable, seeds were installed in the bottom of the molds and glued in place with alumina cement. Ceramic felt was attached to the bottom of the mold with alumina cement to prevent run-out during the pour. In some cases, as explained in subsequent chapters, the mold was strengthened through utilization of alumina fiber and cement. The fiber was Nextel 440 supplied by 3M. The alumina cement was AL-CEM and Caulkrete100 supplied by Zircar and Ransom & Randolph, respectively. The fiber was tightly wrapped several times around the area of the mold requiring additional strength and tied. The fiber was then wetted with alumina cement for additional strength.

Thermocouples were attached to the surface of the mold and bored into the interior of the mold for acquisition of the thermal data during solidification. The thermocouples were type S, composed of Platinum and Platinum-Rhodium, which are capable of measuring temperature up to 1600°C. The wires were electrically insulated by sheathing with alumina fiber and use of alumina rods near the thermocouple junction. Because the tin coolant was electrically conductive, the sheathed thermocouples were then wetted with alumina cement for the LMC process. Holes were drilled into the mold using diamond-coated drill bits and a rotary drill. Mold-embedded thermocouples were positioned at the mold-metal interface by measurement of the shell thickness. Alumina cement was used to seal the thermocouple in place and prevent run-out. Thermocouple wires were attached to the surface of the mold with molybdenum wire to prevent lift-off of the thermocouples after submersion into the tin due to buoyancy effects.

Directional Solidification Furnace

In this effort, SX Ni-base superalloys were cast using a furnace designed by ALD Vacuum Technologies (Figure 2.1). A unique capability of this furnace is that it can be configured in either the Bridgman or LMC mode, so that direct comparison between the two processes can be performed. Various systems are integrated in order to successfully produce directionally-solidified castings. A vacuum system including roughing and diffusion pumps reduces the pressure in the chamber to 10^{-4} mbar before the process is initiated. Due to the evolution of vapor at high temperatures in the melt, the pressure

during casting is observed to be 10^{-1} mbar. At process initiation, the temperature of a graphite mold heater is ramped to the soak temperature and maintained for the duration of the process. The mold heater has two-zone heating, allowing a different soak temperature for the top and bottom portions of the mold heater. For the experiments conducted in this research, both zones of the mold heater are maintained at 1550°C. As soon as the mold heater reaches the soak temperature, an induction system melts a charge of the desired alloy in a crucible for eventual delivery to the mold. The maximum weight of the ingot is 5 kg. The pour temperature is controlled by utilization of a nickel plug at the bottom of the crucible that melts at a higher temperature than the ingot, thus setting the pour temperature as the melting point of the plug. The pour rate is controlled by the diameter of a hole bored into the bottom of the crucible.

For this work, the diameter of the bored hole was 7.9 mm while the pour temperature was approximately 1475°C. After the ingot was melted and poured into the mold, a 10-minute hold was maintained before withdrawal in order for the temperature of the alloy to equilibrate to its surroundings, enabling a steady-state thermal condition prior to withdrawal. Obtaining a steady-state condition prior to withdrawal enabled more accurate prediction of solidification.

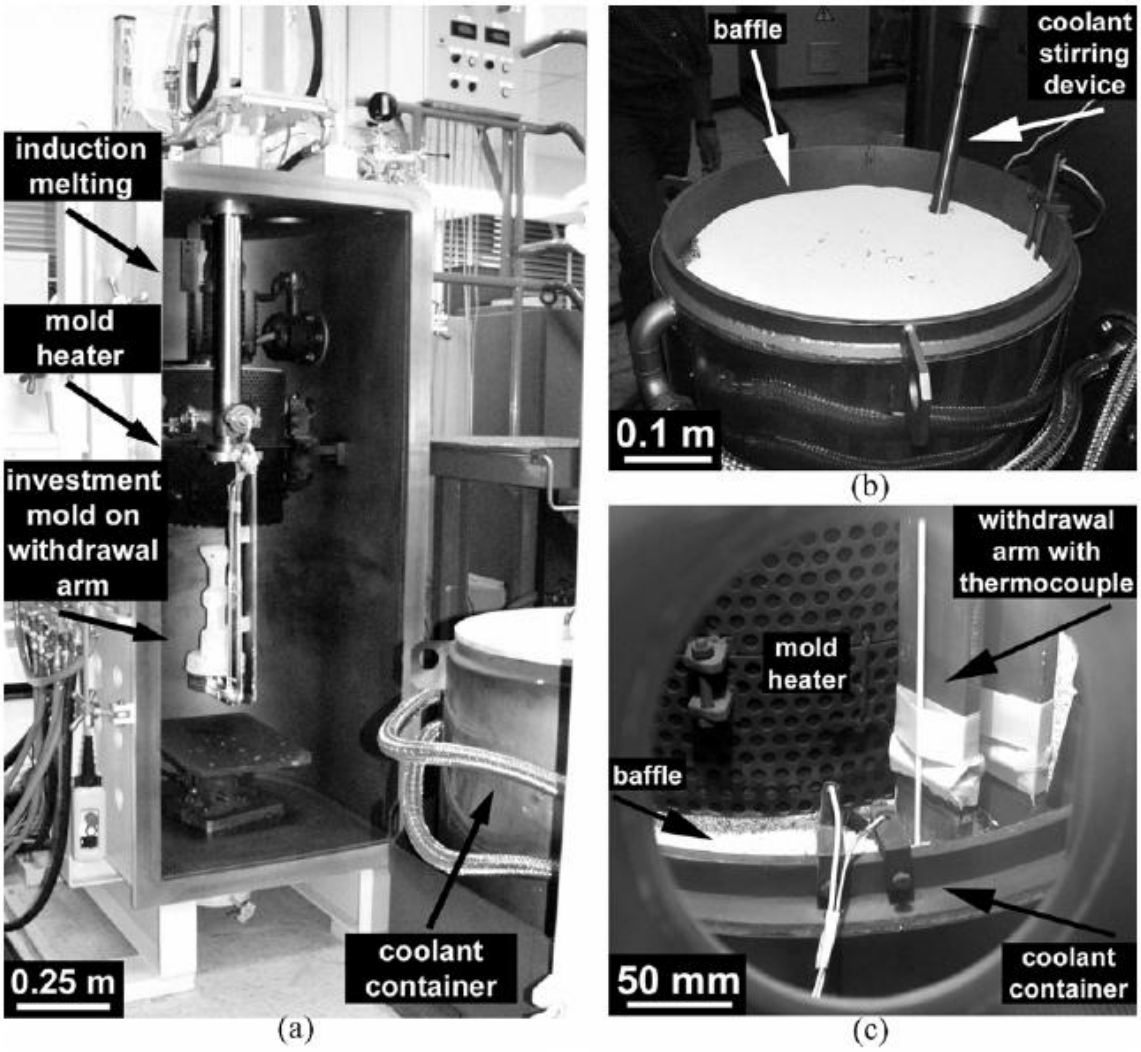

Figure 2.1 – (a) Image of casting furnace with mold seated on chill plate, (b) image of coolant container depicting floating baffle and coolant stiring device, and (c) image of the coolant container positioned below the mold heater during solidification [1].

Withdrawal is controlled by a mechanical withdrawal arm attached to the chill plate, upon which the mold was located. Details of the chill plate are sensitive to the mode (Bridgman or LMC) of the furnace. Thus far, the description of the furnace and its operation has been representative of either the Bridgman or LMC modes, as only the withdrawal sequence is altered depending on directional-solidification mode.

In the Bridgman mode, a water-cooled, copper chill plate is attached to the withdrawal arm and has a diameter of 152 cm. A fixed baffle located at the bottom of the mold heater is used to maintain a high temperature gradient between the hot and cold zones of the furnace. The furnace walls are water-cooled in order to promote cooling of the mold via radiation. In the LMC mode, a coolant and floating baffle are utilized. The coolant is composed of tin and stored in a 75 L bath that is heated through its walls with a thermal-oil system. The coolant is stirred with an impeller and motor to maintain a bulk temperature of 250°C. During withdrawal the temperature of the coolant at the surface of the baffle heats up to 325°C. The floating ceramic baffle is maintained at a thickness of 15 mm and serves as a thermal barrier between the liquid tin and mold heater of the furnace. The floating baffle is composed of mullite beads with a diameter of 3.2 mm. The chill plate has the same diameter as the chill plate in the Bridgman mode. It is composed of molybdenum and cooled by the liquid-metal-coolant bath. In order to ensure efficient cooling of the chill plate by the coolant, the initial position of the chill plate is 50 mm below the standard Bridgman position.

Switching modes of the furnace from Bridgman to LMC requires installation of the LMC bath, removal of the Bridgman chill plate and mounting of the LMC chill plate. The fixed baffle is removed from the mold heater. Before operating the furnace, the thermal-oil system is turned on until the bath reaches the set-point temperature of 250°C. Changing furnace configuration to Bridgman entails removal of the molten bath and LMC chill plate. The Bridgman chill plate is installed and internal water-cooling system

initiated. The fixed baffle at the bottom of the mold heater is also positioned in place. All other systems within the furnace are used equivalently in both modes.

Methods for Microstructure Evaluation

Following solidification, the investment casting mold was removed from the single crystal by careful utilization of a hammer. The casting was then lightly blast with alumina beads and cleaned for surface evaluation. In this effort, a macro-etchant was applied to the surface of the casting for identification of orientation defects, such as stray grains or freckles. The casting was immersed in an etchant for 20-30 minutes. The etchant was composed of 100 mL hydrochloric acid, 14 mL water, 2.5 mL nitric acid and 20 g of ferric chloride. Thereafter, the material was sectioned for microstructural evaluation at specific locations and orientations within the casting. After sectioning, the surfaces were metallographically prepared through standard grinding and polishing techniques. An etchant was applied to the polished surfaces for 3-5 seconds to reveal the dendritic structure. The etchant was composed of 33 pct acetic acid, 33 pct nitric acid, 33 pct water and 1 pct hydrofluoric acid. Optical micrographs were taken using a Keyence VHX-600E and a Reichert-Jung MeF3-A optical microscope at 10-50x magnification. The microstructure scale was assessed by measurement of the primary and secondary dendrite arm spacing. The primary dendrite arm spacing (PDAS) is a measurement of the area-average distance between neighboring primary dendrites by quantification of dendrite cores in a section transverse to the growth direction (Figure 2.2a). A minimum

of 100 cores were manually measured in order to obtain a PDAS. The equation for PDAS is described by Equation 2.1, in which n_p is the number of dendrite cores per area.

$$\lambda_1 = {n_p}^{-1/2} \tag{2.1}$$

The secondary dendrite arm spacing (SDAS) is a measurement of the average distance between secondary arms along a primary dendrite arm (Figure 2.2b). A minimum number of 50 secondary arms were manually measured for a given SDAS. The equation for SDAS is Equation 2.2, where L is the length of the primary arm evaluated and n_s is the number of secondaries along the length.

$$\lambda_2 = \frac{L}{n_s - 1} \tag{2.2}$$

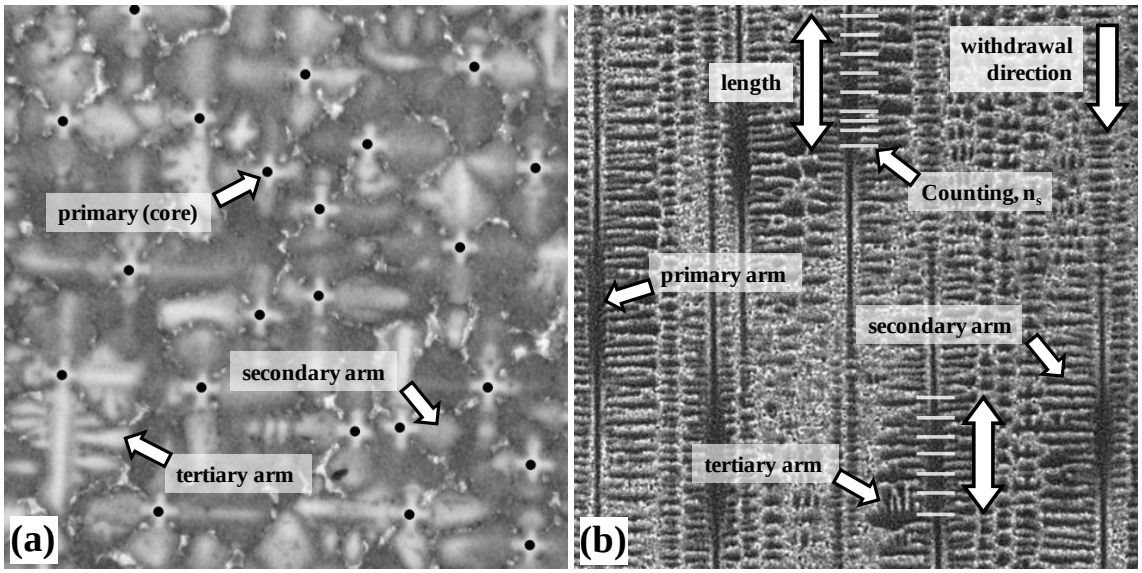

Figure 2.2 – Example micrographs (a) transverse to the growth direction, indicating the core-counting technique for measurement of the primary dendrite arm spacing and (b) longitudinal to the growth direction, indicating the technique for measurement of the secondary dendrite arm spacing.

All other details regarding experimental methods are specific to each chapter and are discussed in the respective sections.

Methods for Modeling the Directional Solidification Process

The ProCAST^{TM} model consisted of a mesh of the casting mold and the furnace equipment based on CAD files of the various elements of the furnace and mold (Figure 2.3a). Thermophysical material properties and initial temperature conditions for each material were applied to each domain, respectively. Interface heat transfer coefficients, emissivities and temperature boundary conditions were applied to appropriate surfaces. Radiation was simulated with complex view factor calculations. The withdrawal from the heater was simulated by moving domains relative to each other within the simulation.

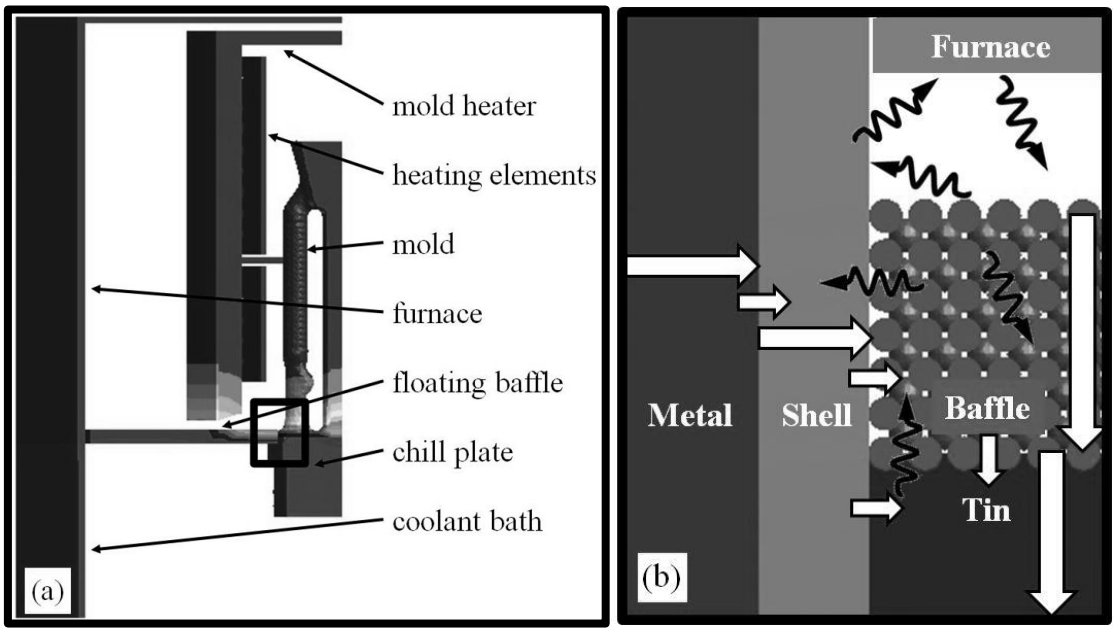

Figure 2.3 – (a) Image of ProCAST^{TM} representation of a casting mold within the furnace and (b) schematic representation of heat transfer during LMC, in which arrows represent assigned heat transfer conditions. The large white arrows represent thermal conductivity, the smaller white arrows depict an interface heat transfer coefficient and the black arrows signify radiation heat transfer.

The parameters used for the solidification modeling are summarized in the following discussion. These parameters were determined from the detailed modeling and validation effort discussed in Chapter 5. Simulation conditions that apply to both process modes are as follows. The casting domain utilized thermophysical properties predicted from a thermodynamic model based on the alloy composition (Table 2.1). Key thermophysical properties are density, heat capacity, heat of fusion, and the solidus and liquidus temperatures.

Table 2.1 – Key alloy properties for use in FE-based solidification modeling.

Alloy Designation	Liquidus (°C)	Solidus (°C)	Melting Range (°C)	Heat Capacity ($kJ\text{-}kg^{-1}\text{-}°C^{-1}$)	Latent Heat ($kJ\text{-}kg^{-1}$)	Thermal Conductivity ($W\text{-}m^{-1}\text{-}°C^{-1}$)
René N5	1402	1352	50	0.5-2.0	200	39-42
René N4	1345	1300	45	0.5-2.0	200	25-34
CMSX-486	1395	1330	65	0.5-2.0	200	25-34

The mold heater was modeled by assignment of thermophysical properties representative of graphite materials. An emissivity of 0.8 was applied to the surfaces of the domains representing the mold heater. In addition, a temperature boundary condition equal to the furnace temperature was applied to the heating elements. The water-cooled furnace walls were assigned material properties representative of stainless steel. A temperature boundary condition of 150 °C and an emissivity of 0.2 were applied to the interior surface of the domain representing the furnace. The investment-mold domain was assigned thermophysical properties representative of fused silica. An emissivity of 0.4 was assigned to the exterior surface of the investment mold. Quartz and alumina rods utilized to support the weight of the mold were simulated with thermophysical properties

representative of the respective materials. The material thermal properties (Table 2.2) and boundary conditions (Table 2.3) are tabulated for convenience.

Table 2.2 – Thermal properties of process materials utilized in FE-based simulations.

Material	Heat Capacity ($kJ\text{-}kg^{-1}\text{-}°C^{-1}$)	Thermal Conductivity ($W\text{-}m^{-1}\text{-}°C^{-1}$)
Furnace	0.5	16.4
Mold Heater	1.1	4.0
Floating Baffle	1.0	1.0
Mold	1.0	2.5
Support Rod	1.3	6.0

Table 2.3 – Emissivity and temperature boundary conditions for FE-based simulations.

Free Surface	Boundary Condition	Value
Mold Heater Interior	Emissivity	0.8
Mold Heater Exterior	Emissivity	0
Heating Elements	Temperature	1550 °C
Furnace Walls	Emissivity	0.2
Furnace Walls	Temperature	150 °C
Mold	Emissivity	0.4
Chill Plate	Emissivity	0.2
Chill-Plate Bottom	Temperature	150 °C
Floating-Baffle Top	Emissivity	0.2
Floating-Baffle Bottom	Temperature	325 °C

Interface heat-transfer coefficients (HTC) were assigned to adjacent domains (Table 2.4). The interface between the casting and investment mold was assigned an HTC representative of the metal shrinking away from the mold during solidification. This interface HTC had an initial value of 750 $W\text{-}m^{-2}\text{-}K^{-1}$ and decayed according to a power-law relationship representative of radiation heat transfer (Figure 2.4). The interface between the casting and chill plate was modeled by an interface HTC of 1000 $W\text{-}m^{-2}\text{-}K^{-1}$.

All other interface heat transfer coefficients were representative of ceramic-ceramic interfaces and were 500 $W\text{-}m^{-2}\text{-}K^{-1}$.

Table 2.4 – Interface heat-transfer coefficients between domains for FE-based simulations.

Interface	Value ($W\text{-}m^{-2}\text{-}°C^{-1}$)
Metal-Mold	See Figure 2.4
Metal-Chill	1000
Mold-Chill	500
Mold-Support	500

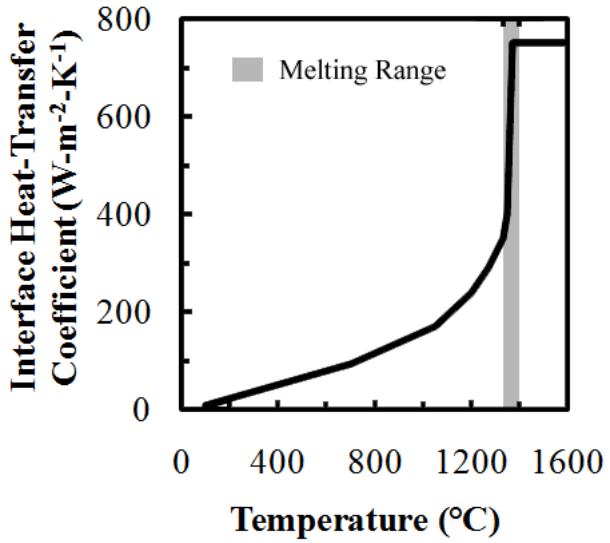

Figure 2.4 – Temperature-dependent interface heat-transfer coefficient between the casting and mold domains. The temperature is in reference to the casting temperature at the interface.

An element size of 0.5 mm was assigned to all casting domains, while an element size of 2 mm was assigned to all furnace domains. The time step for the simulations is governed by the convergence of the solution and is determined by the ProCAST™ software. The

maximum time step was assigned in relation to the withdrawal rate in order to provide an equal withdrawal distance of 0.4 mm between steps.

In the Bridgman mode, the water-cooling of the chill plate was simulated by assignment of a temperature boundary condition of 150 °C on the bottom surface of the chill plate. In the LMC mode, the floating baffle and coolant bath were simulated using a location-dependent heat transfer condition on the surface of the investment mold and chill plate. This boundary condition consisted of a location-dependent emissivity, ambient temperature and interface heat transfer coefficient (Table 2.5). The emissivity boundary condition simulated the emissivity of the investment mold and chill plate above the floating baffle and was turned off when the position of the node was below the top of the floating baffle. An ambient temperature condition was turned on below the top of the floating baffle for use in Newton's Law of Cooling, Equation 1.3. This boundary condition simulated the temperature gradient through the baffle and a uniform temperature within the coolant bath. Specifically, the temperature of the baffle was assumed to be 1100 °C at the top of the floating baffle and 325 °C at the bottom of the floating baffle based on experimental measurement [2]. The temperature in the coolant region, below the bottom of the baffle, was 250 °C as controlled by a thermal-oil system. The location-dependent interface heat-transfer coefficient at the surface of the mold was 0 $W\text{-}m^{-2}\text{-}K^{-1}$ above the floating baffle, 500 $W\text{-}m^{-2}\text{-}K^{-1}$within the floating baffle and 4000 $W\text{-}m^{-2}\text{-}K^{-1}$ within the coolant-bath region.

Table 2.5 – Location-dependent boundary conditions applied to surface of the mold in order to simulate interaction with the furnace, baffle and coolant.

Location	Emissivity	Interface Heat Transfer Coefficient ($W\text{-}m^{-2}\text{-}°C^{-1}$)	Ambient Temperature (°C)
Above Baffle	0.4	0	----
Within Baffle	0	500	1100 - 325 °C
Below Baffle	0	4000	250

In addition, in the LMC mode, a domain representing the floating baffle was positioned at the appropriate location but had an opening in the center to allow the mold to pass through, thus avoiding interpenetrating meshes. A thermal conductivity of 1 $W\text{-}m^{-1}\text{-}K^{-1}$ was assigned to the floating baffle. An emissivity of 0.2 was assigned to the top surface of the floating baffle domain. This condition allowed for simulation of radiation heat transfer between the floating baffle and mold heater which affects the temperature of the mold heater. A temperature boundary condition of 325 °C was applied to the bottom of the floating baffle domain to represent interaction with the coolant bath in order to maintain an appropriate temperature at the top of the baffle.

For each simulation, the thermal gradient, solidification rate and cooling rate at the solidification front were calculated at specific locations within the casting. From this data, the PDAS and SDAS were predicted according to dendrite-growth models (Equations 5.1 and 5.2) [3,4] .

$$\lambda_1 = A_1 G^{-1/2} V^{-1/4} \tag{2.3}$$

$$\lambda_2 = A_2 (GV)^{-1/3} \tag{2.4}$$

In these equations A_1 and A_2 are material-dependent constants, G is the *axial* temperature gradient, and V is the solidification rate. Because A_1 and A_2 are alloy dependent, one

location within one casting for each alloy was used to calibrate the constants. All other calculations for a given alloy were based on the same A_1 and A_2 values. A_1 was 4.60×10^{-2} $cm^{3/4}\text{-}s^{-1/4}\text{-}°C^{1/2}$ for CMSX-486 and 4.50×10^{-2} $cm^{3/4}\text{-}s^{-1/4}\text{-}°C^{1/2}$ for René N4. A_2 was 4.0×10^{-3} $cm\text{-}°C^{1/3}\text{-}s^{-1/3}$ for CMSX-486.

It is important to note that these dendrite-growth models assume ideal heat transfer conditions, including the assumption that all heat is extracted parallel to the primary dendritic-growth direction. This assumption may invalidate the use of these equations depending on casting geometry or solidification process, as discussed in future chapters. However, comparing predictions of these models to measurements from castings produced under non-ideal conditions can provide insight to the sensitivity of the model to the assumptions. Modifications to the equations were also considered that utilized the axial thermal gradient and pulling velocity rather than the total thermal gradient and solidification rate.

In cases when the solidification front is not absolutely orthogonal to the pulling direction, the inclination angle (θ) of the solid-liquid interface is used to evaluate the degree by which the thermal field is inclined with respect to the pulling direction. The solidification-front inclination angle, herein referred to as the "inclination angle", can be calculated from the relative magnitudes of the thermal gradient parallel and orthogonal to the pulling direction locally (Equation 1.5). The total thermal gradient can then be calculated from the axial thermal gradient and inclination angle (Equation 1.6).

$$\theta = \tan^{-1}\left(G_{\perp}/G_{\parallel}\right) \tag{2.5}$$

$$G = {G_{\parallel}}/{\cos\theta} \tag{2.6}$$

Additionally, the solidification rate is not merely the pulling velocity because the solidification front may be moving at an inclined angle relative to the pulling velocity. In this research, the solidification rate is the magnitude of the local solidification-front velocity. When the solid-liquid interface is inclined, these subtle adjustments to the calculation are critically important, as they may affect the thermal gradient and solidification rate by up to 40 pct. for inclination angles less than 45 degrees. All other details of the solidification modeling are discussed in the subsequent chapters.

In the upcoming chapters, the approach and results of the research are presented with a focus on (1) fundamental aspects of heat transfer within the floating baffle, (2) evaluation of heat transfer during directional solidification, (3) application and validation of heat-transfer considerations, (4) stability of dendrite growth in the presence of a non-axial thermal field, and (5) modeling of dendritic growth and associated morphologies. Finally, the relevance of the current research and its implications on future production of DS and SX materials are discussed and summarized.

References

1. A.J. Elliott, "Directional Solidification of Large Cross-Section Ni-Base Superalloy Castings via Liquid Metal Cooling," (Ph.D. thesis, University of Michigan, 2005).

2. K. Gallup, J.D. Miller and T.M. Pollock, unpublished research, 2010.

2. J.D. Hunt, *Solidification and Casting of Metals*, ed. J.D. Hunt (London: The Metals Society, 1979), 3-9.

3. W. Kurz and D.J. Fisher, *Acta Metall*, 29 (1) (1981) 11-20.

CHAPTER 3

HEAT TRANSFER IN A GRANULAR FLOATING LAYER DURING LIQUID COOLANT-ASSISTED DIRECTIONAL SOLIDIFICATION

Directional solidification by the Bridgman method relies on a sustained thermal gradient in the withdrawal direction. By increasing the thermal gradient, the dendrite structure is refined, resulting in a mechanically superior single crystal with reduced defect occurrence. One method to achieve higher thermal gradients is the utilization of the Liquid Metal Cooling (LMC) process. This process utilizes a liquid-metal coolant below the hot zone of the furnace to provide enhanced heat extraction. A floating ceramic baffle is used to shield the coolant from the heat flux of the mold-heater, thus maintaining a high thermal gradient in the transition zone between the furnace and coolant. While the benefit of the floating baffle has previously been demonstrated, optimization of the LMC process with the baffle has been limited by a lack of the fundamental understanding of the various heat transfer processes associated with the technique. In this effort, three-dimensional finite-element (FE) modeling was utilized to investigate heat-transfer mechanisms and baffle properties. Simulations were conducted at the scale of individual baffle beads to evaluate heat transfer mechanisms through the baffle and to develop physically realistic heat-transfer coefficients for use in continuum-scale models. The thermal field within the floating baffle is radiation dominant and sensitive to baffle thickness, coolant impregnation and the baffle emissivity. Thermal profiles within the baffle are insensitive to bead size, packing fraction and distance to the mold heater.

Analysis of thermal conditions within the mold identified a sensitivity of the thermal profile to exposure of the liquid-metal coolant to radiation from the mold heater and no sensitivity to baffle thickness, coolant impregnation or baffle morphology, provided a thermal barrier was maintained between the furnace and coolant. This indicates the dominance of the conduction heat transfer between the mold and coolant.

Introduction

The LMC process is an emerging approach for production of directionally-solidified and single-crystal materials and is based on the widely-accepted Bridgman method (Figure 3.1) [1-9]. The primary difference between the LMC and conventional Bridgman processes is the use of a stirred coolant-bath that supports a floating baffle comprised of ceramic beads [4-9]. The use of these materials alters the heat transfer process from the surface of the mold, resulting in conduction and convection rather than radiation cooling [10]. Much experimentation has been performed to evaluate the effect of the change in heat transfer processes to microstructure formation and mechanical performance [4-9,11-14]. During the LMC process, the coolant is heated by the bath walls and stirred with an impeller to distribute the heat throughout the bath. The stirring is critical to the successful application of the process due to heating of the tin from the mold and casting during withdrawal [11,12]. The floating baffle is also a key element to the successful application of the LMC process [9,11]. The key characteristics of the baffle system with and without the presence of an investment mold are addressed in this research.

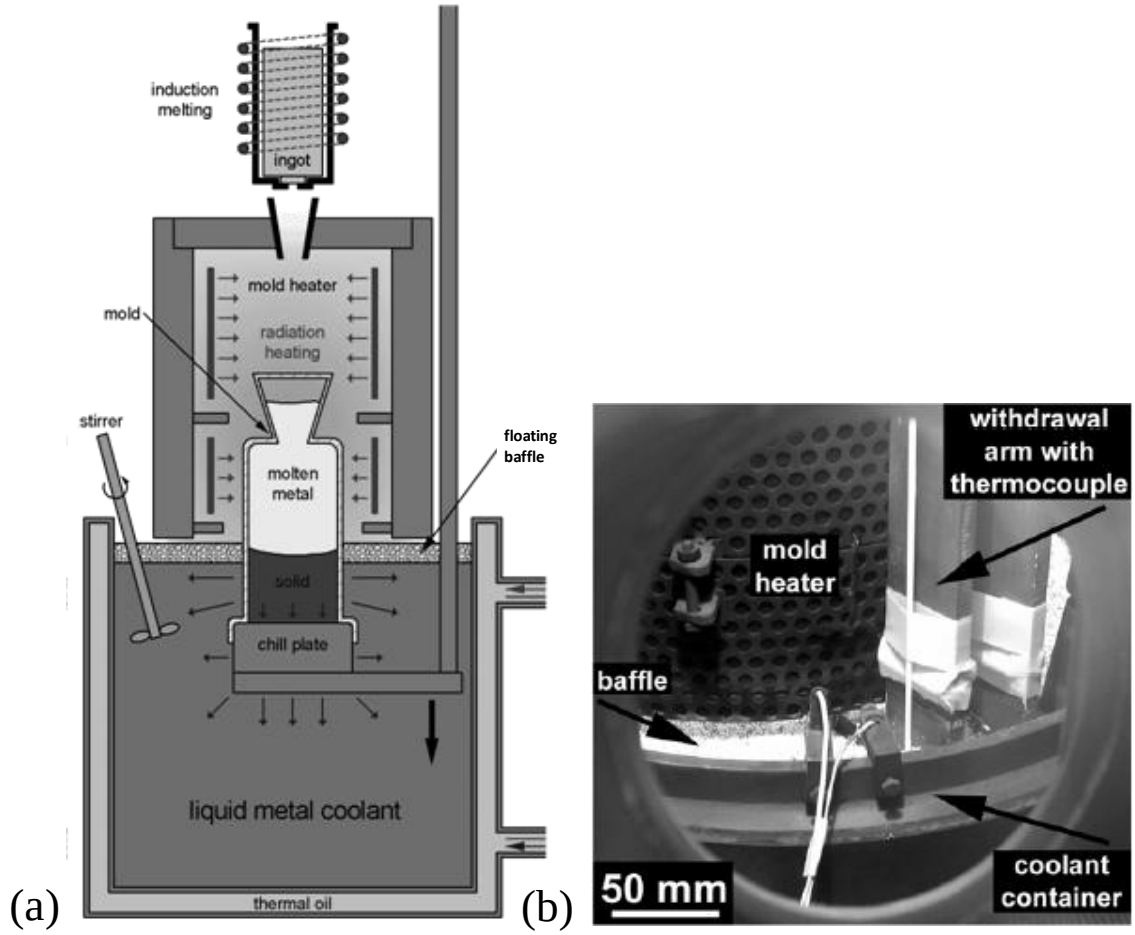

Figure 3.1 – (a) Schematic of LMC process and (b) image of floating baffle and coolant container positioned below the mold heater during solidification [12].

The floating baffle is a collection of spherical, hollow ceramic beads that float on the surface of the liquid-metal coolant, flow around the mold as it is lowered into the coolant and act as a radiation barrier between the mold heater and coolant. The beads are buoyant on the liquid metal coolant but can be submerged into the coolant due to the weight of the floating baffle and mechanical immersion as the investment mold is withdrawn into the coolant. The beads also have the ability to flow as a granular material.

During the solidification process, many factors may influence the efficiency of the floating baffle as a barrier to heat transfer. Carbon from the heating elements and/or elements subject to vaporization from the superalloy melt may condense on the surface of the baffle beads during the process. The floating baffle may also agglomerate due to coolant interpenetration. Because the beads are mechanically unconstrained, they tend to form a random packing. Heat transfer among the beads is radiation dominant, due to the low thermal conductivity of the ceramic material and the small contact area between beads [15]. The temperature on the surface of the floating baffle is on the order of the furnace temperature, nominally 1500 °C, while the bottom of the floating baffle is cooled by the liquid-metal coolant and nominally 300 °C [15]. Generally, the floating baffle material is used for multiple process cycles. Over time, the thickness may decrease as baffle material may remain attached to the surface of the mold. Based on this description, the floating baffle is continually changing over time and may not always provide a continuous barrier between the mold heater and coolant. The importance of these details relative to the quality of the casting produced is not well understood.

The effect of the presence of a 1.5 mm thick floating baffle on as-solidified dendritic structure was evaluated by Elliott [11]. The floating baffle was beneficial for the refinement of dendritic microstructure, and the coarser structure that developed without the baffle was attributed to overheating of the coolant and thus reduction of the thermal gradient at the solidification front [11]. Gallup obtained thermal measurements within the floating baffle under steady state conditions and during processing for different floating baffle materials [15]. The accuracy of the experimental results was limited by

the high thermal gradient through the baffle, interference of thermocouple with the thermal environment due to the relative scale of the thermocouples and accuracy of the position of the thermocouples relative to the baffle-tin interface as it is displaced by submersion of the mold. Significant thermal gradients existed over the scale of the individual baffle beads, and this indicated the need for a finite element model that considered the details of the baffle structure. In addition, the parametric experiments required to evaluate the important baffle parameters such as baffle thickness, bead size, packing density and coolant interpenetration would be very difficult to control and conduct. In order to determine the optimum baffle conditions thermal simulations are needed to improve the understanding of the importance of the floating baffle.

Analytical and finite element models have been utilized to obtain a fundamental understanding of the LMC process [6,10,13,16-18]. In order to properly simulate the heat transfer during LMC directional solidification, all heat transfer steps have been considered (Figure 3.2). Due to the complex interaction of the ceramic beads within the floating baffle and the submersion of the mold into the liquid-metal coolant, simplifications have been made in order to improve computational efficiency. For example, the floating baffle has been simplified to a single continuous domain in which the bead-bead radiation heat transfer was simulated as an effective thermal conductivity [10,13,19-21]. In addition, contact of the floating baffle and tin with the mold has been simulated by elimination of a radiation boundary condition and inclusion of a location-dependent heat transfer coefficient on the surface of the mold at the appropriate heights to represent baffle-mold and tin-mold interaction [13]. The assumption that these simulated

interfaces appropriately capture the physics of the process has not been verified. Moreover, the parameters that govern the approximations have not been optimized. For instance, radiation is the dominant heat transfer mechanism within the floating baffle and at the mold-baffle interface, thus the effective thermal conductivity and interface heat transfer coefficient, respectively, should decay with decreasing temperature. However, calibration of the parameters relies on experimental measurements, which have not been available until recently [15].

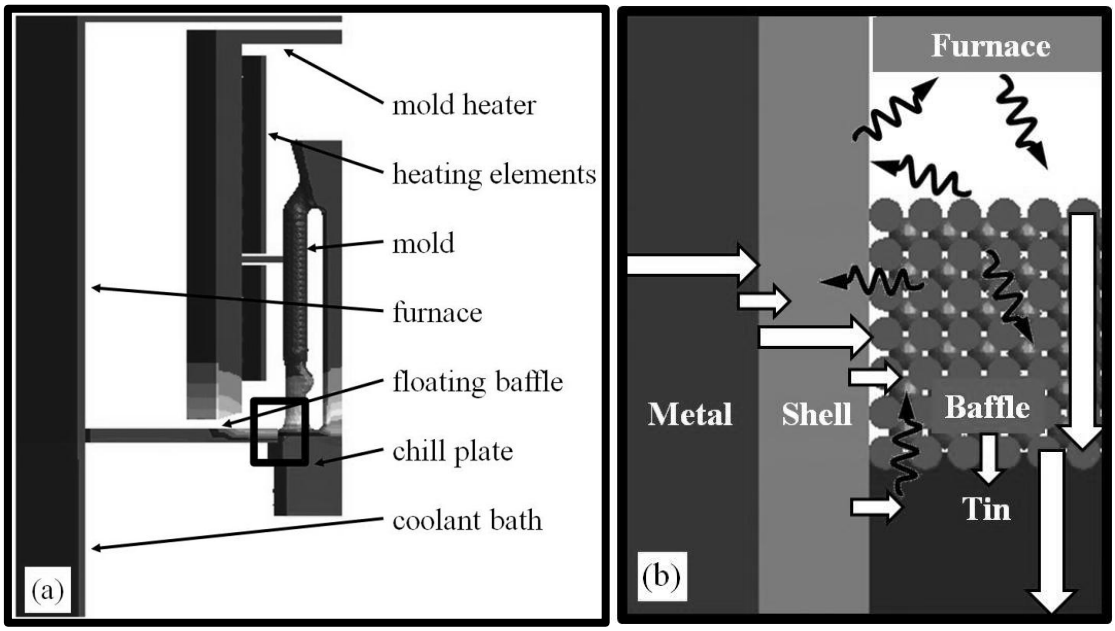

Figure 3.2 – (a) Image of a simulation of the LMC process indicating the floating-baffle domain and its interaction with the submerged mold, and (b) schematic of heat transfer mechanisms during directional solidification at this location.

Initial thermal simulation of the floating baffle has been performed to evaluate the sensitivity of predictions to the contact assumptions of the beads and floating baffle material selection [15]. Similar analyses are needed for the sensitivity of other floating baffle parameters. Overall, finite-element modeling has been conducted to quantitatively

evaluate key features of the LMC process. However, to date, these simulations have not considered the baffle in detail. Based on the complexity of the thermal environment during the LMC process detailed above, thermal simulations have been conducted to obtain a better understanding of heat transfer during the LMC process, validate the assumptions made with current process simulation techniques, optimize the floating baffle configuration and determine the sensitivity of the thermal field to variations in the floating baffle conditions, while comparing predicted thermal conditions to experimental measurements previously obtained (Figure 3.3).

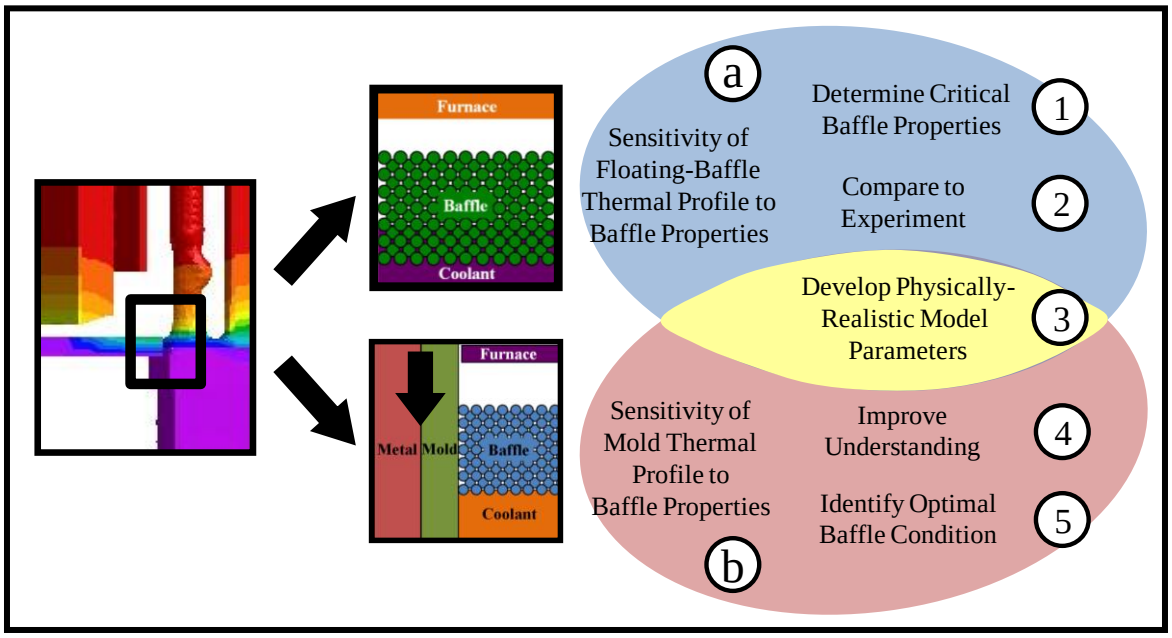

Figure 3.3 – Flow chart for baffle-modeling approach: apply component-scale baffle conditions to meso-scale FE-based models to analyze steady state temperature profiles within (a) a baffle absent of a mold and (b) a mold withdrawn into the coolant and baffle in order to optimize LMC process and improve component-scale modeling (1 – 5).

Approach and Simulation Methods

In order to improve the understanding of heat transfer during the LMC process, a meso-scale model of the transition region of the furnace during directional solidification was analyzed with approximately 50 simulations using the commercial ProCAST^{TM} code, a FEM-based tool specifically designed for analysis of solidification processes. Rather than modeling the floating-baffle system as a continuous domain of simplified geometry, this model consisted of a geometrical representation of the critical region of the directional solidification process: the transition between the hot and cold zones of the furnace. For the LMC process, this region is at the position of the floating baffle. The heat transfer mechanisms within the transition zone of the furnace were identified. The floating baffle configuration has a range of process variables that are considered for the parametric analysis, including the distance between the top of the baffle and the bottom of the mold heater, the floating baffle thickness, the depth of coolant interpenetration and bead size (Figure 3.4).

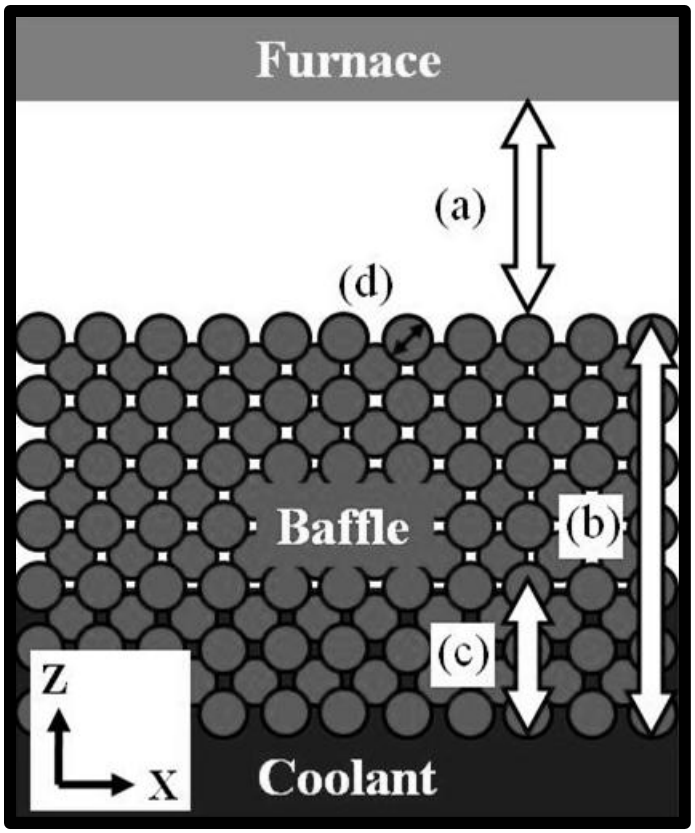

Figure 3.4 – Floating-baffle process variables, (a) baffle surface-mold heater distance, (b) baffle thickness, (c) liquid-metal coolant impregnation and (d) bead size.

Two floating baffle models were considered: a steady state model absent of a mold and another with mold submerged. The steady-state thermal model was used to evaluate the heat-transfer process within the baffle without having the complication of a mold contributing to heat flow and is referred to as the "mold absent" model. On the other hand, the mold-submerged model considers the full complexity of the directional-solidification process and is referred to as the "mold submerged" model. Combined, the predictions of these two models provide further insight into the thermal behavior of the floating baffle material.

The steady state model considered the thermal profile of the baffle far from the mold and consisted of a hot plate, baffle, tin and enclosure (Figure 3.5). The "Z" direction corresponded to the withdrawal direction of the directional solidification process. The hot plate simulated the mold heater, applying heat to the floating baffle surface. The floating baffle utilized a periodic boundary condition in "Y" and mirror-symmetry boundary condition in "X", effectively increasing the simulation domain to a size capable of representing the bulk steady state behavior. The tin domain fully contacted the bottom half of the bottom layer of baffle beads and had a constant temperature condition at the bottom of the domain. The enclosure enabled appropriate conditions for radiation view factor calculations, while preventing thermal interaction with the other domains.

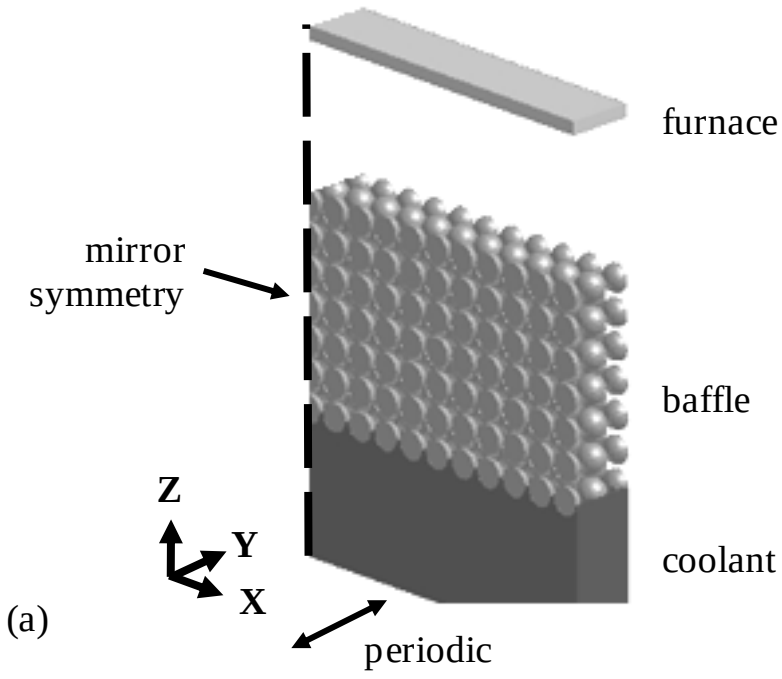

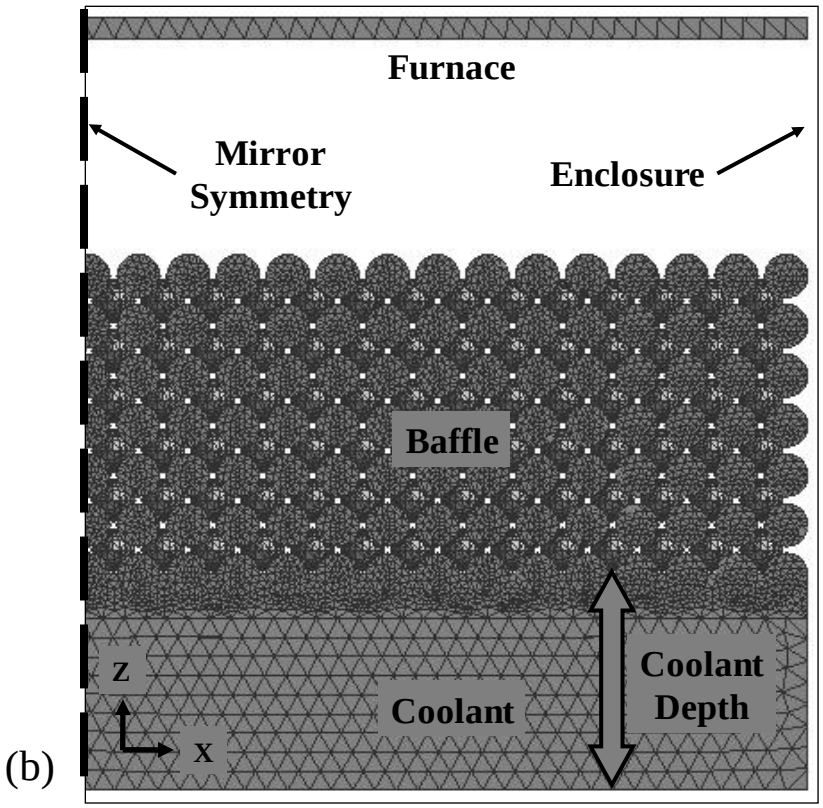

Figure 3.5 – Steady-state baffle model setup, (a) full model and (b) corresponding mesh.

The sensitivity of the thermal conditions of the floating baffle and critical heat transfer zone to floating-baffle packing fraction, baffle emissivity, baffle bead size, baffle thickness, coolant penetration into the floating baffle and distance from the furnace was evaluated (Table 3.1). Herein, this parametric analysis is referred to as the "baffle parameter analysis". As previously discussed, the floating baffle is comprised of randomly packed beads. The packing fraction of randomly distributed spheres is 0.64 [15]. The body-centered cubic structure has a structured packing fraction closest to random at 0.68 and thus served as the baseline packing configuration for the simulations. Simple cubic and face centered cubic represent packing fractions lower (0.52) and higher (0.74) than the baseline, respectively. The emissivity was evaluated at 0.2 and 0.8, representative of the new and used baffle emissivity [15]. Available bead sizes utilized

during LMC processing are 1, 2 and 3.2 mm in diameter, and these sizes are used to evaluate the effect of bead size on the thermal conditions in the baffle. The baseline baffle thickness for the LMC process is 15 mm through thickness. The sensitivity of baffle thickness was evaluated 50 pct thinner and thicker than the baseline baffle thickness. During the LMC process, the floating baffle can be impregnated by the liquid-metal coolant [11-12]. Half- and full-thickness penetration models were studied. Over a series of casting runs, the tin level can decline due to losses to the mold, so the distance between the floating baffle and the bottom of the mold heater is maintained within 10 mm. Therefore, the distance was evaluated 5 mm above and below the baseline.

Table 3.1 – Baseline values and ranges for "baffle parameter analysis" evaluated with the "mold absent" model.

Property	Baseline	Other Values
Emissivity	0.2	0.1, 0.3, 0.5, 0.8
Thickness (mm)	15	7, 22
Coolant Impregnation (mm)	0	7, 15
Packing Fraction	0.68	0.52, 0.74
Bead Diameter (mm)	2	1, 3
Furnace Distance (mm)	10	5, 15

Comparison to a model in which the floating baffle was represented as a continuous domain was also completed to evaluate the assumptions employed during thermal simulation of the directional solidification process. Other model parameters were studied to ensure that model predictions were insensitive to parameters within the model that were used to reduce the model size and simplify its geometry. These parameters were analyzed in a "model parameter" analysis and included liquid-metal coolant depth, enclosure emissivity, initial temperature and mesh size (Table 3.2).

Table 3.2 – Baseline values and ranges for “model parameter analysis” evaluated with the “mold absent” model.

Property	Baseline	Other Values
Mesh Geometry	Discrete Bead	"Continuum"
Coolant Depth (mm)	10	75
Initial Temperature (°C)	25	1500
Enclosure Emissivity	0.2	0.99
Mesh Size (mm)	0.3	0.2

The liquid-metal coolant depth was evaluated at the baseline depth and a significantly thicker depth to ensure that a sufficient volume of coolant was modeled representative of bulk coolant temperatures (Figure 3.5b). The baseline coolant depth in the model was 10 mm and an extended coolant depth of 75 mm was also evaluated. The extended depth was selected to match the distance at which control thermocouples were positioned within the coolant bath, so that direct comparison to measurement could establish the temperature boundary condition of 250 °C.

An enclosure was used in the model to allow calculation of radiation heat transfer between the surface of the coolant, baffle beads and mold heater. The enclosure was meant to account for the temperature of the surroundings, in this case the surrounding baffle beads, so an emissivity equal to the emissivity of the floating baffle was utilized as the baseline value. An emissivity of 0.99 was also investigated to ensure insensitivity of the thermal conditions to the enclosure emissivity.

The initial temperature of the domains was also investigated. The simulation is performed until a steady-state thermal condition is obtained, thus by definition the thermal condition should be independent of the initial condition. To confirm the insensitivity of the initial condition, an initial temperature of 25 °C and 1500 °C were assigned to all nodes and results compared. Finally, the mesh size within all domains was parametrically evaluated to ensure insensitivity of thermal conditions. The baseline mesh size within the baffle was 0.3 mm while a fine mesh size of 0.2 mm was also evaluated.

Other material properties were assigned to emulate the conditions of the process that were not parametrically evaluated. The thermal conductivity of the material representing the discrete baffle beads was 1 $W\text{-}m^{-1}\text{-}K^{-1}$ and included conductivity between baffle beads. The coolant utilized a free-surface emissivity of 0.3, typical of liquid metals, and a thermal conductivity of 34 $W\text{-}m^{-1}\text{-}K^{-1}$. A constant-temperature boundary condition of 250 °C was applied to the bottom of the coolant domain. This assignment was consistent with experimentally measured temperatures at this axial height within the baffle [15]. A constant-temperature boundary condition was applied to the hot plate. The specific temperature was selected in order to maintain the established relationship between the temperature at the top of the baffle and the corresponding baffle emissivity based on process simulations as discussed in Chapter 4. For a baffle emissivity of 0.1, 0.2, 0.3, 0.5 or 0.8 the temperature of the hot plate was 1200, 1250, 1350, 1400 or 1550 °C, respectively. The emissivity of the hot plate was 0.8, consistent with previously-assigned

values of emissivity for the mold heater [10,13]. All other model parameters were evaluated parametrically and were previously discussed as shown in Tables 3.1 and 3.2.

In order to evaluate the steady state temperature profile, heat transfer was simulated until the temperature at all locations was essentially constant. The temperature profile through the thickness of the baffle (along "Z") was then obtained by averaging the temperature at multiple horizontal ("X" and "Y") positions.

Another model considered the impact of a submerging mold to the heat transfer within the transition region. The predictions from this model provide insight to the effect of the heat-transfer in the floating baffle region on the thermal field within the mold. The thermal field within the mold is of particular interest because the conduction through the mold is the dominant heat transfer step at solidification temperatures for the LMC process, as is discussed in Chapter 4. Thus, the thermal field predicted within the mold will provide insight to the thermal conditions of the metal during solidification. At the component scale, this level of modeling detail is not feasible due to computational expense. Therefore, in order to establish the interaction between the mold, tin and baffle, a simple geometry and non-coincident interfaces were used within ProCAST^{TM} at the scale of the structure of the floating baffle. A non-coincident interface is used to allow the sliding of domains relative to each other but avoids the problem of interpenetrating meshes. This type of analysis allowed movement of the casting and mold relative to the heater, floating baffle and coolant while maintaining contact and thus heat transfer across the interfaces.

The model setup required to evaluate direct interaction of mold, baffle and tin domains is shown in detail in Figure 3.6. The hot plate, floating baffle, tin and enclosure of the steady state model were used as part of the mold-submerged model. The "Z" direction is the withdrawal direction of the model. A periodic boundary condition was applied in the "Y" direction. The floating baffle beads were individually represented as spheres. A domain representing the mold was positioned along one side of the baffle. The mold thickness was set at 6.4 mm, equivalent to the experimentally-measured shell thickness. A domain for the metal was positioned alongside the mold, opposite the baffle. The thickness of this domain was 8 mm. A mirror-symmetry boundary condition was applied to the surface of the metal opposite the mold. With the utilization of a periodic boundary condition in "Y" and a mirror boundary condition in "X", the simulation is evaluating directional solidification of an 8 mm thick, infinitely-wide slab. The withdrawal rate of the mold and casting was 12.7 mm-min^{-1} based on a typical withdrawal rate for this casting thickness [14]. The height of the metal and mold domains was 152 mm to allow for a withdrawal time representative of a typical casting. The tin domain was extended to allow for interaction along the entire length of the bar during the complete withdrawal of the bar. A domain representing the mold heater was positioned above the hot plate near the mold surface to represent the mold heater by heating the mold and baffle materials. The initial temperature of each of the domains was obtained by running the simulation with the mold present but not withdrawing until the temperature profiles reached a steady state. The temperature for each node was then input as the initial condition for the mold-submerged model.

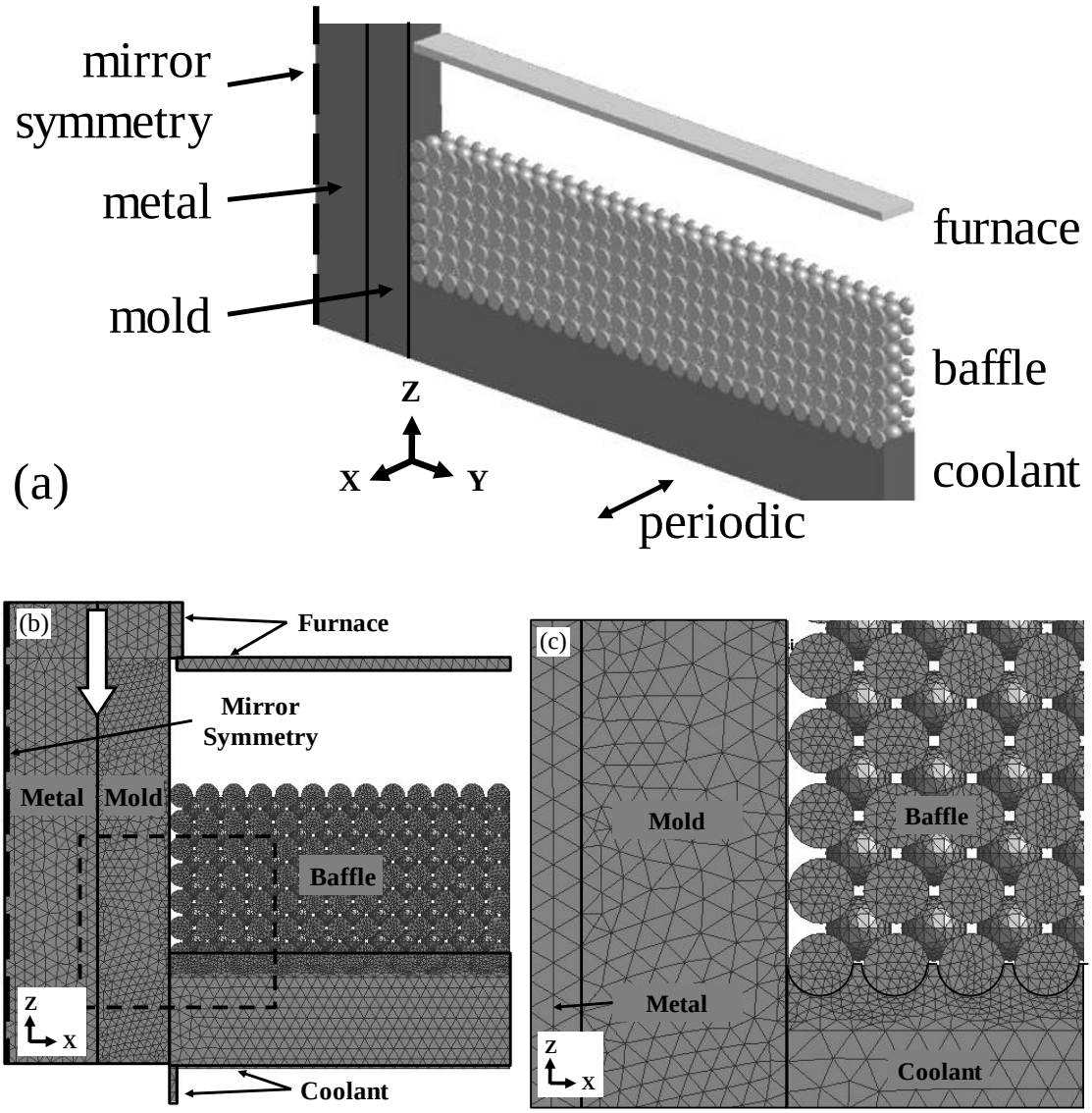

Figure 3.6 – Mold-submerged model setup, (a) full model of critical domains, (b) mesh of critical domains and (c) mesh at the interfaces between the baffle, mold and coolant.

The fixed model parameters from the "mold absent" model were also applied to the "mold submerged" model. The bead size, packing configuration and furnace distance of this model utilized the baseline values from the "mold absent" model. Additional model parameters were required due to the presence of the mold and metal. The values of the thermophysical properties of the metal and mold were assigned according to previous

research [10,13]. The properties of the mold simulated a fused silica mold typical of investment castings and utilized a thermal conductivity of 2.5 $W\text{-}m^{-1}\text{-}K^{-1}$. The emissivity of the mold was assigned to be 0.3, based on previous research [13]. The properties of the metal were assigned to represent René N4, a SX Ni-base superalloy with a liquidus and solidus of 1345 °C and 1300 °C, respectively. The mold-metal interface heat transfer coefficient was temperature-dependent and included a constant value of 750 $W\text{-}m^{-2}\text{-}K^{-1}$ above the liquidus followed by an exponential decay to 100 $W\text{-}m^{-2}\text{-}K^{-1}$ due to metal shrink from the mold wall.

Variations in baffle thickness, baffle emissivity and penetration depth of the coolant were evaluated with the "mold submerged" model (Table 3.3). The baffle thickness was evaluated at 7, 15 and 22 mm, corresponding to one-half, one and two times the standard baffle thickness used experimentally. Liquid-metal coolant penetration was analyzed for depths of 0, 7 and 15mm, so that no, half and full penetration of the baffle could be evaluated, corresponding to 15 mm, 7 mm and 0 mm of baffle thickness above the coolant surface, respectively. Baffle emissivity was evaluated at 0.2 and 0.8, which were determined to be the emissivities of new and used baffle material, respectively [15]. Comparison to a model that represented the baffle as a continuous domain was also completed.

Table 3.3 – Baseline values and ranges of baffle properties evaluated via the "mold submerged" model.

Property	Baseline	Other Values
Emissivity	0.2	0.8
Thickness (mm)	15	7, 22
Coolant Impregnation (mm)	0	7, 15
Mold-Surface Morphology	Flat	See Figure 3.6

In addition, the morphology of the baffle at the mold interface was investigated. At the surface of the mold as it is submerged into the baffle, the baffle beads flow with variations in mold geometry, causing a different morphology of the floating-baffle system. The angle of repose for the beads used in the LMC process was 30° [15]. Therefore, extreme baffle-morphology scenarios were evaluated, whereby the standard baffle thickness was considered to be present far from the mold with an altered arrangement at the surface of the mold. Variations in baffle thicknesses at the surface of the mold were evaluated with a 50 pct increase and decrease from the baseline baffle thickness. Due to the combination of baffle-bead arrangement and metal-coolant impregnation, a variety of possible floating-baffle morphologies at the surface of the mold were considered (Figure 3.7).

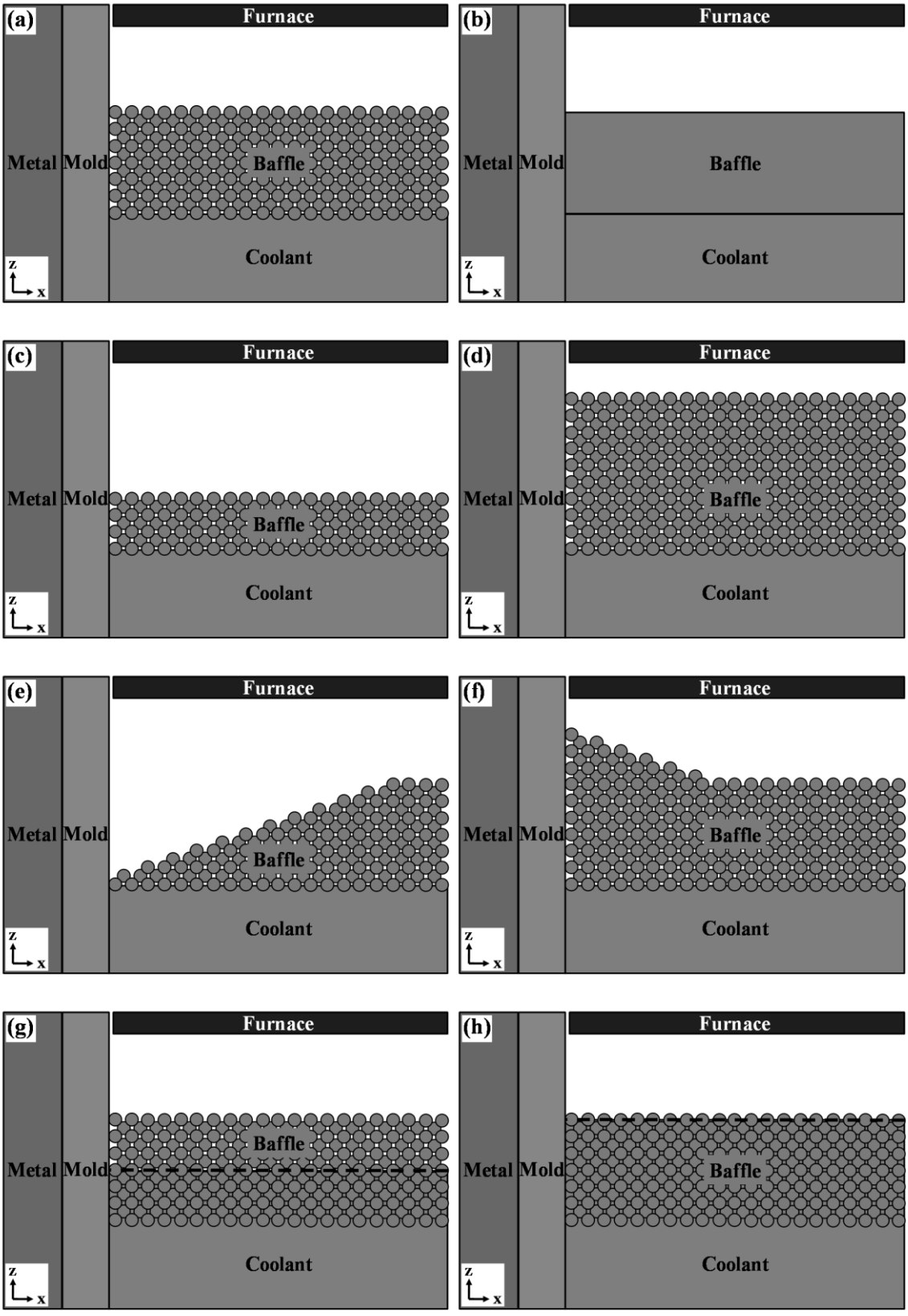
(a)
Furnace
Metal
Mold
Baffle
Coolant
z
x
(b)
Furnace
Metal
Mold
Baffle
Coolant
z
x
(c)
Furnace
Metal
Mold
Baffle
Coolant
z
x
(d)
Furnace
Metal
Mold
Baffle
Coolant
z
x
(e)
Furnace
Metal
Mold
Baffle
Coolant
z
x
(f)
Furnace
Metal
Mold
Baffle
Coolant
z
x
(g)
Furnace
Metal
Mold
Baffle
Coolant
z
x
(h)
Furnace
Metal
Mold
Baffle
Coolant
z
x

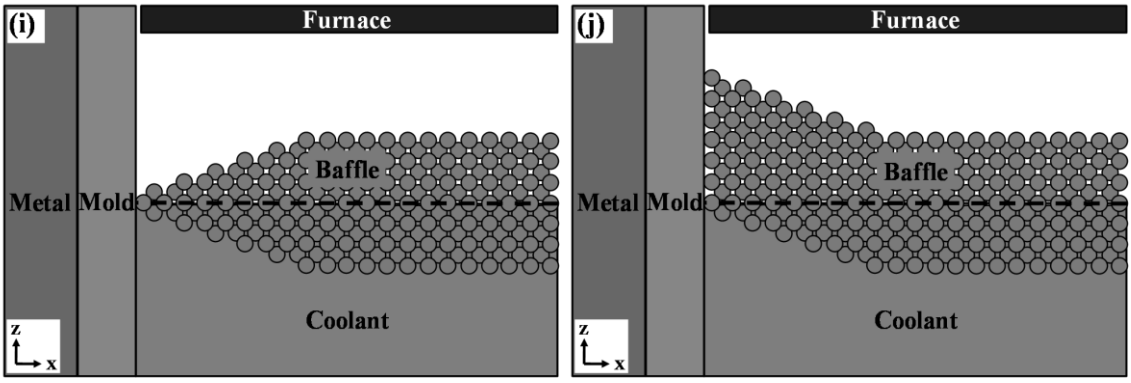

Figure 3.7 – Schematics of investigated floating-baffle morphologies for the "mold submerged" model: (a) flat, (b) continuum, (c) thin, (d) thick, (e) receding, (f) accumulating, (g) partially penetrated, (h) fully penetrated, (i) partially penetrated and twice receding and (j) partially penetrated and translated upward. Note: The horizontal line indicates the coolant free surface.

Steady-State Thermal Prediction of the Floating Baffle

In order to illustrate the steady-state "no mold" thermal prediction, the result from the standard baffle configuration is shown (Figure 3.8). As stated in the previous section, there is a periodic boundary condition in "Y" and a mirror-symmetry boundary condition in "X" on the right side of Figure 3.8. All free surfaces within the model have been assigned an emissivity, while conduction is considered within each domain. Thermal boundary conditions are applied to the hot plate and bottom surface of the coolant domain. The prediction of the steady-state thermal profile is stable across the entire geometry, with the exception of the three beads along the edge which are affected by radiation heat loss to the enclosure. This is not representative of the furnace environment and does not impact the predictions near the symmetry plane, where thermal predictions from different variants of the model were compared.

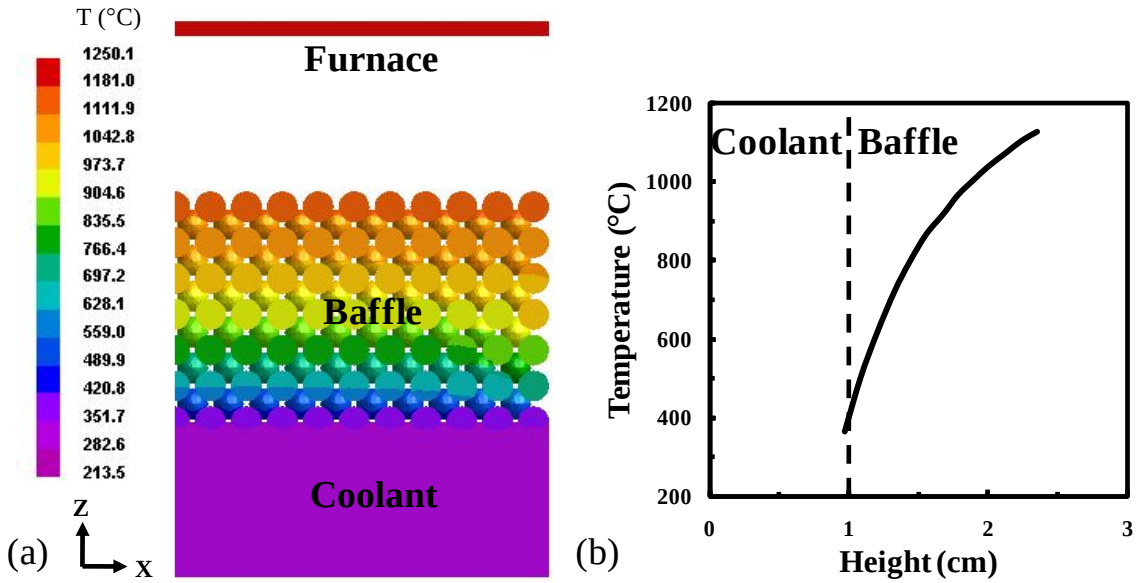

Figure 3.8 – Steady-state solution for the standard baffle configuration as described by Tables 3.1 and 3.2, (a) temperature contour plot and (b) axial temperature profile through baffle. Note: The dashed line indicates the height of the bottom of the floating baffle with a positive height proceeding along the "+Z" axis through the baffle in the direction of the mold heater.

The parabolic shape of the thermal profile through the thickness of the baffle was consistent with the temperature dependence of radiation heat transfer. Data shown in Figure 3.8b were used to calculate a temperature-dependent thermal conductivity that would provide a similar thermal profile in a continuous domain representing the entire floating baffle. The temperature-dependent thermal conductivity was used in a continuum model for both models evaluated and is discussed in the respective sections.

Predictions from the "mold absent, baffle parameter" analysis of the steady-state thermal profile through the baffle far from the mold indicated a sensitivity of the thermal profile through the baffle to changes in the baffle material and configuration (Figure 3.9). The shape of the thermal profile through the thickness of the baffle was parabolic for all baffle conditions. Overall, the thermal profile through the baffle is insensitive to bead

size, packing fraction and furnace distance (Figure 3.9d-f). Changes in emissivity, baffle thickness and coolant impregnation affect the predicted thermal profile.

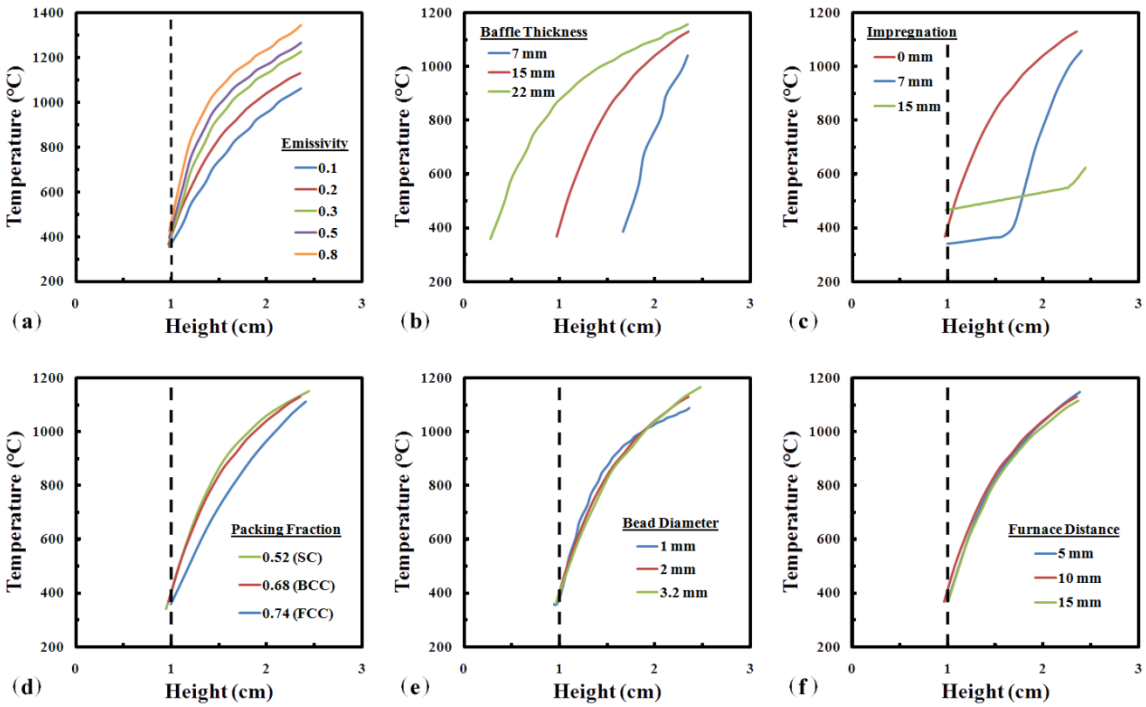

Figure 3.9 – Sensitivity of through-thickness, steady-state thermal profile of baffle to changes in floating-baffle process variables, (a) emissivity, (b) baffle thickness, (c) coolant impregnation, (d) packing fraction, (e) bead diameter and (f) baffle surface-mold heater distance. Note: The dashed line indicates the height of the bottom of the floating baffle with a positive height proceeding along the "+Z" axis through the baffle in the direction of the mold heater.

An increase in the emissivity of the baffle increased the surface temperature at the top of the baffle by up to 28 pct for a change in emissivity from 0.1 to 0.8 (Figure 3.9a). In turn, the increase in the temperature of the top of the baffle increased the overall axial temperature gradient throughout the baffle. Increasing the baffle thickness had the opposite effect by increasing the distance over which the temperature change occurred (Figure 3.9b). This was expected since a similar surface temperature was anticipated at

the top of the floating baffle with an increased distance, thus resulting in a reduction of the overall thermal gradient throughout the baffle.

Increasing the level of coolant impregnation from 0 mm to 7 mm decreased the distance over which the temperature change occurred above the coolant in the upper portion of the baffle (Figure 3.9c). However a further increase in penetration depth to 15 mm reduced the thermal gradient by 84 pct and increased the coolant temperature by 100 °C compared to the 0 mm coolant-penetrated prediction. The abrupt change in the thermal profiles (Figure 3.9c) corresponded to the height of the coolant free surface. Baffle penetration by the coolant effectively reduced the thickness of the baffle to its height above the free surface of the coolant, which was observed by comparison of the thin baffle (Figure 3.9b) and partial penetration (Figure 3.9c) predictions. This data suggest that the thermal gradient within the floating baffle is only sensitive to changes in baffle emissivity and effective thickness (non-impregnated thickness) of the baffle.

Thermal profiles from the "mold absent, model parameter" analysis were compared to the thermal profile of the standard configuration and include coolant depth, initial temperature, enclosure emissivity and mesh size, as defined by Table 3.1 (Figure 3.10). As was discussed in the previous section, these parameter values were used to simplify the "absent mold" model boundary conditions and reduce its size. In addition, the thermal profile of the standard configuration was used to generate an effective thermal conductivity for use with a simplified representation of the floating baffle that did not

consider the geometry of individual beads. This model simplification is referred to as "continuum" and was compared to the thermal profile of the standard configuration.

Comparison of the "continuum" model predictions and the standard configuration of the "mold absent" model demonstrated that the effective thermal conductivity can appropriately capture the thermal field within the floating baffle, Figure 3.10a. The implications of this observation are discussed at the end of this chapter. The thermal profile within the baffle was insensitive to tin depth (Figure 3.10b), initial temperature of the entire model (Figure3.10c), enclosure emissivity (Figure 3.10d), and mesh size (Figure 3.10e) for the ranges evaluated. Thus, the model conditions employed in the "mold absent" model were sufficient to isolate the correct physical effects.

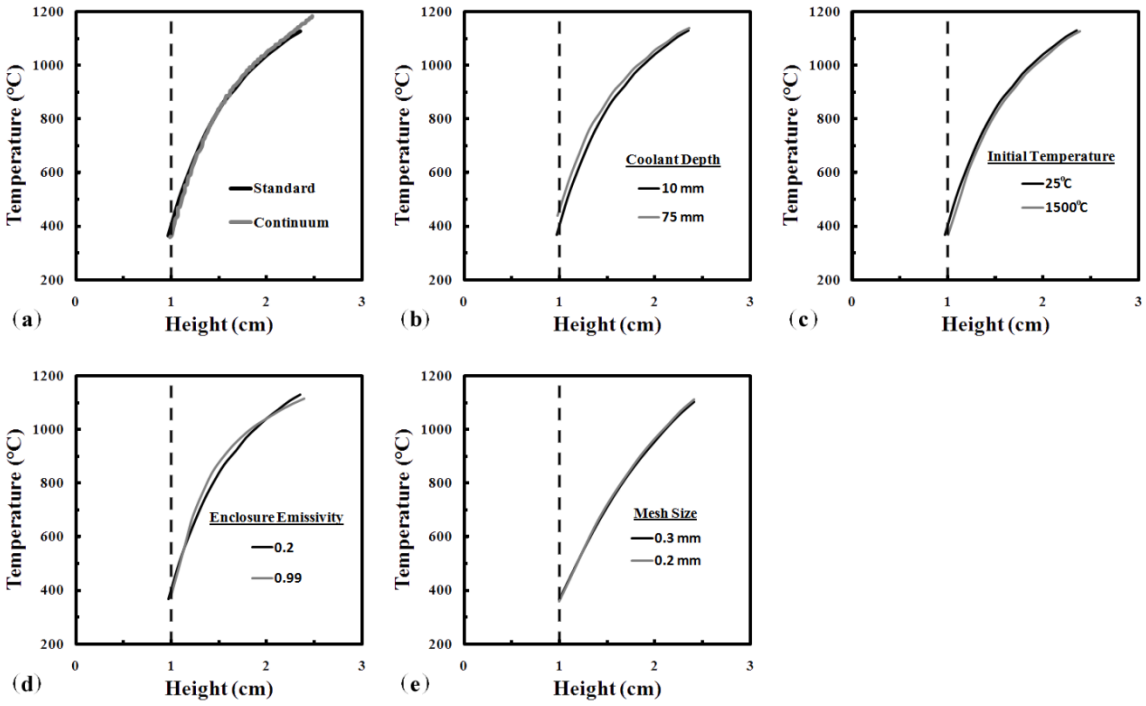

Figure 3.10 – Sensitivity of through-thickness steady-state thermal profile of baffle to changes in model parameters: (a) continuum domain representing floating baffle system as a single material, (b) depth of coolant, (c) initial temperature, (d) enclosure emissivity and (e) mesh size. Note: The dashed line indicates the bottom of the floating baffle and free surface of the coolant with a positive height proceeding along the "+Z" axis through the baffle in the direction of the mold heater.

Steady-State Thermal Prediction of Mold during Submersion

As discussed previously, when a mold is immersed into the floating baffle, the thermal field within the mold is more complex than the thermal profile through the surrounding floating-baffle system. Thus, a "mold submerged" scenario was modeled using a periodic boundary condition in "Y", a mirror-symmetry boundary condition on the inner metal surface (the left-most surface, "-X", in Figure 3.11), a non-coincident interface between the free surface of the mold and the coolant, and temperature boundary conditions on the mold heater and bottom surface of the coolant. Conduction within all

of the materials was calculated, including the bead-bead interfaces. A heat transfer coefficient was used for the mold-metal interface and considered the metal shrinking away from the mold. The mold and casting was withdrawn into the furnace at a constant velocity of 12.7 mm-min^{-1} in the "–Z" direction until the thermal profile within the mold relative to the position of the floating baffle reached a steady state. The thermal prediction of the baseline configuration is shown (Figure 3.10) as demonstration of the steady-state thermal conditions as the casting and mold are withdrawn into the cooling zone of the furnace.

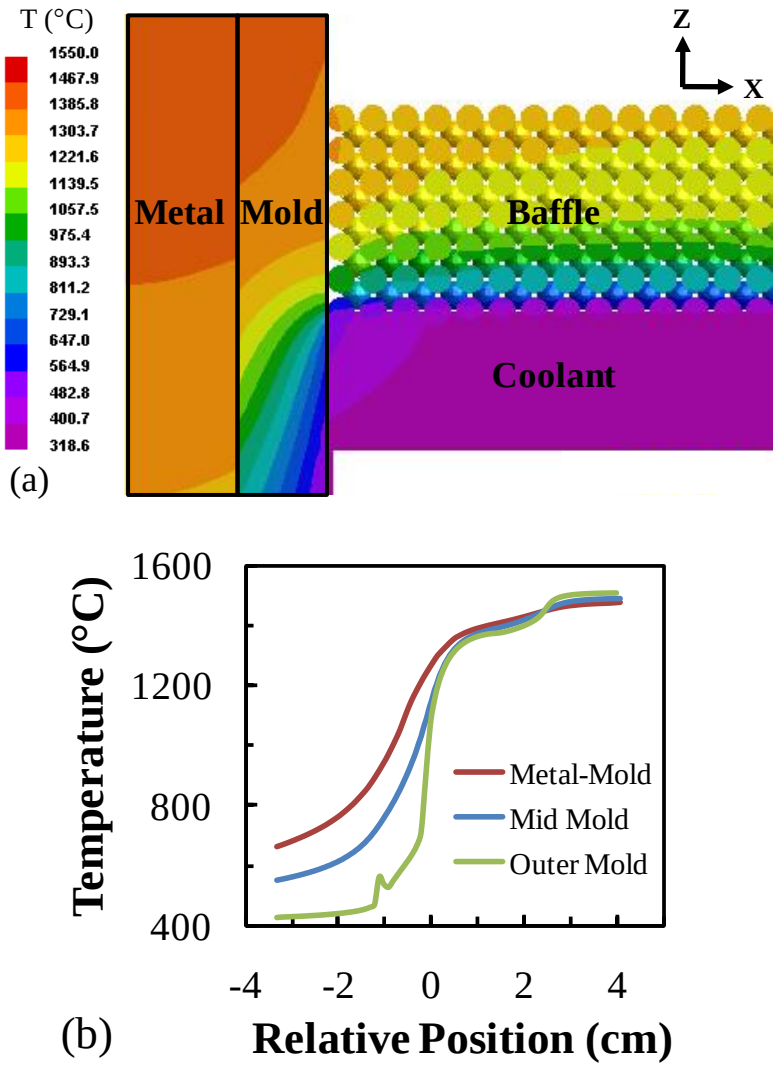

Figure 3.11 – Steady-state thermal prediction of the "mold submerged" model for the standard configuration as described by Table 3.3, (a) temperature contour plot and (b) temperature profiles through mold. The position is plotted relative to the position of the coolant free surface.

The axial thermal profile through the baffle changed with distance from the mold but reached a steady profile far from the mold as indicating by the isotherms in Figure 3.11a, indicating that the model was sufficiently large in the "X" direction in order to evaluate physical effects of the mold immersion. In general, a maximum thermal gradient in the mold was observed at the baffle-coolant interface. A 50 pct increase in the coolant

temperature was observed at the top of the baffle near the interface with the mold, which was attributed to conduction from the hot mold as it was continuously submerged into the stagnant cooling media. This indicated the importance of stirring the liquid coolant but was not anticipated to affect the thermal profile within the mold due to the relatively small increase in temperature (175 °C) compared to the large thermal gradient observed within the mold at the same location (greater than 1000 °C-cm^{-1}).

Steady-state thermal profiles parallel to the withdrawal direction within the mold along the mold-metal interface, at the mid-thickness of the mold, and along the outer surface were used to quantitatively evaluate the thermal field within the mold (Figure 3.11b). This was performed by plotting the temperature of individual nodes as a function of their axial position ("Z") relative to the free surface of the coolant. A positive relative position represents a point in the model whose "Z" position is above ("+Z") the coolant surface.

The thermal profiles of the mold along the withdrawal direction (along "Z") described the complex heat transfer conditions during processing. The maximum thermal gradient decreased with lateral distance from the surface of the mold, which was expected as the thermal conductivity of the mold impeded heat transfer. High into the mold heater at a relative position of approximately 2.5 cm (Figure 3.11b), a crossover in relative temperature occurred between the different thermal profiles within the mold. This can be explained because the outer mold surface was the hottest of the three profiles above this location due to its relative closeness to the heating elements. At the same time, this

profile was cooled first as it contacted the cooler baffle then cooling media below this position.

The baffle thickness, coolant impregnation and baffle emissivity parameters were evaluated in the "submerged mold" scenario since these parameters affected the steady-state thermal profile through the baffle far from the mold. Baffle-bead arrangement at the surface of the mold was also evaluated in this model scenario. Comparison of the three thermal profiles for different baffle conditions to the standard configuration revealed the dependence of the thermal profiles within the mold to baffle thickness, coolant impregnation, baffle emissivity and baffle-bead arrangement (Figure 3.12). For the purposes of this discussion, "standard" refers to the same baffle conditions as the "mold absent" model but includes the presence of a withdrawn mold, Figure 3.11.

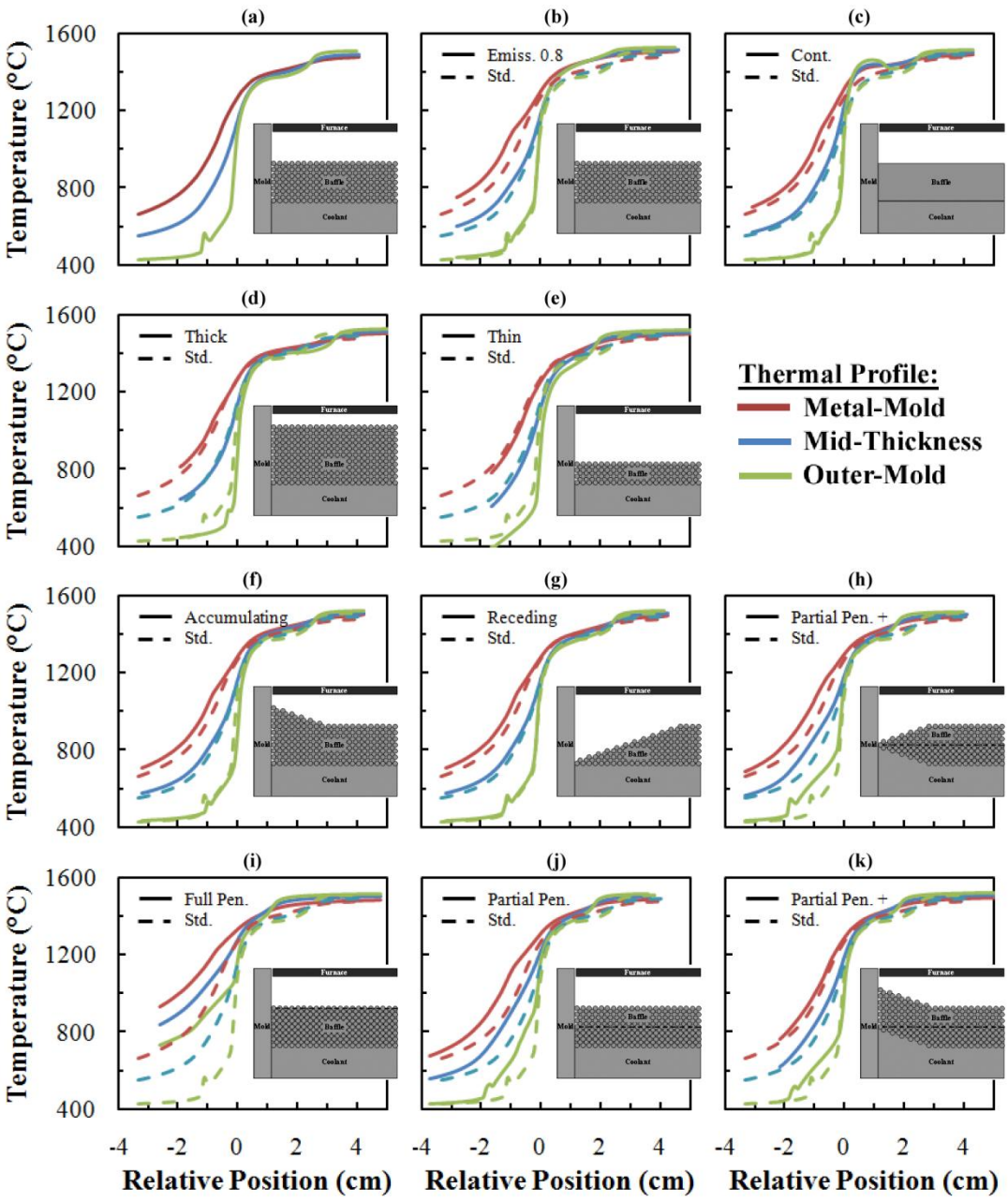

Figure 3.12 – Sensitivity of mold-wall through-thickness steady-state thermal profile relative to the free surface of the coolant for changes in baffle process variables (a) standard, (b) emissivity 0.8, (c) "continuum", (d) thick, (e) thin, (f) accumulating, (g) receding, (h) partial coolant penetration with twice receding, (i) full coolant penetration, (j) partial coolant penetration and (k) partial penetration with upwards translation. Note: The dark horizontal line indicates the surface of the coolant to which the relevant position is plotted.

Simplifying the baffle geometry to a continuous domain and utilization of the temperature-dependent effective thermal conductivity in order to mimic radiation heat transfer did not alter the thermal conditions within the mold, Figure 3.12c. Relative to the baseline configuration, there was no significant difference for changes in baffle thickness or bead arrangement, with the exception of a fully-impregnated baffle (Figure 3.12d-k). In the case of the fully-impregnated baffle, the thermal gradient is approximately half that of the standard configuration, corresponding to an increase in the temperature of the cooling media as the mold heater directly heats the surface of the coolant, Figure 3.12i. Significantly increasing the emissivity of the baffle resulted in a minimal change in the thermal profiles through the mold (Figure 3.12b). Overall, this analysis further demonstrated the insensitivity of the thermal conditions to changes in baffle conditions except when the coolant was exposed to the heat flux of the furnace.

Discussion

The predictions of the steady state thermal profile through the mold at the height of the baffle were compared to thermocouple measurements and similar models from previous efforts studied by Gallup (Figure 3.13) [15]. Predictions of the thermal profile through the thickness of the baffle were within measurement error of the thermocouple data for a limited set of baffle conditions. The curvature of the thermal profile through the thickness of the baffle is consistent with experimental data, Figure 3.13. The thermal gradient within the baffle is sufficiently large that location sensitivity of the thermocouples can significantly contribute to measurement error, especially for a floating

baffle consisting of large beads [15]. In addition, the size of the junction at the end of the thermocouples used in the experiments was on the order of the ceramic bead size, which could cause interference with the thermal field, particularly when multiple thermocouples are densely positioned within the baffle [15]. Finally, comparison of thermal predictions in this effort with thermal predictions from the modeling effort of Gallup verified the assumptions that radiation is the dominant heat transfer mode, conduction between beads occurs, and body-centered cubic is a representative packing configuration [15].

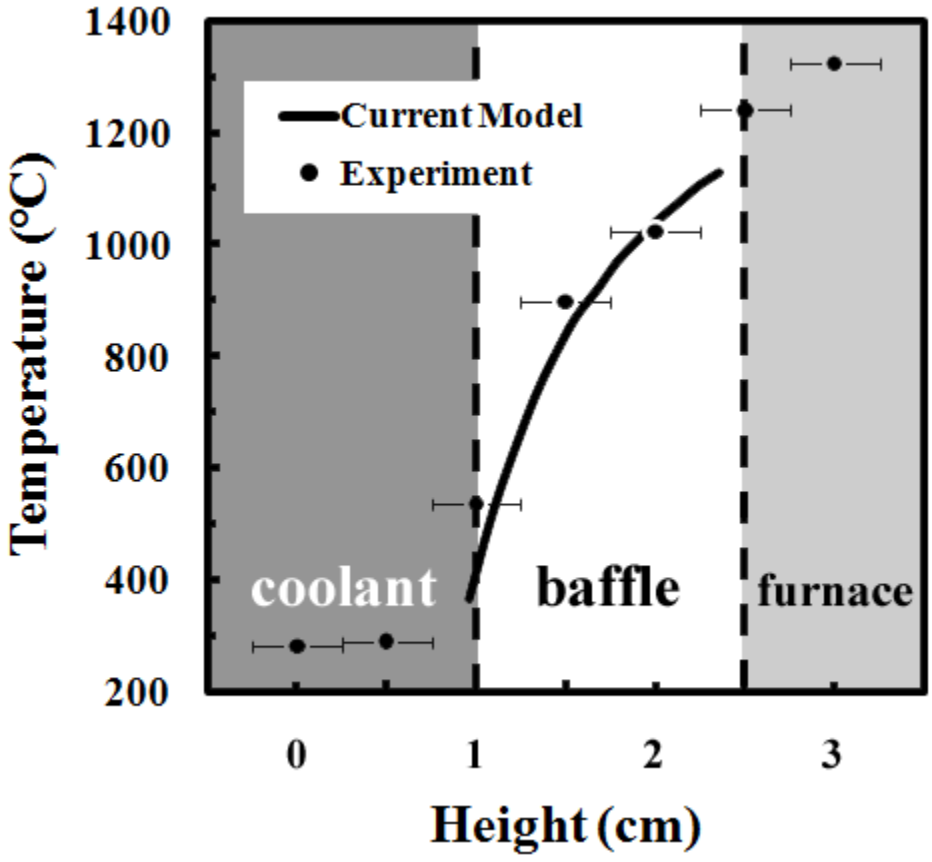

Figure 3.13 – Comparison between experimentally measured (from [15]) and predicted thermal profiles from the individual-bead model in the absence of a withdrawn mold.

The use of a simplified continuum domain that utilizes a temperature-dependent, effective thermal conductivity to model the radiation heat transfer between beads was validated by agreement between the continuum model predictions and the standard baffle configuration predictions (Figures 3.10a and 3.12b). This agreement provides a physical basis for the imposed heat transfer coefficients for use in larger scale casting simulations. Thus process simulations that have utilized this assumption are accurate, assuming the temperature-dependent conductivity has been adjusted appropriately [10,13]. This approach is utilized for the research conducted in the other chapters of this work. The effective thermal conductivity assumption breaks down if the floating baffle is interpenetrated by the coolant as previously discussed.

The predictions of the fully-penetrated baffle were consistent with Elliott's observations of reduced thermal gradient and coolant heat-up in the absence of a floating baffle, which can be observed in the steady state thermal predictions within the fully-penetrated baffle (Figure 3.9) [11]. Furthermore, heat-up of the coolant by submersion of the heated mold was demonstrated in the mold-submerged model (Figure 3.11).

In general, the thermal profile within the mold is insensitive to changes in the baffle conditions, specifically changes in baffle material, bead size, packing fraction, thickness, heater distance and tin impregnation, with the exception of a fully-penetrated baffle. From a heat-transfer perspective, the abrupt change in heat transfer at the mold surface from radiation cooling to conduction and convection within the coolant localizes the thermal gradient at the baffle-coolant interface, regardless of baffle conditions.

Therefore, the floating baffle serves a single purpose: to act as a thermal barrier, preventing the extreme temperature of the heater from overheating the liquid-metal coolant. The low thermal conductivity of hollow ceramic beads and small contact area of adjacent beads is such that only a thin layer of beads was needed to prevent the drastic change in the thermal profile within the mold. A deviation in the thermal profile within the mold was observed when sufficient coolant impregnation exposed the coolant to radiation heating by the mold heater, thus raising the temperature of the baffle, increasing the reactivity between the coolant and casting and reducing the thermal gradient during solidification.

Based on this analysis, a robust process configuration would include a conservatively thick baffle, such that the granular flow across horizontal mold surfaces guaranteed complete coverage of the liquid-metal coolant. This calculation is based on the angle of repose for the granular material, which is 30° for the materials investigated [15]. An approximate minimum thickness would be equivalent to the maximum horizontal distance that the baffle would need to flow in order to maintain a continuous thermal barrier for the coolant (Figure 3.14). For example, directionally-solidified industrial gas turbine components have platforms that extend approximately 5 cm beyond the airfoil, so a baffle thickness of 5 cm would provide enough thickness to flow baffle beads to the vertical surface of the airfoil [12]. The increased thickness of the baffle simplifies current process control requirements that regulate baffle thickness within a few millimeters. Further research is needed to determine the effect of the age of the baffle on

the resultant thermal conditions within the mold and casting, since during heatup carbon deposits on the baffle beads and impregnated tin melts.

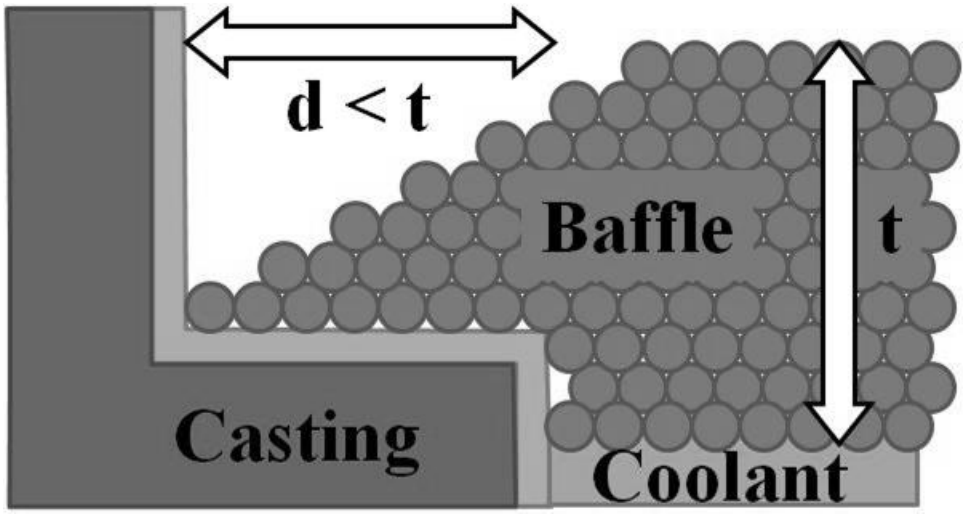

Figure 3.14 – Schematic of the minimum baffle thickness required to sufficiently fill horizontal surfaces of the mold during withdrawal due to abrupt changes in geometry.

Conclusion

Overall, this effort utilized an individual-bead baffle model to assess the effect of configurational changes to the floating baffle on thermal conditions present in the baffle and within the mold during solidification. Effective heat transfer coefficients developed in this model can be used in larger scale process simulations and are based on the relevant heat-transfer physics. Specific findings include:

- Steady state thermal conditions within the baffle are sensitive to baffle thickness, tin impregnation and baffle emissivity.

- The thermal field within the mold is insensitive to changes in the baffle provided there is a thermal barrier of minimal thickness between the mold heater and tin in order to maintain the desired thermal gradient.
- Predictions of thermal profiles within the baffle from representative baffle conditions were in agreement with observations made by Elliott and Gallup.
- A very thick (cm-scale) baffle represents the most conservative baffle condition since an increase in thickness had no effect on the resultant thermal gradient in the mold and provided the best opportunity for granular flow.

References

1. L.W. Sink, "Method of Casting Directionally Solidified Articles," (U.S. Patent No 3,417,809), 1968.
2. F.L. Versnyder and M.E. Shank, *Mat Sci Eng*, 6 (1970) 213.
3. J.G. Tshinkel, A.F. Giamei and B.H. Kearn, "Apparatus for Casting of Directionally Solidified Articles," (U.S. Patent No 3,763,926), 1973.
4. A.F. Giamei and J.G Tschinkel, *Metall and Mater Trans A*, 7A (1976) 1427-1434.
5. J. Grossmann, J. Preuhs, W. Esser and R.F. Singer, *Proceedings of the 1999 International Symposium on Liquid Metal Processing and Casting*, eds. A. Mitchell, L. Ridgway and M. Baldwin (The Minerals, Metals & Materials Society, 1999) 31-40.
6. F. Hugo, U. Betz and J. Ren, S.-C. Huang, J.A. Bondarenko and V Gerasimov, *Proceedings of the 1999 International Symposium on Liquid Metal Processing and Casting*, eds. A. Mitchell, L. Ridgway and M. Baldwin (The Minerals, Metals and Materials Society, 1999) 16-30.
7. A. Lohmüller, W. Esser, J. Grossman, M. Hördler, J. Preuhs and R.F. Singer, *Superalloys 2000*, ed. T.M. Pollock, R.D. Kissinger, R.R. Bowman, K.A. Green, M. McLean, S.L. Olson, and J.J. Schirra (Warrendale, PA: TMS, 2000) 181-188.

8. M. Konter and M. Thumann *Journal of Materials Processing Technology*, 117 (2001) 386-390.

9. M. Lamm and R.F. Singer, *Metall and Mater Trans A*, 38A (2007) 1177.

10. A.J. Elliott and T.M. Pollock, *Metall and Mater Trans A*, 38A (2007) 871-882.

11. A.J. Elliott, G.B. Karney, M.F.X. Gigliotti and T.M. Pollock, *Superalloys 2004*, eds. K.A. Green, T.M. Pollock, H. Harada, T.E. Howson, R.C. Reed, J.J. Schirra and S. Walston (The Minerals, Metals & Materials Society, 2004) 421-430.

12. A.J. Elliott, S. Tin, W.T. King, S.-C. Huang, M.F.X. Gigliotti and T.M. Pollock, *Metall and Mater Trans A*, 35A (2004) 3221-3231.

13. J.D. Miller and T.M. Pollock, *Proceedings of the 2009 International Symposium on Liquid Metal Processing and Casting*, ed. P.D. Lee, A. Mitchell and R. Williamson (The Minerals, Metals & Materials Society, 2009) 119-126.

14. C. Brundidge, D. VanDrasek, B. Wang and T.M. Pollock, *Proceedings of the 2009 International Symposium on Liquid Metal Processing and Casting*, ed. P.D. Lee, A. Mitchell and R. Williamson (The Minerals, Metals & Materials Society, 2009) 107-117.

15. K. Gallup, J.D. Miller and T.M. Pollock, unpublished research, 2010.

16. T.J. Fitzgerald and R.F. Singer, *Metall Trans A*, 28A (1997) 1377-1383.

17. A. Kermanpur, N. Varahram, P. Davami and M. Rappaz, *Metall and Mater Trans B*, 31 (2000) 1293-1304.

18. J. Zhang and L.H. Lou, *J Mater Sci Technol*, 23 (2007) 289-300.

19. A.V. Luikov, A.G. Sashkov, L.L. Vasiliev and YU.E. Fraiman, *Int J Heat and Mass Transfer*, 11 (1968) 117-149.

20. T.H. Bauer, *Int J Heat and Mass Transfer*, 36 (17) (1993) 4181-4191.

21. B. Chaudhuri, F.J. Muzzio and M.S. Tomasonne, *Powder Technol*, 198 (1) (2010) 6-15.

CHAPTER 4

EVALUATION OF HEAT TRANSFER DURING DIRECTIONAL SOLIDIFICATION VIA THE BRIDGMAN AND LMC PROCESSES

The application of models to predict microstructure from solidification-processing conditions and inform process design has been an expanding area of research. Physically-representative boundary conditions have been implemented within a finte-element model for broad applicability of model predictions. Finite-element-based solidification modeling has been used to investigate the thermal characteristics of the Bridgman and Liquid Metal Cooling (LMC) directional-solidification (DS) processes. The dominant heat transfer step for each case has been identified. Relationships between thermal gradient and the solid-liquid interface position relative to the transition region of the furnace have been developed. Solidification rate and cooling rate as a function of withdrawal rate have been analyzed. The curvature of the solid-liquid interface varies with processing conditions and influences the morphological development of dendritic structure during solidification. An extensive sensitivity analysis of process conditions has been conducted with a model that has been validated for the prediction of thermal behavior for Bridgman and LMC techniques. A means to determine preferred process conditions independent of mold geometry has been defined. Extension of modeling techniques to complex geometries for the benefit of process design is discussed.

Introduction

The ability of solidification models to optimize casting conditions and predict the formation of solidification defects and undesirable casting conditions has improved dramatically over the past decade as the maturity of process models has improved. However, in order to accurately predict solidification conditions, appropriate boundary conditions and correct thermo-physical properties are required. These material and process parameters are only attainable through careful experimental measurements or complex inverse calculations [1]. Obtaining the experimental data needed to validate the model conditions is challenging, as a unique experimental setup is needed in most cases [1]. Model boundary conditions representative of a broad range of process conditions in an investment-casting environment are needed to improve the fundamental understanding of heat transfer during directional solidification, particularly in new approaches, such as the LMC process.

The development of models to predict microstructure from solidification-processing conditions that inform process design is critical for an ICME approach for cast materials. For single crystal turbine airfoils, a major challenge for integrating these models is the development of robust solidification models that are transferrable across casting geometries and solidification processing approaches. Determination of the optimal process conditions for an arbitrary casting geometry can be challenging. Optimization of process conditions is primarily experience-based, despite the predictive capability of

simulation tools. The lack of configuration-independent, quantitative metrics for determining optimal thermal conditions has limited the refinement of process conditions and hindered development of new single-crystal-growth approaches.

Once a set of model parameters is determined, the variability of the process conditions and sensitivity of model parameters can be assessed via a parametric analysis to bound the variability of the process and identify critical process variables. Parametric analyses are difficult to conduct experimentally since many process conditions are interdependent. Finally, as the configuration of the furnace or casting geometry changes, identifying the validity of extrapolated model conditions is challenging. Generalization of the sensitivity of thermal conditions to process conditions and casting geometries could enable a broader application of model predictions.

The liquid metal cooling (LMC) directional solidification process has been evaluated extensively over the past decade. The LMC process is an emerging directional-solidification technique that offers enhanced heat extraction compared to the conventional Bridgman process, thus providing refinement of dendritic structure and defects. However, associating microstructure scale with thermal predictions and optimization of process conditions have been limited by a lack of the fundamental understanding of the various heat transfer processes associated with the technique.

In this research, a well-validated finite-element (FE) model (Chapter 2) of the directional solidification process was developed to thoroughly investigate the thermal characteristics

of the directional solidification. Predictions of the thermal field were utilized to predict microstructure scale and determine optimal process conditions. A parametric analysis identified the relative importance of different process control parameters. A method to determine the optimal withdrawal rate and furnace temperature independent of mold configuration or alloy has been developed.

Simulation Methods

Directional solidification via the Bridgman and Liquid Metal Cooling (LMC) process was simulated using ProCAST^{TM}, a commercial solidification-modeling software package discussed in Chapter 1. In this effort, only fluid flow and heat transfer (with phase transformation) were considered. The modeling investigation utilized material and process conditions representative of the directional-solidification furnace in both conventional Bridgman and LMC modes, as discussed in Chapter 2. The model parameters utilized in this effort are summarized in Table 4.1. Details of the model conditions are summarized in Chapter 2.

Table 4.1 – Model parameters for FE-based solidification modeling.

Thermophysical Properties		
Baffle Thermal Cond.	1.0	W/mK
Shell Thermal Cond.	2.5	W/mK
Shell Thickness	6.4	mm

Interface Heat Transfer Coefficients		
Superalloy-Ceramic	*750	W/m^2K
Ceramic-Ceramic	500	W/m^2K
Tin-Ceramic	4000	W/m^2K

Boundary Conditions		
Shell Emissivity	0.4	
Baffle Emissivity	0.2	
Tin Temperature	250	°C

Run Parameters		
Maximum Time Step	**	
Spatial Step	0.5	mm
Critical Fraction Solid	0.4	

*Initial value reported with exponential decay to 100 W/m^2K during solidification
**Scaled by withdrawal rate to provide equal withdrawal distance (0.4mm) between steps

The casting configuration simulated in this research was a 5-bar cluster mold (Figure 4.1a). The rotational symmetry of the mold was utilized to improve computational time (Figure 4.1b). The nominal diameter of each bar was 1.6 cm, and the nominal length was 15 cm. The shell thickness of the investment mold was 6.4 mm. The alloy properties utilized were representative of CMSX-486 unless otherwise specified. Other alloys investigated were René N4 and Rene N5, first- and second-generation SX Ni-base superalloys, respectively. The thermal properties of these alloys are summarized in Table 4.2.

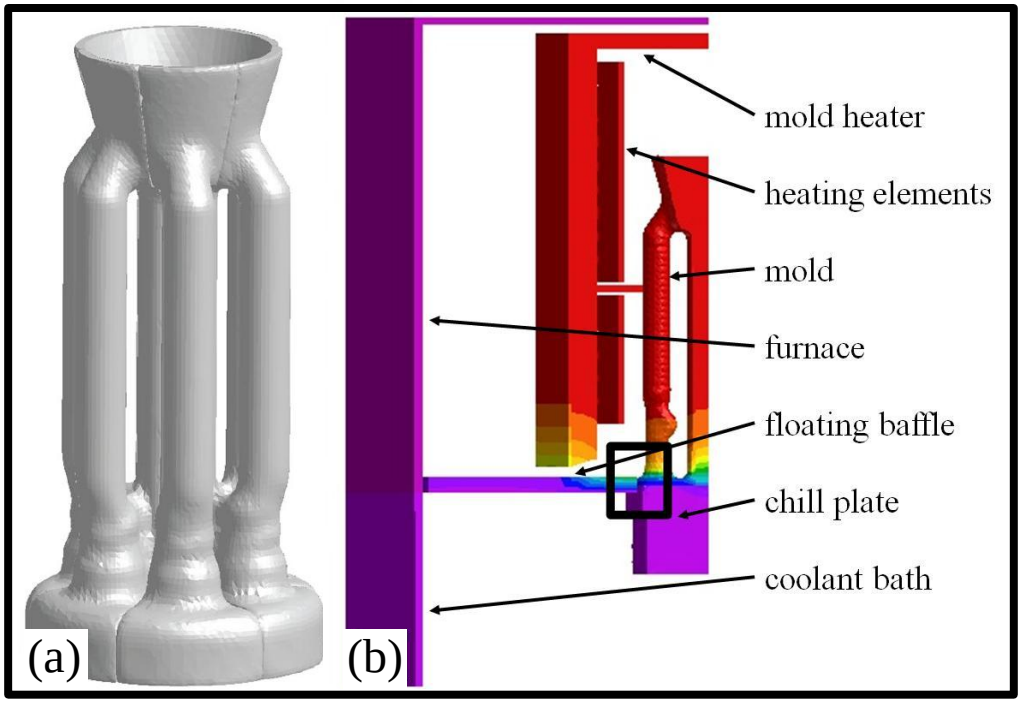

Figure 4.1 – Models of the (a) 5-bar mold configuration and (b) casting process.

Table 4.2 – Thermophysical properties of investigated alloys.

Alloy Designation	Liquidus (°C)	Solidus (°C)	Melting Range (°C)	Heat Capacity ($kJ\text{-}kg^{-1}\text{-}°C^{-1}$)	Latent Heat ($kJ\text{-}kg^{-1}$)	Thermal Conductivity ($W\text{-}m^{-1}\text{-}°C^{-1}$)
René N5	1402	1352	50	0.5-2.0	200	39-42
René N4	1345	1300	45	0.5-2.0	200	25-34
CMSX-486	1395	1330	65	0.5-2.0	200	25-34

In order to assess thermal gradient, solidification rate and cooling rate at the solidification front, a reference condition for the thermal gradient and solidification rate and a temperature range for the cooling rate must be defined. Since structure development and defect formation typically occur in the mushy zone, a critical fraction solid of the solidifying material is an appropriate reference condition. No standard value of fraction solid is routinely used for evaluation of the process thermal characteristics. This sensitivity analysis was conducted in which different solid fractions (and corresponding

temperatures) were selected for analysis of thermal gradient, solidification rate and cooling rate.

A comparative analysis of the thermal characteristics of the Bridgman and LMC processes was conducted. The major difference between LMC and conventional Bridgman is the use of a stirred coolant bath and floating baffle comprised of ceramic beads, rather than radiation cooling from the mold surface. The dominant heat transfer step for each process was identified based on calculations of thermal resistance in each heat transfer step. One-dimensional heat-transfer equations were used to calculate heat flow utilizing the input parameters - thermal conductivity, emissivity and heat transfer coefficients – and predicted temperature change for each heat-transfer step. The dominant heat transfer step was determined for a range of shell thicknesses at the critical temperature representing 0.40 fraction solid. In addition, the dominant heat transfer step was evaluated for a broad range of temperatures for the LMC process.

An extensive sensitivity analysis was also conducted in order to evaluate the effect of various mold and process conditions on the solidification behavior of the casting. A total of approximately 170 simulations were conducted in order to assess the key characteristics of the Bridgman and LMC processes. Each parameter was evaluated independently while all other parameters were assigned a baseline value (Table 4.3). Withdrawal rate, heater temperature, pour temperature, shell thickness, bar thickness and number of bars per cluster were assessed. In addition two-factor parametric analyses were performed in which a process parameter and the withdrawal rate were both varied

with all other parameters at the respective baseline values (Figure 4.2). These conditions were investigated in order to identify trends for optimal withdrawal rate for variations in alloy and bar thickness. All parametric analyses were conducted by evaluating local solidification conditions, including solidification front location and curvature, as well as the thermal gradient, solidification rate and cooling rate during solidification at the casting center and surface at the mid-height of the bar. The initial thermal condition of the chill plate and starter were also investigated.

Table 4.3 – Baseline process conditions and range of investigated values for the parametric analysis.

Parameter	Units	Baseline	Low	High
Alloy		CMSX-486	René N4	René N5
Bridgman Withdrawal Rate	mm-min^{-1}	3.4	0.8, 1.7	5.1, 6.8, 8.5
LMC Withdrawal Rate	mm-min^{-1}	12.7	4.2, 8.5	16.9, 21.2, 25.4
Mold-Heater Temperature	°C	1550	1475, 1500, 1525	1575, 1600
Pour Temperature	°C	1475		1500
Number of Bars per Cluster		5	1, 4	6, 8, 10
Shell Thickness	mm	6.4	4.8	7.9, 9.5
Bar Thickness	cm	1.6	1.3, 1.9, 2.5, 3.8, 5.1, 7.6, 10.2, 12.7	

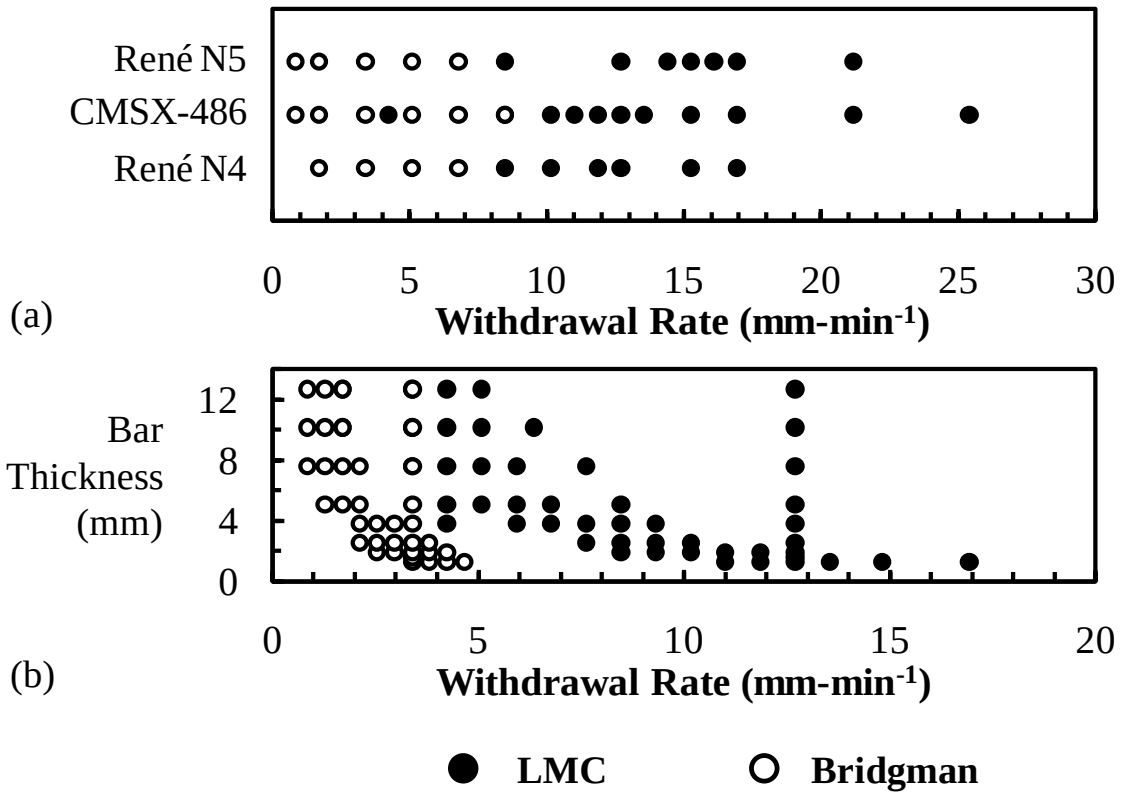

Figure 4.2 – Conditions evaluated using a two-factor parametric analysis for withdrawal rate and (a) alloy and (b) bar thickness.

Finally, solidification modeling was utilized to iterate process conditions in order to optimize solidification conditions for a range of geometrical configurations. The optimum solidification condition was obtained by balancing an increased thermal gradient and cooling rate with an undesirably inclined solid-liquid interface during solidification. The thermal gradient and solidification-front curvature were related to the solid-liquid interface position relative to the transition region in the furnace, either the fixed baffle in Bridgman or the floating baffle in the LMC process (Figure 4.3). The dependence of the inclination angle at the surface of the casting on the relative position of the solidification front was determined for a range of withdrawal rates. Solidification rate and cooling rate were also evaluated for the range of process conditions.

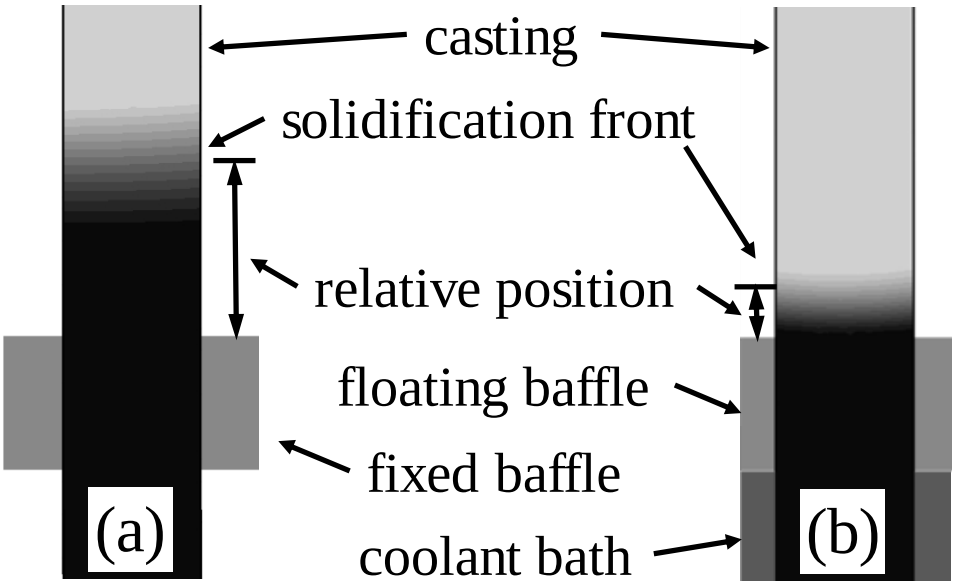

Figure 4.3 – Schematic of the position of the solidification front for (a) Bridgman and (b) LMC relative to the transition region within the furnace.

Fundamental Heat-Transfer Analysis

Simulations of the Bridgman and LMC process predicted the thermal field within the casting and investment mold (Figure 4.4). An abrupt change in temperature within the casting was observed near the transition region of the furnace. This was due to the change in heat-transfer direction from heat input in the mold heater to heat extraction within the cooling region of the furnace. From this data, the thermal gradient, solidification rate, cooling rate at the solid-liquid interface as well as the solid-liquid interface inclination angle were determined for the entire casting domain.

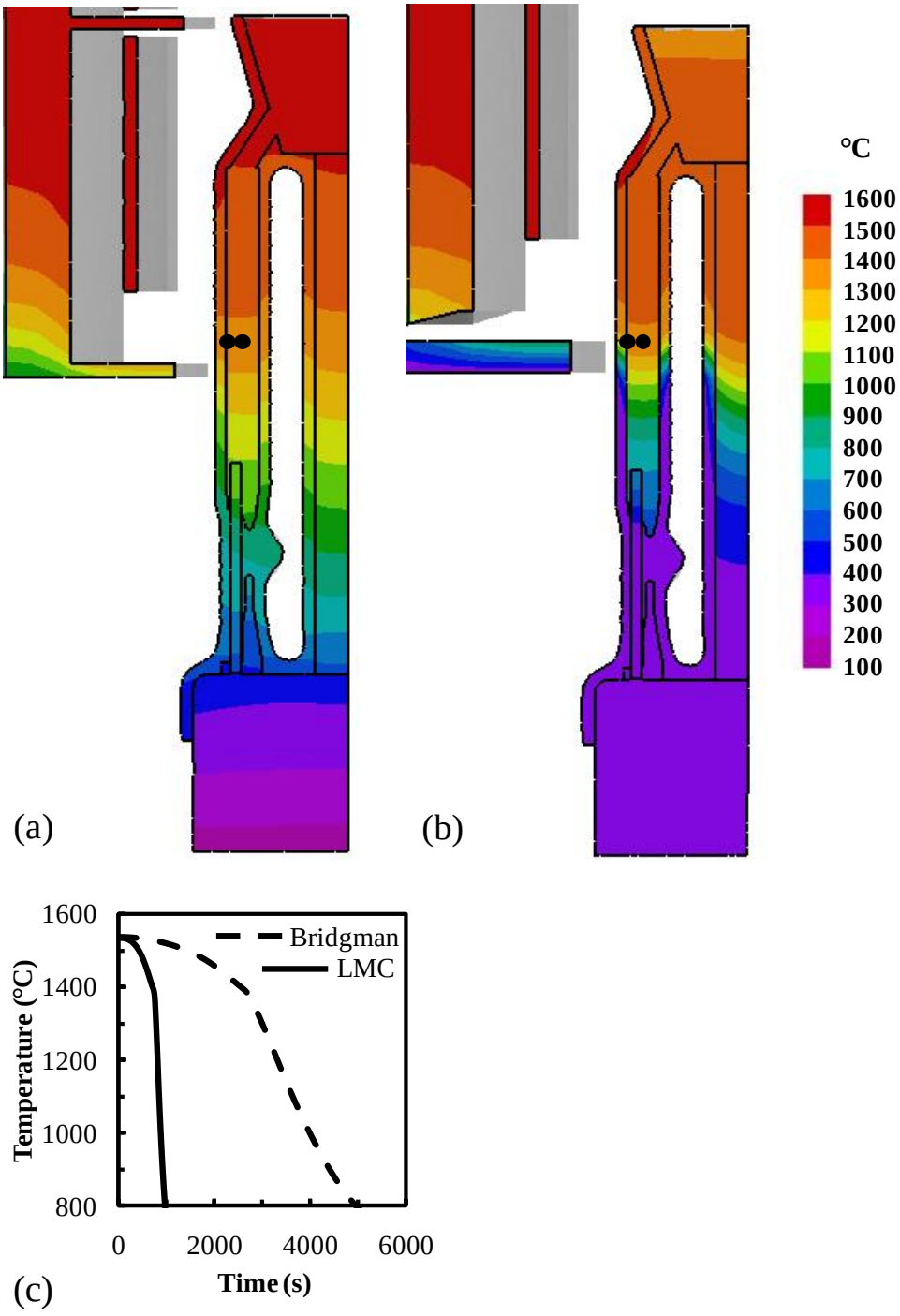

Figure 4.4 – Contour plots of temperature during a simulation of (a) Bridgman and (b) LMC processes with (c) corresponding thermal profiles at the specified locations within the casting for the baseline configurations. The black points in (a) and (b) indicate the "center" and "edge" locations within the casting for thermal comparison between different simulations.

The predicted thermal characteristics at the solidification front were compared for the baseline process conditions of the Bridgman and LMC processes (Figure 4.5). A steady-state condition was present for approximately half of the bar centered at its mid-height for both the Bridgman and LMC processes. At steady state for the Bridgman process, a thermal gradient of 39 °C-cm^{-1} and cooling rate of 0.22 °C-s^{-1} were observed for the 5-bar mold geometry and typical process conditions. On the other hand, a thermal gradient of 81 °C-cm^{-1} and cooling rate of 1.26 °C-s^{-1} were observed for the same casting at typical LMC process conditions. In addition, the thermal field within the bar cast via LMC was axisymmetric, while the thermal field within the bar cast via Bridgman varied due to the reduced radiation heat transfer on the surface of the casting at the the interior of the cluster mold (Figure 4.5). With this casting configuration, utilization of the LMC process provided more than a two times increase in the thermal gradient and five times increase in cooling rate. The observed four times increase in the solidification rate was due to the increase in withdrawal rate, while the 50 pct increase in inclination angle was a result from the enhanced lateral heat extraction of the LMC process compared to Bridgman. The enhanced heat extraction results in a predicted 55 pct reduction in PDAS and SDAS with utilization of the LMC process. Hereafter, thermal predictions of different simulations were compared by evaluation of these thermal characteristics for nodes at the outer diameter and center of the bar at its mid-height (Figure 4.4).

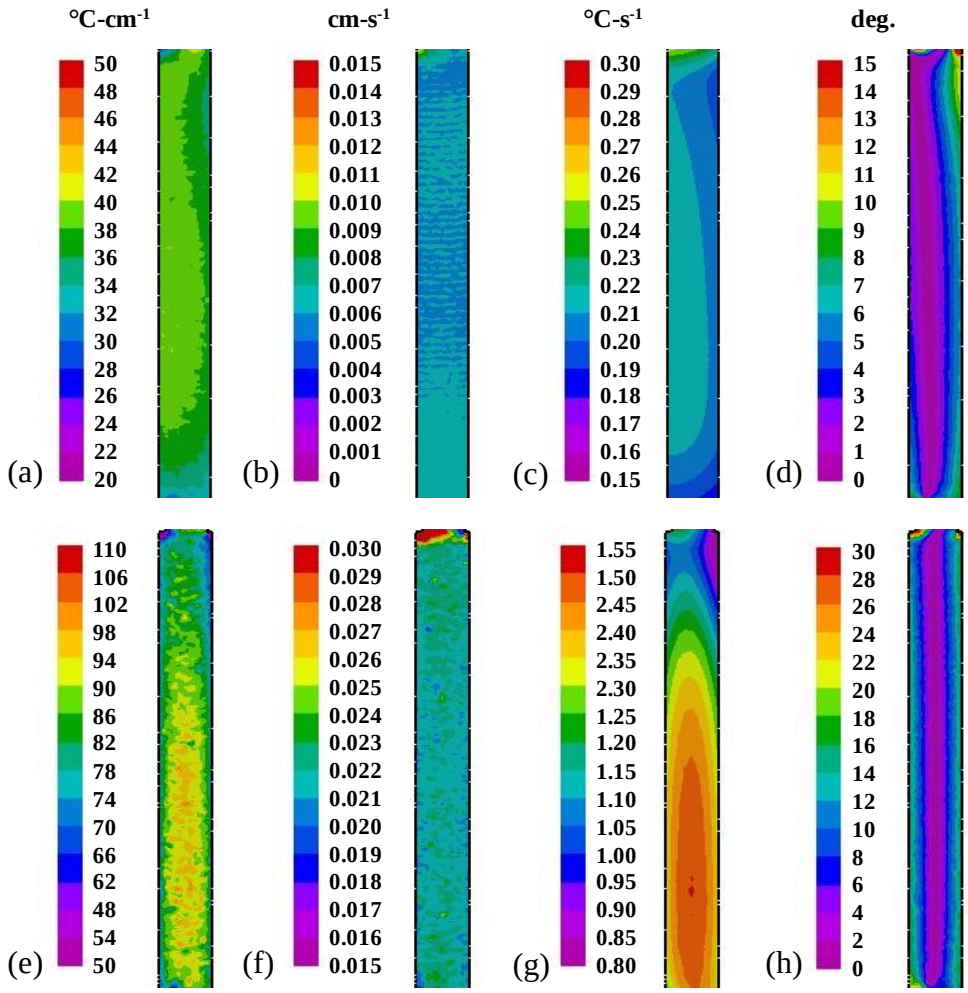

Figure 4.5 – Predicted contour plots of thermal characteristics for the baseline configuration of the Bridgman and LMC processes, (a) Bridgman axial thermal gradient, (b) Bridgman solidification rate, (c) Bridgman cooling rate, (d) Bridgman solidification-front inclination angle, (e) LMC axial thermal gradient, (f) LMC solidification rate, (g) LMC cooling rate, and (h) LMC solidification-front inclination angle.

Investigating the temperature-sensitivity of the thermal-field characteristics – thermal gradient, solidification rate, cooling rate and inclination angle – throughout the melting range provided insight to the sensitivity of the thermal field to the critical fraction solid (Figure 4.6). The thermal gradient increased with increasing fraction solid. The difference between the thermal gradient normal to the solidification front and the axial thermal gradient was relatively constant for the range of fraction solid. Solidification rate

was insensitive to changes in the fraction solid. Inclination angle decreased with increasing fraction solid. The cooling rate increased with increasing fraction solid. The sensitivity of the thermal field to the critical fraction solid affected predictions for dendrite scale (Figure 4.6e-f). A decrease in both the PDAS and SDAS was observed with increase in the critical fraction solid. The prediction for SDAS is insensitive to changes in the critical fraction solid above 0.3.

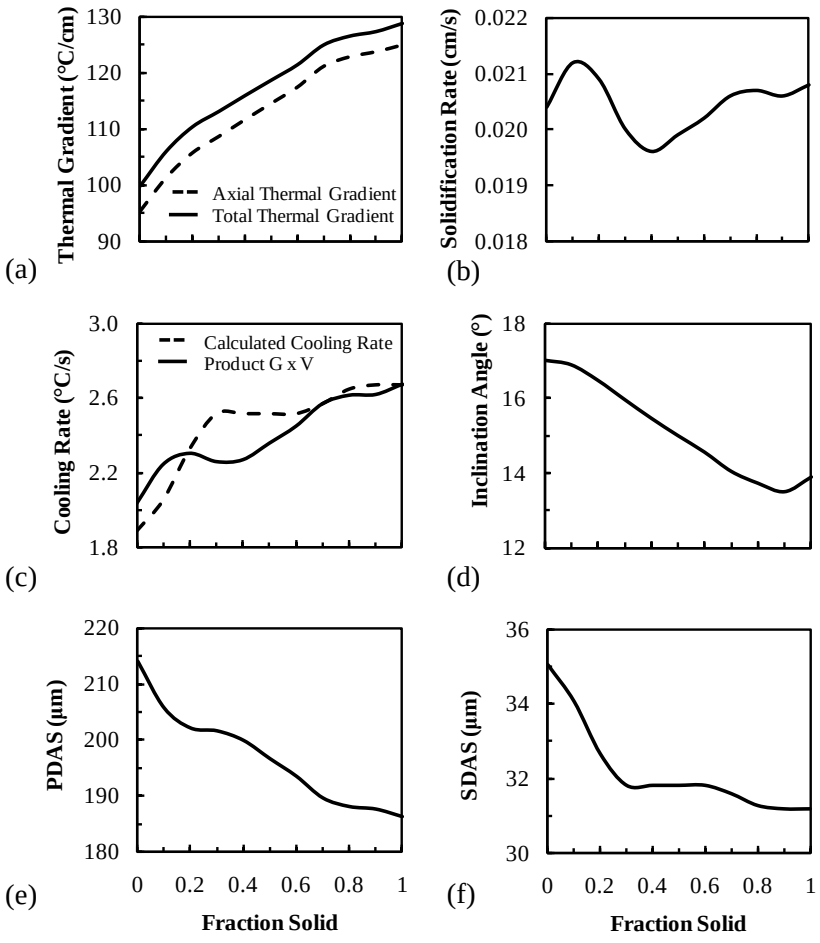

Figure 4.6 – Sensitivity of (a) thermal gradient, (b) solidification rate, (c) cooling rate, (d) solidification-front inclination angle, (e) PDAS and (f) SDAS to the critical fraction solid for a 5-bar mold cast via the LMC process and withdrawn at 12.7 mm-min^{-1}.

Overall, dendrite growth models utilize the thermal characteristics at the solidification front to predict primary and secondary dendrite arm spacings, as described in Chapter 1. Assumptions of the dendrite growth models are based on average thermal gradient and cooling rate values for the melting range [2,3]. A fraction solid of 0.4 yielded the same value as the average for the thermal gradient and cooling rate. Therefore, 0.4 is the critical fraction solid for evaluation of the thermal gradient and solidification rate at the solidification front, hereafter. Since the cooling rate is evaluated over a temperature range and SDAS dendrite growth models utilize the time it takes for the alloy to solidify, the cooling rate are evaluated between the liquidus and solidus temperatures.

An analysis of the relative thermal resistances of the heat transfer steps during directional solidification via the Bridgman and LMC processes was conducted. The heat-transfer steps that occur between the cold outer walls of the furnace to the center of the casting include heat transfer (i) from the surface of the shell, (ii) through the thickness of the shell, (iii) across the shell-metal interface and (iv) through the bulk metal (Figure 4.7d).

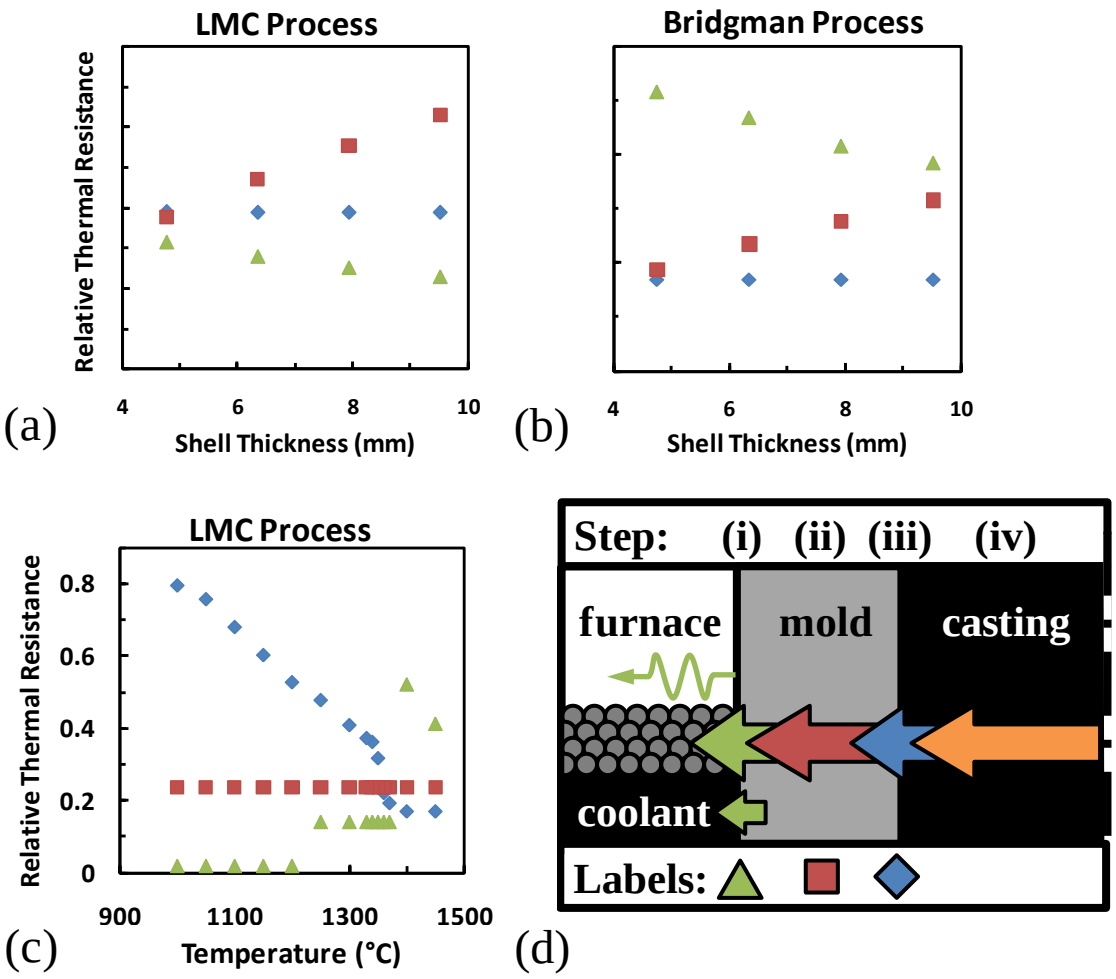

Figure 4.7 – Dependence of dominant heat transfer step on (a) shell thickness at a casting-surface temperature of 1370 °C (corresponding to the critical fraction solid) for the LMC and Bridgman processes and (c) casting surface temperature for the baseline shell thickness.

Thermal resistance was calculated from a 1-D equation for heat flow at steady state for each heat-transfer step. Cylindrical coordinates were utilized since the heat transfer occurred radially within a bar-mold casting configuration. Thermal resistance of radiation from the surface of the mold was calculated according to the Stefan-Boltzmann Law by factoring the temperature term and is described in Equation 4.1.

$$R = [2\pi r_2 F\varepsilon\sigma(T^2 + T_a^2)(T + T_a)]^{-1} \quad (4.1)$$

In this equation, R is the thermal resistance, r_2 is the outer radius of the mold, F is the view factor for radiation, ε is the emissivity, σ is the Stefan-Boltzmann constant, T is the temperature of the mold surface and T_a is the ambient temperature. Thermal resistance of heat-transfer from the mold surface to the floating baffle and coolant was determined from Newton's Law of Cooling as described by Equation 4.2.

$$R = [2\pi r_2 h_2]^{-1} \tag{4.2}$$

In this equation h_2 is the heat-transfer coefficient from the mold to the floating baffle (or coolant, depending on the position of the solidification front). Thermal resistance of conduction through the mold was calculated according to an energy balance in conjunction with Fourier's Law as in Equation 4.3.

$$R = \frac{ln(r_2/r_1)}{2\pi k} \tag{4.3}$$

In this equation, r_1 is the inner radius of the mold and k is the thermal conductivity of the mold. Thermal resistance across the mold-metal interface was calculated from Newton's Law of Cooling and is described by Equation 4.4.

$$R = [2\pi r_1 h_1]^{-1} \tag{4.4}$$

In this equation, h_1 is the heat-transfer coefficient across the mold-metal interface. The thermal properties and temperatures for each equation were extracted from the model parameters and simulations at the mid-height of the bar when the critical fraction solid of the metal was positioned at the surface of the casting.

A range of shell thickness was evaluated to determine the sensitivity of the dominant heat transfer step at mushy-zone temperatures to variations in processing conditions for both the Bridgman and LMC processes (Figure 4.7a-b). The conductivity through the metal

was not considered due to order of magnitude increase in thermal conductivity of nickel-base superalloy as compared to the mold. For the Bridgman process, the thermal resistance of the radiation cooling from the mold surface to the chamber walls is higher than all other heat transfer steps for the range of typical shell thicknesses. The least thermally resistant step is the heat transfer between the mold and metal, despite the radiation gap forming during solidification. Conversely, the most thermally resistant step for the LMC process is conduction though the mold, except for very thin shell thicknesses, in this case 4.8 mm, in which the mold-metal interface has a similar thermal resistance. Overall heat extraction is much more efficient for the LMC process.

In addition, the dominant heat transfer step in the LMC process was determined for a range of temperatures for the standard shell thickness of 6.4 mm (Figure 4.7c). The thermal resistance of each heat transfer step was evaluated for a range of temperatures from 1000 °C to 1450 °C. As the temperature decreases, a radiation gap forms between the casting and the mold surface that is represented by a drop in the interface heat transfer coefficient with temperature. Thus, the mold-metal interface becomes the most thermally resistant step with decreasing temperature. For temperatures greater than the liquidus, when the furnace is applying heat to the mold via radiation, the heat transfer to the mold surface is the dominant heat-transfer step.

Parametric Analysis of Process and Mold Conditions

A parametric analysis revealed the relative sensitivity of the thermal conditions to changes in casting configuration and process conditions for both the Bridgman and LMC processes. Pour temperature and mold-heater temperature were the evaluated process conditions, while bar thickness, shell thickness and number of bars per cluster were the casting-configuration parameters evaluated. Because the withdrawal rate is used to optimize the thermal conditions during solidification, analysis of the effect of withdrawal rate on the thermal characteristics is discussed in the following section.

Variation of the furnace temperature from 1450 °C to 1600 °C demonstrated a moderate effect on the thermal conditions (Figures 4.8). An increase in furnace temperature increased axial thermal gradient and cooling rate while lowering the solidification front toward the tin. The inclination angle slightly increased while the solidification rate slightly decreased for significant increase in furnace temperature. Thus, by increasing the furnace temperature, an increased thermal gradient could be achieved without negatively increasing the inclination angle.

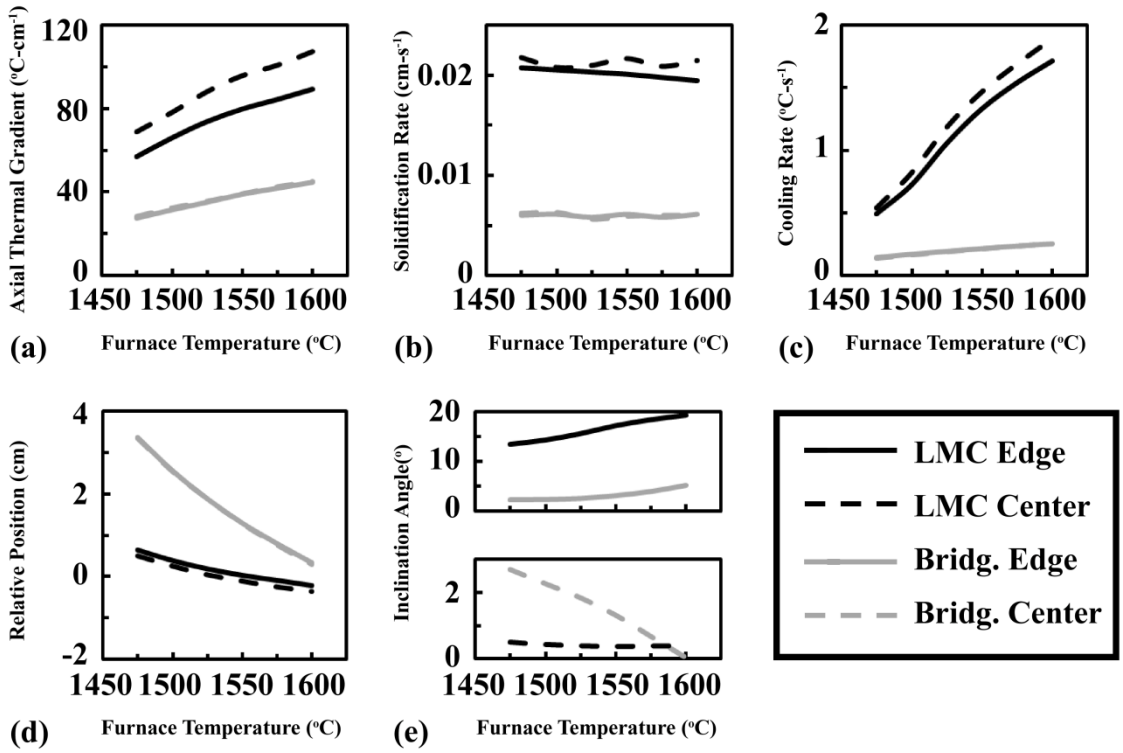

Figure 4.8 – Sensitivity of thermal conditions to furnace temperature for the Bridgman and LMC processes at the center and edge at the mid-height of a SX bar, (a) axial thermal gradient, (b) solidification rate, (c) cooling rate, (d) position of the solidification front relative to the top of the transition region and (e) inclination angle.

Pour temperature had no impact on the thermal conditions during solidification for either the Bridgman or LMC processes for the range evaluated (Figures 4.9). Prior to withdrawal of the casting, a hold time at the soak temperature, after the charge was poured into the mold, was employed during casting. This condition allowed the molten metal and mold to reach a steady state temperature prior to withdrawal regardless of pour temperature. For the Bridgman process, the equilibrium temperature of 1537 °C was reached within a 10 minute hold at temperature for either the 1475 or 1500 °C pour temperature. Similarly, for the LMC process, simulations of both pour temperatures investigated reached a steady state temperature of 1532 °C within a 10 minute hold time.

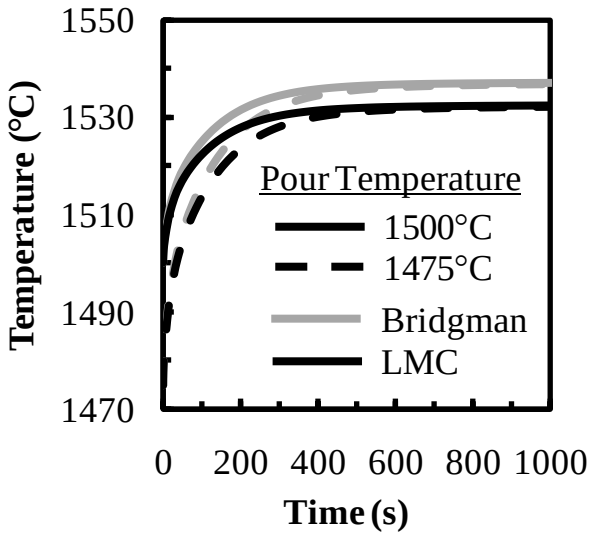

Figure 4.9 – Thermal prediction of temperature equilibration for castings with pour temperatures of 1475 °C and 1500 °C for both the Bridgman and LMC processes.

The thermal field was generally insensitive to the number of bars per cluster for either the Bridgman or LMC processes for clusters ranging from 1 to 10 bars (Figure 4.10). For the Bridgman process, the insensitivity of the thermal conditions to the number of bars per mold for the range evaluated was not expected as the reduction in view factor with increasing number of bars was anticipated to negatively affect the thermal field. The relatively small thickness of these castings may explain the insensitivity for the Bridgman process.

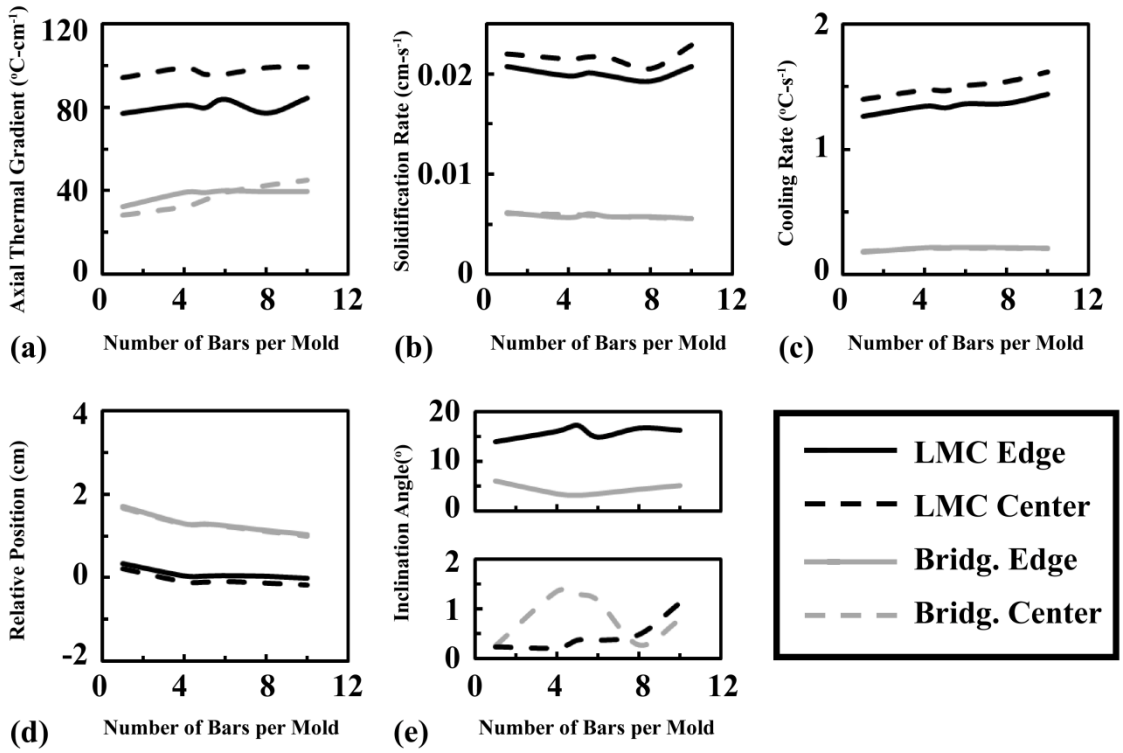

Figure 4.10 – Sensitivity of thermal conditions to number of bars per mold for the Bridgman and LMC processes at the center and edge at the mid-height of a SX bar, (a) axial thermal gradient, (b) solidification rate, (c) cooling rate, (d) position of the solidification front relative to the top of the transition region and (e) inclination angle.

The thickness of the investment mold was also evaluated parametrically (Figure 4.11). In the case of the Bridgman mode, the thermal condition was insensitive to changes in shell thickness. This was in agreement with the rate-limiting heat-transfer analysis, in which the shell thickness was not the rate-limiting heat-transfer step. However, the thermal field was sensitive to shell thickness for LMC. A change in the dominant heat transfer mechanism between 4.8 and 6.4 mm shell thickness was previously observed (Figure 4.7). At this transition, the dominant heat transfer step changes from the mold metal interface (at 4.8 mm) to the thermal conductivity through the shell (at 6.4 mm). The change in dominant heat-transfer mechanism caused an abrupt change in the thermal conditions at a shell thickness of 6.4 mm. Thus, an increase in shell thickness from 4.8

mm to 6.4 mm caused an increase in thermal gradient, inclination angle and cooling rate with a decrease in solidification rate. A further increase in shell thickness from 6.4 mm to 7.9 mm resulted in the opposite trend for each of the thermal conditions. Considering that the change in shell thickness evaluated was a 2 times increase and the thermal gradient, solidification rate and cooling rate change by less than 20 pct, the only parameter sensitive to changes in shell thickness was the inclination angle but only for the shell thicknesses less than 6.4 mm.

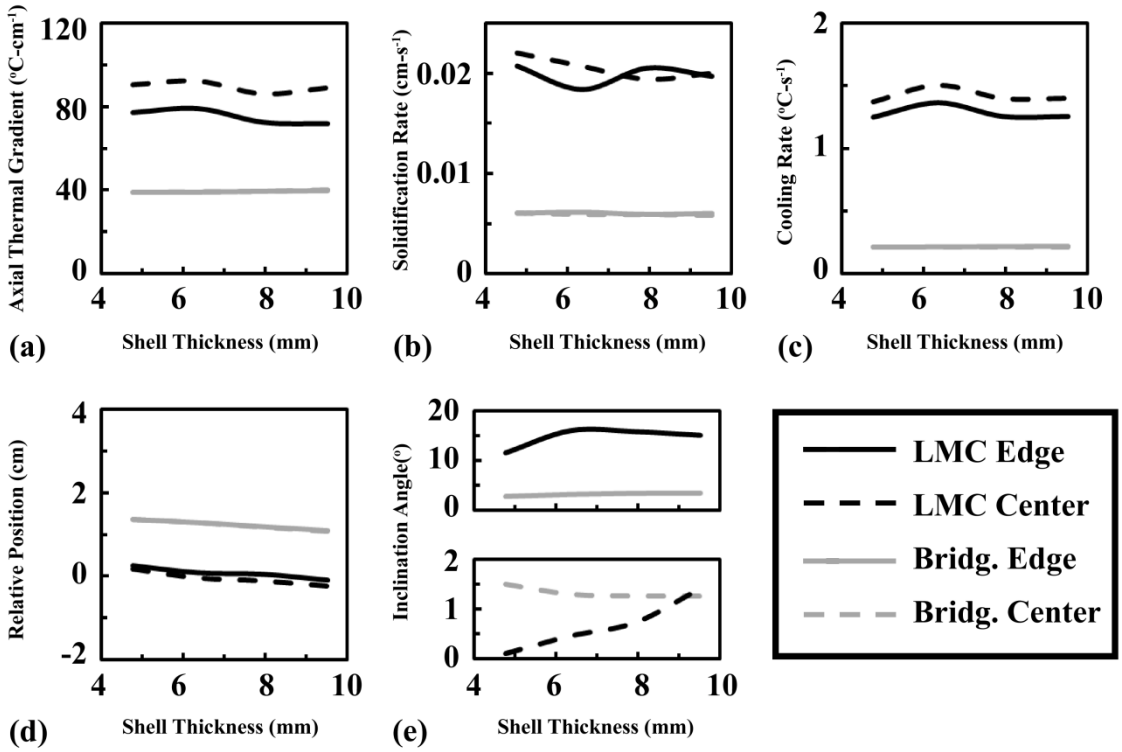

Figure 4.11 – Sensitivity of thermal conditions to shell thickness for the Bridgman and LMC processes at the center and edge at the mid-height of a SX bar, (a) axial thermal gradient, (b) solidification rate, (c) cooling rate, (d) position of the solidification front relative to the top of the transition region and (e) inclination angle.

Modification of the bar thickness significantly affected the thermal condition at the solidification front (Figure 4.12). An increase in bar thickness decreased the thermal

gradient, cooling rate and solidification rate. The solidification-front inclination angle increased with increasing bar thickness as the solidification front lowered into the tin due to the increased thermal mass. This analysis was conducted at a single withdrawal rate. It would be more appropriate to compare the optimal process condition for each bar thickness as is discussed in the following section. It is anticipated that an increase in bar thickness causes a decrease in the optimal withdrawal rate. The effect of bar thickness on optimal withdrawal rate is also discussed in the following section.

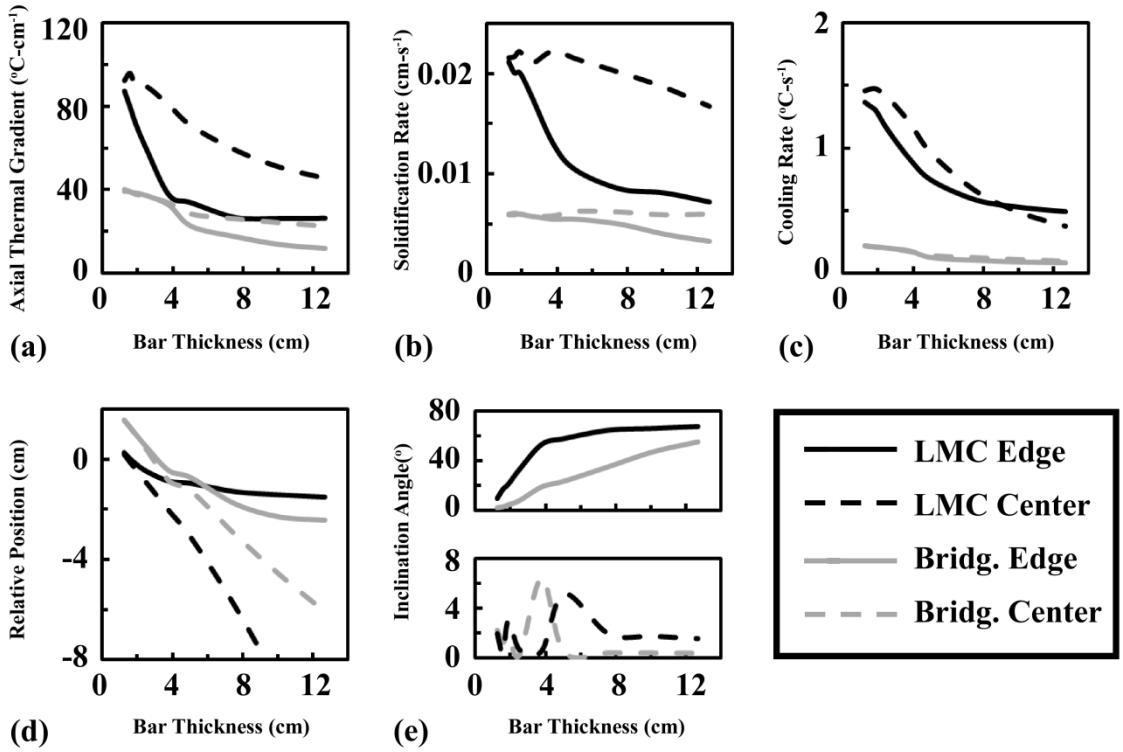

Figure 4.12 – Sensitivity of thermal conditions to bar thickness for the Bridgman and LMC processes at the center and edge at the mid-height of a SX bar, (a) axial thermal gradient, (b) solidification rate, (c) cooling rate, (d) position of the solidification front relative to the top of the transition region and (e) inclination angle.

The effect of the initial conditions on the solidification thermal conditions was evaluated. The initial height of the chill plate, hold time prior to withdrawal and chill plate material

were investigated for variability of the thermal condition within the casting and within the starter. No impact of these parameters on the thermal field within the bar casting was observed, while a difference in the solidification within the starter was identified. This analysis was motivated by the observation of increased nucleation defects and off-axis misorientation of the single crystal above the starter region during the LMC process (Figure 4.13c). Thermal simulation of the casting process predicted grain nucleation due to significant undercooling within the starter region (Figure 4.13a-b). The isolated region of solidification identified in Figure 4.13b indicated sufficient undercooling for nucleation to occur.

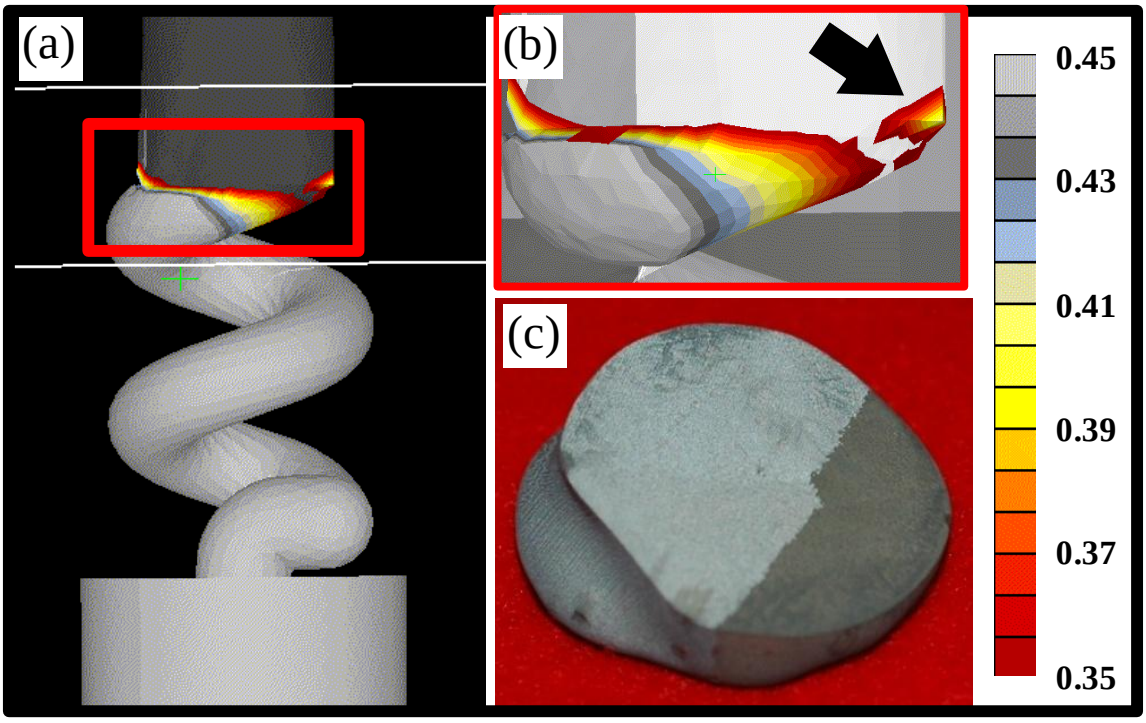

Figure 4.13 – (a) Predicted fraction solid contour plot of the starter region with (b) higher magnification identifying potential nucleation site above the starter and (c) macrograph of etched surface at the top of the starter indicating the presence of a nucleated grain (indicated by color contrast) at the same location.

When these observations were made, the chill plate was comprised of stainless steel and was cooled by the coolant bath. The low thermal conductivity of stainless steel limited the heat flow from the surface of the chill plate, causing a chill-plate surface temperature of 1100 °C, near the melting point of the alloy. With this configuration, significant seed melt-back and over-heating of the casting within the starter was limiting its efficiency. By utilizing a chill plate composed of molybdenum, the surface temperature reduced to 800 °C. Furthermore, lowering the position of the chill by 50 mm reduced the temperature at the top surface of the chill to 700 °C, due to the increased coolant-chill contact area. Overall these changes provided an increased thermal gradient just above the chill plate, thus improving the directional solidification within the starter. Thermal analysis via process simulation provided an informed process change that was later confirmed via thermocouple measurement of chill plate temperatures.

Optimization of the Directional Solidification Process

The sensitivity of thermal conditions to withdrawal rate was evaluated for both the Bridgman and LMC processes in order to identify the thermal characteristics associated to an optimal thermal condition. Overall, it was demonstrated that for either Bridgman or LMC an increase in withdrawal rate decreased mushy-zone height while increasing cooling rate, solidification rate and solidification-front inclination angle (Figure 4.14). Increasing withdrawal rate also lowered the solid-liquid-interface position within the furnace, thus changing the axial thermal gradient at the solidification front (Figures 4.14). An abrupt change in the thermal condition was observed when the solidification front

lowered into the tin, significantly increasing the inclination angle. Because all of these thermal characteristics were affected by the processing conditions interdependently, an optimal casting condition provided a balance between minimization of the solidification-front inclination angle and maximization of the thermal gradient. A maximum axial thermal gradient at the surface of the casting was achieved at an intermediate withdrawal rate for both Bridgman and LMC. For LMC, a minimum inclination angle was observed in the center of the casting for the same conditions. However, the inclination angle in the center of the casting was not minimized for the condition that caused the maximum axial thermal gradient for the Bridgman process. The absence of correspondence of the maximum axial thermal gradient and minimum inclination angle in the Bridgman process was attributed to the non-axisymmetric nature of the thermal field as shown previously (Figure 4.5).

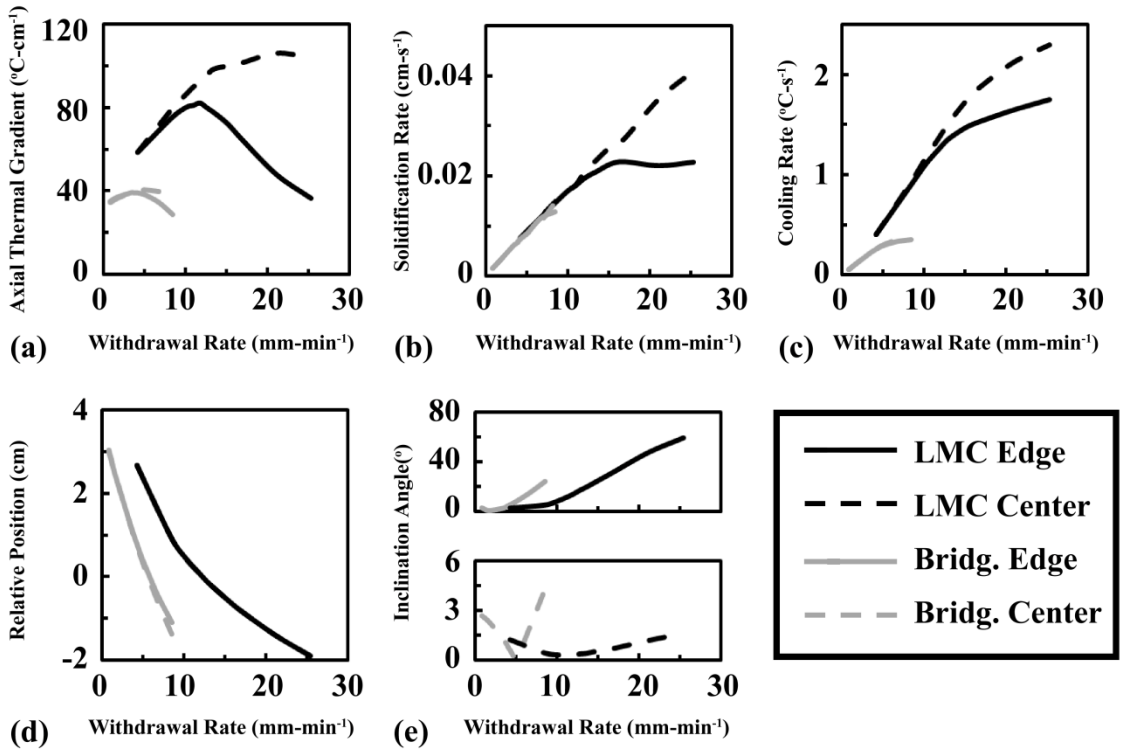

Figure 4.14 – Sensitivity of thermal conditions to withdrawal rate for Bridgman and LMC, (a) axial thermal gradient, (b) solidification rate, (c) cooling rate, (d) position relative to the baffle and (e) inclination angle. Note: for (d) the position is relative to the top of the baffle with positive values above the baffle.

The same analysis approach described above was completed for two additional alloys. The sensitivity of the thermal field to changes in the alloy was assessed (Figure 4.15 and 4.16). Qualitatively, similar changes in thermal conditions are observed from variation of the withdrawal rate. Overall, alloys with a higher liquidus temperature had a lower thermal gradient, cooling rate and inclination angle for the same casting conditions. Alloys with a higher liquidus solidified earlier in the solidification process (higher in the furnace) than alloys processed in the same manner with a lower liquidus, thus providing a reduced inclination angle. At the same time, however, these alloys had a reduced thermal gradient and cooling rate since the superheat of the melt was less for alloys with a higher liquidus temperature and equivalent process conditions. Comparison of different alloys

at different withdrawal rates is discussed later in this section. Comparison of the Bridgman and LMC process conditions demonstrated a significant increase all of the thermal conditions with utilization of the LMC process. The abrupt change in thermal conditions due to a significant increase in inclination angle observed with bars cast with the LMC process was much less pronounced with bars cast via the Bridgman process (Figure 4.16).

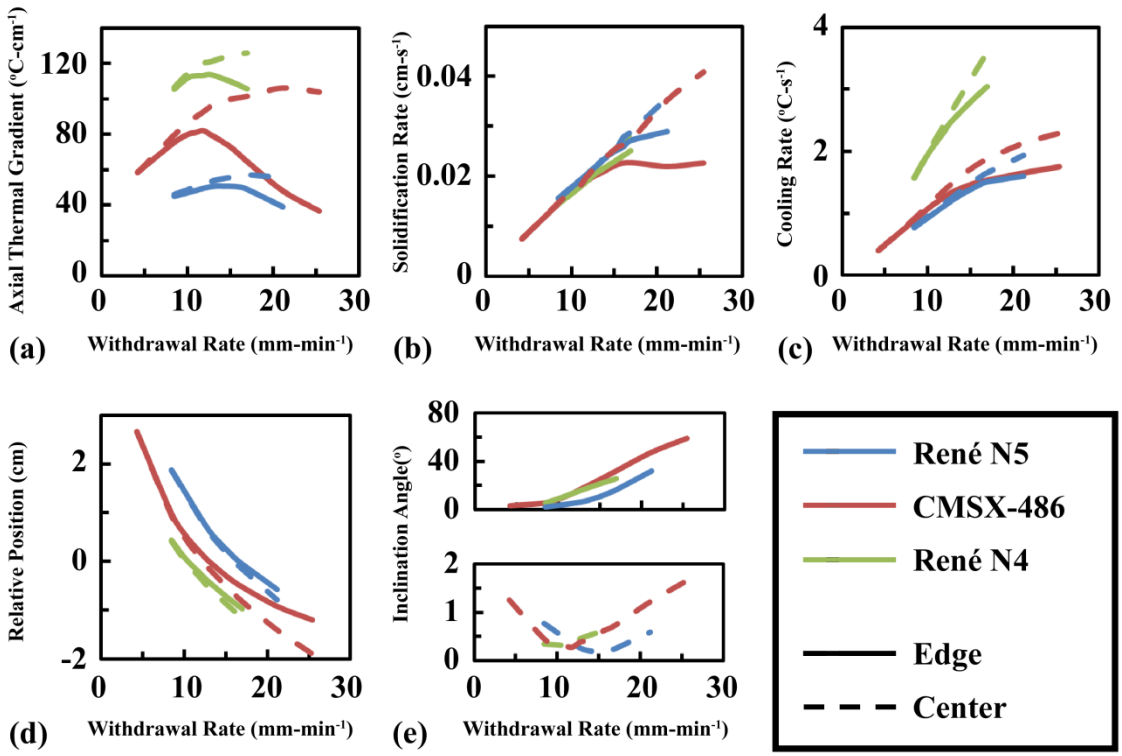

Figure 4.15 – Sensitivity of thermal conditions to alloy and withdrawal rate for bars cast via LMC, (a) thermal gradient, (b) solidification rate, (c) cooling rate, (d) solidification-front position relative to the top of the baffle and (e) inclination angle.

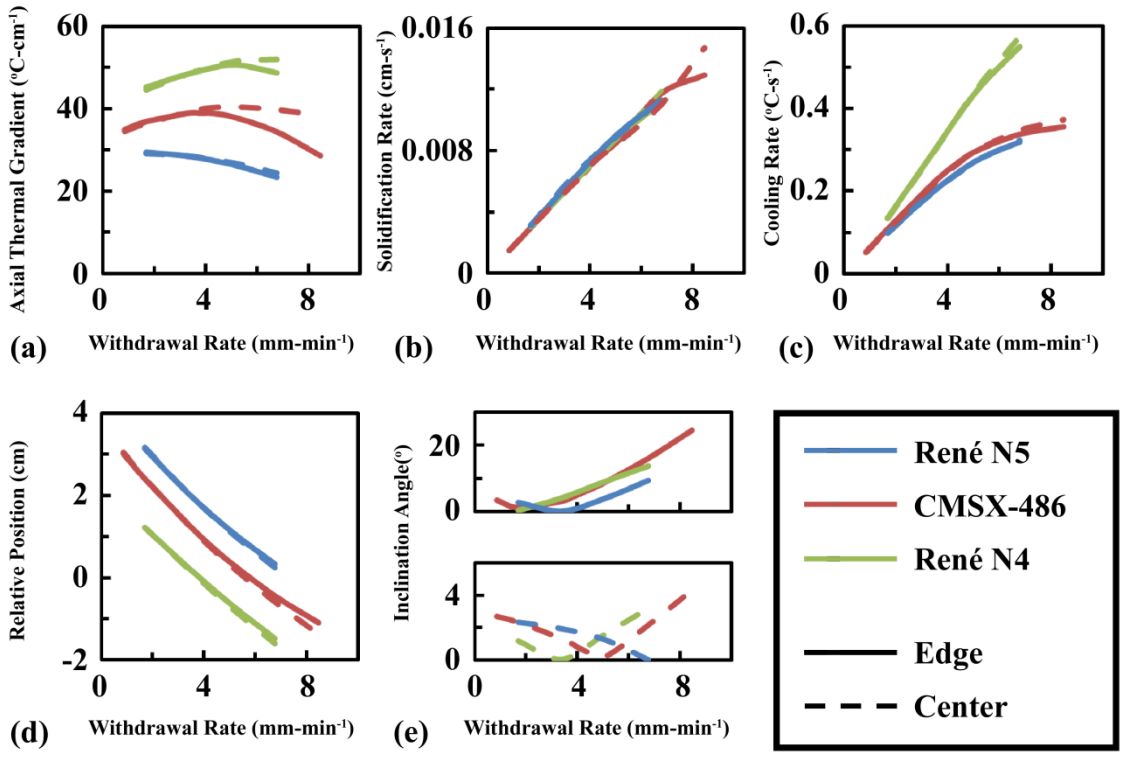

Figure 4.16 – Sensitivity of thermal conditions to alloy and withdrawal rate for bars cast via Bridgman, (a) thermal gradient, (b) solidification rate, (c) cooling rate, (d) solidification-front position relative to the top of the baffle and (e) inclination angle.

The thermal conditions at the optimized withdrawal rate for each alloy were also compared (Figure 4.17). The thermal condition of the edge and center of the bars was similar for the optimized thermal condition for each alloy. The same trend of decreased axial thermal gradient, cooling rate and inclination angle with increased alloy liquidus was observed for the optimized thermal conditions of each alloy. The optimal position also increased with increasing alloy liquidus. The optimal withdrawal rate and solidification rate increased with increasing alloy liquidus for LMC and decreased with increasing alloy liquidus for Bridgman. There are many other alloy properties that should also be considered that may affect solidification conditions including melting range,

latent heat of fusion and heat capacity. Further research is needed to identify the sensitivity of the thermal field to these conditions.

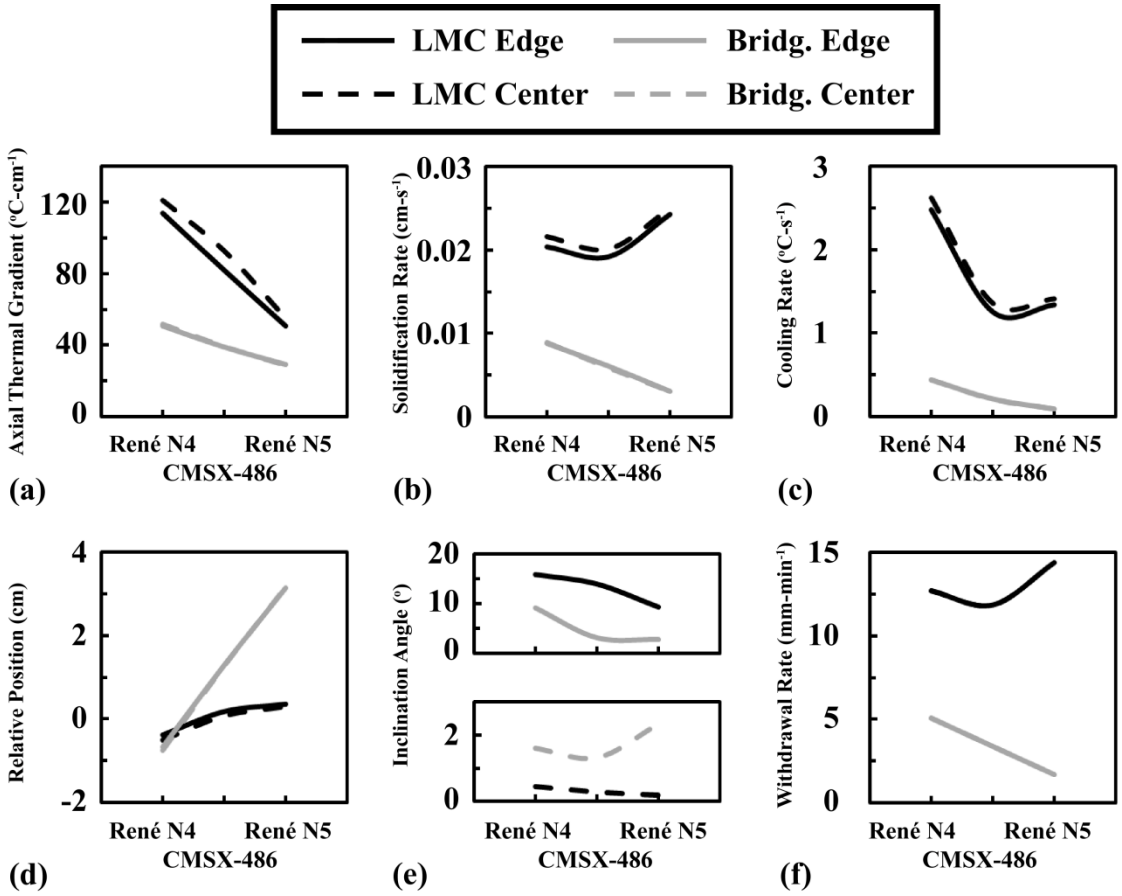

Figure 4.17 – Comparison of optimized thermal conditions for castings with different alloy compositions processed via the Bridgman and LMC conditions, (a) axial thermal gradient, (b) solidification rate, (c) cooling rate, (d) solidification-front position relative to the top of the baffle, (e) solidification-front inclination angle and (f) withdrawal rate.

The dependence of thermal conditions on withdrawal rate was also assessed for a range of bar thicknesses. The parametric analysis conducted in the previous section identified a strong dependence of the thermal conditions to casting thickness for the same withdrawal rate. As was discussed in that section, a more appropriate analysis would have evaluated different withdrawal rates for each bar thickness. Thermal conditions from a range of

withdrawal rates were compared for each bar thickness and both processes (Figure 4.18 and 4.19).

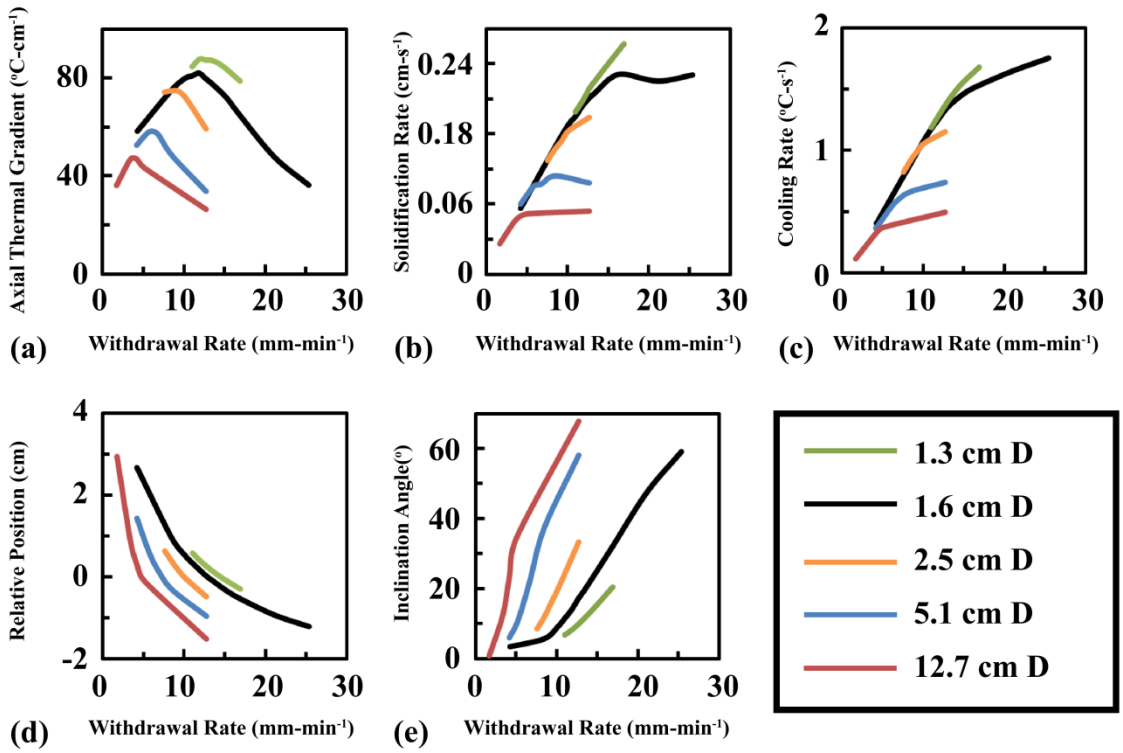

Figure 4.18 – Sensitivity of thermal conditions to bar thickness and withdrawal rate for bars cast via LMC, (a) thermal gradient, (b) solidification rate, (c) cooling rate, (d) solidification-front position relative to the top of the baffle and (e) inclination angle.

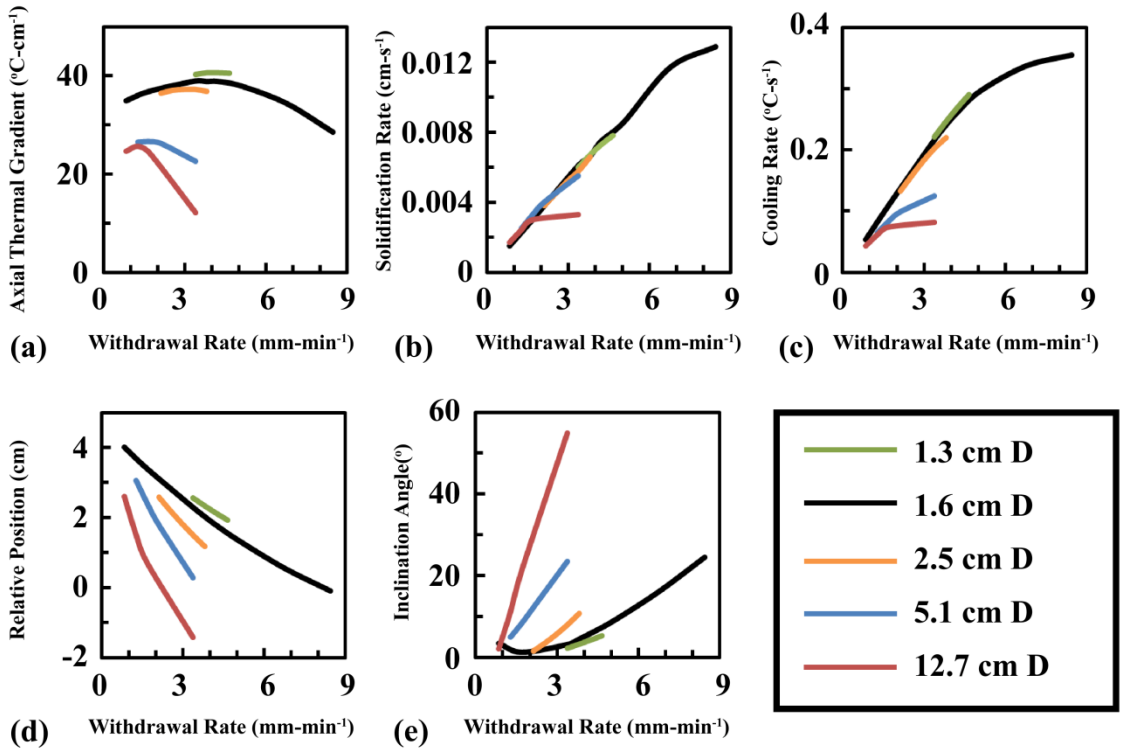

Figure 4.19 – Sensitivity of thermal conditions to bar thickness and withdrawal rate for bars cast via Bridgman, (a) thermal gradient, (b) solidification rate, (c) cooling rate, (d) inclination angle and (e) solidification-front position relative to the top of the baffle.

The optimal withdrawal rate for each bar thickness was determined according to a maximum axial thermal gradient at the surface of the casting. Thermal conditions at the optimal withdrawal rates were then compared for each bar thickness for both the Bridgman and LMC processes (Figure 4.20). An increase in bar thickness resulted in a reduction in the withdrawal rate for the optimal thermal condition. In addition, a decrease in thermal gradient, solidification rate and cooling rate was observed with increase in bar thickness for the optimum withdrawal rate. The inclination angle at the surface of the casting increased with increasing bar thickness for the optimal withdrawal rate. For an increase in bar thickness, the optimal position at the surface of the casting increased while the optimal position in the center decreased. The same trends were

observed with increased bar thickness for the Bridgman process, with the exception of the relative position.

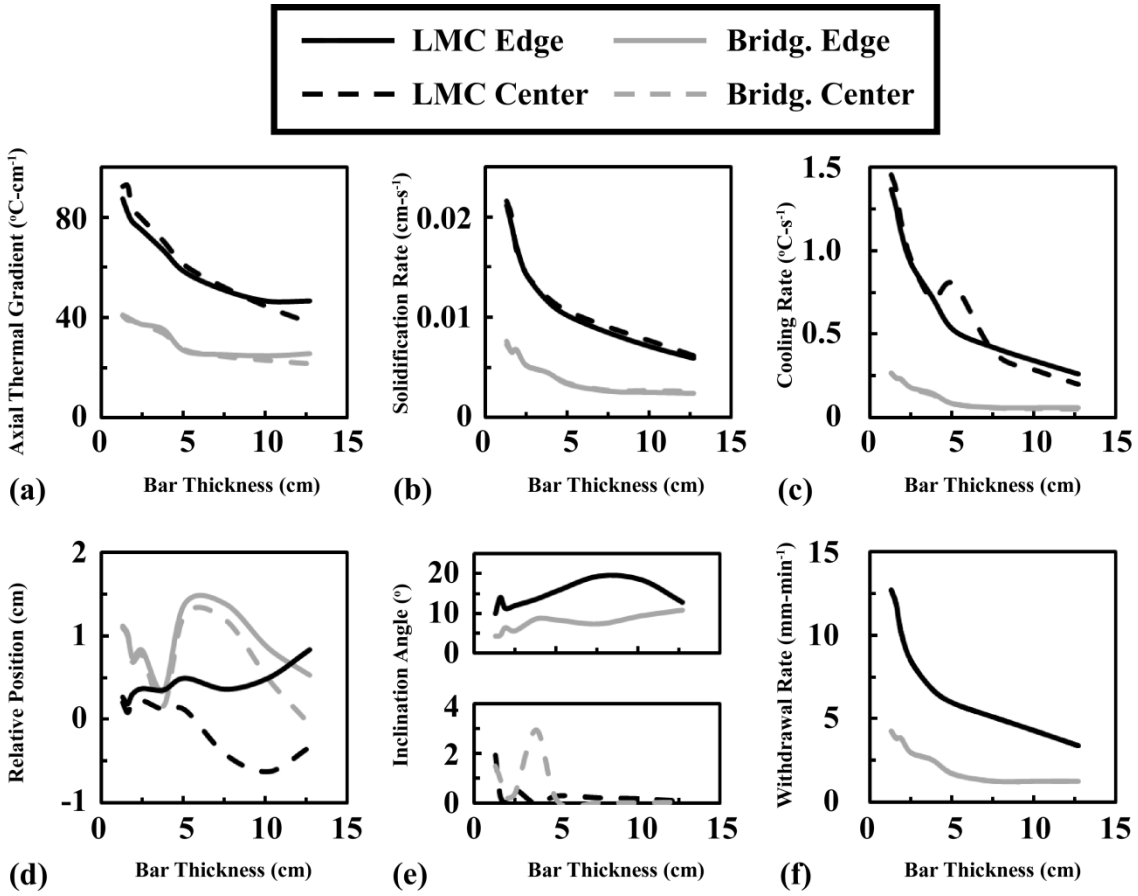

Figure 4.20 – Comparison of optimized thermal conditions for castings with a range of bar thicknesses processed via the Bridgman and LMC conditions, (a) axial thermal gradient, (b) solidification rate, (c) cooling rate, (d) solidification-front position relative to the top of the baffle, (e) solidification-front inclination angle and (f) withdrawal rate.

In order to determine if the optimal process condition was related to the height of the solidification interface in the furnace, the position of the solidification front relative to the transition region of the furnace was also evaluated (Figure 4.3). Previously in this section, the thermal conditions were compared to the withdrawal rate to establish correlations between the thermal conditions and withdrawal rate (Figure 4.14). In

addition, the position of the solidification-front relative to the top of the floating baffle was compared to the model predictions in order to determine potential relationships between solidification conditions and position. For the baseline condition, a maximum axial thermal gradient at the surface of the casting occurred when the solidification front at the surface of the casting was just above the top of the baffle for both Bridgman and LMC (Figure 4.21). The correspondence of position in the furnace and optimal thermal conditions provided a means to determine the optimal withdrawal rate, regardless of casting configuration. Specifically, the optimal position of the solidification front was 1 - 3 mm above the top of the floating baffle for LMC and 5 – 20 mm above the top of the fixed baffle for Bridgman for the baseline configuration (Figure 4.21a). A range was provided because analysis was conducted for discrete process conditions that resulted in discrete solidification-front positions.

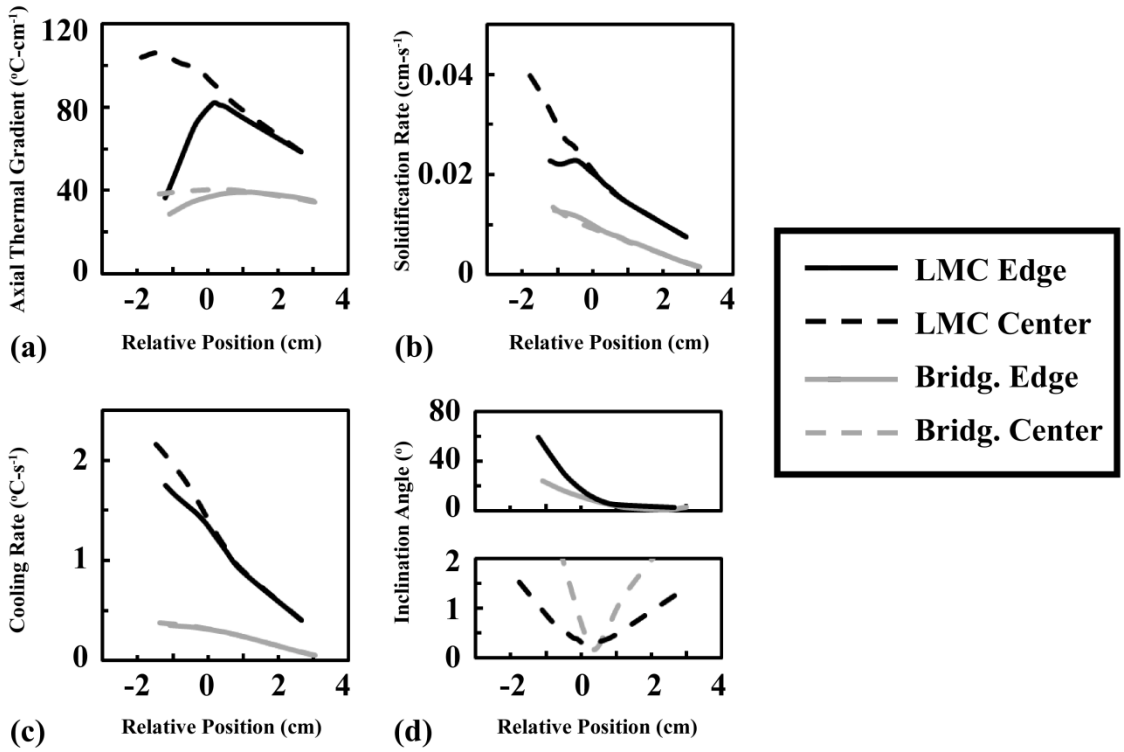

Figure 4.21 – Dependence of (a) thermal gradient, (b) solidification rate, (c) cooling rate and (d) solidification-front inclination angle on solidification-front position relative to the transition zone in the furnace for the Bridgman and LMC processes. The top of the baffle is at position 0 cm with positive distances above the baffle.

Overall, solidification modeling revealed significant differences in thermal gradient, solidification rate, cooling rate and solid-liquid-interface inclination angle for the Bridgman and LMC processes. For the optimized process condition, the axial thermal gradient approximately doubled while the solidification rate tripled and the cooling rate increased by a factor of six for LMC as compared to Bridgman. Consequently, the solidification-front inclination angle at the surface of the casting increased by a factor of four through utilization of the LMC process. Significant deviation in thermal conditions between edge and center locations was observed when the solidification-front location was below the top of the baffle. The values of the thermal conditions correlated to

withdrawal rate and not the relative position, with the exception of the axial thermal gradient and inclination angle.

Changes in casting geometry and alloy have been shown in this section to affect the thermal field within the casting, thus changing the optimal process conditions. Through comparison of solidification-front position and model predictions for a range of alloys and bar thicknesses, the relationship between solidification-front position and optimal process conditions was determined. For each alloy, the position of the solidification front for the optimal condition was near the top of the transition region but decreased slightly with decreasing alloy liquidus (Figure 4.22). This result suggests that a similar temperature should be observed at a given position within the furnace, but this analysis was beyond the scope of this effort. For the LMC process at the same furnace temperature for all simulations, an optimal position of 4 mm below the top of the baffle for Rene N4, 2 mm above the top of the baffle for CMSX-486 and 4 mm above the top of the baffle for Rene N5 was identified. For the Bridgman process, the optimal position relative to the top of the fixed baffle was 7 below, 13 above and 31 mm above for Rene N4, CMSX-486 and Rene N5, respectively. The optimal position for Bridgman was nearly 5 times more sensitive to alloy than LMC. The optimal position of LMC was more insensitive to alloy than Bridgman due to the abrupt change in heat-extraction at the coolant-baffle interface, as discussed in Chapter 3. The inclination angle increased with decreasing position below the floating baffle.

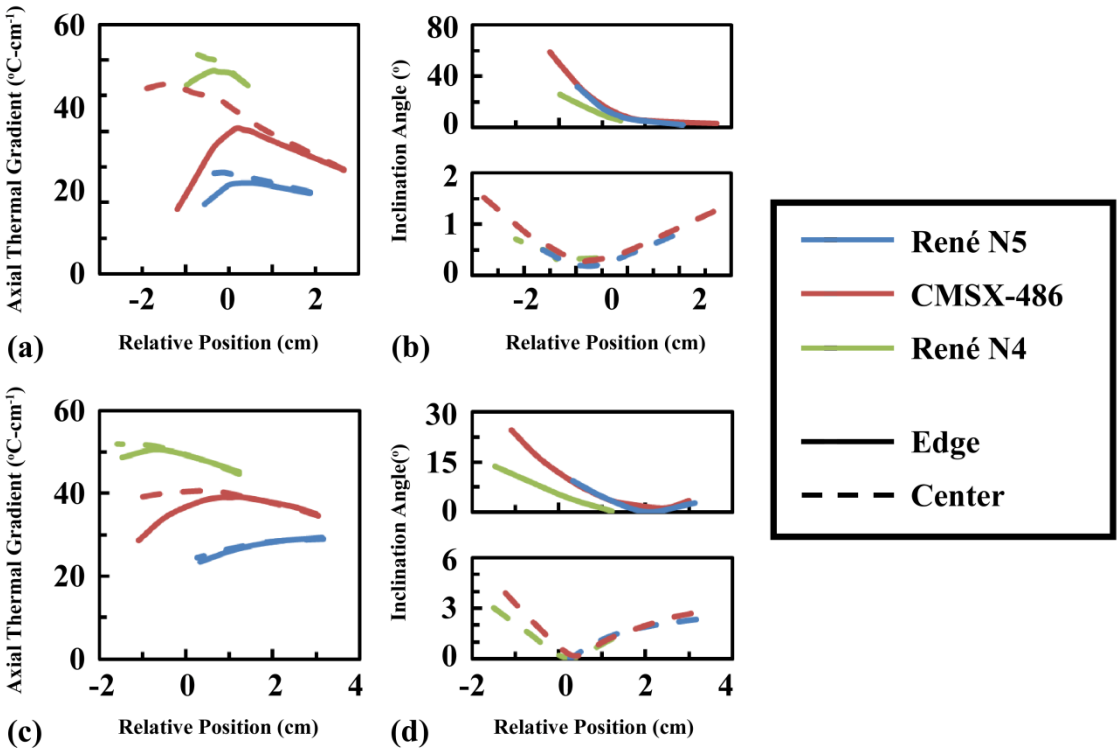

Figure 4.22 – Sensitivity of thermal conditions to alloy and position in the furnace relative to the floating baffle, (a) axial thermal gradient and (b) inclination angle for the LMC process, and (c) axial thermal gradient and (d) inclination angle for the Bridgman process.

For the optimal withdrawal rate of each bar thickness, the position of the solidification front was between 2 and 6 mm from the top of the baffle for the LMC process and between 5 and 15 mm for the Bridgman process (Figure 4.23). The inclination angle at the surface of the casting was insensitive to bar thickness and increased below the top of the baffle. These results indicated an insensitivity of optimal solidification-front position with variations in section thickness. *Thus, it has been demonstrated that the solid-liquid interface position can be utilized as the analysis tool for optimization of process conditions, independent of casting geometry and relatively insensitive to changes in alloy for the conditions evaluated.*

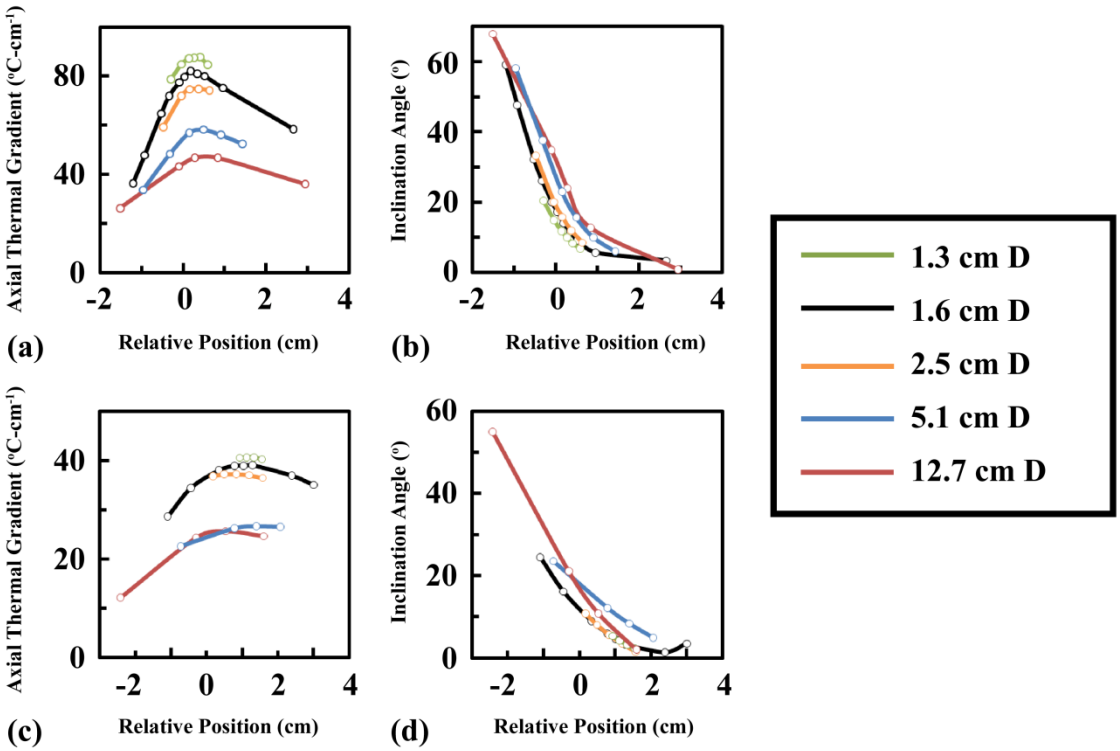

Figure 4.23 – Sensitivity of thermal conditions to bar thickness and position in the furnace relative to the floating baffle, (a) axial thermal gradient and (b) inclination angle for the LMC process, and (c) axial thermal gradient and (d) inclination angle for the Bridgman process.

Discussion

Previous solidification simulations of the LMC process identified a difference in the "rate-limiting" heat-transfer step during solidification [5]. Heat-transfer analysis of thick-section directional solidification was also conducted by Elliott [5]. The results reported in this research were consistent with Elliott's findings with the exception of the LMC rate-limiting heat-transfer step. In his analysis, the rate-limiting heat-transfer step of LMC was the shell-metal interface. His analysis considered much lower temperatures for heat-transfer evaluation. Analysis of the sensitivity of heat transfer to evaluation temperature of the metal (Figure 4.2b) exhibited a change in rate-limiting step after

solidification, thus confirming Elliott's findings at lower temperatures. However, for consideration of solidification behavior, the more appropriate evaluation temperature of the metal is within the melting range, at the critical fraction solid.

Analysis of the sensitivity of the thermal conditions to the mold-heater temperature indicated a 50 pct increase in thermal gradient and 2-3 times increase in cooling rate with only a 50 pct increase in the inclination angle across the range of furnace temperatures evaluated. For castings with relatively low inclination angles, a maximum furnace temperature may provide the most preferred thermal condition, especially for alloys with a higher liquidus. The effect of the interdependence of withdrawal rate and furnace temperature on solidification-front position was not evaluated. Further analysis of the effect of furnace temperature on optimal position of the solidification front could provide improved thermal conditions during solidification, especially in cases when the inclination angle is low. However, this analysis does not consider other potential negative consequences for altering the furnace temperature, such as grain nucleation or thermal stress.

Predictions of the thermal field within the casting prior to withdrawal showed the effect of initial process conditions on the initial solidification and ability to correlate predicted and measured cooling curves. The utilization of a hold time proved crucial to the success of validating simulation parameters with thermocouple measurements because a steady-state condition was attained within the entire casting and mold materials prior to withdrawal. In addition, the predicted temperature of the chill plate and solidification

within the starter were dependent on the initial position of the casting relative to the baffle as previously discussed. By understanding the heat transfer within the casting, the initial solidification conditions were improved, resulting in reduced nucleation in the starter region of the casting. A preferred initial condition includes utilization of a molybdenum chill, lowering the casting 50 mm relative to the baffle and utilizing a 10 minute hold time prior to withdrawal for the specific furnace investigated in this thesis.

The thermal conditions during solidification can be related to the position of the solid-liquid interface relative to the transition region of the furnace. The relationship between optimal conditions and solidification-front position is applicable to other furnaces, assuming that the furnace design is similar. Thus, simulation tools can be utilized to iterate withdrawal rate, evaluate solidification-front position, and determine the optimum process conditions. This method also provides the ability to determine optimal withdrawal rates that vary with position in a casting. Finally, processing maps can be generated for generic casting geometries such that a near-optimal withdrawal rate can be identified without casting trials or simulations. Further research is needed in this area to apply these optimization criteria to complex geometries and evaluate their performance.

A critical fraction solid at which thermal conditions are calculated in order to determine dendrite scale was determined to be 0.4 in this work. The thermal conditions at this fraction solid corresponded to the average thermal conditions of the melting range. Measurements from a 3D microstructure reconstruction of a decanted casting reported an abrupt change in permeability at a fraction solid of 0.4, which is in agreement with the

predictions in this work [4]. Thus, a critical fraction solid of 0.4 is used throughout this thesis for evaluation of the thermal conditions at the solidification front and prediction of dendrite scale.

Conclusion

Parametric analyses of directional solidification have been conducted for a wide range of process and alloy conditions with a validated solidification model. These simulations demonstrated the following:

- The dominant heat transfer step is radiation from the mold surface for Bridgman and mold thermal conductivity or mold-metal interface heat transfer for LMC depending on shell thickness and temperature.
- For the LMC process at temperatures within the melting range, a transition in the dominant heat-transfer mechanism occurred at a mold thicknesses of 5 mm. For mold thicknesses greater than 5 mm, conduction through the mold was the dominant mechanism, while heat transfer across the mold-metal interface was dominant for mold thicknesses less than 5 mm.
- The critical fraction solid for evaluation of thermal conditions during solidification is 0.4, at which the thermal gradient and cooling rate are equal to the respective average values for the melting range.
- The withdrawal rate is the primary process parameter of importance that significantly affects the thermal field during solidification.

- The position of the solidification front relative to the transition zone in the furnace can be used to optimize process conditions. The maximum axial thermal gradient at the surface was achieved when the solidification front was approximately 2 - 6 mm and 5 - 15 mm above the top of the baffle for LMC and Bridgman processes, respectively, for bar thicknesses ranging from 1.3 to 12.7 cm. Through-thickness variability of thermal conditions was observed when the solidification front resided below the top of the baffle.
- Furnace temperature is a process variable that affected the thermal conditions at the solidification front, but not as significantly as the withdrawal rate. Increasing the furnace temperature and reducing the withdrawal rate may provide for enhanced thermal conditions but may have deleterious effects for other considerations such as grain nucleation and mold strength.
- Shell thickness variation from 5 to 10 mm and number of bars per mold from 1 to 10 did not significantly affect thermal conditions, while a variation of 5 mm or more of bar thickness significantly altered the position of the solidification front, thus modifying the thermal field during solidification.
- The reduction of defects within the starter region of LMC-processed castings was attained by utilizing a molybdenum chill plate, lowering the position of the mold relative to the cooling bath by 50 mm and utilizing a 10 min hold time after pour and before withdrawal.

References

1. A.J. Elliott, "Directional Solidification of Large Cross-Section Ni-Base Superalloy Castings via Liquid Metal Cooling," (Ph.D. thesis, University of Michigan, 2005).

2. J.D. Hunt, *Solidification and Casting of Metals*, ed. J.D. Hunt (London: The Metals Society, 1979), 3-9.

3. W. Kurz and D.J. Fisher, *Acta Metall*, 29 (1) (1981) 11-20.

5. J. Madison, "Investigation of Solidification Defect Formation by Three Dimensional Reconstruction of Dendritic Structure," (Ph.D. thesis, University of Michigan, 2010).

6. A.J. Elliott and T.M. Pollock, *Metall and Mater Trans A*, 38A (2007) 871-882.

CHAPTER 5

APPLICATION OF SOLIDIFICATION MODELING TO HEAT TRANSFER DURING DIRECTIONAL SOLIDIFICATION

The degree of structure refinement has been investigated in castings with varying cross-sectional areas. The feasibility of a mono-crystalline ring comprised of a multiply-seeded, single-crystal ring separated by low-angle boundaries has been investigated for two thicknesses and two processing techniques. Solidification experiments using 1.9 cm and 5.1 cm thick tri-crystal castings have been conducted in a furnace capable of either the Bridgman or LMC modes. Solidification modeling has been used to optimize process conditions and investigate the thermal characteristics of each process for both casting configurations. Relationships between dendritic structure, cooling rate and thermal gradients in the axial and transverse directions are presented. A model for the prediction of thermal behavior for Bridgman and LMC techniques using complex casting configurations with section-thickness variations, encompassing a broad range of thermal conditions has been validated. A viable processing route for a mono-crystalline ring has been identified.

Introduction

Increased temperature capability within the hot-section of modern turbine engines has relied on the use of single-crystal materials for blade applications. Typical single-crystal

geometries consist of a relatively small cross-section and long axial dimension, as this geometry is favorable for the directional solidification process. In order to increase turbine inlet temperatures further, single-crystal materials have been considered for other engineering components within the turbine-section possessing significantly different geometries than those typical of SX materials [1,2]. Thus, the design of such components is limited by the means by which these materials could be produced.

The liquid metal cooling process is an emerging, high-gradient directional-solidification process [3-9]. This process is capable of providing improved mechanical performance of engineering components due to refined dendritic structure and corresponding defect scales [7-15]. The benefits of the process derive from the enhanced heat extraction of the casting by a liquid-metal coolant during solidification [16,17]. Application of the process to thick sections and/or complex geometries has been ongoing [4-12].

Previously, the solidification and mechanical performance of bi-crystal castings have been investigated transverse to the growth direction. The motivation for this work was to determine the effect of a low-angle boundary on the creep rupture strength of the material [1,18]. Alloys have been designed to maintain single-crystal rupture strength with low-angle boundaries up to 18°, depending on temperature and stress level [1]. The design of such alloys has allowed the presence of low-angle boundaries in engineering components [18].

Recently, a design for a large-diameter single-crystal ring has been developed [2]. A ring whose crystallographic orientation comprises a <100> oriented crystal in the axial, radial, and circumferential directions has been proposed. Casting such a component requires multiple seeds around the circumference of the ring such that low-angle boundaries exist between segments, thus maintaining the mechanical performance of a single crystal while producing the desired rotational symmetry of the crystallographic orientation (Figure 5.1). For example, a full ring with a 10° low-angle boundary between each segment requires 36 seeds, Figure 5.1.

Finally, the development and maturity of solidification-modeling tools has enabled a more fundamental understanding of the physics associated with solidifying materials. By application of these models to new geometries and novel processing techniques, much information about the solidification behavior can be obtained. In addition, optimization of process design within the simulation environment may allow for fewer casting trials to assess the feasibility of novel casting geometries and processes.

The objectives of this research were twofold: (1) to demonstrate the feasibililty of manufacturing such a component by evaluating thick- and thin-section tricrystal segments via the Bridgman and LMC processes and (2) apply well-validated, continuum solidification-modeling capabilities to assist with process design.

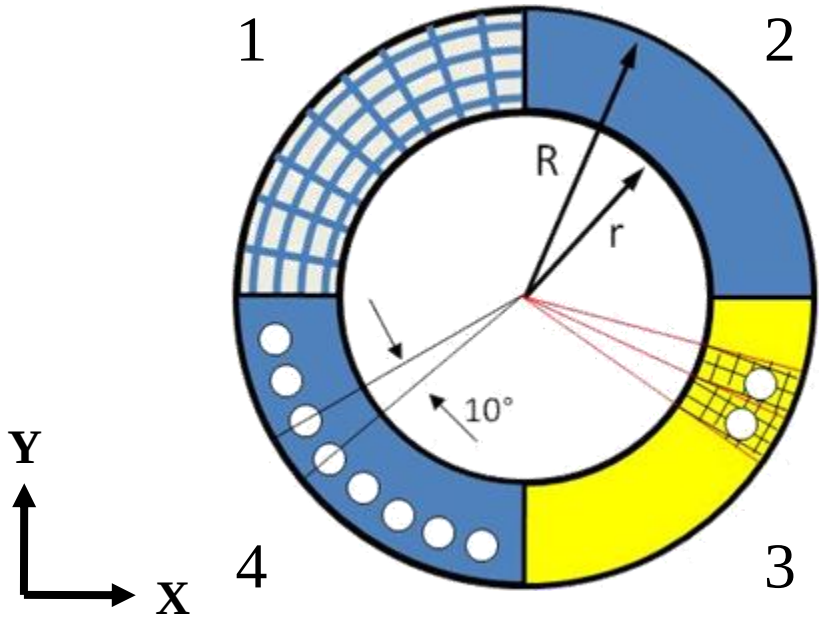

Figure 5.1 – Configuration of a single-crystal ring. A ring whose axial, radial and circumferential directions are parallel to < 1 0 0 > of the crystal (1) and has an inner and outer radius of r and R, respectively (2). In order to achieve this configuration, seeds are used that have a 10 degree rotational misorientation relative to adjacent seeds (3). In order to achieve a full ring, 36 seeds are needed that are 10 degrees apart (4).

Experimental Materials and Methods

Single-crystal Ni-base superalloy components were cast using an LMC furnace designed by ALD Vacuum Technologies. Details on the capabilities of this furnace are described in Chapter 2. A unique capability of this furnace is that it can be configured in either the Bridgman or LMC mode, so that direct comparison between the two processes can be performed. In the LMC mode, molten tin and a ceramic floating baffle are utilized as previously described.

To acquire thermal data during directional solidification, type-C thermocouples were positioned on the mold surface and through the mold wall at the mold-metal interface. In

addition, type-C thermocouples were placed in various locations within the furnace in order to acquire appropriate parameters for use in boundary conditions for the modeling effort. The thermal data was incorporated into a simulation of the process using ProCAST^{TM}, a FE-based modeling tool as is discussed in the following section.

The casting configuration used for this effort was a tri-crystal with the characteristics shown in Figure 5.2a. A tri-crystal is a reduced-size representation of a full ring due to its rotational symmetry and the absence of an edge effect in the middle single-crystal segment. Two geometries were investigated: a thick-section tri-crystal with a thickness of 5.1 cm and a thin-section tri-crystal with a thickness of 1.9 cm. Both geometries were 2.5 cm in height, Figure 5.2a. Doubly-oriented seeds, in which the orientation of both the primary and secondary dendrite arms is controlled, and single-crystal selectors were used to form orientation-controlled tri-crystal castings. Ramps were utilized to reduce the sharp transition to the thick section. Thermocouples were attached to the surface of the mold and embedded within the mold in locations that provided insight into the various heat transfer steps and avoided thermally unstable regions (Figure 5.2a). Both configurations were cast in Bridgman and LMC modes.

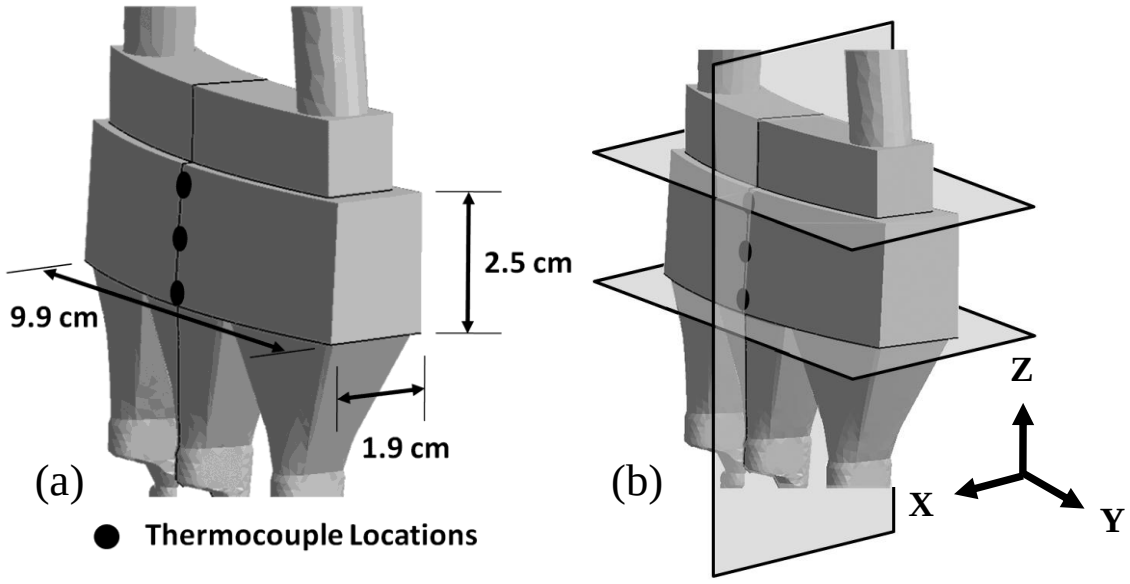

Figure 5.2 – Configuration of thin-section casting with (a) thermocouple locations and dimensions identified and (b) sections for microstructural evaluation identified, including a longitudinal plane and two transverse planes at the top and bottom of the casting. Note: the difference between the thin- and thick-section casting is that the section thickness is 1.9 cm for the thin-section casting and 5.1 cm for the thick-section casting.

The solidification experiments utilized CMSX-486, a grain-boundary strengthened SX Ni-base superalloy [1]. It has been reported that this alloy maintains stable creep rupture properties transverse to a misoriented boundary having a misorientation of up to 18 degrees [1]. The nominal alloy composition (in wt %) for CMSX-486 is Ni-9.3Co-8.6W-5.7Al-5.0Cr-4.5Ta-3Re-1.2Hf-0.7Mo-0.7Ti-0.07C-0.015B-0.005Zr [1].

The furnace temperature and withdrawal rate were determined by a simulated design-of-experiments approach using a solidification model for evaluation of the predicted thermal field at the solidification front. The details of this work are described in the next section. The optimized casting parameters used for the thick- and thin-section castings in the Bridgman and LMC modes are described in Table 5.1.

Table 5.1 – Optimized process conditions for tricrystal casting trials.

Casting Mode	Bridgman		LMC	
Section Thickness (cm)	5.1	1.9	5.1	1.9
Withdrawal Rate (mm/min)	3.4	3.4	5.9	8.5
Furnace Temperature (°C)	1550	1550	1550	1550

Following casting, the tri-crystals were etched to evaluate the macrostructure, including the formation of casting defects and morphology of the misoriented boundaries. The components were then sectioned to evaluate the microstructure (Figure 5.2b). Both transverse and longitudinal sections were evaluated for measurement of primary dendrite arm spacing (PDAS) and secondary dendrite arm spacing (SDAS) as described in Chapter 2 near regions where the thermocouples were inserted into the molten metal.

Simulation Methods

Finite-element based solidification modeling was conducted to provide further insight to directional solidification via the Bridgman and LMC processes. ProCAST^{TM}, a commercially-available solidification-modeling software package, was utilized to predict the thermal conditions during solidification. A parametric analysis including 55 simulations was conducted to determine optimal process conditions for experimentation. Cooling curves from thermocouple measurements were compared to thermal predictions within the simulations at the respective locations in order to validate model predictions. Approximately 125 additional simulations were conducted to determine optimal model

parameters. The model conditions utilized in this effort are detailed in Chapter 2 and summarized in Table 5.2.

Table 5.2 – Model parameters for FE-based solidification modeling.

Thermophysical Properties		
Superalloy Solidus	1330	°C
Superalloy Liquidus	1395	°C
Baffle Thermal Cond.	1.0	W/mK
Shell Thermal Cond.	2.5	W/mK
Shell Thickness	6.4	mm

Boundary Conditions		
Shell Emissivity	0.4	
Baffle Emissivity	0.2	
Tin Temperature	250	°C

Interface Heat Transfer Coefficients		
Superalloy-Ceramic	*750	W/m^2K
Ceramic-Ceramic	500	W/m^2K
Tin-Ceramic	4000	W/m^2K

Run Parameters		
Maximum Time Step	**	
Spatial Step	0.5	mm
Critical Fraction Solid	0.4	

*Initial value reported with exponential decay to 100 W/m^2K during solidification
**Scaled by withdrawal rate to provide equal withdrawal distance (0.4mm) between steps

The withdrawal rate was parametrically evaluated in order to identify the optimal process condition. This was completed by evaluation of the thermal characteristics at the solidification front for each simulation. In general, an optimal thermal condition has been defined in Chapter 4 as a minimal curvature at the center of the casting with a maximum axial thermal gradient at the surface of the casting. The investigated withdrawal rates for each process and both casting configurations are summarized in Table 5.3.

Table 5.3 – Simulated withdrawal rates for casting configurations and processes investigated.

Casting Mode	Bridgman		LMC	
Section Thickness(cm)	5.1	1.9	5.1	1.9
Withdrawal Rate	0.8	1.7	4.2	5.1
(mm/min)	1.7	2.5	5.9	6.8
	2.5	3.4	6.8	8.5
	3.4	4.2	7.6	10.2
	4.2	5.1	9.3	11.9

Once the solidification modeling parameters were optimized, the thermal gradient, solidification rate and cooling rate were calculated at the locations where metallographic sectioning studies were conducted. From this data, the PDAS and SDAS were predicted according to well established, models for dendritic growth as discussed in Chapter 2. The Bridgman-processed, thin-section casting was utilized to determine the coefficient of the dendrite growth model as described in Chapter 2.

Experimental Investigation of Tri-crystal Castings

Four casting trials were conducted to demonstrate the feasibility of casting tri-crystals with thick and thin sections via both the Bridgman and LMC processes. Macrostructural evaluation demonstrated that the boundaries between single-crystal segments were relatively planar in both the axial and radial directions (Figure 5.3). The tri-crystal boundaries were designed to have a 10° low-angle boundary. Measurements of the misorientation across the boundaries with respect to the [001] indicated an average and standard deviation of 10° and 2°, respectively, which was within the desired low-angle-

boundary limits of the tricrystal. No nucleated grains or freckle chains formed at the surface of the castings.

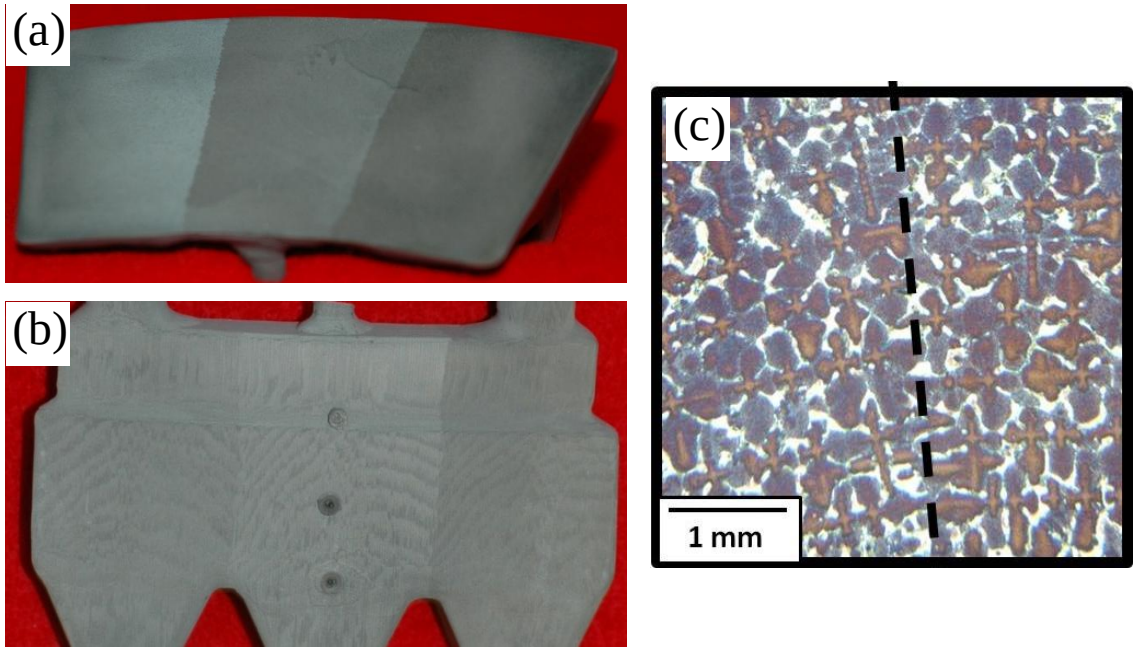

Figure 5.3 – (a) Macro-photograph transverse to the growth direction, (b) macro-photograph parallel to growth direction, and (c) micrograph of the boundary between single-crystal segments identified by a dashed line, transverse to the growth direction.

Microstructural analysis of transverse sections taken at the center of the bottom plane (Figure 5.2b) of each segment revealed significant variations in dendritic structure with casting process and section thickness (Figure 5.4). Likewise, SDAS measurements taken from the center of the mid-plane longitudinal sections showed similar trends (Figure 5.5). Quantitative measurements demonstrated a 25 pct. reduction in PDAS and a 20 pct reduction in SDAS for the thin-section casting compared to the thick-section casting for the LMC process (Table 5.4). In addition, there was a 45 pct reduction of PDAS and a 50 pct reduction of SDAS, respectively, for the LMC process as compared to the Bridgman

process. A significant reduction in eutectic fraction was also observed with utilization of the LMC process. The importance of this observation is discussed later.

Table 5.4 – Measured and predicted PDAS at the center of the bottom plane and SDAS at the center of the longitudinal mid-plane of the tricrystal segment for each casting trial.

Casting Mode		Bridgman		LMC	
Section Thickness (cm)		5.1	1.9	5.1	1.9
PDAS (μm)	Measured	406	334	248	187
	Predicted	420	334	210	158
SDAS (μm)	Measured	86	72	43	35
	Predicted	89	72	49	41

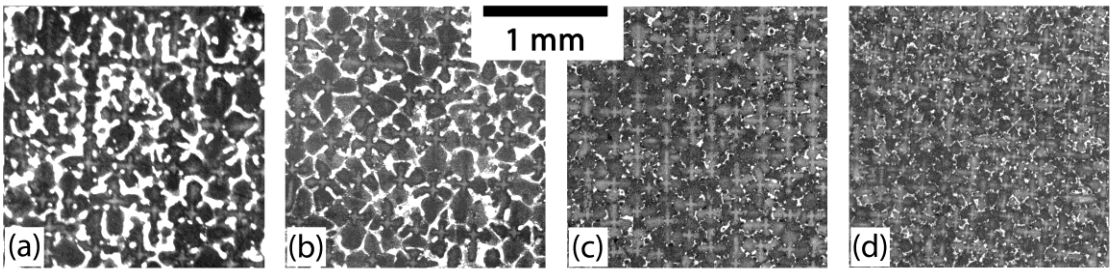

Figure 5.4 – Transverse sections at the center of the bottom plane for the (a) thick-section Bridgman casting, (b) thin-section Bridgman casting, (c) thick-section LMC casting, and (d) thin-section LMC casting.

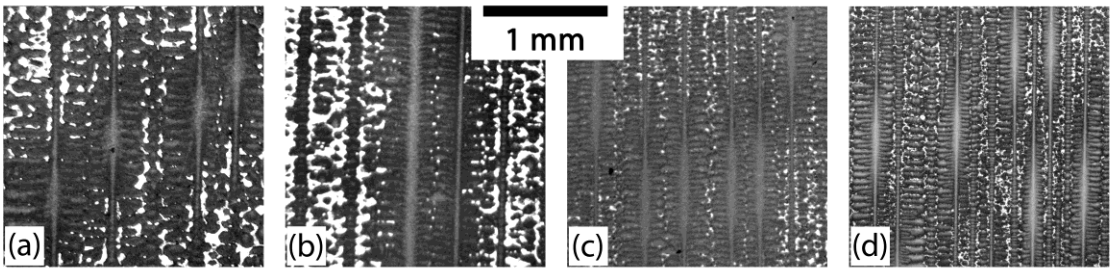

Figure 5.5 – Longitudinal sections at the center of the mid-plane for the (a) thick-section Bridgman casting, (b) thin-section Bridgman casting, (c) thick-section LMC casting, and (d) thin-section LMC casting.

Thin-section castings had smaller dendrite arm spacings as compared to thick-section castings, Table 5.4. This is expected, as thinner sections have a smaller thermal mass and thus a higher thermal gradient, as compared to thick sections. Similarly, LMC castings had a finer structure than Bridgman castings, which is comparable to previous work showing a refinement of dendritic structure for the LMC process due to the enhanced heat extraction by the molten-metal cooling bath [8].

Cooling curves from thermocouple measurements for each casting trial are shown in Figure 5.6. The LMC process provided cooling rates 4-5 times the cooling rates of the Bridgman process for the same casting thickness. The cooling rate of thin-section castings was approximately double the cooling rate of the thick-section castings. Comparison of the measured and predicted cooling profiles are discussed in the following section.

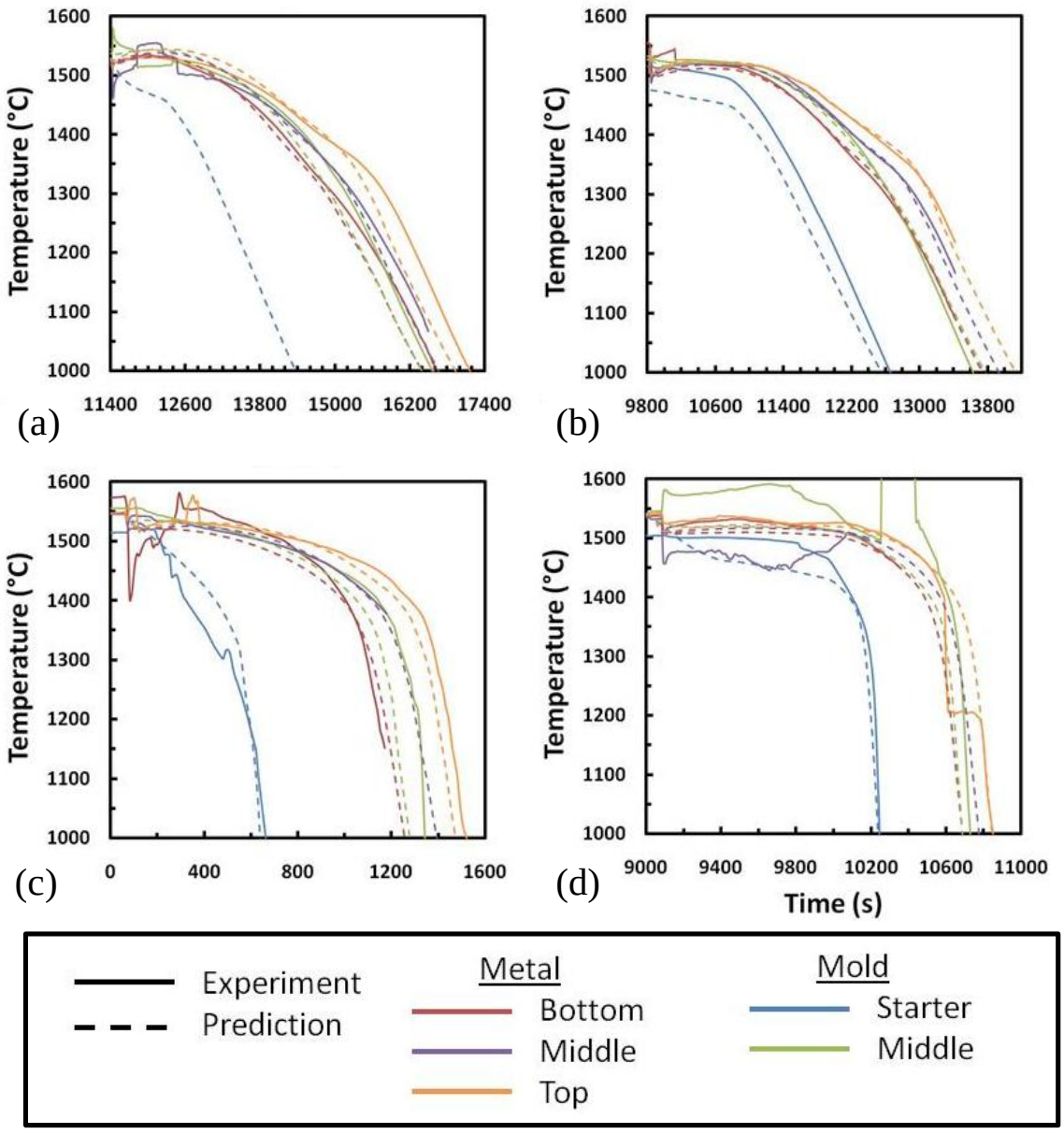

Figure 5.6 – Comparison of experimental thermocouple data and time temperature model predictions: (a) Bridgman-processed, thick tricrystal; (b) Bridgman-processed, thin tricrystal; (c) LMC-processed, thick tricrystal and (d) LMC-processed thin tricrystal.

Modeling Investigation of Tri-crystal Castings

Predictions of the thermal characteristics for each casting configuration and both processes were evaluated for a range of withdrawal rates in order to determine the sensitivity of thermal conditions and identify the optimal condition for experimentation as described in Chapter 4 (Figure 5.7). A maximum axial thermal gradient at the surface of the casting was predicted at an intermediate withdrawal rate for each casting condition. The solidification rate, cooling rate and inclination angle of the solidification front increased with increasing withdrawal rate. The withdrawal rate that provided the maximum axial thermal gradient corresponded to the withdrawal rate selected for the experimental investigation.

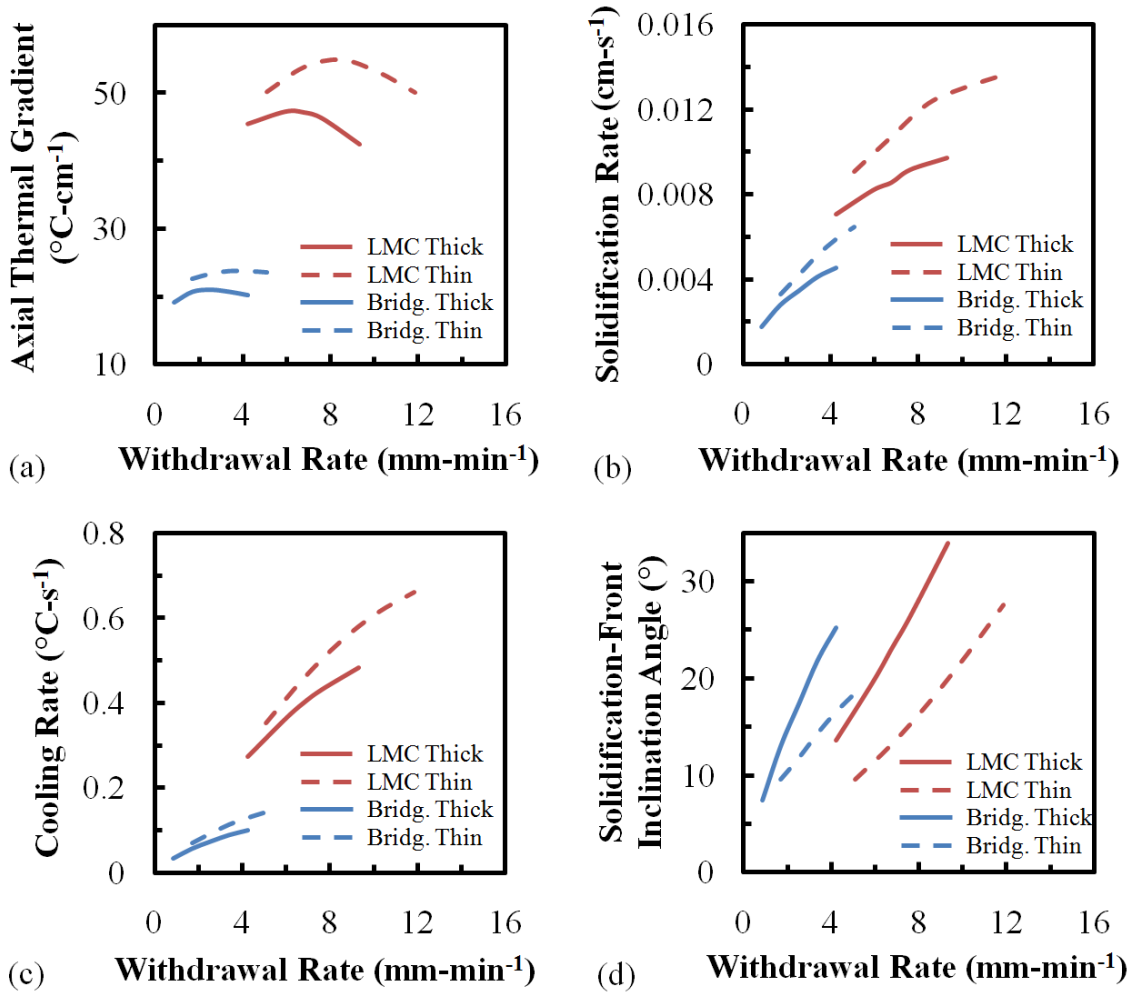

Figure 5.7 – Sensitivity of thermal condition to withdrawal rate for each casting configuration and both processes, (a) axial thermal gradient, (b) solidification rate, (c) cooling rate and (d) solidification-front inclination angle.

Thermal predictions from the withdrawal rate analysis were also related to the position of the solidification front relative to the top of the transition region in the furnace (Figure 5.8). The top of the transition region corresponded to the top of the fixed baffle in Bridgman mode and the top of the floating baffle in LMC mode. The maximum axial thermal gradient was obtained with a withdrawal rate that resulted in a solidification-front position near the top of the baffle, regardless of casting configuration (Figure 5.8). As

discussed in Chapter 4, this is an optimal location for the solidification front and in agreement with the optimal position of the solidification front for bar-mold castings.

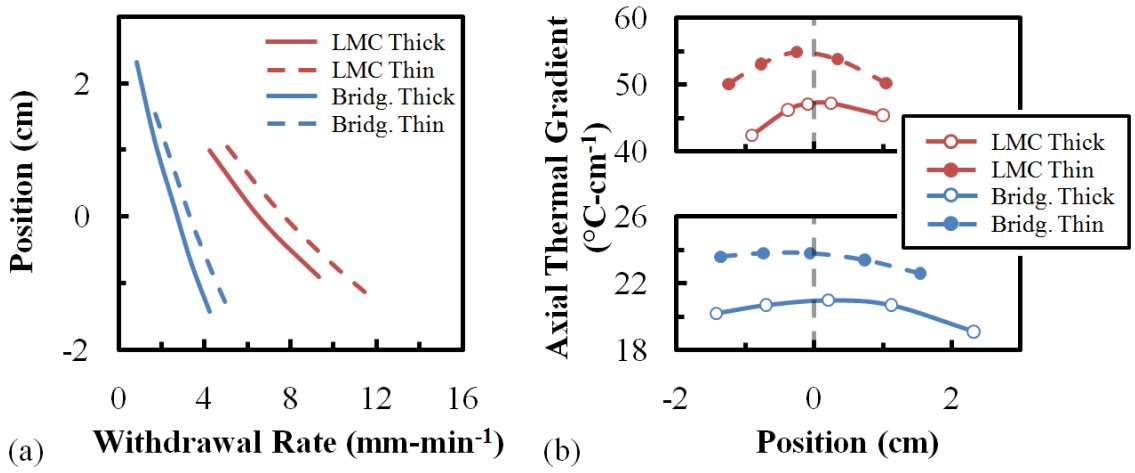

Figure 5.8 – (a) Withdrawal-rate sensitivity of the position of the solidification front relative to the top of the transition region and (b) predicted axial thermal gradient as related to the position of the solidification front relative to the top of the transition region of the furnace.

Herein, the results from the modeling investigation pertaining to the experimental conditions are evaluated. Predictions of the temperature at the location of the thermocouples were compared to cooling curves from thermocouple measurements for each casting trial (Figure 5.6). Good agreement (a cooling rate within 0.05 °C-s^{-1} through the melting range) between the predicted temperature profiles and thermocouple measurements was obtained for the three positions near the mold-metal interface of each casting trial, demonstrating the applicability of the process simulation for a range of thermal conditions.

Predictions of the thermal conditions for each casting configuration were compared to each other. The magnitude of the axial thermal gradient doubled for LMC as compared to Bridgman and increased by 25 pct for thin-section as compared to thick-section castings (Figure 5.9). A similar solidification-front curvature was observed for both the Bridgman and LMC processes for the same casting thickness (Figure 5.10). In addition, thick-section castings had an increased solidification-front curvature as compared to thin-section castings. The inclination angle of the solidification front at the inner diameter for the thin-section casting was half the inclination angle of the thick-section casting. The effect of increased solidification-front curvature on the stability of dendritic growth is addressed in Chapter 6. The height of the melting range was three times larger for Bridgman as compared to LMC for the same casting thickness. Values of the thermal gradient, solidification rate and cooling rate were recorded at the location of the microstructure assessments (Table 5.5).

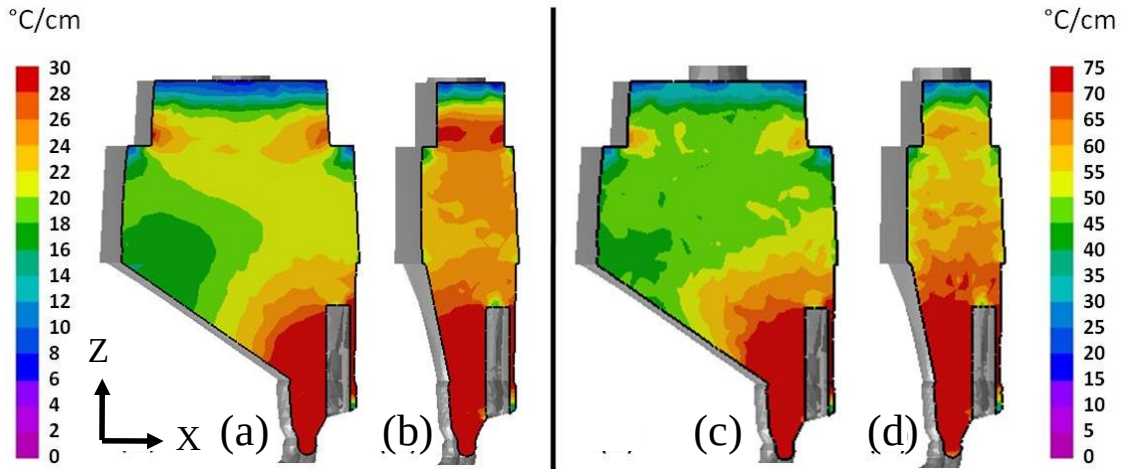

Figure 5.9 – Contour plots of axial thermal gradient for (a) thick-section Bridgman, (b) thin-section Bridgman, (c) thick-section LMC and (d) thin-section LMC castings.

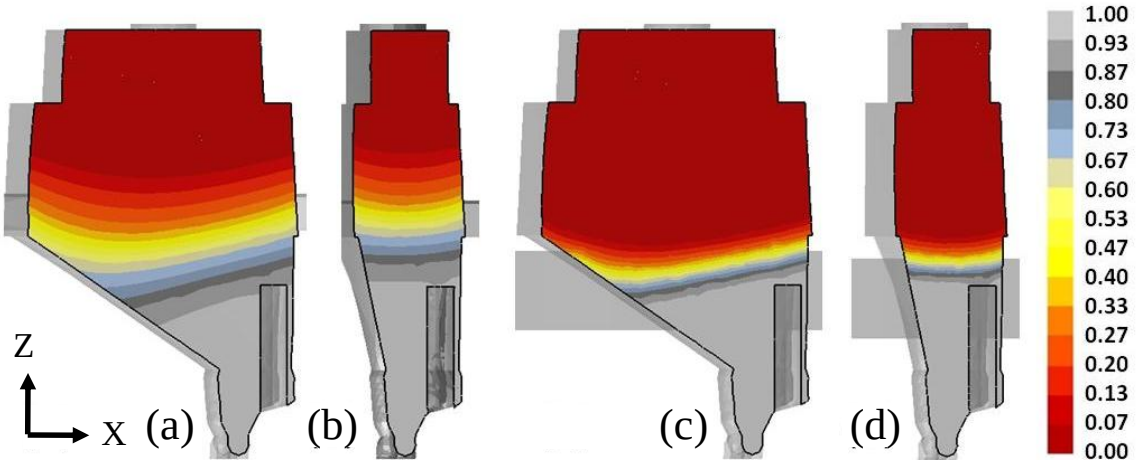

Figure 5.10 – Contour plots of fraction solid for (a) thick-section Bridgman, (b) thin-section Bridgman, (c) thick-section LMC and (d) thin-section LMC castings.

Table 5.5 – Predicted thermal characteristics at each measurement location for the experimentally-evaluated casting geometries and process conditions.

Casting Mode	Bridgman		LMC	
Section Thickness (cm)	5.1	1.9	5.1	1.9
Axial Thermal Gradient (°C/cm)	19	24	45	58
Solidification Rate (cm/s)	0.004	0.005	0.007	0.011
"Cooling Rate": G*V, (°C/s)	0.07	0.11	0.33	0.64
Cooling Rate (°C/s)	0.08	0.11	0.36	0.54

The predicted thermal conditions were then used to predict microstructure scale according to Chapter 2 (Figure 5.11 and 5.12). The predicted PDAS and SDAS for each casting revealed a dependence on thickness and a strong reduction of microstructure scale from utilization of the LMC process. Quantitatively, this amounted to a 50 pct reduction in PDAS and 40 pct reduction in SDAS for LMC compared to Bridgman, as well as a 20 pct reduction in both PDAS and SDAS for the thin-section casting compared to the thick-section casting. The predicted variability of PDAS within a casting scaled in a similar manner as the microstructure scale: decreasing from thick- to thin-section castings and significantly decreasing through utilization of the LMC process. Depending on the

location within the ring shape – that is, ignoring the ramp and riser sections - predicted PDAS ranged from 320 - 400 µm for the thick-section, Bridgman casting, while the thin-section, LMC casting possessed a PDAS of 160 - 200 µm, reducing the predicted variability by 50 pct. A similar trend was observed with SDAS, although the predicted SDAS variability is less than the predicted PDAS variability.

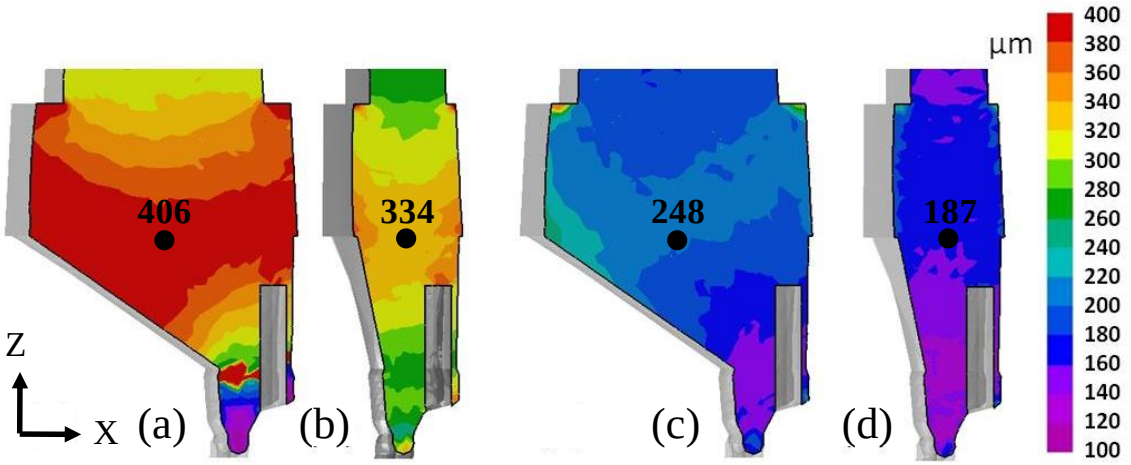

Figure 5.11 – Contour plots of PDAS for (a) thick-section Bridgman, (b) thin-section Bridgman, (c) thick-section LMC and (d) thin-section LMC castings with labeled experimental measurements by location.

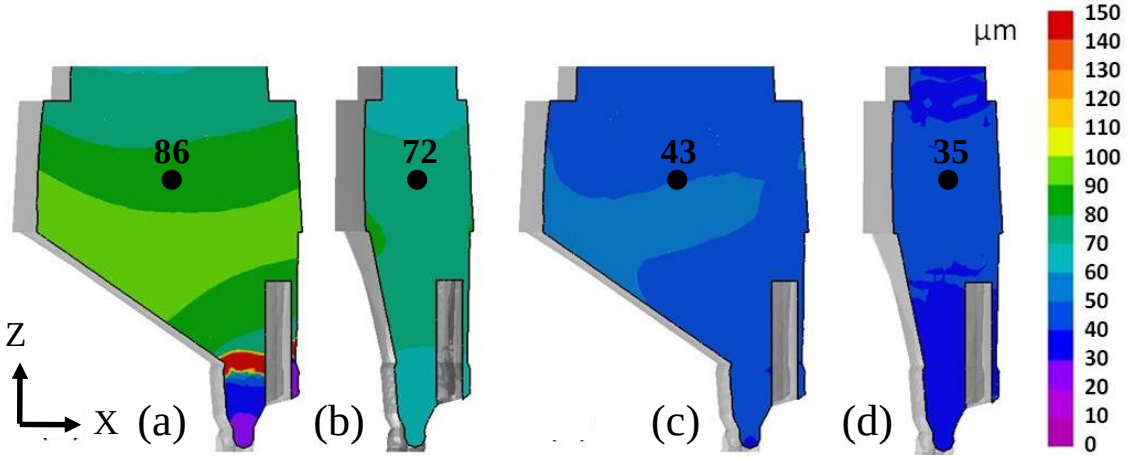

Figure 5.12 – Contour plots of SDAS for (a) thick-section Bridgman, (b) thin-section Bridgman, (c) thick-section LMC and (d) thin-section LMC castings with labeled experimental measurements by location.

Predictions of microstructure scale were consistent with experimental measurements (Table 5.4). Predictions of PDAS and SDAS for the Bridgman process were within 3 pct of measured values. There was a deviation (~15 pct) from the predicted PDAS and SDAS for the LMC experiments. A breakdown in the assumptions of the dendrite growth models could contribute to this error. Specifically, the models assume that heat is only extracted parallel to the growth direction of the dendrites, which is not necessarily the case for the LMC process. This aspect of the LMC process is addressed in Chapter 8.

Discussion

The LMC process has demonstrated the feasibility of casting tricrystalss, suggesting a viable processing route for a single-crystal ring. The laboratory-scale, multi-seeded tricrystal research conducted in this work may not directly apply to the solidification of a full SX ring, depending on the heat transfer mechanisms of the process employed. In the case of the Bridgman mode, radiation heat transfer from the surface of the mold relies on distance to the furnace walls, as well as line-of-sight. The inner-diameter of the ring has poor radiation heat transfer because it primarily radiates to itself, which is different than the tricrystal inner-diameter that radiated to the other side of the furnace. The thermal conditions present at the inner diameter of the ring suggest the potential for convective instabilities and freckle formation [21,22]. Thus, the Bridgman tricrystal castings solidified in this research are likely a best-case scenario for the process due to the absence of a poor radiation view factor at the inner diameter. In this case, the thermal

gradient of the inner-diameter of the thick-section casting is too low to maintain directional solidification. Therefore, it is unlikely that the thick-section casting is feasible via the Bridgman process. The thin-section thermal gradient is relatively low as well, but a small processing window may be present.

In the case of LMC, on the other hand, heat transfer from the mold surface is controlled by convection and conduction through the liquid-metal coolant. As long as the stirring of the liquid-metal coolant is sufficient to remove heat from the center of the ring, there is no anticipated difference between the sub-scale tricrystal experiments and a full ring. The reduced amount of eutectic observed with the LMC process indicated a potential benefit to mechanical performance by improved heat-treatment capability, as determined by Elliott [8]. Therefore, the LMC process provides a viable processing route for directional solidification of a single-crystal ring structure.

Solidification modeling of the different casting configurations revealed significant differences in thermal gradient magnitude and direction, curvature of the solid-liquid interface, and predicted dendrite-arm spacings for the Bridgman and LMC processes. As expected, increasing the thermal gradient decreased the dendrite arm spacings. Likewise, by changing the thermal gradient direction, the curvature of the solid-liquid interface increased. Thus, the variation in the inclination angle and axial thermal gradient for each casting technique and section thickness was important to the formation of the final casting structure for the configurations investigated.

The accuracy of the solidification modeling and applicability of the optimization technique described in Chapter 4 is also noteworthy. The solidification model has been validated with a broad range of process conditions. The independence of casting geometry has been demonstrated for the optimization technique proposed in Chapter 4.

Conclusion

The feasibility of casting multiple-seeded, thick-section segments with both the LMC and Bridgman techniques has been demonstrated. A viable processing route has been established for manufacture of a single-crystal ring. The scale of dendritic structure of the castings decreases with reduction in section thickness and strongly decreases with utilization of the LMC process. A model that quantitatively predicts the thermal behavior during solidification has been validated. Predictions of primary and secondary dendrite arm spacing based on thermal conditions during solidification are in agreement with experimental measurement.

References

1. K. Harris and J.B. Wahl, "Improved Single Crystal Superalloys, CMSX-4®(SLS)[La+Y] and CMSX-486®," *Superalloys 2004,* ed. K.A. Green et al. (The Minerals, Metals & Materials Society, 2004) 45-52.

2. T. Strangman, "Integral turbine composed of a cast single crystal blade ring diffusion bonded to a high strength disk," (U.S. Patent No. 6,969,240), 29 Nov 2005.

3. J.G. Tschinkel, A.F. Giamei and B.H. Kearn, "Apparatus for Casting of Directionally Solidified Articles," (U.S. Patent No 3,763,926), 1973.

4. F. Hugo, U. Betz, and J. Ren, "Casting of Directionally Solidified and Single Crystal Components Using Liquid Metal Cooling (LMC)," *Proceedings of the 1999 International Symposium on Liquid Metal Processing and Casting*, A. Mitchell, L. Ridgway and M. Baldwin, eds. (The Minerals, Metals & Materials Society, 1999) 16-30.

5. A. Lohmüller, W. Esser, J. Grossman, M. Hördler, J. Preuhs and R.F. Singer, *Superalloys 2000*, ed. T.M. Pollock, R.D. Kissinger, R.R. Bowman, K.A. Green, M. McLean, S.L. Olson, and J.J. Schirra (Warrendale, PA: TMS, 2000) 181-188.

6. M. Konter and M. Thumann *Journal of Materials Processing Technology*, 117 (2001) 386-390.

7. M. Lamm and R.F. Singer, *Metall and Mater Trans A*, 38A (2007) 1177.

8. A.J. Elliott et al., "Directional Solidification of Large Superalloy Castings with Radiation and Liquid-Metal Cooling: A Comparative Assessment," *Metall Mater Trans A*, 35A (2004), 3221-3231.

9. J. Grossmann, J. Preuhs, W. Esser and R.F. Singer, Proceedings of the 1999 International Symposium on Liquid Metal Processing and Casting, eds. A. Mitchell, L. Ridgway and M. Baldwin (The Minerals, Metals & Materials Society, 1999) 31-40.

10. S. Balsone, G. Feng, L. Peterson and J. Schaeffer, *Solidification Processes and Microstructures: A Symposium in Honor of Wilfried Kurz*, ed. M. Rappaz, C. Beckermann and R. Trivedi (The Minerals, Metals & Materials Society, 2004) 77-83.

11. A. Kermanpur, N. Varahraam, E. Engilehei, M. Mohammadzadeh and P. Davami, *Mat Sci Technol*, 16 (5) (2000) 579-586.

12. C. Brundidge, D. VanDrasek, B. Wang and T.M. Pollock, *Proceedings of the 2009 International Symposium on Liquid Metal Processing and Casting*, ed. P.D. Lee, A. Mitchell and R. Williamson (The Minerals, Metals & Materials Society, 2009) 107-117.

13. P.N. Quested and M. McLean, *Mat Sci Eng*, 65 (1984) 171-180.

14. L. Liu, T.W. Huang, J. Zhang and H.Z. Fu, *Material Letters*, 61 (2007) 227-230.

15. C. Liu, J. Shen, J. Zhang and L. Lou, *J Mater Sci Technol*, 26 (4) (2010) 306-310.

16. T.J. Fitzgerald and R.F. Singer, "An Analytical Model for Optimal Directional Solidification using Liquid Metal Cooling," *Metall Mater Trans A*, 28A (1997), 1377-1383.

17. A.J. Elliott and T.M. Pollock, *Metall and Mater Trans A*, 38A (2007) 871-882.

18. E.W. Ross and K.S. O'Hara, *Superalloys 1996*, eds. R.D. Kissinger, D.J. Dye, D.L. Anton, A.D. Cetel, M.V. Nathal, T.M. Pollock and D.A. Woodford (The Minerals, Metals & Materials Society, 1996) 19-25.

19. J.D. Hunt, "Cellular and Primary Dendrite Arm Spacings," *Solidification and Casting of Metals*, ed. J.D. Hunt (London: The Metals Society, 1979), 3-9.

20. W. Kurz and D.J. Fisher, "Dendrite Growth at the Limit of Stability: Tip Radius and Spacing," *Acta Metall.*, 29 (1) (1981), 11-20.

21. T.M. Pollock and W.H. Murphy, *Metall Trans A*, 27 (1996) 1081-1094.

22. S. Tin and T.M. Pollock, *Metall and Mater Trans A*, 21 (7) (2001) 1743-1753.

CHAPTER 6

STABILITY OF DENDRITE GROWTH IN THE PRESENCE OF A NON-AXIAL THERMAL FIELD

The liquid-metal-cooling (LMC) directional-solidification process offers refinement of dendritic structure due to increased cooling rate from enhanced heat extraction. However, under some conditions in the LMC process substantial lateral heat extraction occurs that leads to a change in dendrite morphology, resulting in grain nucleation or *lateral growth* – the formation of long secondary dendrite arms overgrowing favorably aligned primary dendrites. The conditions under which lateral growth occurs during solidification of alloys CMSX-486 and René N4 have been studied experimentally and via solidification modeling using ProCAST^{TM}. Solidification experiments have been conducted in a LMC furnace that utilizes liquid tin as the cooling medium and a floating ceramic baffle. A mold geometry was designed to evaluate a range of thermal conditions and assess the tendency for lateral growth. Correlations between dendritic structure, solidification-front curvature, solidification rate and thermal gradients have been analyzed. The presence of lateral growth is strongly dependent on the inclination of the solidification front at the casting surface.

Introduction

Utilization of the LMC process has demonstrated benefits with respect to the refinement of dendritic structure and suppression of defect-formation processes due to enhanced heat extraction. However, the presence of enhanced lateral heat extraction under some processing conditions can lead to a significant inclination of the solidification front. Increases in the inclination angle of the solidification front can be attributed to (1) sharp changes in geometry or (2) non-axial thermal conditions during solidification. Increase in the curvature of the solidification front can promote deviations in dendrite morphology.

Lateral overgrowth of primary dendrites by secondary dendrites is one example of transient dendrite growth during single-crystal solidification. The conditions under which lateral growth occurs are not well understood. The onset of lateral growth is complicated by casting geometry [1-4], and it is unclear how mechanical performance is influenced by regions of lateral growth and at the interface between axial and lateral growth.

A change in dendrite morphology due to unstable process conditions may result in grain nucleation [5,6]. A nucleated grain forms probabilistically due to the presence of a nucleus in the melt and a sufficient undercooling in the melt ahead of the dendrite growth front. Ni-base superalloys are comprised of 10+ chemical elements that maintain the presence of nuclei in the melt due to heterogeneities in alloy composition. Thus, the

preferred means to avoid grain nucleation is to solidify in a manner that minimizes undercooling, particularly for castings with complex geometry. The degree of undercooling required to nucleate a grain is alloy-dependent and difficult to predict quantitatively.

Overall, the dendrite morphology that evolves in conjunction with the non-axial thermal field is not well understood, including the critical inclination angle required to significantly alter the dendrite morphology. In this research, a casting experiment has been designed to interrogate the evolution of dendrite growth in the presence of varying degrees of non-axial heat extraction. Solidification modeling is also utilized to improve the understanding of the relationship between the thermal field during solidification and the resultant dendrite structure. Development of a criterion for transitions in dendrite growth mode independent of mold geometry is a primary goal of this research.

Experimental Materials and Methods

Single-crystal (SX) Ni-base superalloys were cast using a furnace designed by ALD Vacuum Technologies in the LMC mode. The furnace configuration has been detailed in Chapter 2. A 10-minute hold was maintained after pour and before withdrawal in order for the temperature of the charge to equilibrate to its surroundings, enabling a steady-state thermal condition prior to withdrawal. A series of 6 different solidification experiments were conducted to provide 24 different solidification conditions for evaluation.

Molds utilized during this research were fabricated by PCC Airfoils, Inc. The casting configuration was a modified 5-bar cluster mold (Figure 6.1). The nominal diameter of each bar was 16 mm, and the nominal height 127 mm.

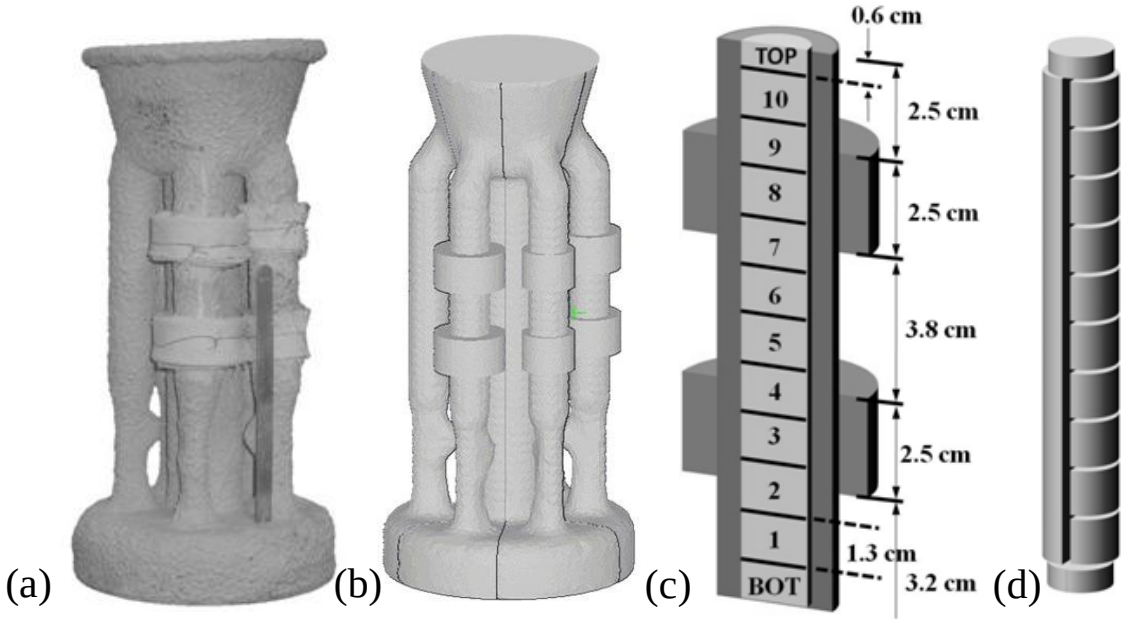

Figure 6.1 – (a) Experimental and (b) simulated mold configuration with (c) plan and (d) exploded view of sectioning.

The thermal field was altered by application of Nextel 440 alumina fabric, manufactured by 3M. The alumina fabric was circumferentially wrapped around the outside of the investment mold at selected regions along the length of the bar to interrupt heat transfer locally. The fabric was added in layers by wetting the investment mold and fabric with alumina cement. Molybdenum wire was used to attach the fabric to the outside of the investment mold locally. This increased the effective shell thickness along a 25 mm height in two sections separated by 38 mm.

The thickness of the alumina-fabric sections, herein described as “wrap thickness”, was varied from 5, 10 and 14 mm in diameter in order to establish a range or processing conditions. Each individual bar was made such that the two sets of additional fabric on each bar were of the same thickness. One bar of the five served as a control with no additional wrap. Thus, each 5-bar cluster mold contained 4 bars with different wrap thicknesses of 0, 5, 10 and 14 mm and 1 replicate bar with a wrap thickness of 10 mm. Six investment molds were fabricated in this fashion for experimental investigation. Variability of the wrap thickness, wrap length and shell thickness were measured for the set of six investment molds.

Two alloys were utilized for directional-solidification experiments in these molds: CMSX-486 and René-N4. The initial investigation employed CMSX-486. The nominal alloy composition (in wt %) for CMSX-486 is Ni-9.3Co-8.6W-5.7Al-5.0Cr-4.5Ta-3Re-1.2Hf-0.7Mo-0.7Ti-0.07C-0.015B-0.005Zr [7]. A further investigation evaluated René-N4 in order to identify the dependence on the evolution of dendrite morphology on alloy chemistry. The nominal alloy composition (in wt pct) for René-N4 is Ni-9.75Cr-7.5Co-6.0W-4.8Ta-4.2Al-3.5Ti-1.5Mo-0.5Cb-0.15Hf-0.05C-0.004B [8].

Seeds, in which the primary and secondary orientations were controlled, were utilized with the René-N4 castings in order to better align the primary orientation with the axial direction of the bar and the secondary orientation with the radial direction of the mold cluster. CMSX-486 bars were then grown with a withdrawal rate of 12.7, 16.9 or 21.2 mm-min^{-1}, while René-N4 castings were withdrawn at 8.5, 12.7 or 16.9 mm- min^{-1}. The

mold configuration, alloy and process conditions for the experimental investigation are summarized in Table 6.1.

Table 6.1 – Number of bars experimentally investigated for each casting condition.

Alloy		CMSX-486			René N4		
Withdrawal Rate (mm-min^{-1})		12.7	16.9	21.2	8.5	12.7	16.9
Wrap Thickness (mm)	0	1	1	1	1	1	1
	5	1	1	1	1	1	1
	10	2	4	2	2	2	2
	14	1	1	1	1	1	1

Following the casting process and removal from the mold, samples were sand-blasted and macro-etched to reveal any orientation defects according to Chapter 2. Following etching, images of the casting surfaces were taken in order to analyze the presence of orientation defects. Samples were then sectioned transverse and parallel to the growth direction in order to evaluate dendrite spacing and morphology at the bottom of the bars and within the alumina-wrap transition regions (Figures 6.1c and 6.1d). The bottom transverse sections were evaluated to confirm establishment of single-crystal growth and identify the secondary orientation so that a longitudinal section parallel to one of the secondary dendrite orientations could be excised. Due to the use of doubly-oriented seeds, the longitudinal section corresponded to a plane including the axial and radial directions of the mold cluster. Finally, transverse sections were taken every 12.7 mm along the length of the casting and selectively evaluated according to the analysis of the longitudinal section.

Following metallographic preparation, polished surfaces were micro-etched to reveal dendritic structure according to Chapter 2. Optical microscopy was performed at magnifications relevant for visualization of the dendritic microstructure. Quantitative metallography was performed on transverse and parallel sections relative to the growth direction according to the procedures set forth in Chapter 2 in order to measure primary dendrite arm spacing (PDAS) and secondary dendrite arm spacing (SDAS), respectively. PDAS was measured at three locations with an area of 4 mm^2 each, resulting in approximately 100 to 200 dendrites per location. Average values for SDAS were obtained from measurement of at least 100 secondary arms. Electron Back-Scatter Diffraction (EBSD) was performed on each sample to evaluate the relative misorientation in regions with varying dendritic morphology.

Simulation Methods

In order to provide insight into the thermal conditions arising from the varying processing conditions considered experimentally, solidification modeling was conducted using ProCAST^{TM}, a commercially available finite element (FE) model. A series of approximately 100 simulations were conducted. The solidification model has been validated via comparison to thermal and microstructural data from multiple casting configurations and a broad range of solidification conditions as described in Chapter 5. Details of the model are described in Chapter 2 and were employed for analysis consistent with the modeling approach of Chapters 4 and 5. A description of the critical model parameters and their values are summarized in Table 6.2.

Table 6.2 – Model parameters for FE-based solidification modeling.

Thermophysical Properties		
Baffle Thermal Cond.	1.0	W/mK
Shell Thermal Cond.	2.5	W/mK
Shell Thickness	6.4	mm

Interface Heat Transfer Coefficients		
Superalloy-Ceramic	*750	W/m^2K
Ceramic-Ceramic	500	W/m^2K
Tin-Ceramic	4000	W/m^2K

Boundary Conditions		
Shell Emissivity	0.4	
Baffle Emissivity	0.2	
Tin Temperature	250	°C

Run Parameters		
Maximum Time Step	**	
Spatial Step	0.5	mm
Critical Fraction Solid	0.4	

*Initial value reported with exponential decay to 100 W/m^2K during solidification
**Scaled by withdrawal rate to provide equal withdrawal distance (0.4mm) between steps

The geometries used for simulation utilized the rotational symmetry of the casting and were representative of the molds prepared for experiment (Figure 6.1b). The only additional boundary condition required for the simulations for the wrapped bars was the interface heat-transfer coefficient between the alumina fabric and mold. Because the alumina cement provided intimate contact at the interface, a value of 500 $Wm^{-2}K^{-1}$ was used, which is consistent with a ceramic-ceramic interface [9]. All other simulation conditions were consistent with those described in Chapter 2 and utilized in Chapters 4 and 5.

The process conditions evaluated in simulations were consistent with those studied experimentally. A two-factor design of experiments approach was employed to evaluate variations in withdrawal rate and wrap thickness. The withdrawal rate was varied from 4.2 $mm\text{-}min^{-1}$ to 25.4 $mm\text{-}min^{-1}$ at an increment of 4.2 $mm\text{-}min^{-1}$, while the wrap

thickness was evaluated from 3.2 mm to 14.3 mm in increments of 1.6 mm, including simulations without wrap.

For each simulation, the thermal gradient, solidification rate and cooling rate were calculated at specific locations within the casting. These predicted thermal conditions were related to the experimental observations of lateral growth and stray grain formation such that a relationship between lateral heat extraction and dendrite morphology could be established. In addition, the PDAS and SDAS were predicted according to well established, dendrite growth models as described in Chapter 2 [10,11]. These predictions at specific locations within the casting were ultimately compared to experimental measurements of dendrite scale.

Inherent variability within the investment casting and directional solidification processes requires a sensitivity analysis of process conditions if direct comparison between experimental and simulation results is desired. More specifically, shell thickness, wrap thickness, and wrap height were evaluated for the measured range of variability. Finally, model parameters such as mesh size and time step were also varied to confirm the numerical validity of simulation predictions.

Experimental Investigation of Axial Dendrite Growth

Measurements of shell thickness at the same location of different investment molds fabricated by the same method demonstrated an average shell thickness of 8 mm with a

variability of +/- 1.5 mm. Following mold preparation, the wrap thickness and height varied by up to +/- 3.2 mm from nominal for the largest wrap thickness. Measurements were based on bar-to-bar and casting-to-casting variability. This variability is used as the bounds of the simulated sensitivity analysis performed as part of the modeling investigation.

Microstructural analysis of transverse sections above the starter revealed that 80 pct of the 15 bars that were not seeded were well-aligned with the axis of the bar, while 100 pct of the 15 seeded castings were aligned with the axis of the bar. The crystallographic orientation of each unseeded bar relative to the growth direction is given in Table 6.3. A preferential crystallographic secondary orientation was observed for bars that were not seeded. The primary [001] growth direction tended to possess an orientation in which the primary dendrite was converging in the transverse direction as indicated by Figure 6.2. This corresponded to the direction of the first "kink" in the starter. In addition, a preferential secondary orientation was also observed, consistent with a preferential tilt of the thermal field through the starter. There was no trend of misorientation and withdrawal rate.

Table 6.3 – Misorientation of the [001] growth direction of selected, unseeded single crystals relative to the bar axis for each withdrawal rate.

Withdrawal Rate ($mm\text{-}min^{-1}$)	Off-Axis Misorientation (°)
12.7	6, 18, 19, 23, 33
16.9	7, 39
21.2	9, 21, 25, 25, 36

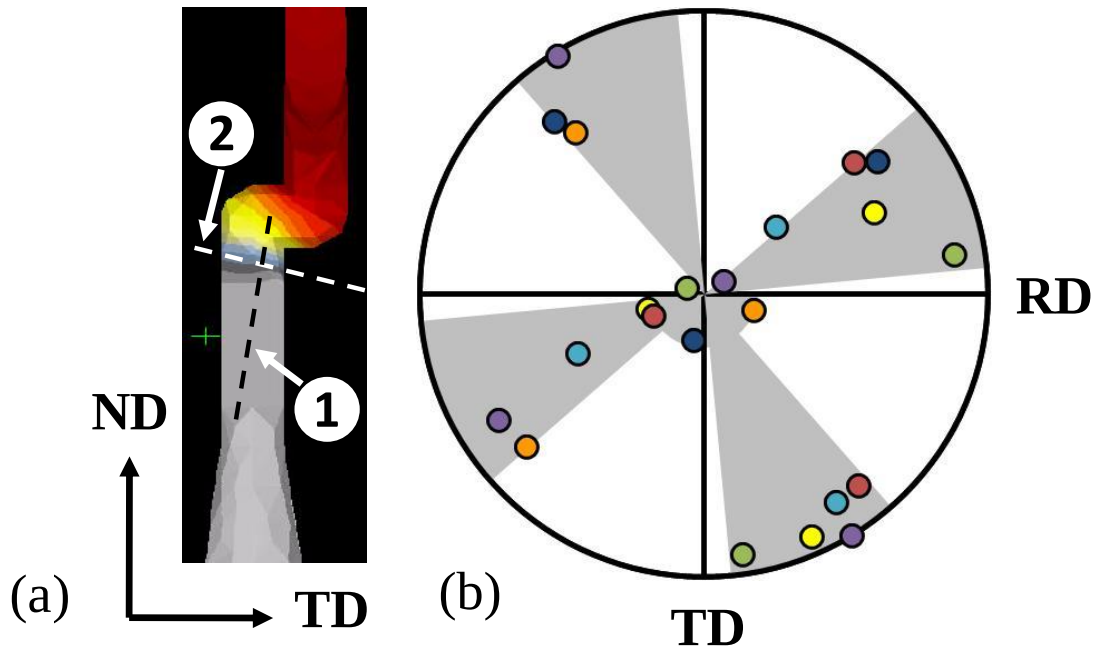

Figure 6.2 – (a) Preferential tilt of primary orientation (1) due to inclined solidification front below the starter (2) and (b) collection of pole figures from surfaces transverse to the withdrawal direction indicating preferential off-axis toward "TD" and rotational orientations of the single crystal. "RD" corresponds to the radial direction and "ND" the growth direction of a 5-bar mold configuration. The ranges have been banded in gray and different colored points correspond to different castings.

Analysis of longitudinal sections revealed the macrostructure of the casting along the length of the bar. The dendritic structure was then analyzed below, within and above the wrap for each bar by metallographic evaluation of transverse and longitudinal sections. The region defined as "below the wrap" corresponded to the bottom of the bar, longitudinal section "1" and transverse section below "1" according to Figure 6.3c. The "within the wrap" region included evaluation of longitudinal sections "3" and "8" and transverse sections at the bottom of samples "4" and "9", Figure 6.3c. Finally, the region designated as "above the wrap" corresponded to longitudinal sections 4, 5, 9 and 10 and transverse sections at the bottom of "5" and "10", Figure 6.3c. For a given withdrawal

rate and wrap thickness, a similar morphology was observed for the upper and lower mold wrap locations, as well as the replicate experiments.

In the region below the wrap, typical axial growth was observed (Figure 6.3). Some lateral growth of nearest neighbors was observed at the edges of the sample but significant overgrowth of primaries was not observed (Figure 6.4). Because the bottom of the mold wrap location is approximately 10 mm above this region, the microstructure at the bottom of the bar was anticipated to be independent of the mold wrap thickness. Therefore, the PDAS observed at this location should be similar for all bars cast with the same alloy at the same withdrawal rate, as was determined from measurement (Table 6.4).

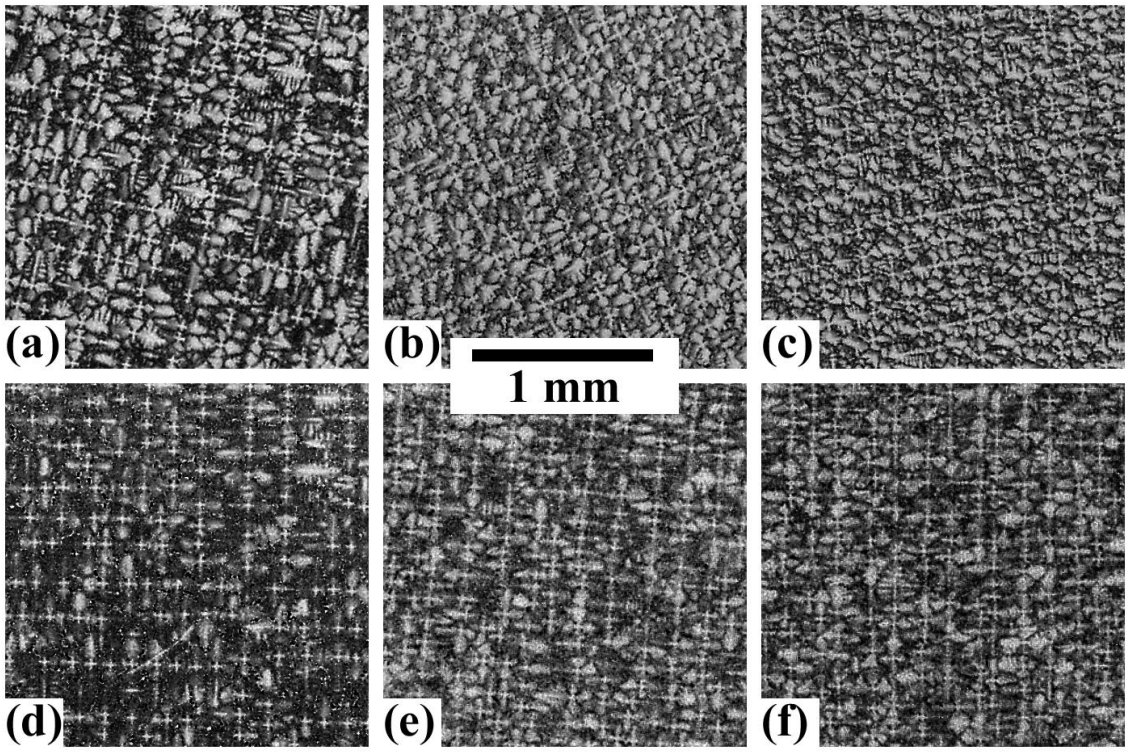

Figure 6.3 – Transverse micrographs of SX bars in the "below the wrap" region for the withdrawal rates and alloys investigated. CMSX-486 at (a) 12.7 mm-min^{-1}, (b) 16.9 mm-min^{-1} and (c) 21.2 mm-min^{-1}. René N4 at (d) 8.5 mm-min^{-1}, (e) 12.7 mm-min^{-1} and (f) 16.9 mm-min^{-1}.

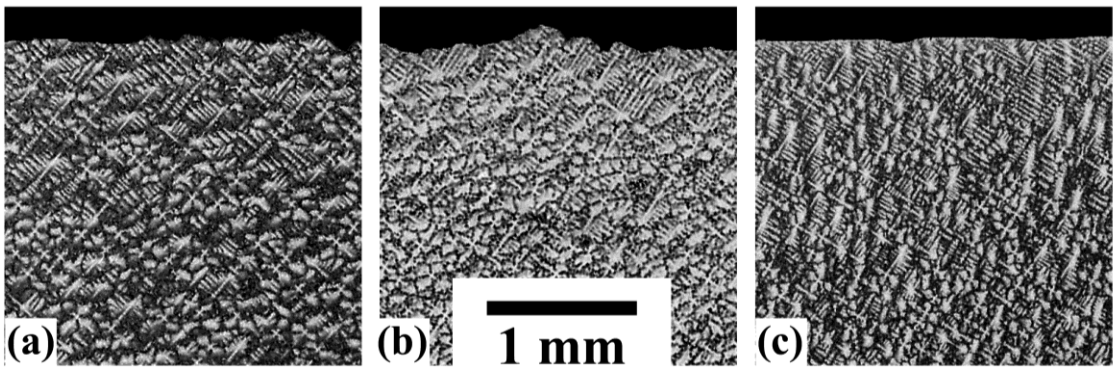

Figure 6.4 – Transverse micrographs at the "below the wrap" region showing lateral growth at casting surface for CMSX-486 with a range of withdrawal rates, (a) 12.7 mm-min^{-1}, (b) 16.9 mm-min^{-1} and (c) 21.2 mm-min^{-1}.

Table 6.4 – Average and standard deviation of measured PDAS below the wrap region.

Alloy	CMSX-486			René N4		
Withdrawal Rate (mm-min^{-1})	12.7	16.9	21.2	8.5	12.7	16.9
Average (μm)	233	228	220	218	195	164
Standard Deviation (μm)	29	29	48	25	26	25

There is moderate variability in PDAS from bar to bar and within the same axial position of a bar, which has also been observed elsewhere [12]. For example, for the cluster of bars cast at 21.2 mm-min^{-1} individual bars had average primary dendrite arm spacings of 206, 188, 193, 209 and 303 μm, with corresponding standard deviations of 16, 6, 8, 15 and 44 μm, Figure 6.5. Note the consistency of measurements and dendritic structure, with the exception of the 303 μm measurement (Figure 6.5e). However, the standard PDAS measurement technique does not consider the morphology of the secondary dendrites, highlighting the need for a new technique that differentiates a coarse dendritic structure and a fine dendritic structure with significant tertiary-arm propagation (Figure 6.5e).

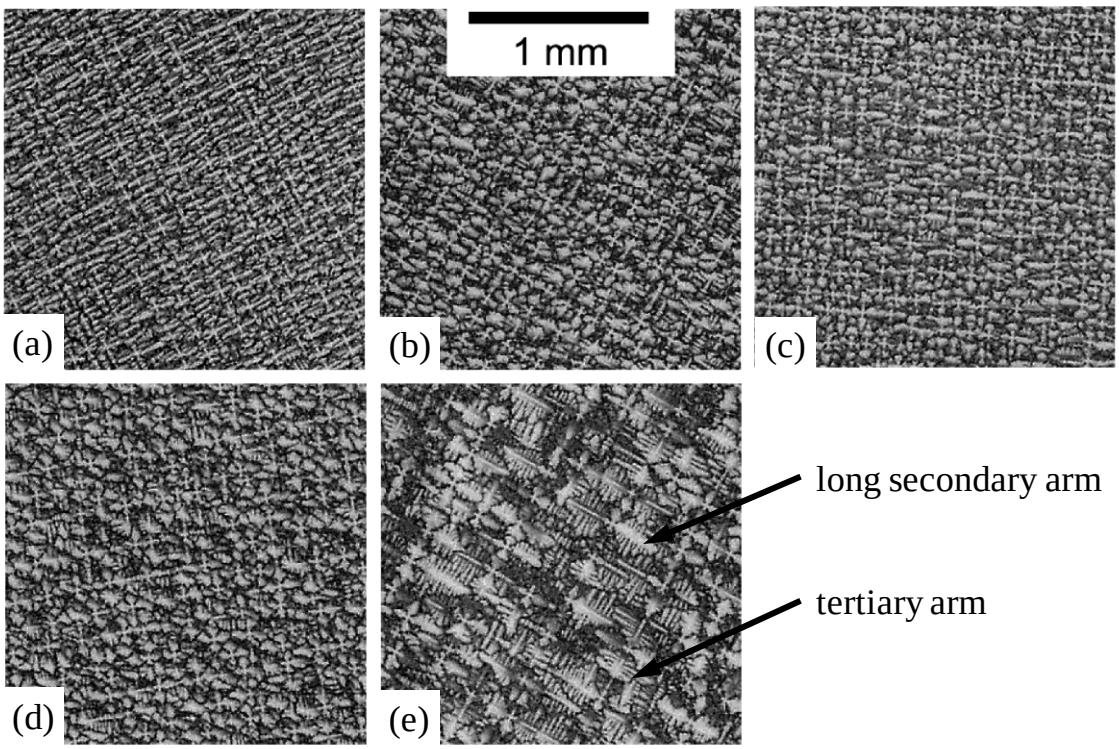

Figure 6.5 – Transverse micrographs at the bottom location for a cluster of five bars composed of CMSX-486 and withdrawn at 21.2 mm-min^{-1}.

At the location of the wrap, the structure remained single crystal. However, a contrast difference was observed macrostructurally following etching. The size of the region with different contrast was independent of wrap thickness or withdrawal rate and was a similar height as the mold-wrap. The contrast difference was attributed to a change in the scale of the dendritic structure. This was observed by comparison of PDAS measurements within and above the wrap locations and is discussed in the following section.

Above the location of the wrap, axial growth, lateral growth and grain nucleation were observed, depending on casting conditions. Each of these dendrite structures is discussed in turn. Axial growth was observed in bars cast of René N4 at a withdrawal rate of 8.5 mm-min^{-1} for all wrap thicknesses evaluated. Axial growth was also observed for both alloys at a withdrawal rate of 12.7 mm-min^{-1} with no additional mold wrap. A representative microstructure for a full cross section of the bar is shown in Figure 6.6.

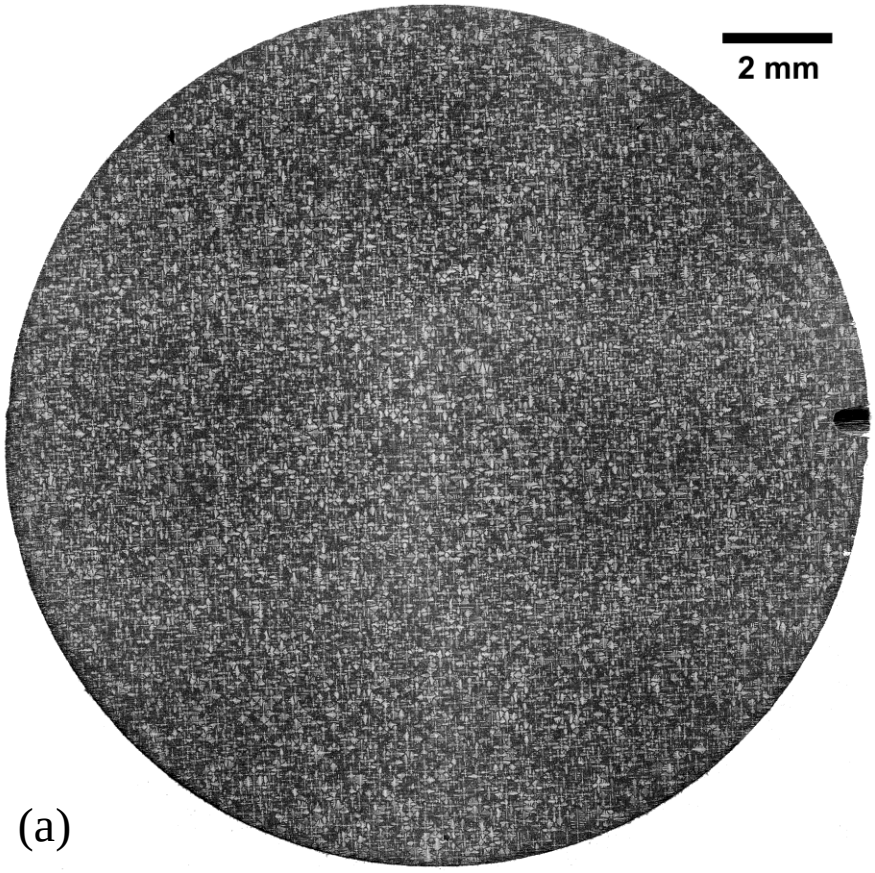

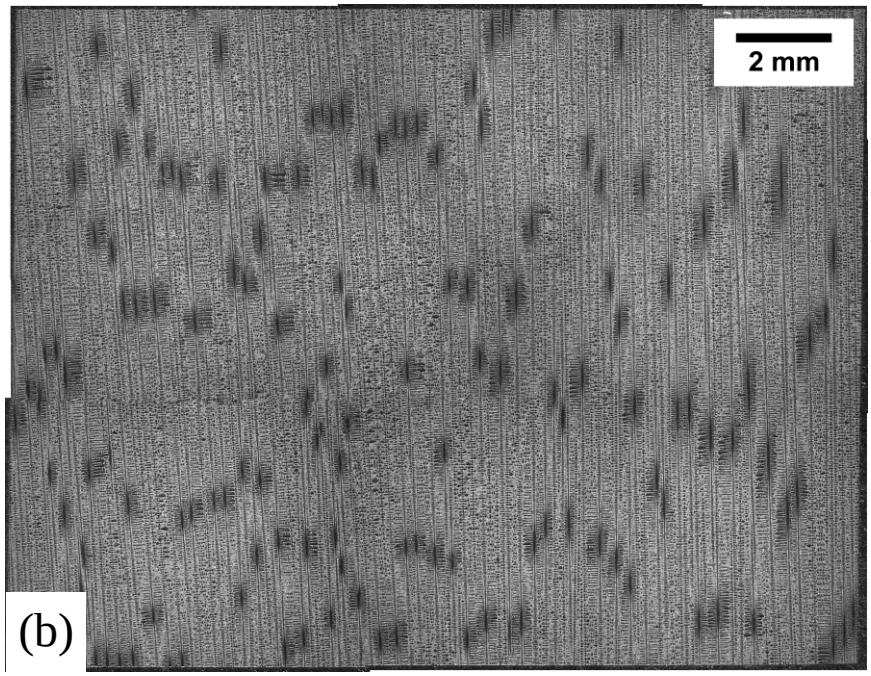

Figure 6.6 – (a) Transverse and (b) longitudinal micrographs "above the wrap" for a bar cast from René N4 at a withdrawal rate of 8.5 mm-min^{-1} and wrap thickness of 5 mm.

As was discussed previously, PDAS measurements within regions of axial growth within and above the wrap locations demonstrated a change in the dendrite structure in the region "within the wrap" (Figure 6.7). The PDAS above the wrap was 215 and 218 μm with corresponding standard deviations of 5 and 2 μm while the PDAS within the wrap was 200 and 186 μm with corresponding standard deviations of 5 and 12 μm. Figure 6.7 demonstrates an increased propensity for tertiary-arm propagation in the "above wrap" locations with minimal tertiary arm growth in the "within wrap" locations. The presence of tertiary arms increased the PDAS as described above due to competition between the secondary and tertiary arms with the primary arms growing in the axial direction of the casting. Thus, the wrap thickness is affecting microstructure scale by 10 pct and is discussed in further detail regarding the simulation results. For the same position relative to the wrap (within wrap 1 and within wrap 2, as well as above wrap 1 and above wrap 2

as shown in Figure 6.7), the PDAS above wrap 1 was within 2 pct of the PDAS above wrap 2, while there was a 7 pct difference between the PDAS within wrap 1 and within wrap 2. This demonstrates that the dendrite structure has sufficient time to recover to a scale consistent with the local thermal conditions.

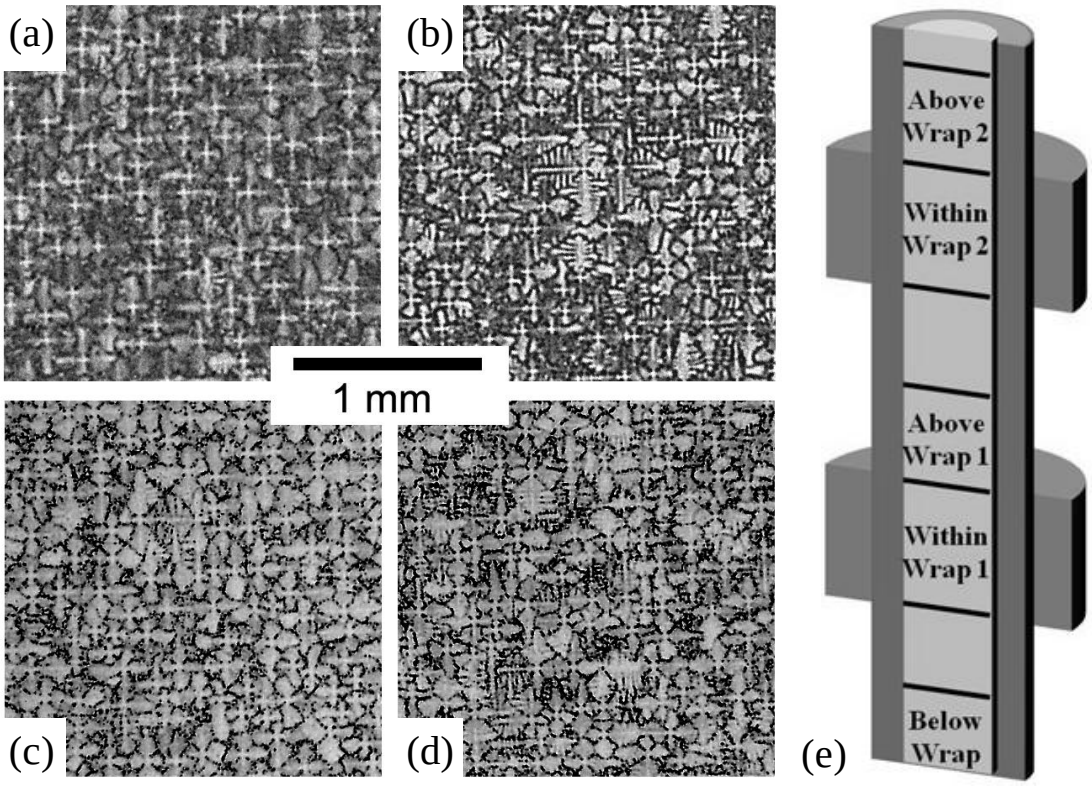

Figure 6.7 – Transverse micrographs of axial growth within a single-crystal bar of René N4 withdrawn at 8.5 mm/min and a wrap thickness of 14 mm at different height locations, (a) within first wrap (b) above first wrap (c) within second wrap, (d) above second wrap and (e) associated schematic of micrograph locations.

Lateral growth was observed in castings with 5, 10 and 14 mm of additional wrap thickness at 12.7 mm-min^{-1} for both alloys investigated (Figure 6.8 and 6.9). Lateral growth was also observed in bars of CMSX-486 withdrawn at 16.9 mm-min^{-1} with 0 and 5 mm wrap thickness, as well as 21.2 mm-min^{-1} with no additional wrap. The bars of

René N4 withdrawn at 16.9 mm-min^{-1} with all wrap thicknesses also exhibited lateral growth. The largest region of lateral growth occurred at the edge of the bar aligned along the [010] and [100] directions parallel to secondary dendrite arms, which grew inward (Figure 6.8a and 6.9a). More specifically, the morphology change was most significant in the quarter of the bar in which the primary orientation converged toward the surface of the casting. This tendency is unrelated to wrap thickness and is therefore further discussed in Chapter 7. EBSD measurements of the crystallographic orientation of the microstructure in transverse sections possessing axial and lateral growth confirmed that the lateral growth originated from the single crystal, within 5 degrees of misorientation (Figure 6.8b). A well-defined interface was observed between the axial and lateral growth regions (Figure 6.9). This boundary reached a steady-state radial position that was maintained for approximately 10 mm and was dependent on withdrawal rate and wrap thickness.

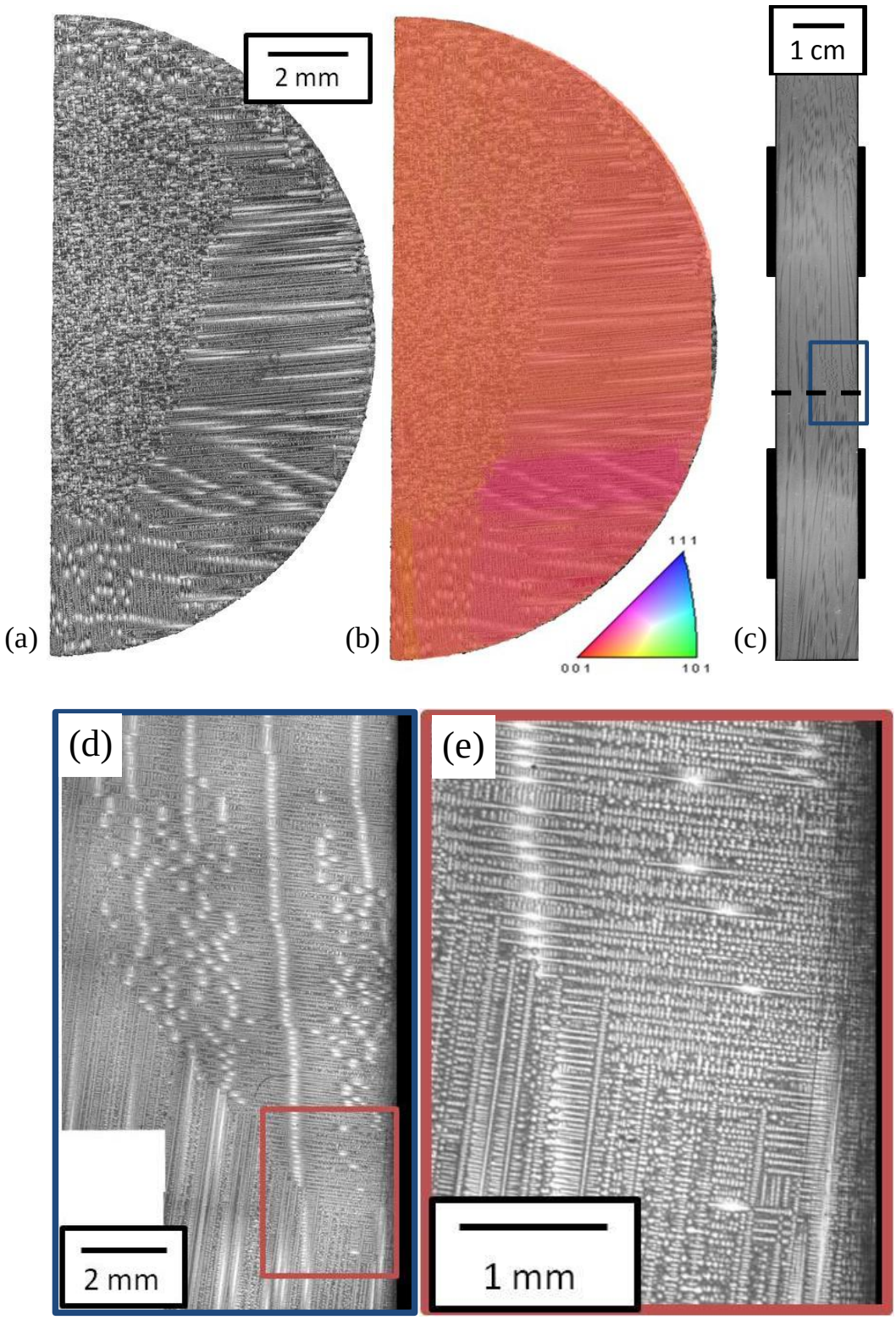

Figure 6.8 – (a) Transverse macrograph of lateral growth in the "above the wrap" region with (b) corresponding inverse pole-figure map superimposed on macrograph and longitudinal micrographs of (c) full bar, (d) lateral growth in the "above the wrap" region

and (e) higher magnification image at the onset of lateral growth for a single-crystal of CMSX-486 at a withdrawal rate of 12.7 mm-min^{-1} and wrap thickness of 10 mm.

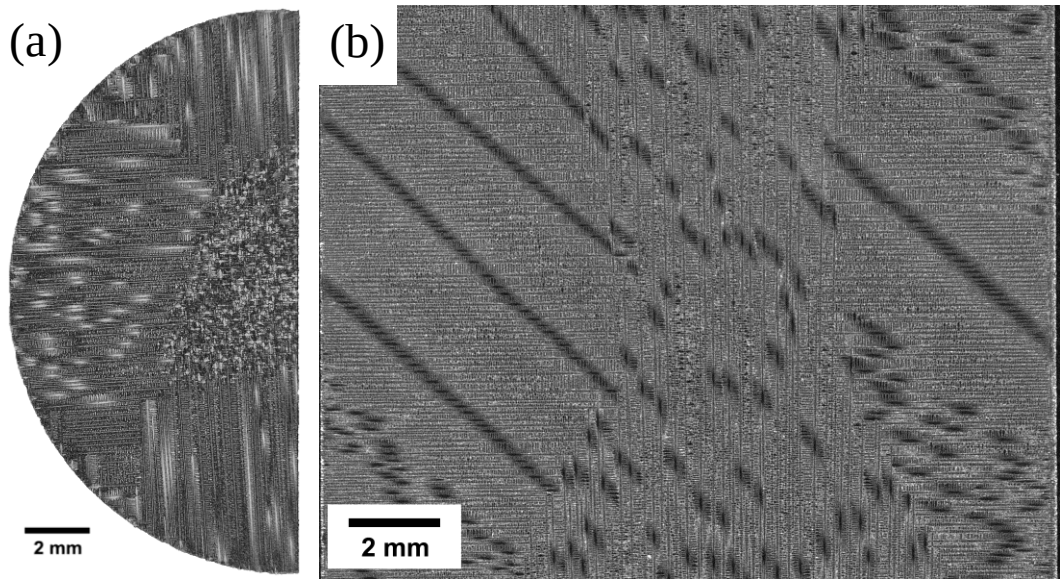

Figure 6.9 – Micrograph of lateral growth at the surface of the casting with axial growth in the center (a) transverse and (b) longitudinal to the growth direction for a single crystal cast of René N4 at 12.7 mm-min^{-1} with a wrap thickness of 10 mm.

For the most severe lateral growth condition, secondary dendrite arms extended to the center of the bar, removing all evidence of axial growth, Figure 6.10. The lateral growth was eventually over-competed within 30 mm beyond the top of the wrap by propagation of tertiary arms (in the axial direction of the bar) from the long secondary dendrite arms. At 30 mm above the top of the mold wrap, roughly the same as the length of the mold wrap, the entire array of dendrites grew axially such that all evidence of lateral growth was absent. Thus, interaction of the two wrap regions was not observed, since the wrap locations were separated by 40 mm.

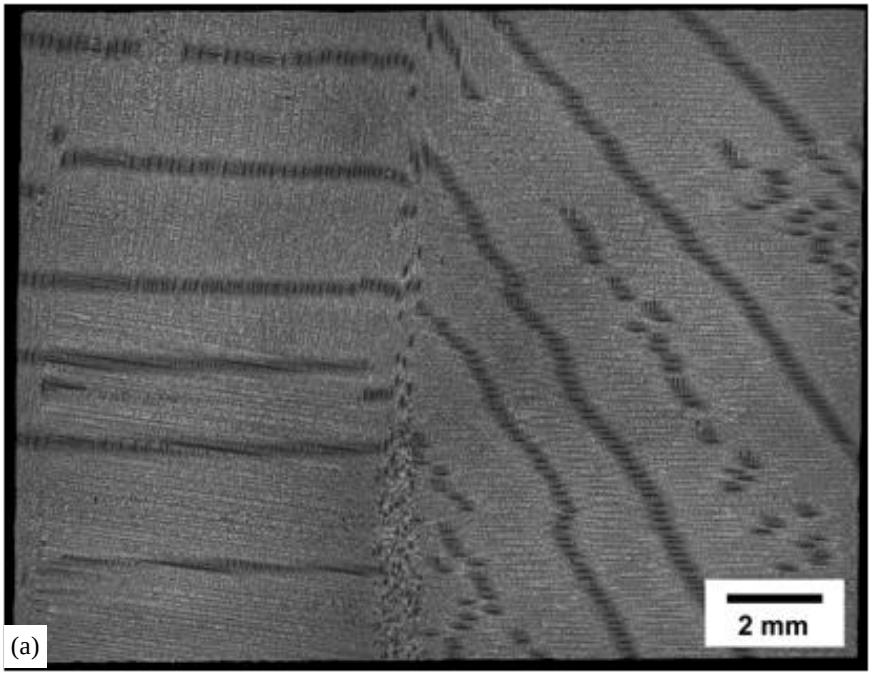

(a)

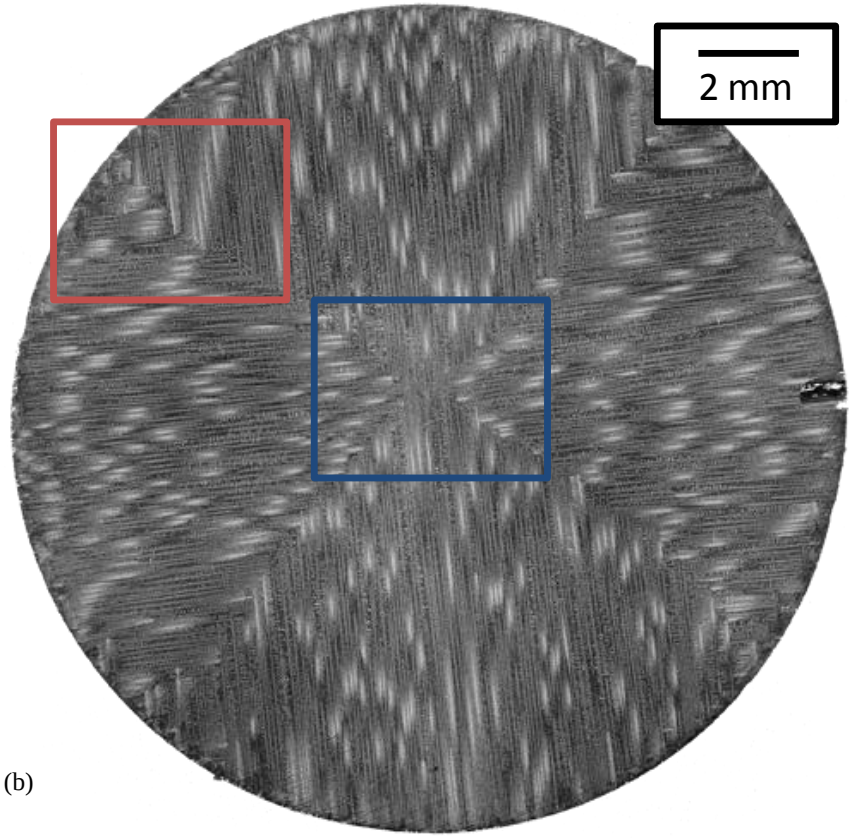

(b)

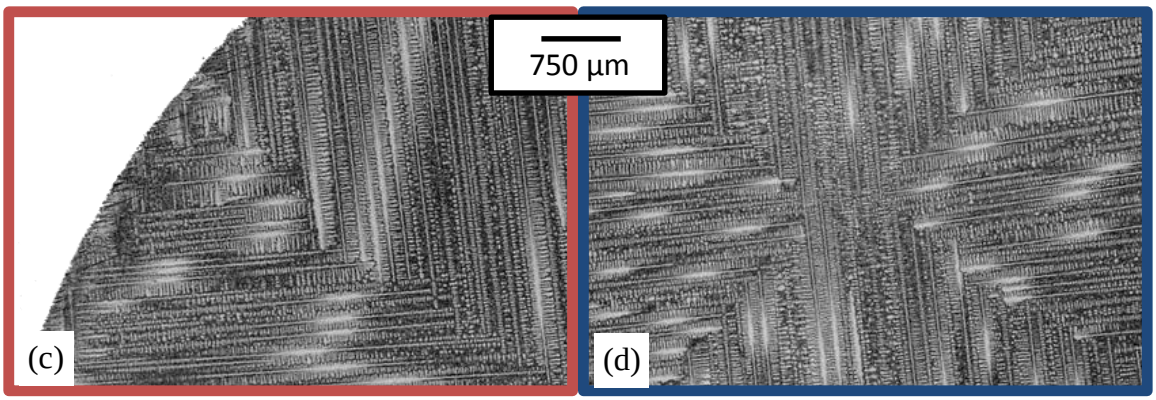

Figure 6.10 – (a) Longitudinal and (b) transverse macrograph with transverse micrographs at (c) the edge and (d) the center of a region with complete lateral growth "above the wrap" within a single-crystal bar cast of René N4 with a wrap thickness of 10 mm withdrawn at 16.9 mm-min^{-1}.

The PDAS and SDAS was measured on sections transverse and parallel to the bar axis for selected casting conditions. The PDAS on a transverse section just below the lateral growth region (Figure 6.11c) was compared to the PDAS within the lateral growth region on a longitudinal section in which the bottom of the longitudinal micrograph intersected the transverse plane (Figure 6.11b). The PDAS in the longitudinal section corresponded to the spacing between long secondary arms growing into the plane (Figure 6.11a). The average PDAS in a region of axial growth from the transverse section was 194 µm compared to 158 µm in a region of lateral growth from the longitudinal plane. This suggests a refinement of PDAS in regions of lateral growth, but more research is needed to confirm this observation. The SDAS in the four regions of lateral growth on a transverse plane (Figure 6.11a) were compared to the SDAS transverse and parallel to the withdrawal direction on a longitudinal plane (Figure 6.11b). The average SDAS in each of these locations was 34 µm with a standard deviation of less than 1 µm. Thus, the SDAS is the same in regions of axial or lateral growth with similar thermal conditions and is independent of the direction of the primary arms relative to the growth direction.

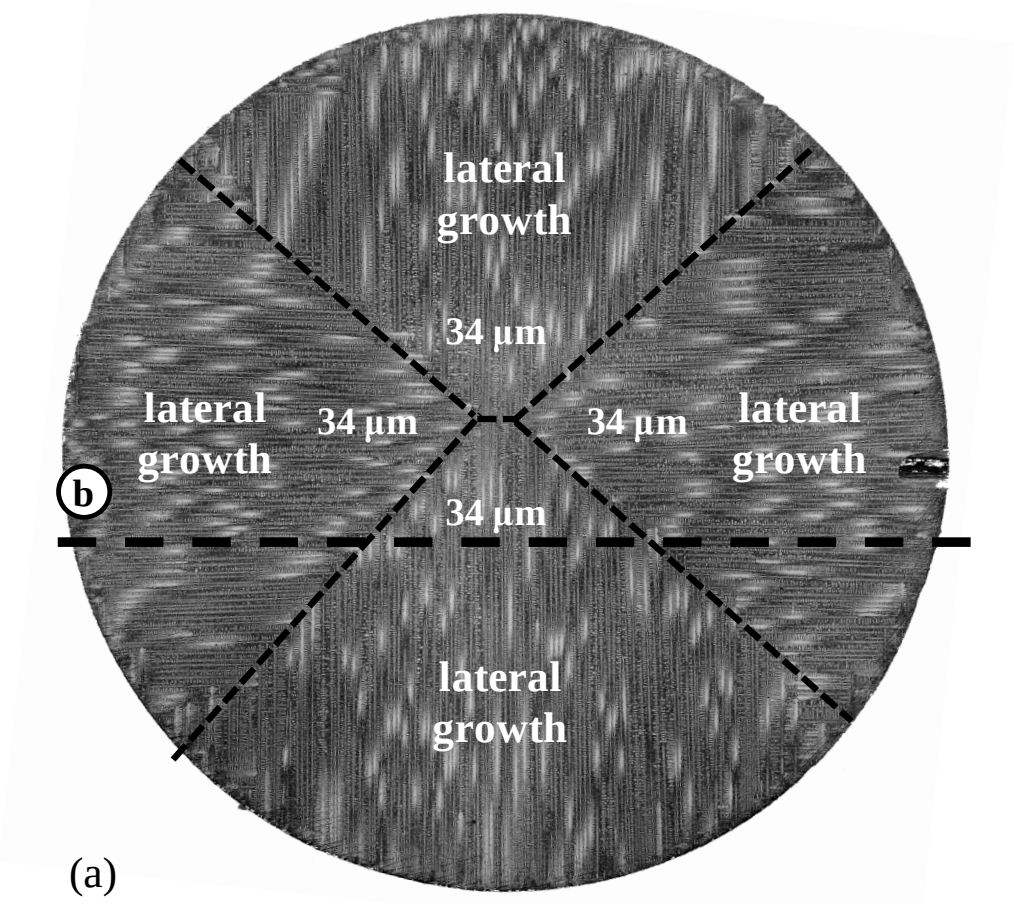
lateral
growth
34 μm
lateral
growth
34 μm
34 μm
lateral
growth
b
34 μm
lateral
growth

(a)

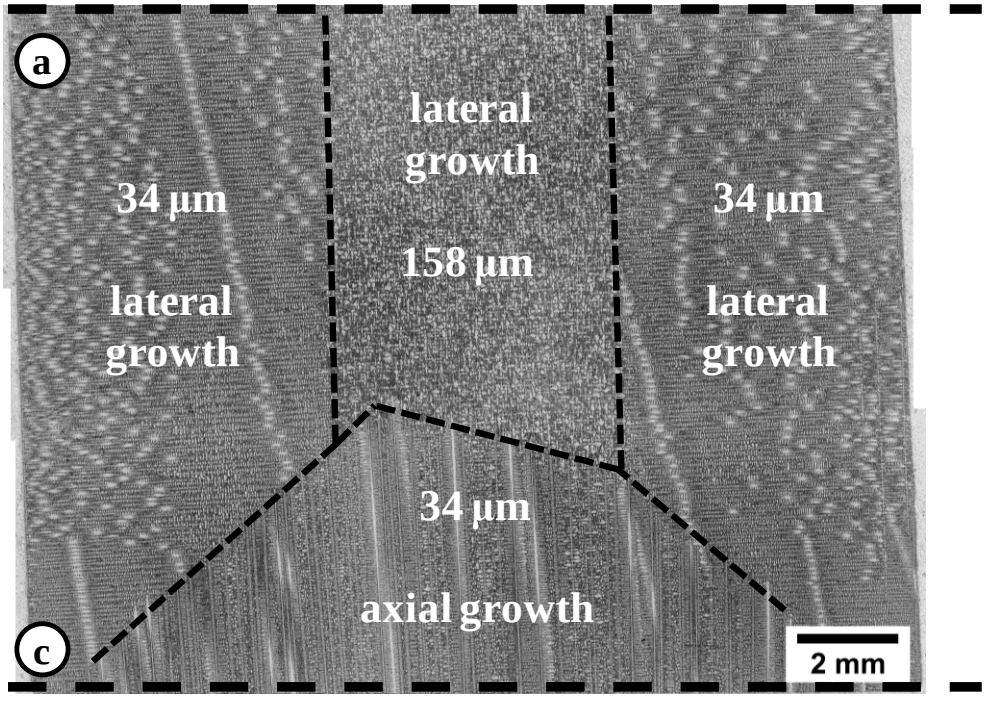
a
lateral
growth
34 μm
34 μm
158 μm
lateral
growth
lateral
growth
34 μm
axial growth
c
2 mm

(b)

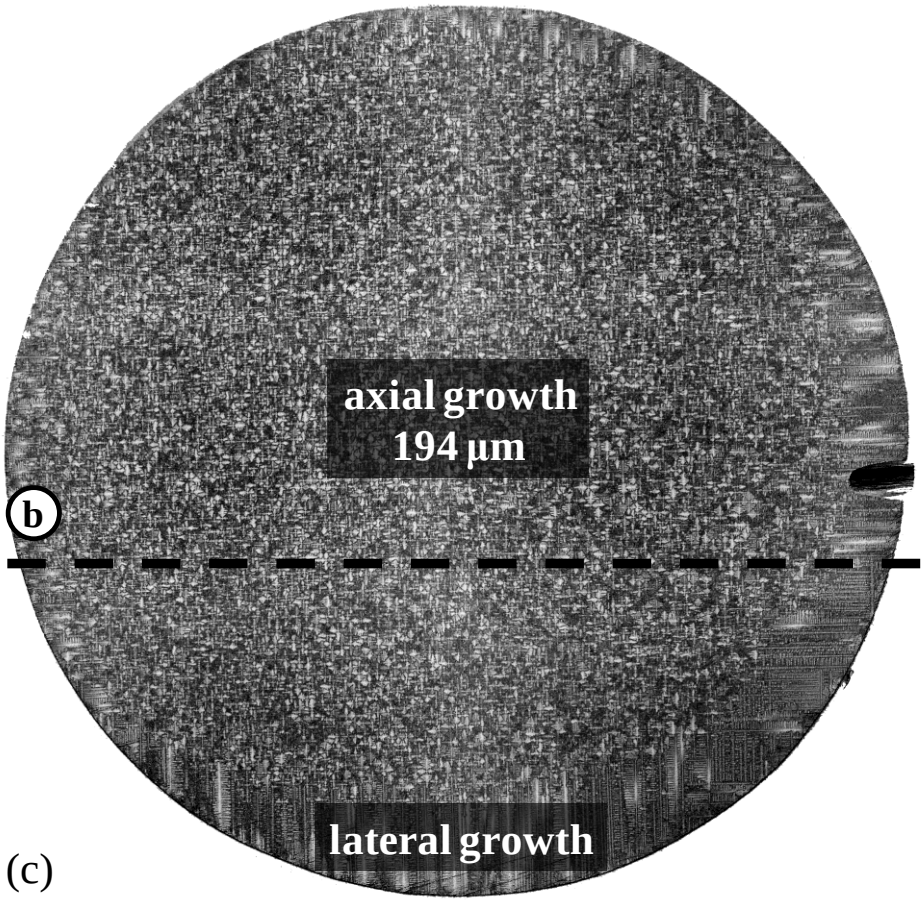

Figure 6.11 – (a) Transverse micrograph within lateral growth region positioned at the top of longitudinal micrograph (b) within transition region. Transverse micrograph (c) corresponds to a transverse section at the bottom of longitudinal micrograph (b). The longitudinal section (b) is marked in (a) and (c) for comparison. Regions of dendrite growth are separated by small dashed lines, and microstructure measurements are shown.

Grain nucleation was observed in the "above the wrap" region with alloy CMSX-486 at 16.9 mm-min^{-1} and wrap thicknesses of 10 or 14 mm and at withdrawal rate of 21.2 mm-min at all wrap thicknesses (Figure 6.12). EBSD measurements confirmed a significant change in crystallographic orientation indicative of nucleated grain. In general, nucleation occurred most prominently at the surface of the casting at a radial location 45 degrees from the orientation of the secondary arms. For all transverse sections in which nucleated grains were present, a nucleated grain was observed in at least one of the 45-

degree locations as previously described. In other words, castings that contained multiple nucleated grains had nucleated grains at the 45 degree location as well as other locations around the circumference of the casting. Figure 6.12e shows a region of lateral growth just below a nucleated grain.

Nucleation was observed in 9 castings with 5 different thermal conditions. Lateral growth preceded grain nucleation in 7 of the 9 castings. In the other cases, grain nucleation occurred at the surface of the casting where the dendrites were diverging from the wall. Based on these observations, the presence of lateral growth was an indication that conditions were approaching those associated with grain nucleation, especially when the primary dendrites of the original single-crystal converge toward the wall of the casting. The competition between the nucleated grain and the primary dendites was unrelated to wrap thickness or the circumferential position of the nucleated grain. Instances of complete overgrowth of the original dendrites and complete overgrowth of the nucleated grain were observed. Instances in which neither crystal was completely overgrown were also observed, as in Figure 6.12.

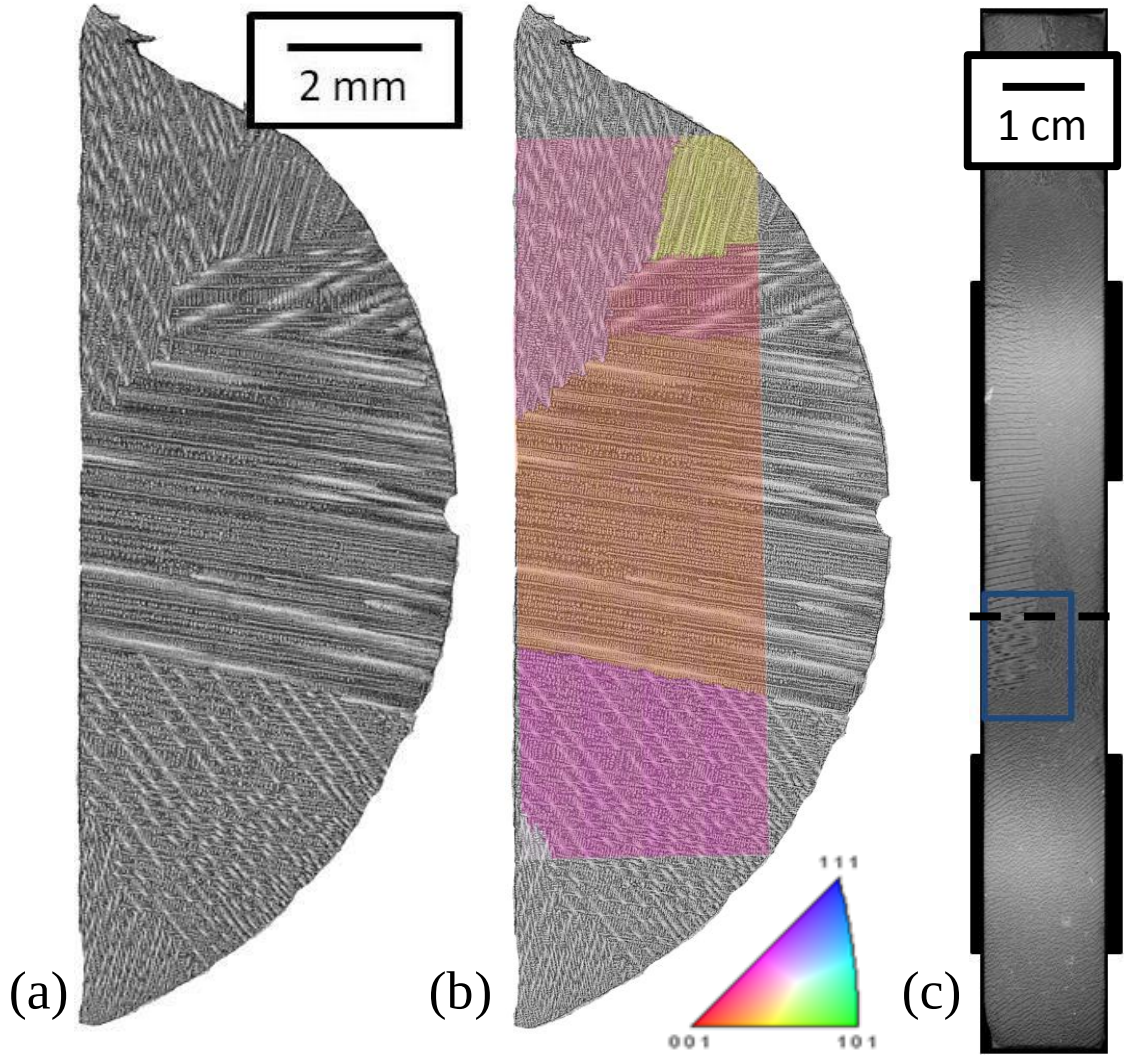
2 mm
(a)
(b)
111
001
101
1 cm
(c)

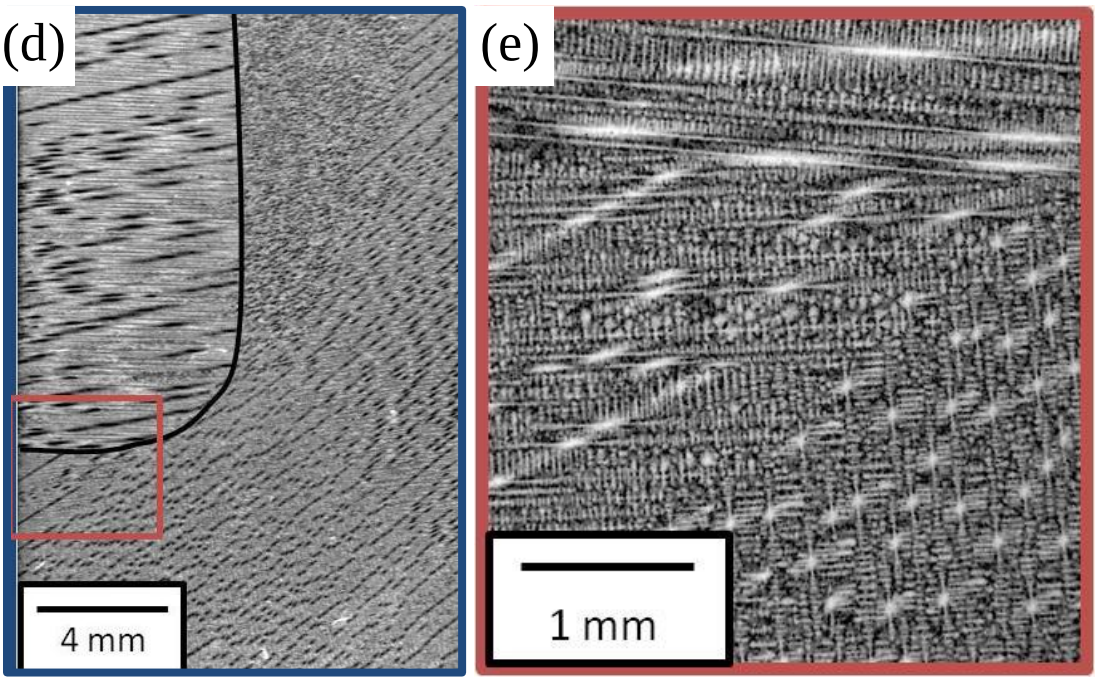

Figure 6.12 – (a) Transverse macrograph of a nucleated grain with (b) corresponding superimposed inverse pole-figure map and longitudinal micrographs of the (c) full bar, (d) "above the wrap" region and (e) higher-magnification image at the specified location depicting a region of lateral growth preceding the nucleated grain within a single-crystal bar of CMSX-486 with a wrap thickness of 10mm and withdrawal rate of 16.9 mm-min^{-1}.

Complete breakdown of the SX structure, resulting from nucleation of several grains, was observed for bars withdrawn at 21.2 mm-min^{-1} with all wrap thicknesses (Figure 6.13). This was attributed to significant curvature of the solidification front resulting in considerable undercooling of the melt ahead of the dendrite front, thus promoting grain nucleation. In one instance, there was an observation of a dendrite in which its primary orientation was changing (Figure 6.13b). The morphology of this dendrite was attributed to continued preferential solidification on the interior side of the dendrite tip due to severe inclination of the thermal field ahead of the solidification front.

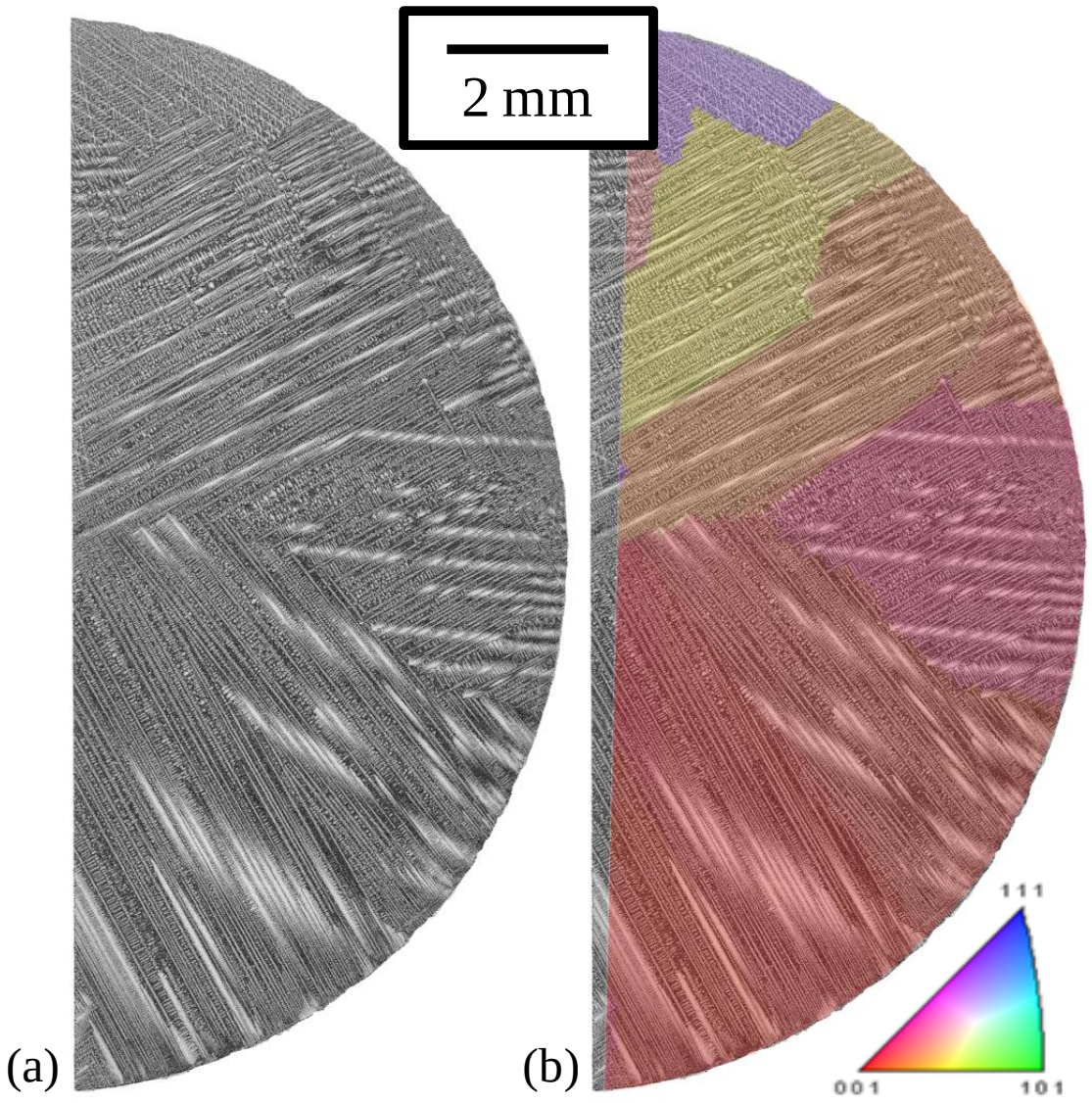
2 mm
(a)
(b)
111
001
101

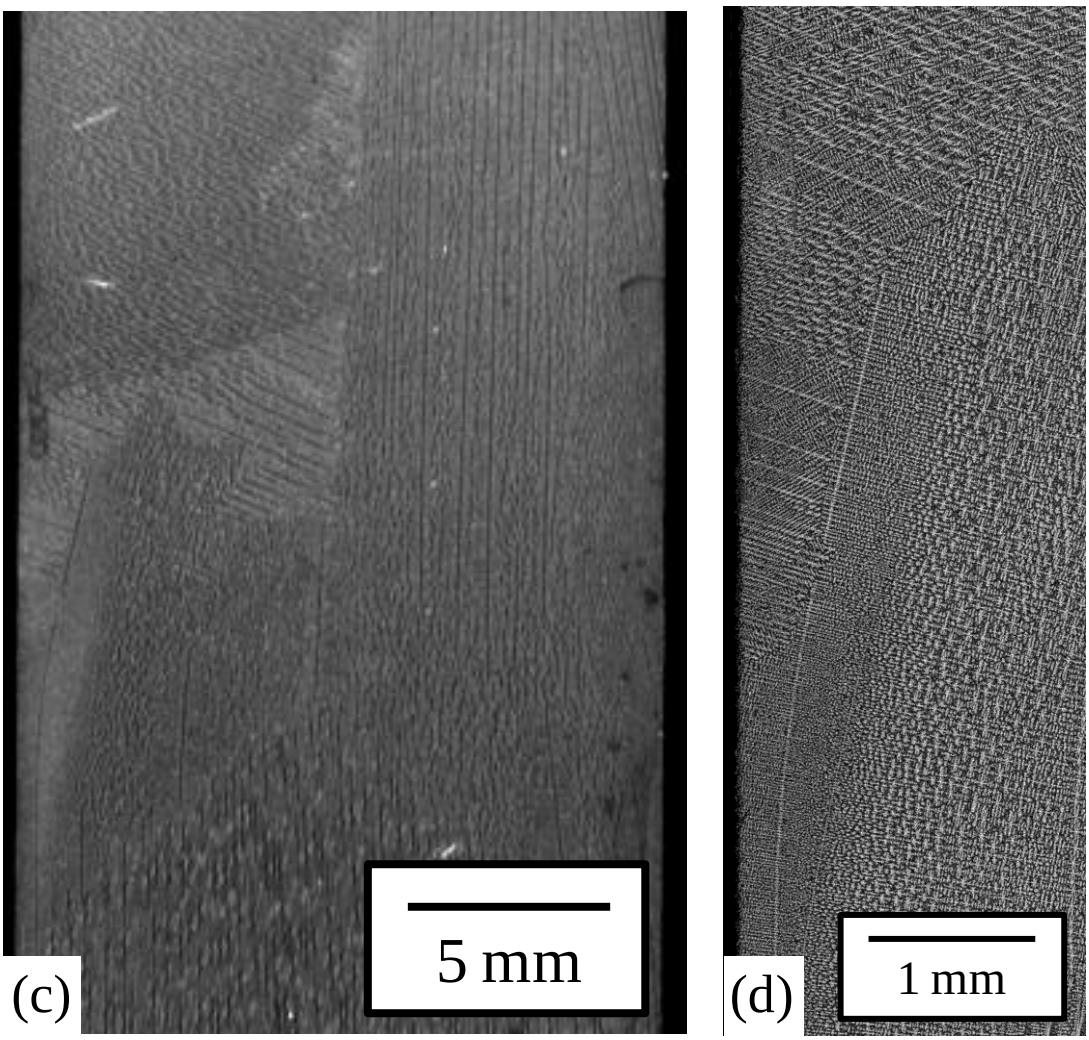

Figure 6.13 – (a) Transverse micrograph in the "above wrap region" with (b) superimposed inverse pole figure map and longitudinal (c) macrograph and (d) micrograph in the "above wrap" region.

In summary, a different microstructure was observed in regions below the wrap, within the wrap, and above the wrap. Varying degrees of axial growth, lateral growth and grain nucleation were observed "above the wrap", and this was in accordance with varying degrees of three-dimensional heat extraction, as is discussed further in the solidification-modeling section. The presence of these morphologies is dependent on alloy, wrap thickness and withdrawal rate. For the same casting conditions, CMSX-486 was more

prone to lateral growth and grain nucleation than René N4, which is further investigated in the solidification-modeling section.

The unstable process conditions – indicated by a transition in the dendrite growth mode, from axial growth to lateral growth and grain nucleation – increased with increasing wrap thickness and significantly increased with increasing withdrawal rate. In general, the thinnest wrap provided a small affected region, with an increase in the size of the region as wrap thickness increased. The lateral-growth propagation and grain nucleation occurred approximately 10 mm above the top of the mold wrap. The variability in this measurement is within the error of the mold wrap location (+/- 3.2 mm).

Ultimately, axial growth over-competed the lateral growth regions within 30 mm beyond the top of the mold wrap. A similar PDAS was observed for equivalent locations (above wrap and within wrap) for the top and bottom mold wrap locations. A similar SDAS was observed in regions of axial and lateral growth. A reduction in PDAS was observed in longitudinal sections within regions of lateral growth, compared to transverse sections in regions of axial growth. Competition between axial growth and the nucleated grain depended on the orientation of the nucleated grain. A summary of the observed dendrite morphology "above the wrap" for each wrap thickness and withdrawal rate is provided (Table 6.5).

Table 6.5 – Observed dendrite morphology above the first wrap for associated process conditions: wrap thickness and withdrawal rate. Note: "A" designates axial growth (Figure 6.6), "L" lateral growth (Figure 6.8) and "N" grain nucleation (Figure 6.12).

Alloy		CMSX-486			René N4		
Withdrawal Rate (mm-min^{-1})		12.7	16.9	21.2	8.5	12.7	16.9
Wrap Thickness (mm)	0	A	L	L	A	A	A
	5	L	N	N	A	L	L
	10	L	N	N	A	L	L
	14	L	N	N	A	L	N

Thermal Simulation

Heat-transfer simulations over the range of experimentally-evaluated process conditions – withdrawal rate and wrap thickness – established a relationship between the various process conditions and the thermal conditions at the solidification front (Figure 6.14). The additional mold wrap reduced the axial thermal gradient just above the wrap allowing the relative magnitude of the transverse thermal gradient to increase. This was evaluated by analysis of the relative magnitudes of the axial and transverse thermal gradients, which is a representation of the inclination angle of the solidification front as described in Chapter 2. The inclination angle reduced to nearly 0° within the wrap and reached a maximum at the surface of the casting just above the wrap, in the same location as lateral growth and grain nucleation were observed. In addition, the solidification rate decreased within the wrap and increased above the wrap, as associated with a contribution of the lateral heat extraction above the mold. Finally, the cooling rate increased below the wrap, reduced to a moderate value within the wrap and further reduced just above the location of the wrap. A higher cooling rate was predicted in the center of the casting as compared to the surface at the same height. Analysis of the range

of experimentally-evaluated process conditions utilized thermal predictions of the thermal gradient, solidification rate and inclination angle.

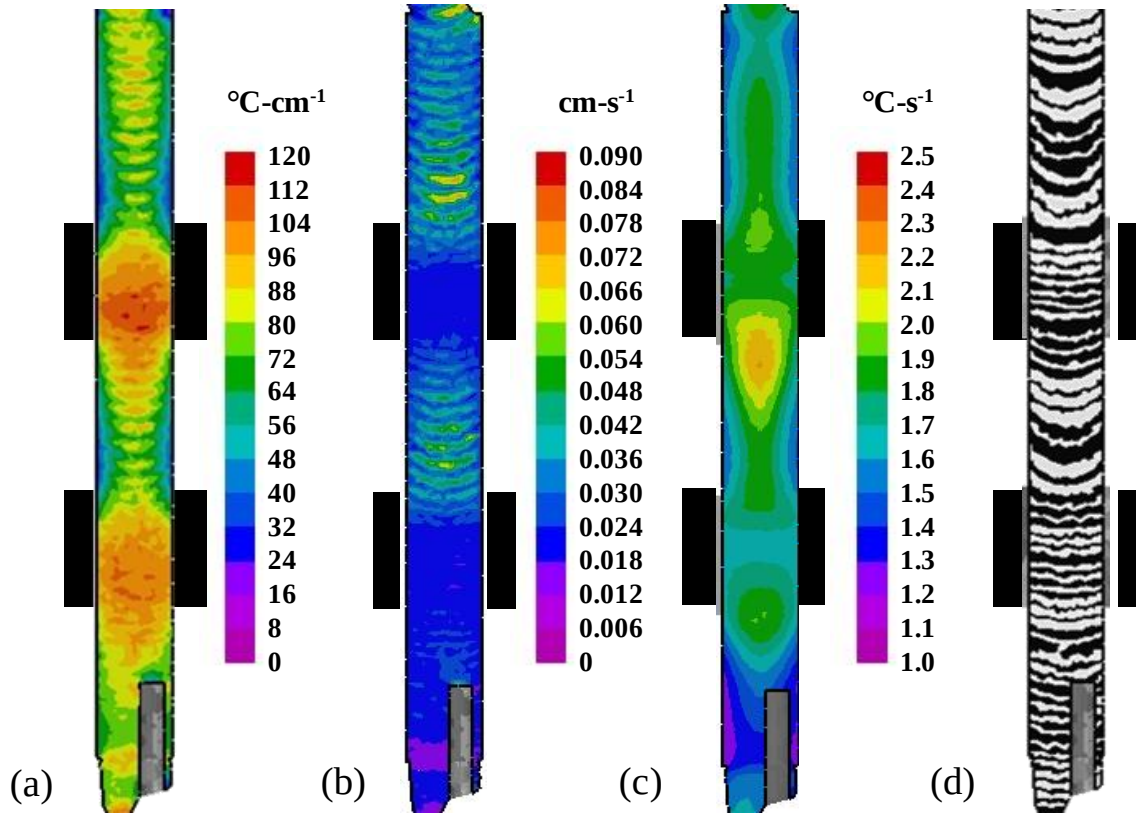

Figure 6.14 – Contour plots of (a) thermal gradient, (b) solidification rate, (c) cooling rate and (d) inclination angle of the solidification front for a bar cast of CMSX-486 at 16.9 mm-min^{-1} with a wrap thickness of 14 mm.

At the bottom of the casting in the "below the wrap" region, thermal predictions from each of the experimental conditions were compared (Table 6.6). Solidification rate and cooling rate increased with increasing withdrawal rate. As the withdrawal rate increased, the solid-liquid interface was lowered relative to the position of the transition region of the furnace as was discussed in Chapter 4. The maximum axial thermal gradient at the surface of the casting and minimum inclination at the center of the casting occurred when

the solidification front was at the top of the floating baffle, corresponding to a withdrawal rate of 12.7 mm-min^{-1} for both investigated alloys. Any further increase in withdrawal rate lowered the solidification front position below the top of the baffle and caused an increase in the solidification-front inclination angle.

Table 6.6 – Predicted thermal conditions at the bottom in the center of the casting for each of the experimentally-evaluated alloys and withdrawal rates.

Alloy	CMSX-486			René N4		
Withdrawal Rate (mm-min^{-1})	12.7	16.9	21.2	8.5	12.7	16.9
Axial Thermal Gradient (°C-cm^{-1})	96	102	106	107	121	126
Solidification Rate (cm-s^{-1})	0.022	0.027	0.035	0.015	0.022	0.028
Cooling Rate (°C-s^{-1})	1.47	1.87	2.13	1.57	2.62	3.60

Within the wrap, solidification-front inclination angle increases with increasing withdrawal rate and decreases with increasing wrap thickness. Increasing wrap thickness slows the solidification rate and flattens the interface within the insulated region. The flattening of the solidification interface occurred within 2.5 mm of the bottom of the mold wrap, indicating the steady-state thermal condition within the mold wrap prior to the abrupt change in the thermal field. The withdrawal rate effect is the same as was explained for the location above the wrap. The axial thermal gradient in this region is generally insensitive to either wrap thickness or withdrawal rate. The solidification rate increases with increasing withdrawal rate and decreases with increasing wrap thickness. The variation of thermal condition with changes in wrap thickness is explained by the reduced heat transfer at the location of the wrap, followed by increased heat transfer just above the wrap as the solidification front proceeds axially and laterally.

Along the edge and above the wrap, the predicted thermal conditions were compared for each experimental condition (Figure 6.15). The solid-liquid interface inclination angle increased with increasing wrap thickness and significantly increased with increasing withdrawal rate. As the wrap thickness increased, lateral heat extraction within the wrap decreased. This caused a significant increase in lateral heat extraction above the wrap, which increased the solidification-front inclination angle. The local solidification rate in this region also increased with increasing withdrawal rate and wrap thickness while the axial thermal gradient followed the opposite trends. The increase of solidification rate with increasing wrap thickness is an indication of transient conditions, and can be assessed by evaluating the ratio of the solidification rate and withdrawal rate (Figure 6.15c). The cooling rate over the melting range at this location was relatively constant. Thermal predictions of René N4 had reduced inclination angle and increased thermal gradient, solidification rate and cooling rate as compared to predictions of CMSX-486.

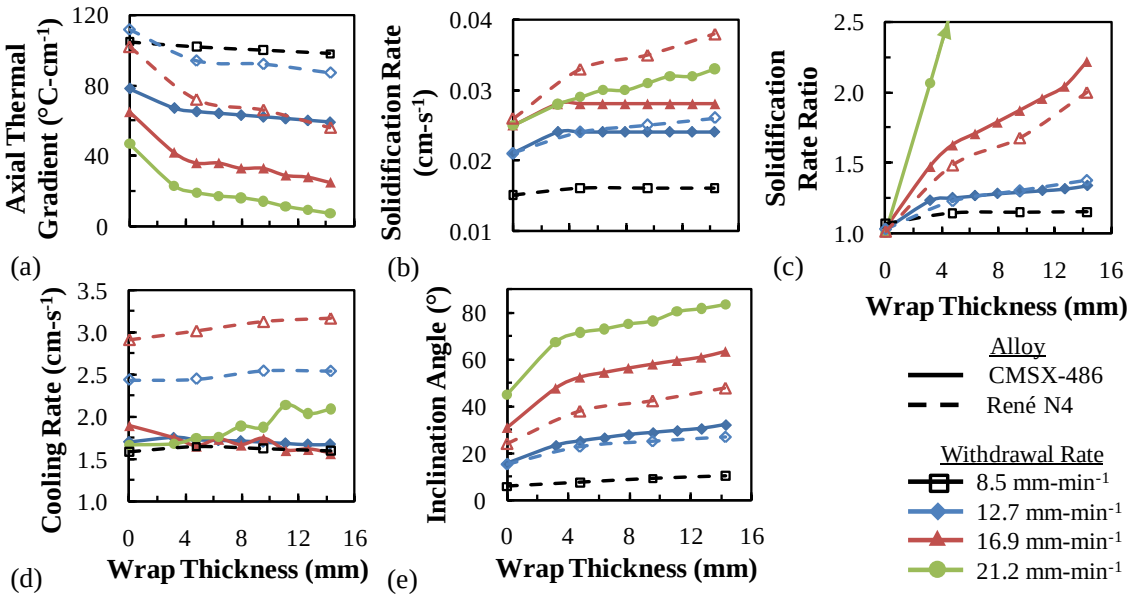

Figure 6.15 – Predictions of (a) axial thermal gradient, (b) solidification rate, (c) solidification rate ratio, (d) cooling rate and (e) solidification-front inclination angle at the surface of the casting just above the location of the wrap as a function of alloy, withdrawal rate and wrap thickness.

Analysis of the predicted thermal conditions identified that a unique thermal condition was observed above the wrap in all cases, strictly following the trend of increased solidification rate and inclination angle and reduced thermal gradient with increasing withdrawal rate and wrap thickness. In general, the axial thermal gradient, solidification rate and solidification-front inclination angle were interdependent, which complicates determination of which thermal characteristics are associated with lateral growth. Thus, parametric evaluation of the individual thermal characteristics – that is, thermal gradient, solidification rate and inclination angle – could not be performed. However, the feature of the solidification front most sensitive to the changes in wrap thickness and withdrawal rate in the "above the wrap" region was the solidification-front inclination angle.

A sensitivity analysis was conducted for shell thickness, wrap thickness and wrap length, in which the range for each experimental variable was based on the measured variability, as determined from the previous section. This analysis indicated that the thermal fields were unaffected by the experimentally-measured variability for shell thickness, wrap thickness and wrap length. In other words, the thermal conditions were significantly more sensitive to wrap thickness and withdrawal rate than the variability of these experimental variables.

Correlation of Dendrite Morphology and Predicted Thermal Field

Microstructure observations of axial growth, lateral growth and grain nucleation were compared to the predicted local thermal conditions. Changes in dendritic morphology and tendency for axial versus lateral growth correlated to the inclination angle of the solid-liquid interface (Figure 6.16). By increasing the inclination angle from 0° to 80° at the surface of the casting, the dendrite morphology changed from axial growth to lateral growth and eventually grain nucleation. For conditions with nearly an identical inclination angle, such as those near 25° (Figure 6.16), experimental observations with a non-zero wrap thickness were more prone to lateral growth than the experimental conditions with no wrap. This difference was attributed to the transient nature above the wrap, compared to the steady-state thermal condition of the bars without wrap. Lateral growth was observed when the inclination angle was 25°, and grain nucleation was observed with an inclination angle greater than 45°. All experimental measurements were consistent with these bounds. *Therefore, utilization of the solidification-front*

inclination angle to predict the dendritic morphology, regardless of alloy or geometry, represents a new approach to predicting dendrite morphological transitions and the onset of grain nucleation in the absence of convective instabilities.

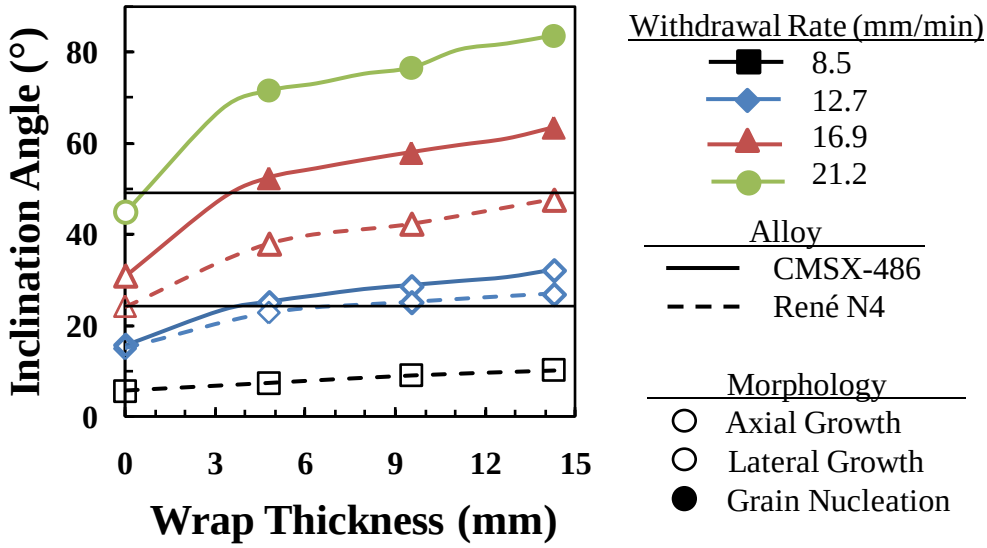

Figure 6.16 – Predicted processing map for the effect of inclination angle on dendrite morphology based on changes in alloy, withdrawal rate and wrap thickness. Note: The data points indicate process conditions evaluated experimentally.

Grain nucleation is a probabilistic event dependent on the presence of nuclei with the presence of undercooling. Undercooling in a multi-component alloy is not predicted by thermal simulation, so defining a thermally-based nucleation criteria would be inappropriate. However, the experimental results confirm that the thermal conditions present with an inclination angle of 45 degrees within this particular geometry could be used to conservatively predict grain nucleation. Yet, the thermal conditions could not be decoupled, so the observed correlation of grain nucleation is more likely to be the local solidification rate, as suggested by others [5]. More research is needed to determine the thermal parameter associated with the onset of grain nucleation.

Prediction of Dendrite Scale

The thermal conditions were also used to predict dendrite scale (Figure 6.17). The noise observed in the predicted PDAS is an artifact of the FE model. Along the centerline of the bar, the predicted PDAS increased within the wrap relative to regions outside of the wrap due to the reduced solidification rate. Above the wrap, the PDAS increased on the surface of the casting due to the decline of the axial thermal gradient and decreased in the center of the casting. The predicted SDAS was lowest just below the wrap, increased slightly within the wrap and further increased above the wrap on the surface of the casting. Quantitatively, the PDAS varied by a factor of two within the casting while the SDAS varied by only 20 pct.

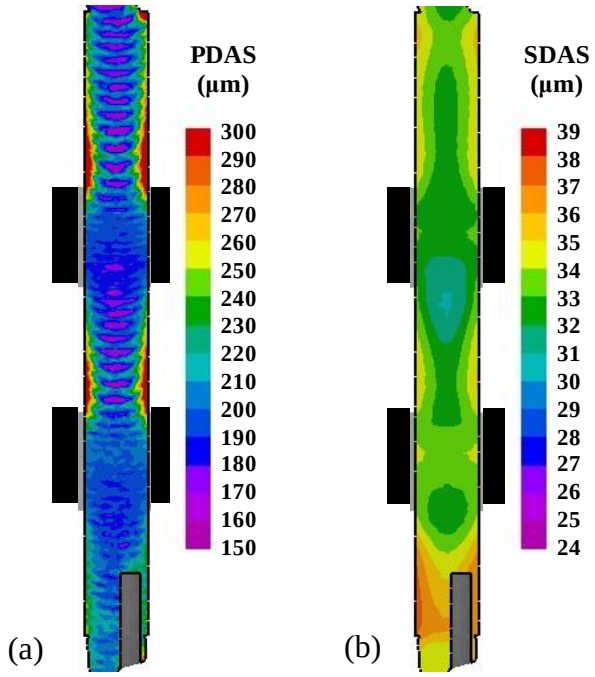

Figure 6.17 – Predicted contour plots of (a) PDAS and (b) SDAS for a SX bar cast of CMSX-486 at 16.9 mm-min^{-1} and a wrap thickness of 14 mm.

For each withdrawal rate, the measured PDAS below the wrap was compared to the thermally-based prediction of PDAS (Table 6.7). The inclination angle at this location was up to 20° at the surface of the casting and always 0° in the center. At an inclination angle of 20°, the axial thermal gradient is 7 pct less than the total thermal gradient, which only amounts to a 4 pct difference in PDAS. Thus, the predicted dendrite scale agreed reasonably with experimental measurement. In addition, the predicted range of microstructure scale was similar to the measured standard deviation greater and less than the measured average dendrite spacing.

Table 6.7: Predicted PDAS at the bottom location within a single crystal bar for the range of withdrawal rates evaluated.

Alloy	CMSX-486			René N4		
Withdrawal Rate (mm-min^{-1})	12.7	16.9	21.2	8.5	12.7	16.9
Minimum (μm)	207	200	199	194	173	173
Maximum (μm)	260	258	258	230	202	202

Moreover, the scale of the dendritic structure within the wrap, as compared to above and below the wrap, was assessed. As stated previously, the predicted PDAS was coarser within the wrap than above the wrap for the center of the casting by approximately 10 pct, while the predicted PDAS at the surface above the wrap was coarser than within the wrap and significantly depended on the wrap thickness. Above the wrap, the combination of the increasing solidification rate and decreasing thermal gradient in the center of the casting resulted in a similar PDAS for a given withdrawal rate and alloy

(Figure 6.17a). A similar cooling rate was also predicted in this region for the same alloy and withdrawal rate, resulting in a similar SDAS (Figure 6.17b).

Along the centerline of the bar, a 10 pct increase in PDAS is predicted within the wrap, relative to regions above and below the wrap, which is the opposite trend from the 10 pct decrease measured experimentally. Above the wrap, the coarser dendrite structure was actually a laterally-competing, finer structure (Figure 6.7). In this region, the dendrite structure was transient, adjusting to the abrupt change in the thermal field, as the competition of secondary and tertiary arms with primary arms was reducing the overall dendrite scale. With abrupt changes in thermal conditions the dendrites cannot instantaneously adjust their spacing, since a reduction in spacing relies on overgrowth of primaries by secondaries. This delay in refinement may have contributed to the discrepancy between measurement and prediction. In addition, the significant variability from center to edge above the wrap may have limited the reliability of the direct comparison.

Discussion

Crystallographic orientation measurements near the starter from unseeded single-crystal bars indicate a preferential misorientation of the single crystal and secondary orientation due to the interference of the efficient heat extraction of the LMC process to the single-crystal selection process within the starter. The off-axis misorientation of the single-crystal is especially important due to (1) the sensitivity of dendrite growth mode to

inclination angle of the solidification front and (2) the increased inclination angles observed with utilization of the LMC process. Starters utilized in this effort were optimized for the Bridgman process in which lateral heat extraction was much less. The increased lateral heat extraction limits the tilting of the solidification front within the starter, which is the primary means for single-crystal selection. Thus, a more efficient starter design is needed for the LMC process in the absence of seeds.

Microstructure measurement of PDAS and SDAS in axial and lateral growth regions in different orientations indicated the relationship between cooling rate and SDAS regardless of orientation. However, initial measurements indicated a refinement in "PDAS" longitudinal to the growth direction in regions of lateral growth as compared to PDAS measurements in transverse sections of axial growth (Figure 6.11). This trend was suggested by Grugel and Zhou, who recommended significant off-axis heat flow as a means to refine dendrite structure [13]. More research is needed to determine the relationship between PDAS and orientation relative to the direction of the thermal gradient.

The variability observed from bar to bar and within a bar at relatively the same thermal conditions has been observed elsewhere in which local measurements at specific locations within a casting were compared to the local thermal field [12]. These data concur with the theories regarding the history dependence of PDAS and proposed stable range of microstructure scale for a given thermal condition [14].

Dendritic structure assessment along the length of the bar demonstrated a complete recovery of axial growth within 30 mm from the top of the wrap. Thus, tertiary arm propagation axially within a lateral growth region and primary-arm competition in an axial growth region are equivalent. At the same time, however, tertiary propagation transverse to the growth direction limits the utility of the typical PDAS measurement as a means to quantify the fineness of dendrite structure. This may require an improved measurement for dendrite scale that can distinguish between a typical coarse structure absent of tertiary arms and a laterally-competing fine structure (Figure 6.7). New dendrite-scale assessments using Voronoi Tesselation techniques may provide a unique insight into these differences in dendritic structure [15].

The importance of the solidification-front inclination angle to transitions in dendrite growth mode was particularly emphasized in this research. The inclination angle can be used as an indication of unstable process conditions, specifically when the inclination angle exceeds 25°. It is important to note that the misorientation of the single crystal relative to the bar axis was not incorporated into the 25° critical inclination angle but is addressed in Chapter 7. In this research, an off-axis misorientation up to 15° was observed.

An alloy dependency of the onset of lateral growth was observed, whereby two different alloys were cast with the same process conditions and formed different dendrite-growth modes. More research is needed to determine what aspects of the alloy properties drive the formation of lateral growth. For the following discussion, it is important to note that

the liquidus of CMSX-486 is 50 °C higher than René N4, and that the alloying elements that provide increased liquidus are associated with slower solute diffusion. Possible explanations for increased propensity for grain nucleation with CMSX-486 are (1) an increased undercooling ahead of the solidification front for dendrites of CMSX-486 due to reduced solute diffusion, (2) decrease in the critical undercooling to cause nucleation, (3) increase of the presence of nuclei in the melt, or (4) strictly increased inclination angle at the surface of the casrting. It is assumed that the diffusion is less in CMSX-486 due to the general trend of reduced solute diffusion with increased liquidus. Based on the work from Chapter 4, the solidus and liquidus temperatures of the alloy strongly influence the position of the solidfication front relative to the position of the floating baffle. For alloys with a reduced liquidus, the steady-state solidification-front position is lower in the furnace, which can lead to a higher inclination angle for the same processing conditions as previously described in Chapter 4. However, in the case of the "above wrap" region, the solidification condition is transient. CMSX-486 exhibited an increased inclination angle compared to Rene N4 for the same process conditions. In any case, more research is needed to investigate the sensitivity of dendrite-growth mode to alloy composition, especially in the case of multi-component alloys.

The conditions under which a nucleated grain is present within the casting have been reported in this Chapter. However, the fundamental mechanisms of grain nucleation were not considered in this effort. A correlation between undercooling and solidification rate could be established but requires more research to determine the critical thermal conditions that cause grain nucleation. Such a correlation should consider the degree of

undercooling based on solute-adjusted diffusion as compared to the alloy-dependent, critical undercooling required to cause grain nucleation. This work suggested that nucleation was occurring due to an increased undercooling in a region ahead of the lateral growth region, especially at the 45° location relative to secondary arms. More research is needed to confirm the presence of an increased undercooling, as this is only a possible explanation for the consistent observations of nucleation at the 45° location relative to the secondary arms and lateral growth preceding grain nucleation.

Overall, lateral growth has been shown to be indicative of thermal conditions approaching those associated to grain nucleation and a complete breakdown in directional solidification. Under these conditions, variability within the process may lead to grain nucleation. Thus, the presence of lateral growth in a component is not preferred, despite the potential refinement in dendrite structure. Process-modeling tools can be utilized to reduce or eliminate the presence of this dendrite morphology through minimization of the solidification-front inclination angle.

Conclusion

- A mold geometry that assessed a broad range of thermal conditions in a single casting was designed and validated.
- A range of dendrite morphology and scale for the experimental conditions was observed, including dendrite morphologies of axial growth with limited and extensive branching, lateral growth and grain nucleation.

- Significant variability in dendrite scale was observed for castings with equivalent process conditions, expressing the need for a means to quantify dendrite scale by measures other than PDAS.
- Complete axial growth was observed in a cross-section above severe lateral growth that grew into the center of the casting, indicating that axial dendritic growth can be recovered from a completely laterally-growing structure without grain nucleation.
- The inclination angle of the solid-liquid interface can be used to predict the onset of lateral growth with a critical angle of 25° and grain nucleation with a critical angle of 45°.
- Lateral growth is indicative of process conditions approaching breakdown of directional dendrite growth.

References

1. M. Meyer ter Vehn, D. Dedecke, U. Paul and P.R. Sahm, *Superalloys 1996*, eds. R.D. Kissinger, D.J. Dye, D.L. Anton, A.D. Cetel, M.V. Nathal, T.M. Pollock and D.A. Woodford (The Minerals, Metals & Materials Society, 1996) 471-479.
2. W. Wang, A. Kermanpur, P.D. Lee and M. McLean, *J Mater Sci*, 38 (2003) 4385-4391.
3. U. Paul and P.R. Sahm, *Mat Sci Eng A*, 173 (1993) 49-54.
4. A. Kermanpur, N. Varahram, P. Davami and M. Rappaz, *Metall and Mater Trans B*, 31 (2000) 1293-1304.
5. X.L. Yang, H.B. Dong, W. Wang and P.D. Lee, *Mat Sci Eng A*, 386 (2004) 129-139.
6. N. D'Souza, P.A. Jennings, X.L. Yang, H.B. Dong, P.D. Lee and M. McLean, *Metall Trans B*, 36 (2005) 657-666.

7. K. Harris and J.B. Wahl, *Superalloys 2004*, eds. K.A. Green, T.M. Pollock, H. Harada, T.E. Howson, R.C. Reed, J.J. Schirra and S. Walston (The Minerals, Metals & Materials Society, 2004) 45-52.

8. E.W. Ross and K.S. O'Hara, *Superalloys 1996*, eds. R.D. Kissinger, D.J. Dye, D.L. Anton, A.D. Cetel, M.V. Nathal, T.M. Pollock and D.A. Woodford (The Minerals, Metals & Materials Society, 1996) 19-25.

9. C.H. Konrad, M. Brunner, K. Kyrgyzbaev, R. Volkl and U. Glatzel, *J Mat Proc Tech.*, (2010), in press.

10. J.D. Hunt, *Solidification and Casting of Metals*, ed. J.D. Hunt (London: The Metals Society, 1979), 3-9.

11. W. Kurz and D.J. Fisher, *Acta Metall*, 29 (1) (1981) 11-20.

12. C. Brundidge, J.D. Miller and T.M. Pollock, unpublished research, 2010.

13. R.N. Grugel and Y. Zhou, *Metall Mater Trans A*, 20 (1989) 969-973.

14. W. Wang, P.D. Lee and M. McLean, *Acta Metall*, 51 (2003) 2971-2987.

15. C. Brundidge, D. VanDrasek, B. Wang and T.M. Pollock, unpublished research, 2010.

CHAPTER 7

DIFFUSIONAL-GROWTH MODELING OF LATERAL OVERGROWTH OF DENDRITES DURING SOLIDIFICATION VIA LIQUID METAL COOLING

Directional solidification via the liquid metal cooling (LMC) process results in refined microstructure and defects, thus providing improved mechanical performance of single crystal (SX) materials. However, the enhanced heat extraction inherent to the process results in a curved solidification front that may lead to non-axial growth of dendrites near the casting walls. The mechanism by which the lateral growth occurs has been investigated by microstructure modeling via solute-adjusted, diffusional-growth modeling of dendrites. Local thermal profiles derived from continuum solidification models have been used as input to a dendrite-growth model capable of simulations in both 2D and 3D simulations. A finite difference (FD) calculation of the diffusion field and a cellular automata (CA) calculation for the growth of the dendrite front are coupled for prediction of the microstructure evolution during directional solidification. Model predictions were compared to experimentally-observed dendritic structures. In addition, a parametric analysis was conducted to evaluate the sensitivity of dendrite-growth mode to changes in thermal, structural (such as dendrite position and spacing) and model parameters. The inclination angle of the solidification front strongly influenced the evolution of dendritic structure. The degree of misorientation from the [001] single crystal orientation from the withdrawal axis significantly contributed to the onset of lateral dendritic growth.

Introduction

The liquid metal cooling (LMC) process is based on the concept of the Bridgman process for directional solidification [1-3] but utilizes a liquid-metal coolant to extract heat from the mold more efficiently [4-7]. The benefits of the process have been identified, especially for large cross-section components requiring significant heat extraction to maintain directional solidification [5-14]. Despite the benefits of the process, the potential for lateral growth is increased, as discussed in Chapter 6. Lateral growth is the overgrowth of well-aligned primary dendrite arms by secondary arms of neighboring dendrites growing transverse to the withdrawal direction, as shown in Figure 1.4b and described in Chapter 6. Further understanding of the mechanism for the onset of lateral growth is needed as related to local thermal conditions, independent of mold geometry.

The evolution of dendrite growth has been modeled extensively over the past few decades. Several dendrite growth models utilizing phase field [15,16], dendrite grain envelope [17,18], level set [19-24] and cellular automata [25-44] techniques have been developed. One weakness of these models is the limitation of model size and time scale, due to their computational expense [45]. Additionally, the ability to associate dendrite-growth predictions to experimental observation limits their widespread acceptance. Investigation of multi-component engineering alloys is a further challenge due to the order-of-magnitude increase in computation time and difficulty obtaining the appropriate alloy properties.

Experiments utilizing a transparent polymer analog were conducted to study the evolution of dendritic structure [46-56]. Grugel and Zhou considered off-axis heat flow relative to the dendrite-growth direction and identified changes in primary dendrite arm spacing with off-axis heat flow. They observed the onset of lateral growth at a solidification-front inclination angle of 45° [46]. Other efforts also evaluated off-axis growth of dendrites through utilization of the polymer analog [47]. While these experiments were valuable with respect to understanding the mechanisms of dendrite growth, the thermal environment in which they were conducted was not directly representative of an investment casting environment typically employed for growth of single crystals.

Likewise, modeling the evolution of dendritic growth at the scale of the dendritic structure in the presence of thermal conditions representative of the investment casting environment is also less common than the uniformly imposed thermal conditions representative of a laboratory environment [8]. In addition, validation of model predictions of dendrite growth with experimental measurement under processing-representative conditions is rare [8,10]. Simulation of the thermal characteristics of the LMC process at the continuum scale have demonstrated the value of modeling in conjunction with careful experimentation as demonstrated in Chapters 4 and 5 [10,11,57]. However, no dendrite-scale modeling has yet been conducted with consideration of the unique thermal characteristics of this process.

Results from Chapter 6 highlighted the importance of the solidification-front inclination angle at the surface of the mold. Prediction of lateral growth and the presence of nucleated grains was primarily based on the thermal field at the component scale. However, the evolution of dendritic structure is controlled by solute diffusion at the solid-liquid interface [45]. Thus, there is a need to consider the thermosolutal kinetics of directional solidification at the scale of the dendrite structure under complex thermal conditions that depart from the ideal model of axial heat extraction during directional solidification. This information could provide key insights to the mechanisms associated with transitions in the mode of dendritc growth and instabilities that lead to the breakdown of the directional solidification process. Based on the understanding at the microstructure scale, macroscopic criteria functions for the component scale could be enhanced by a better understanding of the underlying mechanisms. With utilization of the LMC process, there may be a need for new defect-formation criteria to aid indentifying preferred process conditions and prediction of dendritic scale.

The well-studied mechanisms of competitive dendrite growth [58-62] have demonstrated that the dendrite whose primary orientation is better aligned with the direction of the thermal gradient overgrows less-favorably-aligned neighboring dendrites. However, these studies have not considered the presence of a non-axial thermal field in relationship to the crystallography of the dendrite, which could have significant implications to the reduction of defect structure in complex, single-crystal casting configurations. Preliminary evaluation of the competition between misoriented dendrites is needed to assess if further research is warranted.

In this research, thermal conditions from continuum solidification models reported in Chapter 6 are used as input to a microstructure model that predicts dendrite structure from solute-diffusion and the thermal field. Due to the accompanying experimental observations previously reported, evaluation of a model that incorporates continuum-scale thermal predictions with meso-scale evolution of solute and dendrite structure is possible. Conditions under which lateral growth occurs are identified. Fundamental insights to the mechanism that promotes lateral growth are also evaluated with a parametric analysis.

Modeling Methods

The modeling approach consists of a finite difference (FD) calculation of the diffusion field and a cellular automata (CA) calculation for the growth of the dendrite front. These calculations are coupled for prediction of the evolution of dendrite growth during solidification. An array of dendrites are modeled in a local thermal field representative of thermal conditions predicted by ProCAST^{TM} for the set of experiments from Chapter 6. The parallel experimental observations from directional-solidification experiments together with dendrite-scale modeling suggest a mechanism for transition of dendritic-growth mode. For reference, the thermal conditions and dendrite morphology from the Chapter 6 are summarized (Table 7.1).

Table 7.1 – Predicted thermal conditions - thermal gradient, solidification rate and solidification-front inclination angle - for use as input data for microstructure model.

Thermal Gradient (°C/cm)	Solidification Rate (10^{-2} cm/s)	Inclination Angle (°)	Expeirmental Observation
106	1.5	6	Axial Growth
103	1.6	7	Axial Growth
101	1.6	9	Axial Growth
100	1.6	10	Axial Growth
116	2.1	15	Axial Growth
81	2.1	16	Axial Growth
102	2.4	23	Lateral Growth
112	2.6	24	Axial Growth
72	2.4	25	Lateral Growth
102	2.5	25	Lateral Growth
98	2.6	27	Lateral Growth
71	2.4	29	Lateral Growth
76	2.5	31	Lateral Growth
70	2.4	32	Lateral Growth
91	3.3	38	Lateral Growth
89	3.5	42	Lateral Growth
66	2.5	45	Lateral Growth
83	3.8	48	Lateral Growth
59	2.8	52	Lateral Growth
62	2.8	58	Grain Nucleation
56	2.8	63	Grain Nucleation
60	2.9	72	Grain Nucleation
60	3.1	77	Grain Nucleation
63	3.3	84	Grain Nucleation

Microstructure modeling during solidification was performed with the μMatIC software, developed by Lee and coworkers [26-43]. This model has been utilized extensively for prediction of dendrite scale and evolution of dendrite growth. It was utilized due to its capability to model a relatively large domain, consisting of several dendrites in 3D, relatively long time scale on the order of minutes and short computation time of hours or days compared to other models in this class. This model calculates a solute-adjusted

undercooling in the melt and subsequently calculates diffusional growth of the dendrite. Anisotropy is maintained with a decentered square (2D) or decentered octahedron (3D) adjustment to the diffusion calculation.

The primary calculations utilize well-documented transport, phase diagram and dendrite growth relationships which have been well documented [27,35-39]. The modeling domain is divided into an array of cells of a pre-defined size in which solute diffusion and dendrite growth are calculated. This allows for simplification of the calculations since each cell possesses a single value for each of the parameters used in the calculation. A time scale is introduced to the model by utilization of a time step, an increment of time for which the calculations are performed. This model utilizes a numerical-modeling scheme, so information about adjacent cells at the current time step and values at the current cell from previous time steps are used for the calculations within a cell at the current time step.

A linearized binary phase diagram is used to predict changes in the liquid composition during solidification (Figure 7.1a). A constant partition coefficient, *k*, is assumed, thus resulting in a simplified partition coefficient equation (Equation 7.1).

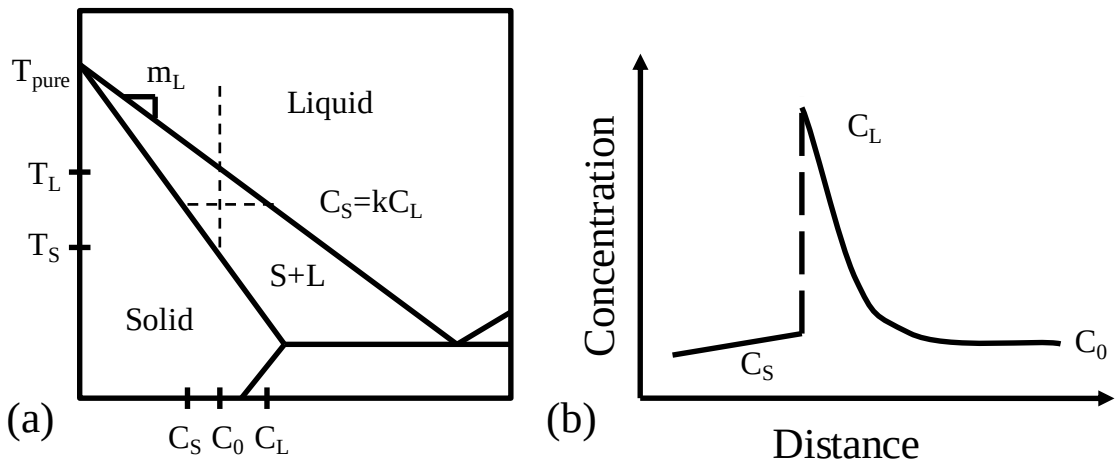

Figure 7.1 – Schematic description of a (a) linearized binary phase diagram and (b) concentration profile through phase transformation, assuming no diffusion in the solid and complete mixing in the liquid.

$$\boldsymbol{C_S = kC_L} \tag{7.1}$$

C_S and C_L are the concentrations of the solid and liquid, respectively. For the alloys investigated, k is less than 1.0 indicating the rejection of solute during solidification, causing an increased concentration of solute ahead of the solidification front (Figure 7.1b). The average concentration, C, within a cell arises from conservation of solute as in Equation 7.2.

$$\boldsymbol{C = C_L(1 - f_s) + C_S f_s} \tag{7.2}$$

In this equation, f_s is the fraction solid of the cell. Time-dependent concentration can be described by Fick's second law (Equation 7.3).

$$\boldsymbol{\frac{\partial C}{\partial t} = \nabla(D_E \nabla C_L)} \tag{7.3}$$

D_E is the equivalent diffusivity calculated according to a rule of mixtures (Equation 7.4).

$$\boldsymbol{D_E = (1 - f_s)D_L + f_s D_S} \tag{7.4}$$

D_L and D_S are the diffusion coefficients of the liquid and solid, respectively. Equations 1-4 set the basis for the governing equations. The concentration of the liquid at the solid-liquid interface is calculated first, for cells containing both solid and liquid, according to Equation 7.5.

$$C_L = C_L^* - \frac{(1-f_s)}{2}\Delta x G_C \tag{7.5}$$

Kinetic undercooling is ignored because its magnitude is much smaller than the contributions of either the curvature or the constitutional undercooling for conventional castings. The last term is used to account for use of data from the previous step. The fraction solid in this case is calculated from the previous time step, Δx is the cell size, G_C is the concentration gradient calculated from the previous time step and C_L^* is the liquid equilibrium concentration (Equation 7.6), which is based on the linearized phase diagram (Figure 7.1a).

$$\boldsymbol{C_L^* = C_0 + \frac{1}{m_l}\left(T_{liq}^0 - \Gamma\kappa - T\right)} \tag{7.6}$$

C_0, the intial concentration, and m_l, the slope of the liquidus line, are defined from the phase diagram, while T_{liq}^0 is the initial liquidus of the base alloy. There is also a term that accounts for the curvature of the solid-liquid interface and includes Γ, the Gibbs-Thomson coefficient, and κ, the curvature, calculated according to Equation 7.7 [63].

$$\kappa = \frac{1}{\Delta x}\left[1 - \frac{2}{N+1}\left(f_s + \sum_{j=1}^{N} f_s^j\right)\right] \tag{7.7}$$

In this equation, *N* is the number of nearest neighbors. This curvature estimation utilizes a nearest neighbor counting methodology, whereby the curvature of the solid-liquid interface at the position of one cell can be calculated by the relative number of nearest neighbors that are solid. The contribution of the curvature term to the overall liquid equilibrium concentration is small, so error in the calculation does not significantly affect

the model predictions. Once the concentration in the liquid is determined, the fraction solid is calculated by substituting Equation 7.1 into Equation 7.2, taking the derivative and equating to Equation 7.3, thus resulting in Equation 7.8.

$$C_L(1-k)\frac{\partial f_s}{\partial t} = -\nabla(D_E \nabla C_L) + [1-(1-k)f_s]\frac{\partial C_L}{\partial t} \tag{7.8}$$

A finite difference method is employed to numerically determine the fraction solid for cells containing both solid and liquid. In addition, the concentration in the liquid is calculated for cells that are entirely solid or liquid according to this equation. Finally the growth of the dendrites is governed by a decentered square (2D) or decentered octahedron (3D), as developed by Gandin and Rappaz [28] and defined by Equations 7.9 and 7.10, where ΔL is the change in the half diagonal of the square (Equation 7.9) or octahedron (Equation 7.10).

$$\Delta L = \sqrt{2} \cdot \Delta x \cdot \Delta f_s \tag{7.9}$$

$$\Delta L = \sqrt{3} \cdot \Delta x \cdot \Delta f_s \tag{7-10}$$

The thermal conditions within the domain, an initial dendrite array and material parameters are required as input data. The initial dendrite array is input by specifying the position of fixed nuclei on the bottom of the simulation domain with solidification proceeding upwards. The thermal conditions are input as a thermal gradient and solidification rate as a function of time and the isotherm shape as a function of space and time. In this case, the solidification rate is the rate at which the temperature profiles proceed through the simulation domain. Under steady state conditions, the dendrite growth velocity is equal to the velocity of the temperature profiles. Material parameters include the initial solute concentration, liquid-phase solute diffusivity, solid-phase solute

diffusivity, slope of the liquidus line from the binary phase diagram, partition coefficient, pure melting temperature, alloy liquidus temperature and alloy solidus temperature. These input parameters are based on a Ni-Ta binary system, based on previous research that associated experimental concentration profiles to predictions of solute concentration [33]. Time-dependent fraction solid, solute concentration and undercooling contours are output for analysis.

Relevant to this effort, the solidification-front inclination angle, thermal gradient and solidification rate were the input thermal conditions for 24 microstructure models based on thermal simulations of the experimental castings at specific times and locations within the casting domain. PDAS measurements at specific locations in representative castings were used to define the initial dendrite spacing. Material parameters were taken from a previous effort for a representative binary for René N4 (Table 7.2) [33]. Model predictions were compared to experimental observations of dendrite-growth stability from Chapter 6.

Table 7.2: Model parameters for CA-FD-based microstructure modeling [64].

Parameter	Value	Parameter	Value
Cell Size	5.0×10^{-6} m	Liquidus Temperature	1387 ºC
Time Step	1.0×10^{-4} s	Liquidus Slope	-4.74 K(wt%)$^{-1}$
Initial Temperature	1386 K	Partition Coefficient	0.68
Initial Concentration	6.5 wt %	Diffusion Coefficient in the Liquid	1.0×10^{-9} m^{2}s^{-1}
Primary Arm Spacing	205 µm	Diffusion Coefficient in the Solid	5.0×10^{-13} m^{2}s^{-1}

The parametric analysis was conducted to evaluate the model parameters that affected the propensity for lateral growth. A total of 300 different 2D model conditions and 125 3D model conditions were evaluated. The deviation of each model parameter from a baseline was assessed. The baseline configuration is defined in Table 7.3. In addition, hypothetical process conditions either based on maximum and minimum thermal conditions from experiment or with a 50 pct difference above and below the baseline parameter value were simulated in order to evaluate the role of each process parameter independently (Table 7.3). These parameters include thermal gradient, solidification rate, inclination angle of the solidification front, temperature perturbation, off-axis misorientation, dendrite spacing and spacing of the first dendrite from the wall, referred to as dendrite-wall spacing.

Table 7.3 – Baseline model parameters and investigated values for parametric analysis.

Parameter	Units	Baseline	Low	High
Thermal Gradient	°C-cm^{-1}	60	30	120
Solidification Front	cm-s^{-1}	0.028	0.014	0.042
Thermal Perturbation	°C	None	-10	10
Off-Axis Misorientation	°	1	Ranging from -16 to 14	
Paritition Coefficient		0.68	0.1, 0.5	0.9
Primary Dendrite Arm Spacing	μm	205	100	310
Dendrite-Wall Spacing	μm	100	50	150
3D Misorientation	°	in-plane	out-of-plane	
Packing Configuration		Square	Hexagonal	
Numerical Noise		0.05	0.01	0.10
Spatial Step	μm	5	1	10, 20
Time Step	1x10^{-4} s	5	1	10

A sensitivity analysis was also conducted to evaluate numerical features of the model, including cell size, time step and numerical noise (Table 7.3). A 2D model was utilized

for the each of the thermal conditions predicted. A smaller number of three-dimensional models were performed on select model conditions to evaluate the effect of a 3D diffusion field. Specifically, square and hexagonal packing of the dendrites and secondary orientation were evaluated using the 3D model.

A schematic of the CAFD model is shown (Figure 7.2a). The size of the two-dimensional model domain was 825 μm wide by 25 mm tall. An initial dendrite spacing of 205 μm was used with a 100 μm distance between the wall and first dendrite, thus resulting in the evaluation of four in-plane dendrites. The left side of the domain was modeled as the wall of the casting domain with a solidification front inclined at an angle ϕ relative to horizontal (Figure 7.2a). Periodic boundary conditions were applied to the third dimension. The relatively tall height of the model allowed the simulation to reach a steady-state growth condition.

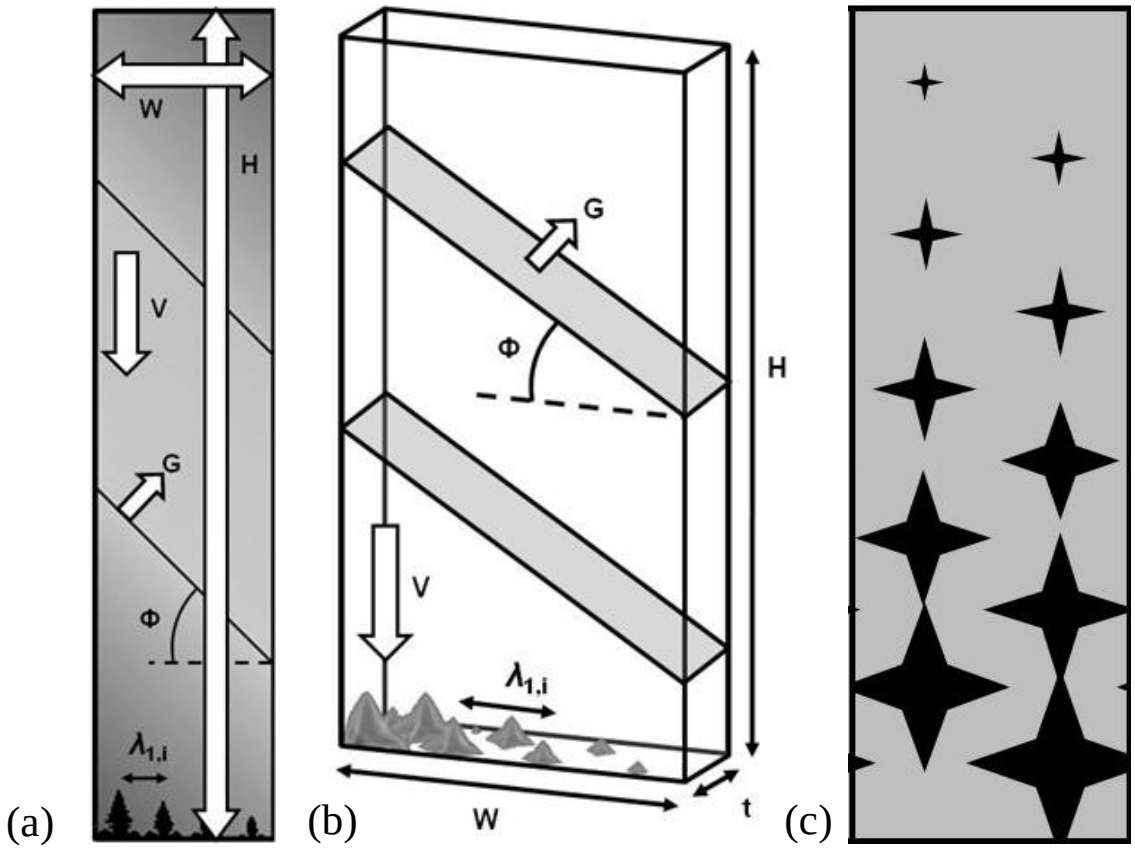

Figure 7.2 – Schematics of CAFD model, (a) 2D setup, (b) 3D setup and (c) view transverse to the growth direction depicting a hexagonal packing with through-thickness periodic boundary condition.

For the case of the three-dimensional model, two dimensions were the same as the 2D model with a through-thickness dimension equivalent to two rows of dendrites, which was 410 and 355 μm for square and hexagonal packing, respectively (Figure 7.2b-c). In these models, 8 dendrites were evaluated. The left side of the domain remained a simulated wall with an inclined solidification front imposed by a plane inclined in one dimension. A periodic boundary condition was applied to the third dimension as in the 2D model. All other model parameters were the same.

Two additional modeling investigations were conducted: (1) the effect of a parabolic curvature of the solidification front on dendrite growth and (2) the competition between neighboring dendrites of different crystallographic orientation. The "parabolic curvature" study (1) modeled a curved interface representative of the curvature observed from casting surface to center. This 2D model utilized a domain size in which the width of the model was the radius of the bar castings from Chapter 6. The "relative misorientation of dendrites" study (2) was performed to evaluate competition mechanisms of dendrite growth in the presence of a non-axial thermal field. This study required an increased width of the model to ensure insensitivity to the initial number of dendrites.

Comparison of Dendrite-Growth Predictions and Experimental Observations

Models were analyzed for the presence of lateral growth by evaluation of the fraction-solid evolution and the dendrite structure. Axial growth was characterized by the absence of competition among the dendrites (Figure 7.3a and c). Lateral overgrowth was observed in the model when a single dendrite overgrew its neighbors from the simulated wall to center (Figure 7.3b). Partial overgrowth was defined as the overgrowth of one but not all dendrites toward the simulated center of the domain. In the case of the 3D model, overgrowth had to be present in both planes of dendrites in order to be characterized as lateral overgrowth (Figure 7.3d). Otherwise, partial overgrowth was recorded. From this information, the propensity for lateral overgrowth was evaluated for the experimental conditions and parametric analysis.

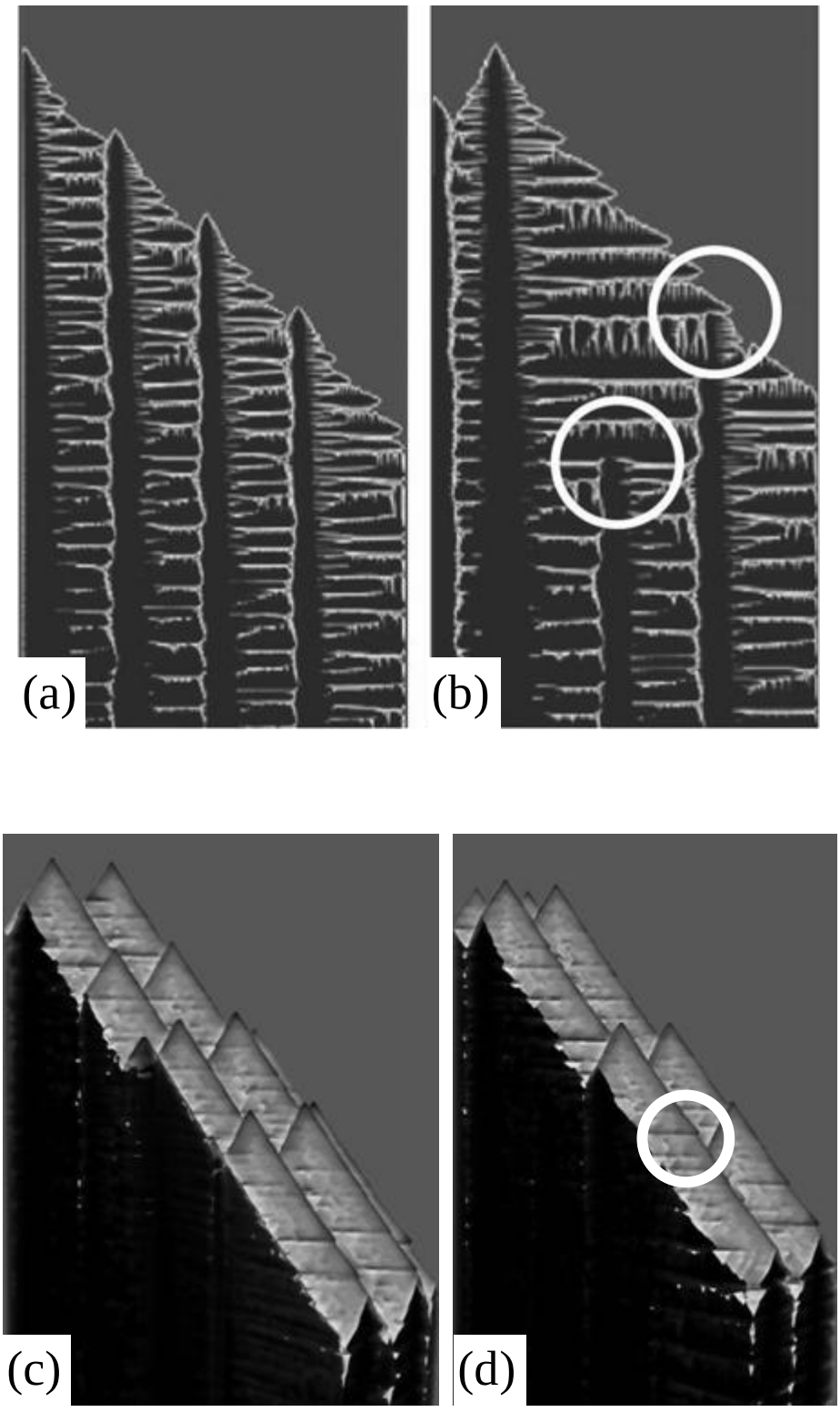

Figure 7.3 – Predicted dendrite growth modes from diffusional-growth modeling in 2D and 3D, (a) 2D axial-growth, (b) 2D lateral-growth, (c) 3D axial-growth and (d) 3D lateral-growth predictions. Lateral-growth events are circled for emphasis.

Results of simulations for the range of thermal conditions in Table 7.1 were compared to the corresponding experimentally-observed dendrite growth modes, axial or lateral growth. Results were assessed for (1) qualitative agreement based on trends of imposed thermal conditions and (2) quantitative agreement of the onset of lateral growth (Figure 7.4).

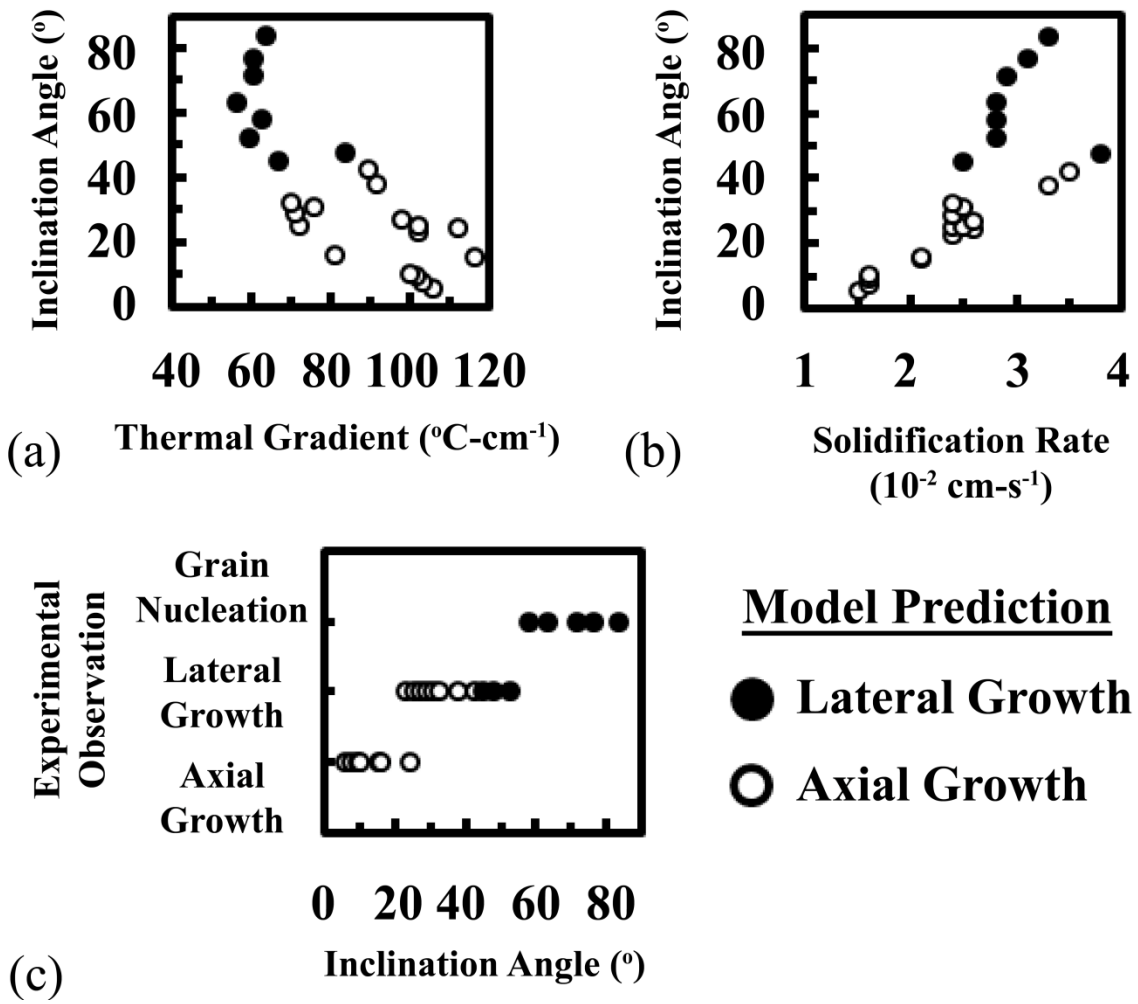

Figure 7.4 – Dendrite growth model predictions of dendrite-growth mode as a function of (a) input thermal conditions and (b) experimental observations.

The interdependence of the thermal field characteristics, as discussed in Chapter 6, complicated the determination of the critical parameter for lateral growth.
In general, an increase in the solidification-front inclination angle decreased the axial thermal gradient and increased the solidification rate. These observations demonstrated that the thermal field within the casting is such that the thermal gradient, solidification rate and solidification-front inclination angle are interdependent. In other words, one of the three thermal parameters could not have been varied independently of the others to obtain a different thermal condition.

A strong trend for propensity for lateral growth was observed with increasing inclination angle, while no trend was observed for either thermal gradient or solidification rate (Figure 7.4). These trends are further assessed during the parametric analysis. Thus, a critical solidification-front inclination angle was deduced, whereby the presence of a solidification-front inclination angle below the value indicated axial growth (white circles), while an angle equal to or above that value indicated the presence of lateral overgrowth (black circles) (Figure 7.4).

Experimentally, the onset of lateral growth occurred at a solidification-front inclination angle of 25°, while the model did not predict lateral growth until 45°. Additional parametric analyses were evaluated for explanation of this discrepancy. The occurrence of grain nucleation was observed experimentally at higher inclination angles but was not considered in this modeling effort, as grain nucleation was suppressed in the model due to lack of realistic input parameters for the nucleation model.

Parametric Analysis of Propensity for Lateral Growth

Parametric analysis indicated a sensitivity of dendrite growth mode to changes in thermal, microstructural and model parameters (Figure 7.5). As indicated by the experiments and confirmed by the parametric analysis, the propensity for lateral growth is insensitive to axial thermal gradient (Figure 7.5a). The onset of lateral growth was also insensitive to PDAS and dendrite-wall spacing (Figure 7.5b-c). A significant increase in solidification rate caused lateral growth to occur at a solidification-front inclination angle 1° less than the baseline (Figure 7.5e). This change in critical inclination angle was attributed to a change in the shape of the dendrite tip. As the solidification rate increased, the length of the dendrite tip (before the first coarsened secondary arm) decreased, allowing the secondary arm to compete with the dendrite tip of the neighboring dendrite at lower inclination angle (Figure 7.6). However, a 50 pct increase in solidification rate resulted in only a 1° reduction in critical inclination angle. Therefore, the propensity for lateral growth was relatively insensitive to axial thermal gradient and solidification rate but highly sensitive to solidification-front inclination angle, thus confirming the results from the comparison to experimental observations in the previous section.

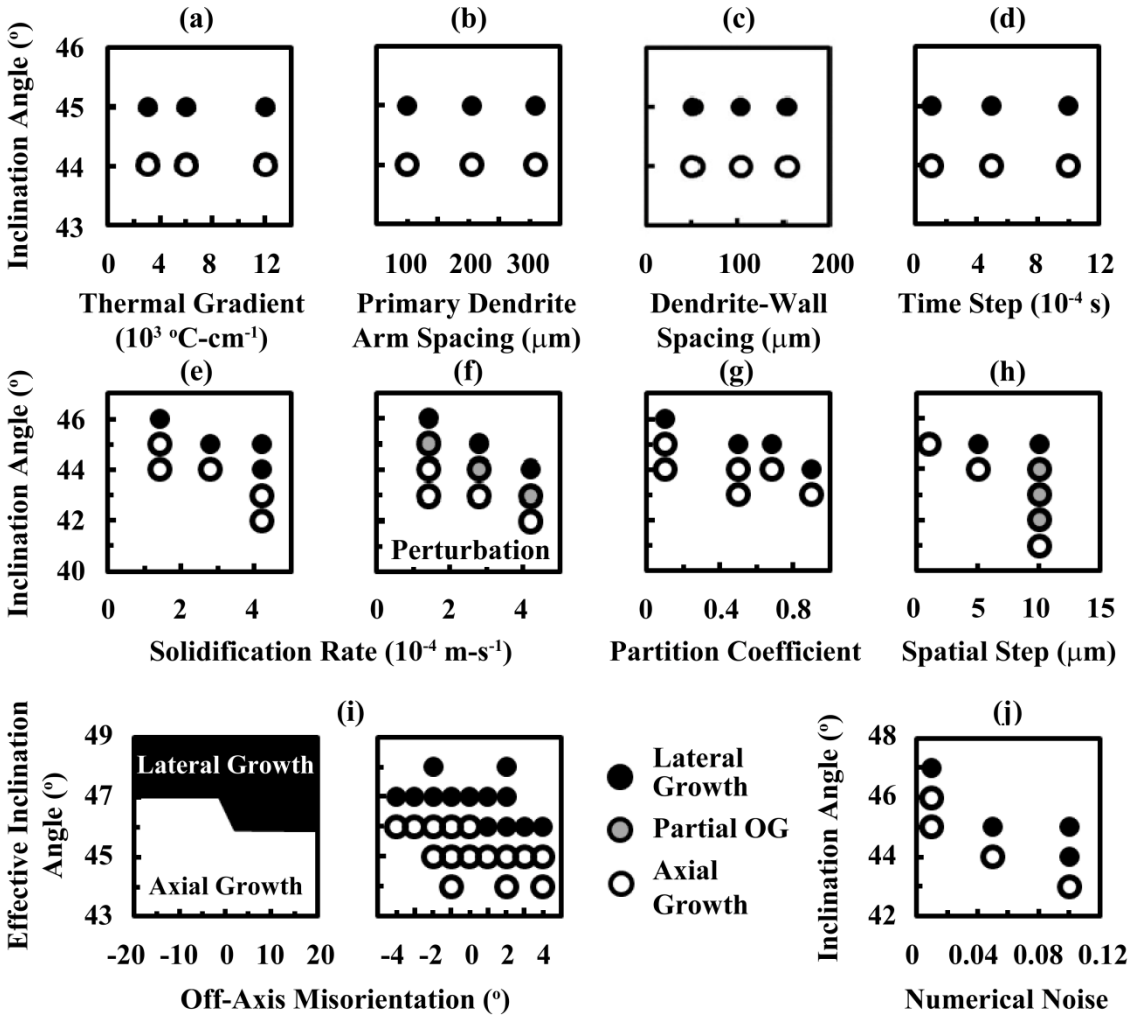

Figure 7.5 – Sensitivity of 2D prediction of onset of lateral growth to (a) thermal gradient, (b) PDAS, (c) dendrite-wall spacing, (d) time step, (e) solidification rate, (f) +/- 10°C thermal perturbation, (g) partition coefficient, (h) spatial step, (i) off-axis misorientation and (j) numerical noise.

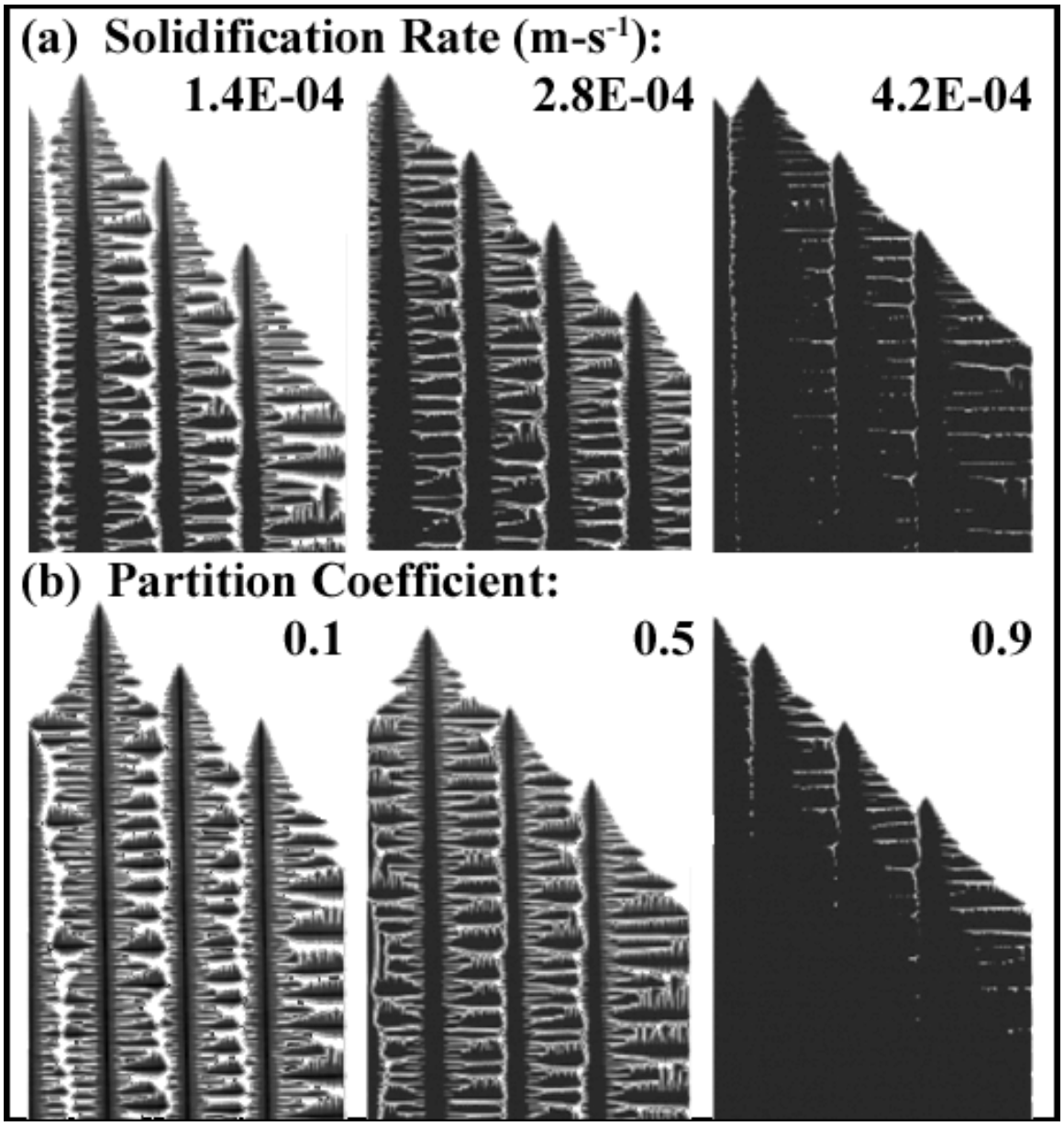

Figure 7.6 – Dendrite-growth predictions indicating a change in dendrite-tip shape from changes in the (a) thermal (solidification rate) and (b) solutal (partition coefficient) fields.

A thermal perturbation was applied to the model domain in order to emulate a perturbation in the thermal conditions arising from imperfections in the investment casting process. When a thermal perturbation of +/- 10°C was applied to the solidification front, the critical solidification-front inclination angle was 44°, regardless

of solidification rate (Figure 7.5f). Thus, the critical inclination angle is relatively insensitive to perturbations of the thermal field.

The partition coefficient of the binary was parametrically evaluated at values of 0.1, 0.5 and 0.9 compared to a baseline value of 0.68. An increase in the critical inclination angle was observed with a decrease in the partition coefficient, ranging from a critical inclination of 44 for a partition coefficient of 0.9 and a critical inclination angle of 46 for 0.1 (Figure 7.5g). The difference was attributed to a lengthening of the dendrite tip with decreasing partition coefficient (Figure 7.6b). Thus, changes to the thermal and solutal fields affected the shape of the dendrite tip which slightly changed the propensity for lateral growth. Since 2° was not considered significant, the critical inclination angle is insensitive to wide variations in partition coefficient.

A parametric analysis of the numerical features of the model was performed to demonstrate the validity of model predictions. The critical inclination angle is insensitive to time step (Figure 7.5d). Large variations of spatial step, or cell size, ranging by up to an order of magnitude between the smallest and largest cell size only caused variation of the critical inclination angle by +/- 1° (Figure 7.5h). Numerical noise at the solidification front was used in the model to promote secondary arm nucleation (Figure 7.5j). The value can be associated to a random increase or decrease in the fraction solid of each cell, not to exceed the noise parameter value. The propensity to form lateral growth with changes in this parameter indicated a trend of reduced critical inclination angle for increase in numerical noise. However, an order of magnitude increase in the numerical

noise resulted in only a 2° decrease in the critical inclination angle. Thus, moderate changes in the model parameters did not significantly affect prediction of the critical inclination angle.

Predictions of the sensitivity of the critical inclination angle to off-axis misorientation of the single crystal were also evaluated with 2D models. The results indicated a one-to-one correspondence of reduced critical inclination angle with increased off-axis misorientation (Figure 7.5i). To demonstrate this relationship, the *effective inclination angle* (ϕ*) relative to the crystal structure was evaluated (Figure 7.7). In this construct, the inclination angle of the solidification front was its angle relative to the secondary arm orientation. For instance, a 10° off-axis single crystal in which the primary orientation is directed toward the wall had a critical inclination angle of 35° relative to horizontal, which corresponds to an effective inclination angle of 45°.

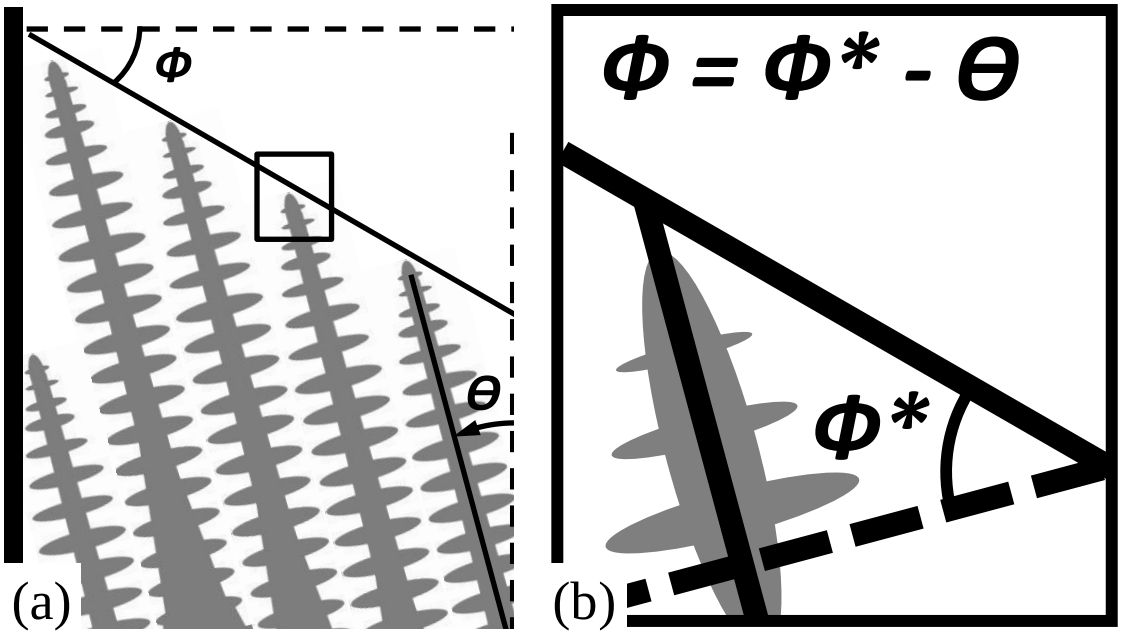

Figure 7.7 – Decrease in the critical solidification-front inclination angle (ϕ) with increase in single-crystal off-axis misorientation (θ). Note: The angle of the solidification front in (100), ϕ*, was approximately 45°.

Diverging dendrites in which primary orientation is pointed inward from the wall, were represented by negative off axis misorientations in this construct. For diverging off-axis misorientations, the effective inclination angle that caused lateral growth was 48° (Figure 7.5i). For example, a 10 degree off-axis misorientation diverging from the wall caused an increase in the critical inclination angle to 58° (Figure 7.8a). Thus, increasing the divergence of the dendrite relative to the wall increased the critical inclination angle.

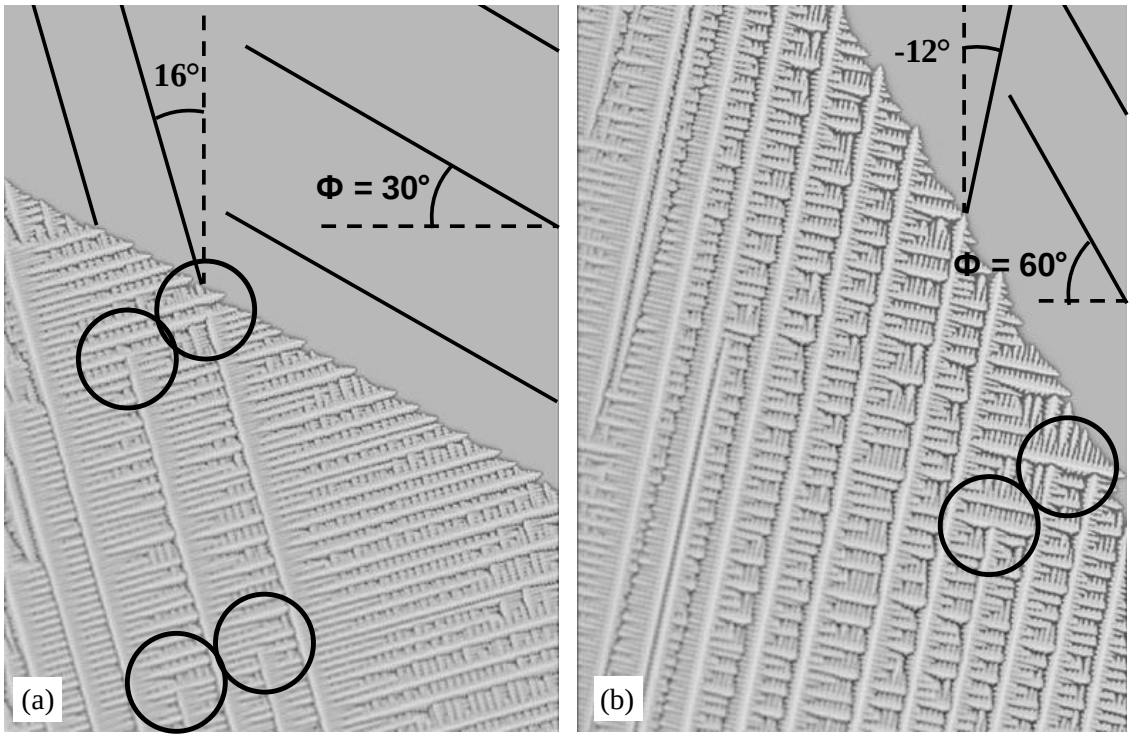

Figure 7.8 – Dendrite growth model predictions for single crystals with (a) 16° wall-converging off-axis misorientation and 30° inclination angle and (b) 12° wall-diverging off-axis misorientation and 60° inclination angle. Lateral-growth events have been circled.

Conversely, converging dendrites, represented by positive off-axis misorientations, resulted in an effective inclination angle of 45° in order to cause lateral growth (Figure 7.5i-j). Therefore, increasing the misorientation of a converging dendrite reduced the critical inclination angle by one degree for every degree misoriented (Figure 7.8b). Castings with an off-[001] crystal have the dendrites converging toward the surface somewhere within the casting. Thus, any misorientation of the single crystal results in a reduction of the critical inclination angle somewhere on the casting surface.

Overall, 2D modeling demonstrated that the critical inclination angle was most sensitive to changes in off-axis misorientation. It was shown that an inclination angle of 45°

relative to the secondary arm orientation in the {100} plane of the single crystal caused lateral growth (Figure 7.8). This parameter is discussed further regarding three-dimensional misorientation relative to the sample orientation.

The sensitivity of 3D predictions of the onset of lateral growth to changes in thermal, microstructural, and model parameters were also evaluated (Table 7.4). Each parameter was investigated independently with all other parameters equal to their baseline values. The critical inclination angle was reduced from 45° to 41°. This difference was likely due to assumptions made in the 2D diffusion-field calculations and effect of increased spatial step.

Table 7.4 – 3D model predictions for the sensitivity of critical inclination angle to thermal, structural and model conditions. "L" and "A" designate lateral and axial growth, respectively. The baseline condition has been highlighted with a dark background.

Parameter		1° Off-Axis Misorientation		Packing Configuration		Dendrite Spacing (μm)		Wall-Dendrite Spacing (μm)		Thermal Gradient (°C-cm^{-1})		Solidification Rate (10^{-2} cm-s^{-1})		Spatial Step (5μm)	
Value		in-plane	out-of-plane	Square	Hex	100	310	100	310	100	310	1.4	4.2	Square	Hex
Inclination Angle (°)	44	L	L	L	L	L	L	L	L	L	L	L	L	L	L
	43	L	L	L	L	L	L	L	L	L	L	L	L	L	A
	42	L	L	L	A	L	L	L	L	L	L	L	L	A	A
	41	L	A	L	A	L	L	L	L	L	L	L	L	A	A
	40	A	A	A	A	A	A	A	A	A	A	A	A	A	A

Thermal gradient and solidification rate had no effect on the critical inclination angle. Likewise, dendrite spacing and wall-dendrite spacing had no effect on critical inclination angle. Changing the direction off the off-axis misorientation from in-plane to out-of-plane increased the inclination by 1°. This result was consistent with the effective inclination angle discussed previously (Figure 7.7). The packing configuration changed the altered the critical inclination angle by 2°. A two-fold decrease in the spatial step

increased the critical inclination angle by 1-2° depending on packing configuration. This result was consistent with the findings in the 2D model, in which the critical inclination angle at a spatial step of 10μm was 2° less than the critical inclination angle for a 5μm spatial step. Thus, the critical inclination angle for 3D is 43-44°. Relative to the predictions of inclination angle obtained from continuum solidification modeling (Table 7.1), a 2° change in the critical inclination angle had no effect on the dendrite growth mode predictions (Figure 7.4). No lateral growth was observed at an inclination angle of 40°.

The 3D misorientation of the single crystal relative to the growth direction had a significant effect on inclination angle but was a more complex relationship than the "one-to-one" correspondence observed in the 2D models. Consideration of the 3D misorientation utilized the approach previously discussed: an inclination angle of 45° or higher relative to the secondary arm orientation in the {100} plane caused lateral growth. By using standard rotation matrices for a cubic-crystal system, all symmetrically-unique single-crystal misorientations in 5 degree increments of the Euler angles were evaluated with a solidification-front inclination angle ranging from -45° to 45°. The solidification-front inclination angle that caused a critical inclination angle of 45° relative to the secondary-arm orientation in the {100} plane of the single crystal was plotted as the intensity on a pole-figure map (Figure 7.9a). In addition, this solidification-front inclination angle was plotted against the off-axis misorientation of the crystal relative to the sample orientation (Figure 7.9b). Simple misorientations were also plotted for

comparison. Select model conditions were evaluated to test this theory and were consistent within 1° for the critical inclination angle.

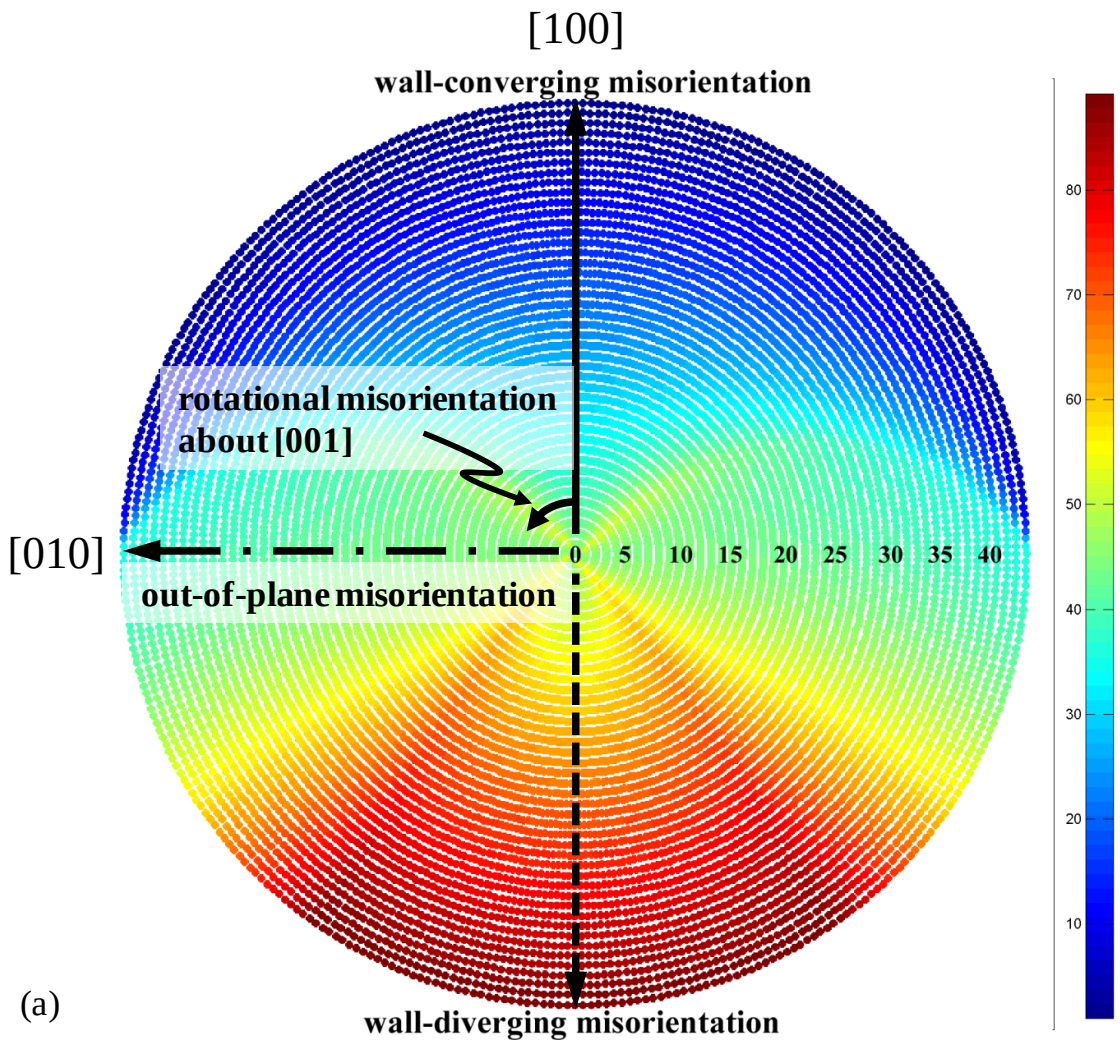

(a)

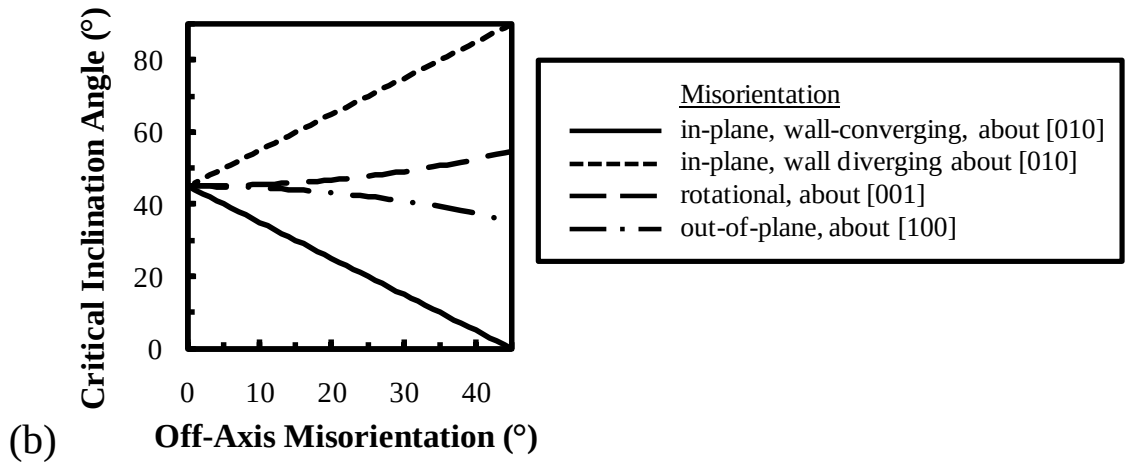

(b)

Figure 7.9 – Sensitivity of 3D prediction of onset of lateral growth to SX dendrite misorientation: (a) pole figure map with critical solidification-front inclination angle plotted as intensity and (b) critical solidification front inclination angle as a function of off-axis misorientation.

From this thought experiment, it was determined that an in-plane misorientation, - relative to the solidification-front inclination angle, in other words converging and diverging dendrites relative to the wall – caused the largest change in critical inclination angle. Since the experiments utilized a bar-mold geometry, this worst-case off-axis misorientation was present somewhere on the bar surface. Thus, any increase in the off-axis misorientation of the dendrites decreased the critical inclination angle by the same angle. Because single-crystal materials are generally accepted with off-axis misorientations up to 10° [65], a solidification front inclination angle of 30° or higher poses significant risk to unidirectional dendritic growth. Combination of the parameters that caused 1° or 2° change in critical inclination could likely reduce the critical inclination angle to 25°. Considering the points addressed above and the presence of thermal fluctuations in the investment casting environment, the 25 degree critical

inclination angle reported in Chapter 6 was in reasonable agreement with the dendrite growth modeling investigated in this effort.

The rotational misorientation of the single crystal also impacted the critical inclination angle. For reference, a rotational misorientation of zero corresponded to alignment of the secondary arms parallel and perpendicular to the wall. An increase in the critical inclination angle up to 55° was observed with substantial increase in rotational misorientation up to 45°.

In a complex geometry, the relationship between critical inclination angle and misorientation of the single crystal suggests that rotational misorientation of the dendrite should be selected such that the secondary dendrite arms be 45° from surfaces with high solidification-front inclination angle. Preferential alignment of secondary orientation can be performed using a seed, but the formation of other defects has not been considered. More research that considers the effect of the thermal conditions and misorientation of the single crystal on grain nucleation is needed before preferential secondary orientation could be proposed.

Dendrite-Growth Predictions for a Curved Solidification Front

Predictions of dendrite-growth mode for a parabolic thermal field were also evaluated with 2D models. The thermal field within the dendrite growth model was input as a parabola in which the inclination angle at the right side of the domain was 0° and

represented the center of a casting. The inclination angle on the left side of the domain represented the surface of the casting and was used to evaluate the onset of lateral growth with changes in the degree of curvature of the thermal field. A single crystal whose primary orientation was well aligned with the growth direction was evaluated with solidification-front inclination angles of 40, 45, 50, 60 and 70° at the surface of the casting (Figure 7.10).

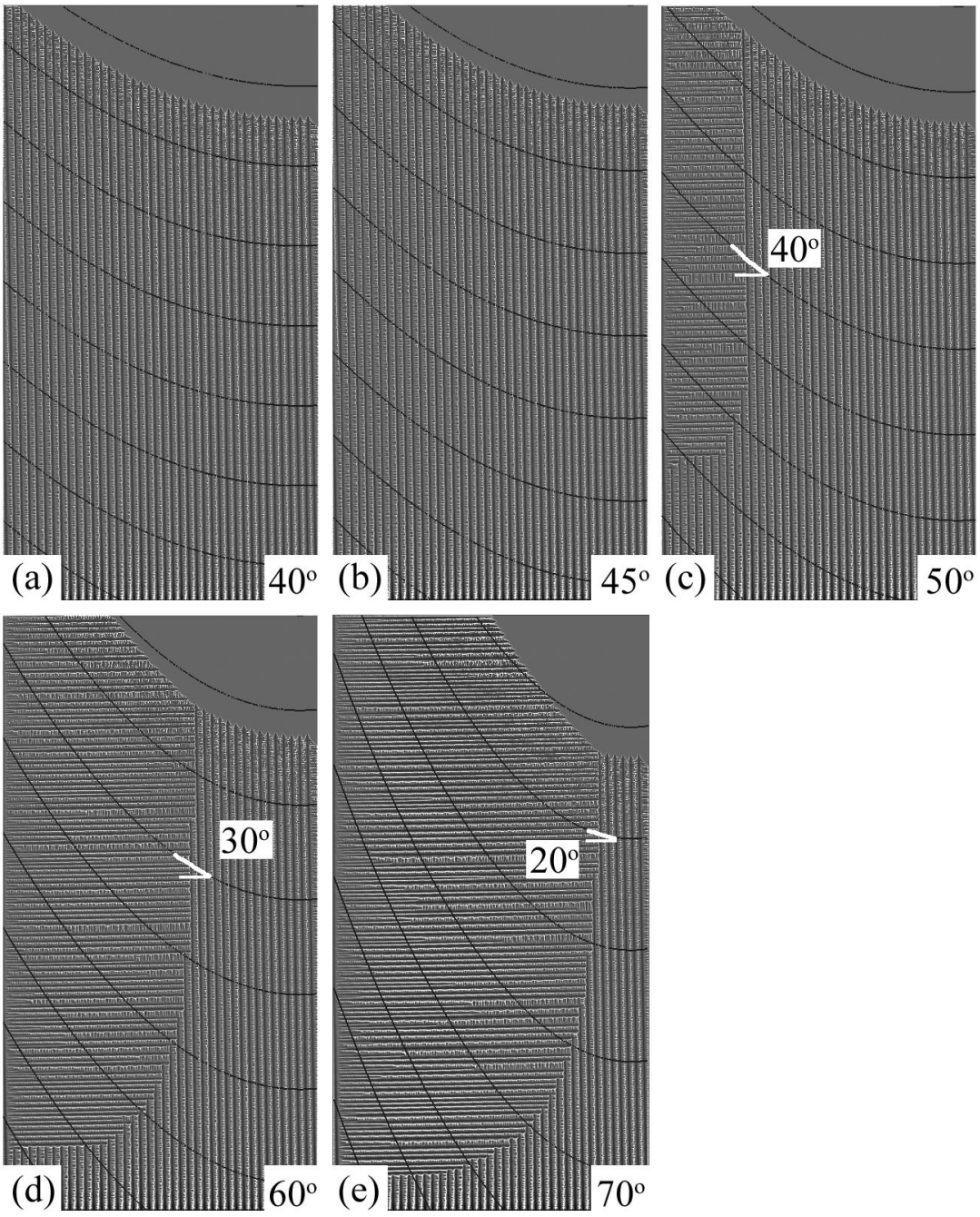

Figure 7.10 – Predicted microstructure for a SX bar with a curved solidification front of (a) 40, (b) 45, (c) 50, (d) 60 and (e) 70° at the wall. Isotherms have been displayed as black lines, and inclination angle at the growth-mode transition has been labeled.

An increase in the lateral-growth domain size was observed with increasing solidification-front inclination angle at the wall. This was expected because as the

inclination angle at the wall increased, the relative inclination angle at any radius within the domain also increased. In addition, the critical inclination angle at the surface of these models was higher than the critical inclination angle determined from the planar solid-liquid interface models. This was attributed to the decay of the solid-liquid interface inclination angle with distance from the wall and the finite distance between the wall and the second dendrite, where the closest opportunity for lateral growth is present. For example, a parabola in which the inclination at the wall is 45° has an inclination angle of 43.8° at a distance 300 μm from the wall where the second dendrite resides. For models in which lateral growth formed at the wall, lateral growth proceeded further into the casting than the radial position corresponding to 45°. This suggests that the critical inclination angle to form lateral growth was higher than the critical inclination to *maintain* lateral growth. Relative to the radial position corresponding to an inclination angle of 45°, the domain size proceeded further into the center of the casting for increased curvatures. For instance, the angle of the isotherm at the interface between the lateral and axial growth regimes for the case of a 60° inclination angle at the wall was approximately 30° at steady state rather than the 45° angle required to form lateral growth at the surface.

In addition, off-axis misorientation was evaluated using a 10° off-axis misoriented single crystal in which the primary orientation of the dendrite front was toward the wall for the same thermal conditions. An off-axis misoriented single crystal oriented in this manner formed a larger lateral-growth domain size for the same thermal condition as compared to an aligned single crystal (Figure 7.11). This was consistent with previous results that an increase in off-axis misorientation increased the propensity for lateral growth.

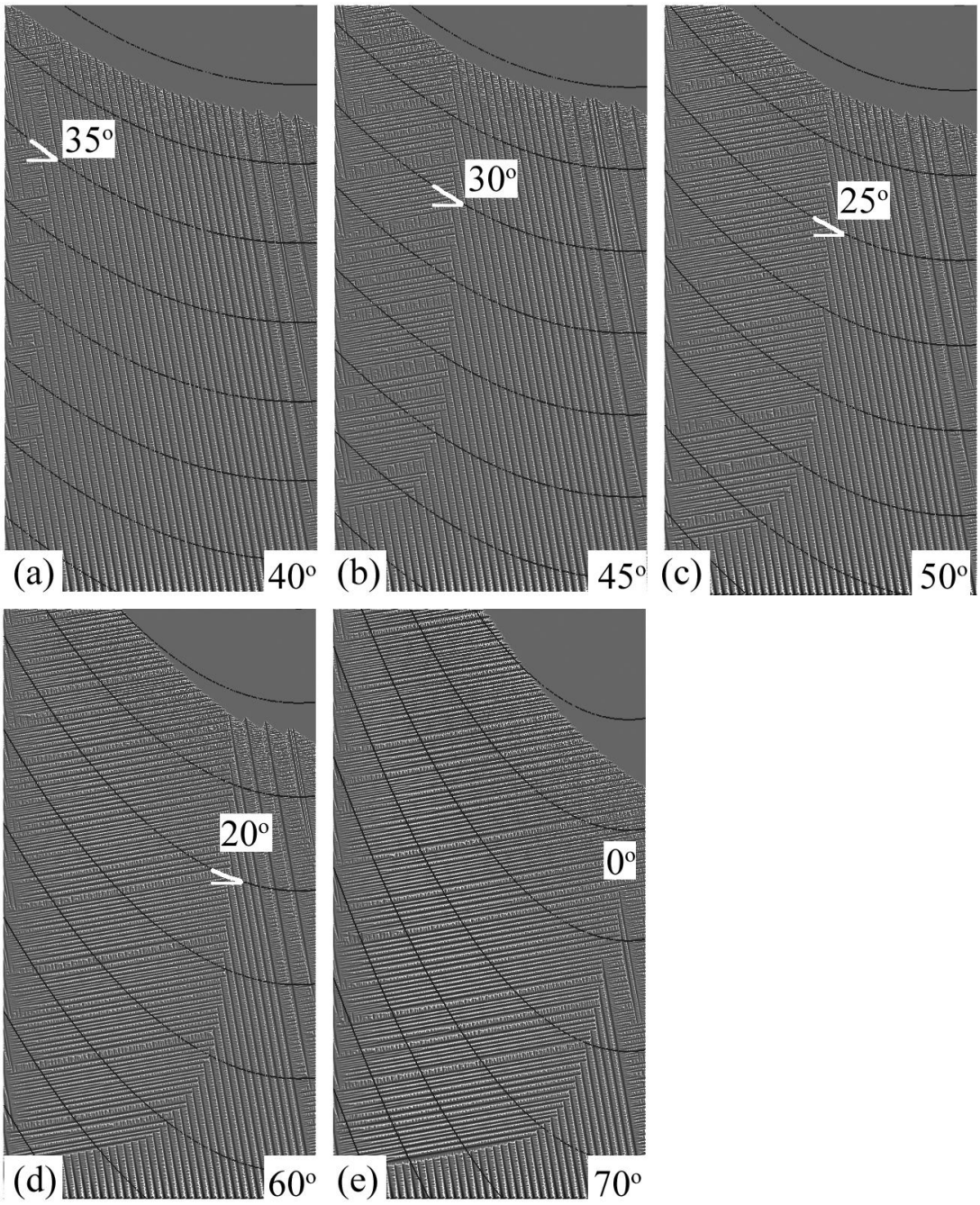

Figure 7.11 – Predicted microstructure for a 10 degree off-axis misoriented single-crystal bar with a curved solidification front of (a) 40, (b) 45, (c) 50, (d) 60 and (e) 70° at the wall. Isotherms have been displayed as black lines, and inclination angle at the growth-mode transition has been labeled.

Discussion

Dendrite growth models based on solute-adjusted diffusion in a binary system were used to assess the tendency for lateral growth under a range of process conditions. In general, the onset of lateral growth is insensitive to changes in thermal and solutal conditions, with the exception of those factors that influence the inclination angle of the solidification front and the crystallographic orientation of the single crystal.

FE-based predictions of the thermal conditions during solidification indicated a dependence of inclination angle on the alloy properties as shown in Chapter 6. The two different alloys exhibited different solidification-front inclination angles for the same process conditions. Thus, the propensity for different alloys to form lateral growth is different for the same mold geometry and processing conditions, assuming the critical inclination angle is approximately 45° for all alloys. The alloy properties that change the shape of the dendrite tip may influence the propensity for lateral growth, as demonstrated with changes in partition coefficient. More research is needed to identify changes in critical inclination angle due to alloy properties, as discussed below.

The simplification of a Ni-base superalloy to a binary can limit the applicability of the dendrite growth model, due to the over-simplified solute field. However, trends of dendrite-growth mode and distribution of solute can be established. Four properties are used to represent the alloy: the liquidus, partition coefficient, diffusion coefficient, and product of the slope of the liquidus line and initial alloy composition. The sensitivity of

the critical inclination angle to these conditions can reveal the relative importance of these material properties to the onset of lateral growth. Further research is needed to define appropriate bounds for analysis and evaluate the onset of lateral growth with these material properties.

As computing performance improves and modeling techniques mature, more sophisticated models are being utilized to predict solidification behavior. The transition of modeling capability to three dimensions has provided improved accuracy of solidification models. The onset of lateral growth occurred with an interface inclination which was lower by 2° within 3D models. In general, this is not significant enough to warrant the additional computational expense of 3D modeling. However, there are features of the dendritic structure that could only be evaluated in three dimensions: packing arrangement of dendrites and complex misorientation of the single crystal.

Lessons learned from 3D modeling were generalized so that future 3D behavior could be inferred to avoid computational expense. Likewise, a macroscopic criterion for the prediction of the onset of lateral growth was developed though prediction of the solidification-front inclination angle and understanding of the insensitivity of lateral growth to other thermal conditions. The inclination angle of the solidification front is higher for LMC as compared to Bridgman. Therefore, the lateral growth criteria may be used primarily for the LMC process, but is applicable to more complex geometries processed via Bridgman.

The simulations of dendritic growth conducted in this chapter demonstrate that the propensity for lateral growth of dendrites increases with increasing solidification-front inclination angle and misorientation of the single crystal relative to the withdrawal direction of the casting. Thus, the orientation quality of the single crystal from the seed or starter is critical to the quality of the single crystal component due to the non-axial thermal field present during the LMC process. Therefore, the use of high-quality seeds reduces tendency for the formation of defects for the LMC process. In addition, starters specifically designed for the increased curvatures of the LMC process may need to be developed to further reduce the propensity for lateral growth and grain nucleation. For the case of the Bridgman process, lateral growth is primarily only observed with abrupt changes in cross-section since the solidification front would have to be far below the baffle to cause inclination angles of this magnitude, as explained in Chapter 4.

Conclusion

- The onset of lateral growth in 2D microstructure models occurred when the solidification front was inclined by at least 45°, provided that the crystal orientation did not deviate from [001] alignment.
- 3D microstructure models predict the onset of lateral growth at a solidification-front inclination angle as low as 40° for typical casting conditions without considering off-[001] misorientation.
- Off-axis misorientation of the single-crystal can reduce the critical inclination angle by 1 degree for every degree of crystal misorientation.

- For the presence of a concave solidification front, lateral growth was observed at a similar inclination angle as the planar front simulations and extended to the center of the casting for a surface inclination angle of 70°.

References

1. L.W. Sink, "Method of Casting Directionally Solidified Articles," (U.S. Patent No 3,417,809), 1968.

2. F.L. Versnyder and R.W. Guard, *Trans ASM*, 52 (1960) 485.

3. F.L. Versnyder and M.E. Shank, *Mat Sci Eng*, 6 (1970) 213.

4. J.G. Tschinkel, A.F. Giamei and B.H. Kearn, "Apparatus for Casting of Directionally Solidified Articles," (U.S. Patent No 3,763,926), 1973.

5. A.F. Giamei and J.G Tschinkel, *Metall and Mater Trans A*, 7A (1976) 1427-1434.

6. J. Grossmann, J. Preuhs, W. Esser and R.F. Singer, *Proceedings of the 1999 International Symposium on Liquid Metal Processing and Casting*, eds. A. Mitchell, L. Ridgway and M. Baldwin (The Minerals, Metals & Materials Society, 1999) 31-40.

7. F. Hugo, U. Betz and J. Ren, *Proceedings of the 1999 International Symposium on Liquid Metal Processing and Casting*, eds. A. Mitchell, L. Ridgway and M. Baldwin (The Minerals, Metals and Materials Society, 1999) 16-30.

8. A.J. Elliott et al. *Metall and Mater Trans A*, 35A (2004) 3221-3231.

9. P.N. Quested and M. McLean, *Mat Sci Eng*, 65 (1984) 171-180.

10. J.D. Miller and T.M. Pollock, *Proceedings of the 2009 International Symposium on Liquid Metal Processing and Casting*, ed. P.D. Lee, A. Mitchell and R. Williamson (The Minerals, Metals & Materials Society, 2009) 119-126.

11. A.J. Elliott and T.M. Pollock, *Metall and Mater Trans A*, 38A (2007) 871-882.

12. M. Lamm and R.F. Singer, *Metall and Mater Trans A*, 38A (2007) 1177.

13. C. Brundidge, D. VanDrasek, B. Wang and T.M. Pollock, *Proceedings of the 2009 International Symposium on Liquid Metal Processing and Casting*, ed. P.D.

Lee, A. Mitchell and R. Williamson (The Minerals, Metals & Materials Society, 2009) 107-117.

14. J. Zhang and L.H. Lou, *J Mater Sci Technol*, 23 (2007) 289-300.

15. W.J. Boettinger and J.A. Warren, *Metall Trans A*, 27A (3) (1996) 657-669.

16. N. Warnken, A. Drevermann, D. Ma, S.G. Fries and I. Steinbach, *Superalloys 2008*, ed. R.C. Reed, K.A. Green, P. Caron, T.P. Gabb, M.G. Fahrmann, E.S. Huron and S.R. Woodard (Warrendale, PA: TMS, 2008) 951-960.

17. Ch.-A. Gandin, R.J. Schaefer and M. Rappaz, *Acta Mater*, 44 (8) (1996) 3339-3347.

18. T.-m. Wang, Y.-q. Su, J.-j. Guo, I. Ohnaka and H. Yusada, *Trans Nonferrous Met Soc China*, 16 (2006) 753-759.

19. S. Chen, B. Merriman, S. Osher and P. Smereka, *J Computational Phys*, 135 (1997) 8-29.

20. F. Gibou, R. Fedkiw, R. Caflisch and S. Osher, *J Sci Computing*, 19 (1-3) (2003) 183-199.

21. L. Tan and N. Zabaras, *J Computational Physics*, 211 (2006) 36-63.

22. N. Zabaras, B. Ganapathysubramanian and L. Tan, *J Computational Physics*, 218 (2006) 200-227.

23. L. Tan and N. Zabaras, *J Computational Physics*, 221 (2007) 9-40.

24. L. Tan and N. Zabaras, *J Computational Physics*, 226 (2007) 131-155.

25. R. Shao, "Numerical and Experimental Study of Constrained Solidification," (Ph.D. thesis, Purdue University, 2007).

26. H.B. Dong, X.L. Yang, P.D. Lee and W. Wang, *J Mater Sci*, 39 (2004) 7207-7212.

27. W. Wang, P.D. Lee and M. McLean, *Acta Metall*, 51 (2003) 2971-2987.

28. Ch.-A. Gandin and M. Rappaz, *Acta Mater*,45 (5) (1997) 2187-2195.

29. X.L. Yang, H.B. Dong, W. Wang and P.D. Lee, *Mat Sci Eng A*, 386 (2004) 129-139.

30. L. Yuan, P.D. Lee, G. Djambazov and K. Pericleous, *Proceedings of the 2009 International Symposium on Liquid Metal Processing and Casting*, ed. P.D. Lee, A. Mitchell and R. Williamson (The Minerals, Metals & Materials Society, 2009) 31-46.

31. N. D'Souza, P.A. Jennings, X.L. Yang, H.B. Dong, P.D. Lee and M. McLean, *Metall Trans B*, 36B (2005) 657-666.

32. X.L. Yang, P.D. Lee and N.D'Souza, *JOM*, (May 2005) 40-44.

33. W. Wang, "A Mathematical Model of Dendritic Microstructures in Nickel-Based Superalloys," (Ph.D. thesis, University of London, 2003).

34. X.L. Yang, D. Ness, P.D. Lee and N. D'Souza, *Mat Sci Eng A*, 413-414 (2005) 571-577.

35. P.D. Lee, A. Chirazi, R.C. Atwood and W. Wang, *Mat Sci Eng A*, 365 (2004) 57-65.

36. R.C. Atwood and P.D. Lee, *Metall and Mater Trans B*, 33B (2002) 209-221.

37. H.B. Dong and P.D. Lee, *Acta Mater*, 53 (2005) 659-668.

38. P.D. Lee and J.D. Hunt, *Acta Mater*, 49 (2001) 1383-1398.

39. P.D. Lee, R.C. Atwood, R.J. Dashwood and H. Nagaumi, *Mat Sci Eng A*, 328 (2002) 213-222.

40. R.C Atwood and P.D. Lee, *Acta Mater*, 51 (2003) 5447-5466.

41. D. See, R.C. Atwood and P.D. Lee, *J Mat Sci*, 36 (2001) 3423-3435.

42. X.L. Yang, P.D. Lee, R.F. Brooks and R. Wunderlich, *Superalloys 2004*, ed. K.A. Green, T.M. Pollock, H. Harada, T.E. Howson, R.C. Reed, J.J. Schirra and S. Walston (The Minerals, Metals & Materials Society, 2004) 951-958.

43. M. Ganesan, D. Dye and P.D. Lee, *Metall and Mater Trans A*, 36A (2005) 2191-2204.

44. L. Beltran-Sanchez and D.M. Stefanescu, *Metall Trans A*, 34A (2) (2003) 367-382.

45. L. Nastac, *Modeling and Simulation of Microstructure Evolution in Solidifying Alloys*, Kluwer Academic Publishers, 2004.

46. R.N. Grugel and Y. Zhou, *Metall Mater Trans A*, 20A (1989) 969-973.

47. Ch.-A. Gandin, M. Eshelman and R. Trivedi, *Metall and Mater Trans A*, 27A (9) (1996) 2727-2737.

48. S-C. Huang and M.E. Glicksman, *Acta Metall*, 29 (1981) 717-734.

49. X. Wan, Q. Han and J.D. Hunt, *Acta Mater*, 45 (10) (1997) 3975-3979.

50. A.F. Giamei and B.H. Kear, *Met Trans*, 1 (1970) 2185.

51. J.D. Hunt and S-Z. Lu, *Metall Trans A*, 27A (3) (1996), 611-623.

52. K. Somboonsuk, J.T. Mason and R. Trivedi, *Metall Trans A*, 15A (6) (1984), 967-975.

53. R. Trivedi, *Metall Trans A*, 15A (6) (1984) 977-982.

54. H. Weidong, G. Xingguo and Z. Yaohe, *J Cryst Growth*, 134 (1993) 105-115.

55. J. Lipton, M.E. Glicksman and W. Kurz, *Mat Sci and Eng*, 65 (1) (1984) 57-63.

56. M.A. Chopra, M.E. Glicksman and N.B. Singh, *Metall and Mater Trans A*, 19 (12) (1988) 3087-3096.

57. K. Gallup and T.M. Pollock, unpublished research, 2010.

58. D. Walton and B. Chalmers, *Trans Metall Soc*, AIME 215 (1959) 447.

59. N. D'Souza, M.G. Ardakani, M. McLean and B.A. Shollock, *Metall Mater Trans A*, 31A (2000) 2877-2886.

60. N. D'Souza, M.G. Ardakani, A. Wagner, B.A. Shollock and M. McLean, *J Mat Sci*, 37 (2002) 481-487.

61. Y. Zhou and N.R. Green, *Superalloys 2008*, ed. R.C. Reed, K.A. Green, P. Caron, T.P. Gabb, M.G. Fahrmann, E.S. Huron and S.R. Woodard (Warrendale, PA: TMS, 2008) 317-324.

62. Y.Z. Zhou, A. Volek and N.R. Green, *Acta Mat*, 56 (2008) 2631-2637.

63. L. Nastac, *Acta Mater*, 47 (17) (1999) 4253-4262.

64. K.C. Mills, *Recommended Values for Thermophysical Properties for Selected Commercial Alloys*, Cambridge, UK: Woodhead Limited Publishing, 2002.

65. E.W. Ross and K.S. O'Hara, *Superalloys 1996*, eds. R.D. Kissinger, D.J. Dye, D.L. Anton, A.D. Cetel, M.V. Nathal, T.M. Pollock and D.A. Woodford (The Minerals, Metals & Materials Society, 1996) 19-25.

CHAPTER 8

DISCUSSION AND CONCLUSIONS

The overall objective of this research was to evaluate the unique thermal characteristics of the LMC process, identify the need for new defect criteria and determine the mechanism for lateral overgrowth of primary dendrites. A combined experimental and modeling approach has been utilized to provide new insights on solidification phenomena that occur during Liquid-Metal-Cooling directional solidification. In this chapter, the key findings are first summarized. Following this, the implications for (1) LMC processing, (2) solidification modeling, (3) microstructure modeling, (4) dendritic growth, (5) non-axial thermal fields and (6) mechanical response of lateral growth are discussed along with recommendations for future research. Finally, a summary of this research is presented.

The key findings from this research are described in detail:

- Physically-realistic boundary conditions that represented the predicted thermal profiles through the floating baffle and mold were developed for component-scale process simulations.
  - The thermal profile within the floating baffle is sensitive to baffle thickness, coolant impregnation, the emissivity of the floating baffle. The thermal profile within the submerged mold is sensitive to complete coverage of the

coolant bath and insensitive to bead size, baffle thickness, partial coolant impregnation, and baffle-bead arrangement at the mold surface. Major (a factor of 3 or more) changes in floating-baffle emissivity affected the thermal profile within the mold.

- The floating baffle serves as a heat-flux barrier between the radiation of the furnace and the coolant bath. A conservatively thick baffle is optimal to ensure complete granular flow of baffle with abrupt changes in mold geometry.

- A fundamental understanding of heat transfer during directional solidification has been established, permitting accurate solidification models for analysis of cast structure and process optimization.
  - A critical fraction solid of 0.40 is physically realistic for evaluation of thermal conditions relevant to dendrite scale. Radiation from the mold is the dominant heat transfer mechanism for the Bridgman process, and conduction through the shell is dominant for LMC at the critical fraction solid.
  - Critical process parameters for the Bridgman process are furnace temperature, withdrawal rate and casting geometry. Critical process parameters for Bridgman are also relevant for LMC along with the presence of the floating baffle and coolant temperature. Significant increase in shell thickness (greater than a factor of two) can reduce thermal gradient and cooling rate.

- The solidification rate and cooling rate increase with increasing withdrawal rate, while axial thermal gradient and solidification-front inclination angle scale with solidification-front position relative to the top of the baffle.
- The position of the solidification front relative to the top of the baffle can be used to define the optimal process conditions for a given casting geometry. A position of 2-6 mm above the floating baffle for LMC and 5-15 mm above the fixed baffle for Bridgman provides the maximum axial thermal gradient at the surface of the casting. This position is sensitive to alloy composition; alloys with a higher liquidus temperature have optimal positions higher above the top of the floating baffle. The position was insensitive to casting geometry.

- Solidification modeling enabled, with minimal casting trials, a process for the directional solidification of a segmented single-crystal ring, demonstrating LMC as a feasible processing path.
  - The feasibility of casting multiple-seeded, thick-section segments with both the LMC and Bridgman techniques has been demonstrated. A viable processing route has been established for manufacture of a single-crystal ring.
  - A model that quantitatively predicts the thermal behavior during solidification has been validated. Predictions of primary and secondary dendrite arm spacing based on thermal conditions during solidification are in agreement with experimental measurement in regions of low solidification-front inclination angle.

- Morphological evolution of dendrite microstructure induced by the unusual heat transfer characteristics of the LMC process was thoroughly investigated experimentally.
  - A mold geometry that assessed a broad range of thermal conditions in a single casting was designed. In the range of experimental conditions investigated, a range of dendrite morphology and scale was observed, including dendrite morphologies produced by axial growth, lateral growth and grain nucleation.
  - Complete axial growth was observed in a cross-section above severe lateral growth that grew into the center of the casting, indicating that axial dendritic growth can be recovered from a completely laterally-growing structure without grain nucleation.
  - Significant variability in dendrite scale was observed for castings with equivalent process conditions, expressing the need for a means to quantify dendrite scale by measures other than PDAS.

- A predictive criterion has been developed for the onset of lateral growth via FE-based thermal simulation in conjunction with experimentation..
  - Lateral growth is indicative of unstable process conditions approaching breakdown of single-crystal growth.
  - The inclination angle of the solid-liquid interface can be used to predict transitions in dendrite-growth mode with the onset of lateral growth at a critical angle of 25° and grain nucleation at a critical angle of 45°.

- The conditions under which lateral growth occurs has been determined through a parametric analysis and validated from experimental evaluation.
  - In CA-FD models of a binary alloy, the onset of lateral growth occurred when the solidification front was inclined by 45° in 2D simulations and 40° for 3D diffusion-based dendrite-growth simulations that considered representative thermal conditions for investment castings for [001] dendritic growth. Misorientation away from [001] single crystals reduces the critical inclination angle by 1 degree for every degree of misorientation. Thus, experimental observations of the onset of lateral growth at a predicted inclination angle of 25° is reasonable, considering typical off-axis misorientations of up to 15°.
  - Simulations of a concave solidification front predicted the onset of lateral growth at a similar inclination angle as the constant inclination-angle simulations. Lateral growth extended to the center of the casting for a surface inclination angle of 70°.

New Considerations for LMC Processing

This research has enabled an improved fundamental understanding of the LMC process and suggests new approaches for the control of its unique features, including the growth of single crystals with highly curved solidification fronts. Control of this aspect of the process enables the production of atypical single-crystal casting geometries that would otherwise be unattainable. The critical process features that influence curvature of the front are withdrawal rate and casting geometry. Optimization of the floating baffle has

contributed to the evaluation of process robustness necessary to transition the LMC process to the production environment. In this section, these four points are discussed in detail.

One major consideration for LMC processing is the increased curvature of the solidification front. To ensure optimal process design, the curvature should be maintained to a controllable level throughout the casting. Abrupt changes in the geometry of the casting can cause increased solidification-front curvature, beyond the desired level. Based on the heat transfer analysis in Chapter 4 and the thermal predictions of the mold-wrapped bars in Chapter 6, local adjustment of the shell thickness can affect the thermal field within the casting. Therefore, shell thickness changes can be used to counteract abrupt changes in geometry and reduce curvature. This is possible since conduction through the shell is the dominant heat-transfer step of the LMC process, as was described in Chapter 4. By locally increasing the shell thickness before the change in geometry, the lateral heat extraction is reduced, causing a flattening of the solidification front as observed in Chapter 6, Figure 6.14d. Local modifications of the mold geometry that are informed by solidification modeling could greatly impact the reduction of grain nucleation in regions of abrupt geometrical change.

Additionally, the LMC process can generate an undesirable thermal field in the starter region. This can be attributed to the use of starters that were originally designed for a much different heat extraction condition. Starters used for the LMC process were directly adopted from the Bridgman process, in which the heat extraction is much less

efficient. Thus, the geometry of the starters should be optimized for the LMC process. Two defects were regularly observed to emanate from the starter in the LMC process: (1) an off-axis single crystal or (2) multiple crystals. In a properly designed starter, the solidification front is flat before the starter and tilted off-axis in multiple directions through the starter to allow for growth competition such that only one crystal remains at the top of the starter. This competition process relies on the lateral growth to overcompete poorly aligned dendrites. The off-axis misorientation occurs when the solid-liquid interface is preferentially tilted in one direction upon entrance into the starter (Figure 8.1). Multiple crystals are also present in LMC and are associated with grain nucleation just above the starter as the cross-sectional area of the casting is increasing.

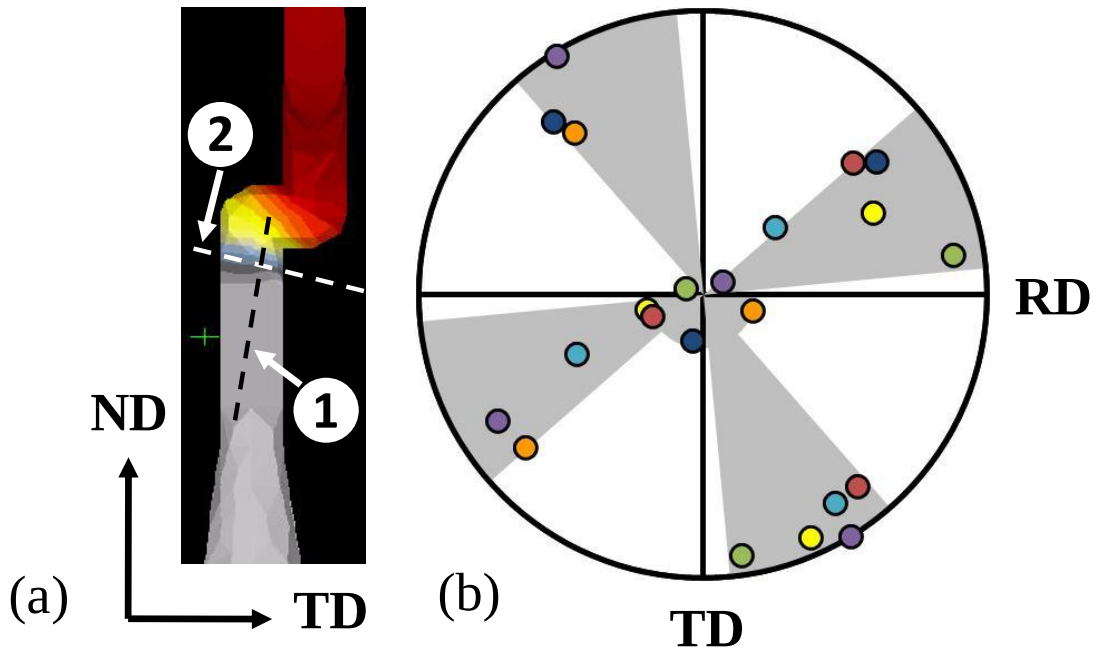

Figure 8.1 – (a) Preferential tilt of primary orientation (1) due to inclined solidification front below the starter (2) and (b) collection of pole figures from surfaces transverse to the withdrawal direction indicating preferential off-axis (from [001]) toward "TD" and rotational (about [001]) orientations of the single crystal. "RD" corresponds to the radial

direction and “ND” the growth direction of a 5-bar mold configuration. The ranges have been banded in gray and different colored points correspond to different castings.

As solidification progresses through the starter, there is a preferential rotational orientation of the secondary arms as observed from EBSD measurements (Figure 8.1b). The preferential rotational misorientation correlates to the sample orientation: primarily in the direction of the first turn of the starter with a slight rotation toward “RD” due to the second turn of the starter interacting with the inclined solidification front (Figure 8.1a). The off-axis misorientation of the single-crystal is important because of the resultant impact on lateral growth propensity. As discussed previously, there is a one-to-one correspondence between off-axis misorientation and reduction of the critical solidification-front inclination angle to cause dendrite instability (Figure 8.2). In other words, a single crystal that is 10° misoriented toward the wall is subject to lateral growth at an inclination angle 10° lower than a single crystal perfectly aligned with the withdrawal direction – a 35° inclination angle rather than a 45° inclination angle. Overall, an optimization of the starter geometry could greatly improve the single-crystal selection within the starter and the stability of the single crystal within the casting. Lengthening the portion of the starter below the first turn may improve the off-axis misorientation of the single crystal. If a particular secondary orientation is desired (aligned with the geometry – “RD” and “TD” – of the starter), lengthening the starter between the first and second turns may reduce the interaction of the two turns that leads to the rotated crystal.

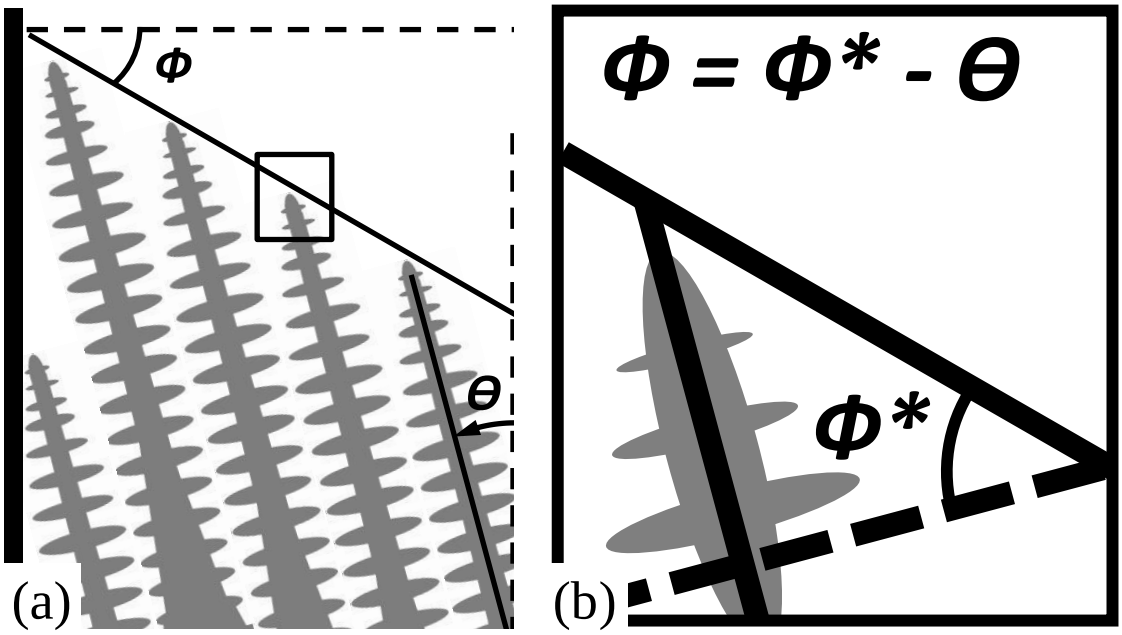

Figure 8.2 – Decrease in the critical solidification-front inclination angle (ϕ) with increase in single-crystal off-axis misorientation (θ). Note: The angle of the solidification front in (1 0 0), ϕ*, is 45° based on this work.

Despite the challenges associated with the increased heat extraction, several benefits of the LMC process have been demonstrated. There are significant benefits with regard to the reduction of microstructure scale. The refinement of the dendrite structure reduces the segregation distance and underlying defect structure. Directionally-solidified and single-crystal components are typically heat treated above the solvus temperature of the γ' phase and rapidly cooled to room temperature. This allows for finely-distributed γ' which improves the mechanical performance, specifically creep resistance. Ni-base superalloys that are comprised of grain-boundary strengtheners have a solution temperature that is near the solidus of the alloy, thus causing incipient melting in the interdendritic region where an increased fraction of low-melting-temperature alloying elements are present. By reducing the segregation distance, the materials are capable of

higher heat-treatment temperatures, thus improving their mechanical performance [1-3]. In addition, the fatigue performance of materials cast via the LMC process is improved. Fatigue resistance of the alloys investigated is limited by the pore size of the material. Because the microstructure scale is reduced by utilization of the LMC process, the defect structure, i.e. pore size, is also reduced, thus increasing the fatigue resistance. These two benefits have been previously documented [4-12].

Another benefit is the ability to cast configurations not easily attained using the conventional Bridgman approach. An example is the single-crystal ring concept, Chapter 5. The single-crystal ring is comprised of single-crystal segments separated by low-angle boundaries of a pre-determined misorientation [13]. This configuration provides a nominally single-crystal ring, in which the <100> crystallographic directions are aligned with the axial, radial and circumferential directions of the ring (Figure 8.3). In any case, the withdrawal direction of the casting must be the axial direction of the ring, due to the rotational misorientation of the dendrites in the radial-circumferential plane. In general, this casting configuration possesses a large cross-section in the transverse plane with a short dimension in the withdrawal direction, which is significantly different than the small cross-sectional area and long axial dimension typically cast during directional solidification. In addition, the inside of the ring is shadowed during radiation heating and cooling, thus not obtaining the thermal gradient needed to maintain a single crystal. Therefore, this geometry is not suitable for the Bridgman process. However, the LMC process is a viable route for production of such a component. Other geometries that have

poor radiation heat transfer due to shadowing may also benefit from utilization of the LMC process.

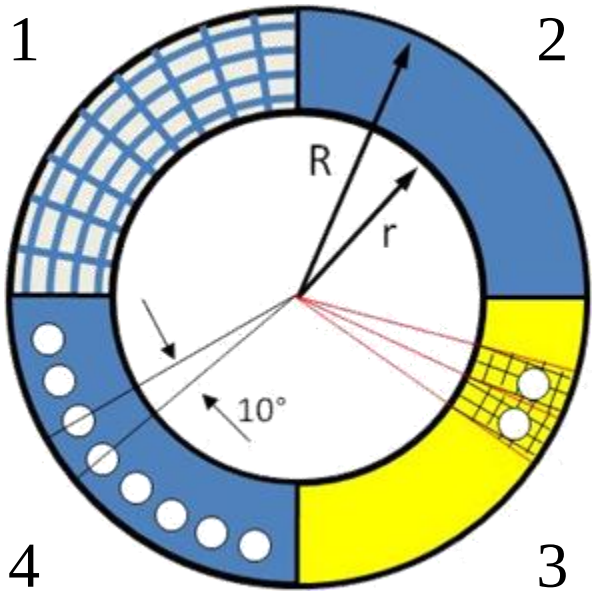

Figure 8.3 – Configuration of a single-crystal ring. A ring whose axial, radial and circumferential directions are parallel to <100> of the crystal (1) and has an inner and outer radius of r and R, respectively (2). In order to achieve this configuration, seeds are used that have a 10 degree rotational misorientation relative to adjacent seeds (3). In order to achieve a full ring, 36 seeds are needed that are 10 degrees apart (4).

In order to prove process robustness, any scale-up risks must be mitigated and all critical process variables must be defined and maintained within prescribed limits. Management of the floating baffle and coolant bath is one possible scale-up concern, especially stirring of the coolant bath. From this research and other previous studies, the critical processing variables have been defined and include all critical Bridgman process variables as well as the floating baffle, coolant temperature and stirring condition of the coolant bath [1,14-17]. As discussed previously, the baffle parameters that must be managed are its

presence, minimum thickness to ensure complete coolant coverage, and maximum age to prevent overheating of the baffle due to carbon pickup and coolant impregnation.

An optimal condition of the floating baffle includes a maximum thermal gradient in the mold through the floating baffle and complete coverage of the coolant regardless of abrupt geometrical changes of the mold. Intuitively, these two factors are competing because a thick baffle is more likely to allow flow and prevent coolant exposure to the furnace while a thin baffle is expected to provide a maximum thermal gradient. Other factors such as baffle material and bead size can also be optimized. By evaluation of the thermal field using a finite element analysis, it was demonstrated in this effort that the thickness of the floating baffle affects the thermal field within the baffle but not within the mold. In addition, the thermal field is generally insensitive to bead size and ceramic material selection. Therefore, the optimal baffle condition is a thick baffle that promotes inward baffle flow when the cross-section of the mold decreases significantly (Figure 8.4). Because baffle flow is determined by the angle of repose for granular material, a conservative thickness would be equal to the maximum horizontal distance necessary for flow. For industrial gas-turbine components, a horizontal distance of approximately 5 cm is typical between the edge of the platform and base of the airfoil. Thus, an optimal floating-baffle thickness of 5 cm is sufficient to maintain a thermal barrier between the furnace and coolant.

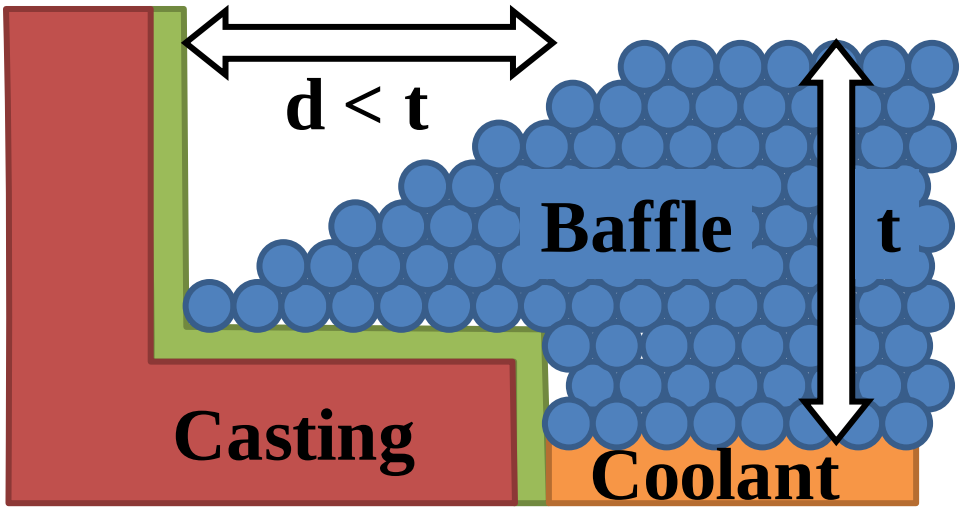

Figure 8.4 – Schematic of optimal baffle thickness (t) as related to the reduction in cross-section thickness (d) of the casting.

Overall, the benefits associated to the LMC process significantly outweigh the disadvantages. The process has also been proven to be robust and ready for the production environment. The optimum baffle condition has been defined and is consistent with manufacturability concerns of the floating baffle.

Benefits of Solidification Modeling

With the advent of computational power and efficiency, solidification modeling has provided new insights to the heat transfer process during directional solidification. In addition, the improved experimental techniques that enable evaluation of the local solidification environment have provided invaluable data for validation of model predictions. With the expense of experimental measurements and difficulty associated with experimental parametric analyses, solidification modeling is valuable for optimization of process conditions and casting geometries. This effort has demonstrated

the utility of finite-element modeling to (1) understand the fundamentals of heat transfer within the floating baffle, (2) establish a set of model parameters that are well-validated and applicable to complex geometries, and (3) define an approach for optimization of process conditions based on the thermal field during solidification. In addition, emerging concepts related to Integrated Computational Materials Engineering (ICME) propose the application of solidification modeling to evaluate processing in the design phase of the casting to avoid conditions that result in defect production, to reduce the number of pre-production casting trials, and to couple with key experimentation to advance the state-of-the-art of solidification. The optimization of the floating baffle and the benefits it provides to evaluation of the directional-solidification process has already been discussed in the previous section. The other benefits to solidification modeling are discussed in turn.

A well-validated baseline model that identifies sensitive process variables has been established. This model can now be used by other researchers to improve the understanding of solidification. The key model parameters are summarized in Table 8.1. Furnace temperature and withdrawal rate have been identified as critical process parameters for the Bridgman and LMC processes. The presence of the floating baffle is important to maintaining a high thermal gradient with the LMC process. Casting geometry (Figure 8.5) affected the thermal field at the solidification front.

Table 8.1 – Key model parameters for FE-based solidification modeling.

Thermophysical Properties		
Baffle Thermal Cond.	1.0	W/mK
Shell Thermal Cond.	2.5	W/mK
Shell Thickness	6.4	mm

Interface Heat Transfer Coefficients		
Superalloy-Ceramic	*750	W/m^2K
Ceramic-Ceramic	500	W/m^2K
Tin-Ceramic	4000	W/m^2K

Boundary Conditions		
Shell Emissivity	0.4	
Baffle Emissivity	0.2	
Tin Temperature	250	°C

Run Parameters		
Maximum Time Step	**	
Spatial Step	0.5	mm
Critical Fraction Solid	0.4	

*Initial value reported with exponential decay to 100 W/m^2K during solidification

**Scaled by withdrawal rate to provide equal withdrawal distance (0.4mm) between steps

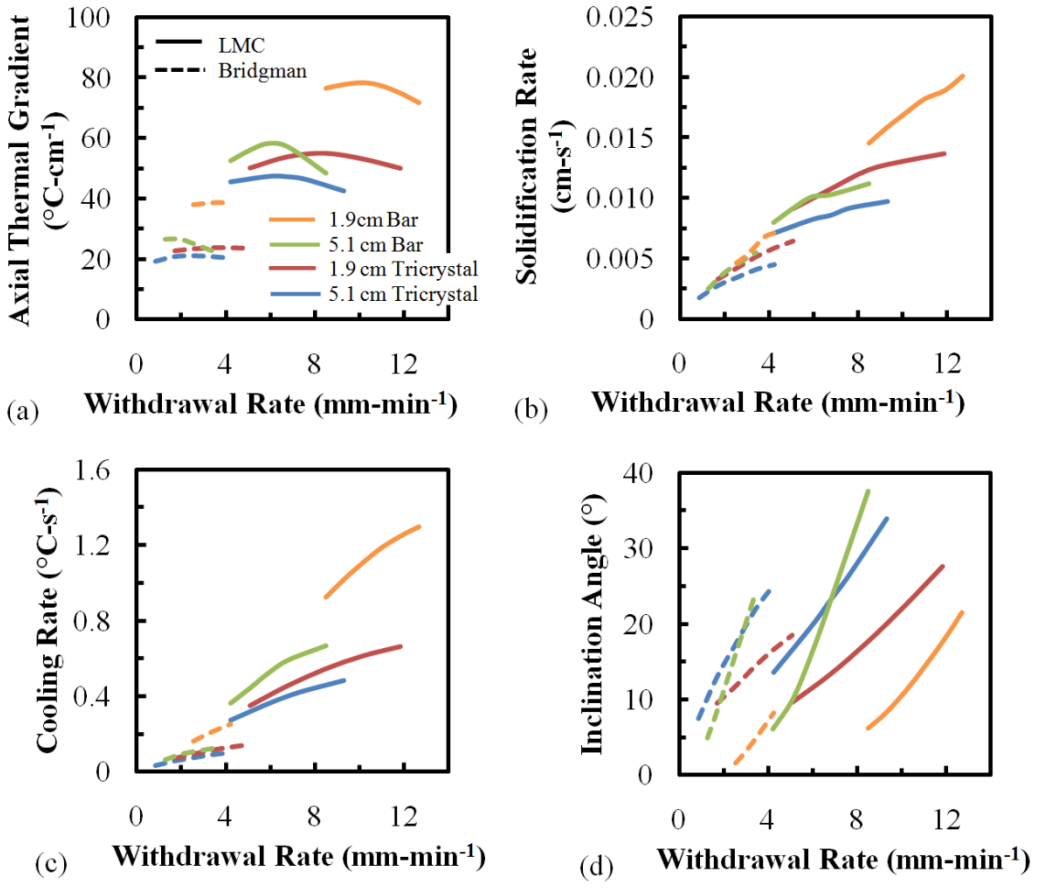

Figure 8.5 – Sensitivity of thermal conditions to withdrawal rate for bar (Chapter 4) and tricrystal (Chapter 5) castings composed of CMSX-486 at two different thicknesses, 1.9 and 5.1 cm: (a) axial thermal gradient, (b) solidification rate, (c) cooling rate and (d) inclination angle.

Alloy composition significantly affected the optimal process conditions and resulting thermal conditions at the solidification front as discussed in Chapter 4. In general, alloys with an increased liquidus temperature had a reduced axial thermal gradient, cooling rate and inclination angle for the same processing conditions. The specific alloy parameters that affect the thermal conditions were not parametrically evaluated. The temperature- and alloy-dependent thermophysical properties utilized as input data to the FE-based solidification modeling are thermal conductivity, heat capacity, heat of fusion, liquidus, melting range, and mold-metal interface heat-transfer coefficient. Future work should evaluate the sensitivity of the thermal conditions to changes in each of these parameters in order to provide a direction for alloy development and castability.

An approach to optimization of thermal conditions was also developed. It was determined that a maximum axial thermal gradient at the surface of the casting occurs when the solidification front (specifically the critical fraction solid of 0.40, Chapter 4) is 3 to 9 mm above the top of the floating baffle for the LMC process and 5 to 15 mm above the fixed baffle for the Bridgman process (Figure 8.6a). The solid-liquid interface inclination angle increases significantly with increasing solidification-front distance below the top of the baffle. In addition, the solidification rate and cooling rate are directly proportional to withdrawal rate, particularly for cases of low inclination angle. By evaluation of multiple withdrawal rates, a maximum axial thermal gradient at a particular location on the surface of the casting can be obtained. Thus, the optimum withdrawal rate can be determined for multiple locations within a casting, ultimately

providing a means to obtain an optimum time-dependent withdrawal rate based on changes in geometry.

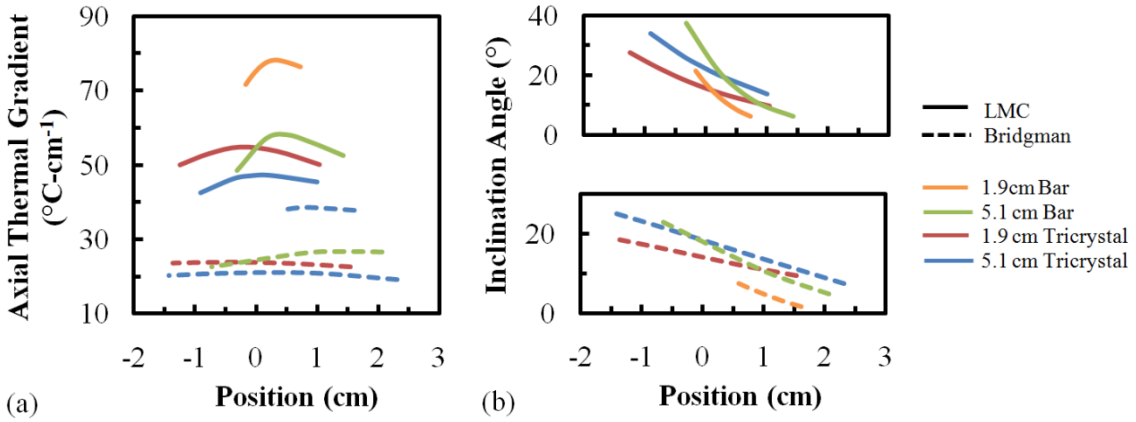

Figure 8.6 – (a) Axial thermal gradient and (b) inclination angle as related to the position in the furnace relative to the top of the baffle.

For instance, this technique can be employed on multiple surface nodes of the casting at different axial heights. By evaluating at least three simulations with different withdrawal rates, the optimal withdrawal rate for each node can be determined. These data can then be combined to define a time-dependent withdrawal rate based on the understanding of solidification front position at different times. More research is needed to demonstrate this approach as a viable means to determine optimal time-dependent withdrawal rate for complex geometries.

In the absence of FE solidification-modeling tools, processing maps for optimized process conditions with changes in section thickness and alloy were obtained for simple casting geometries (Figures 8.7 and 8.8). For the optimal withdrawal rate for each casting thickness, as the section thickness increases, the withdrawal rate, axial thermal

gradient, cooling rate and solidification rate decrease while the inclination angle increases (Figure 8.7). Likewise, for changes in alloy, an increase in liquidus resulted in a decrease in axial thermal gradient, cooling rate and inclination with an increase in solidification rate (Figure 8.8).

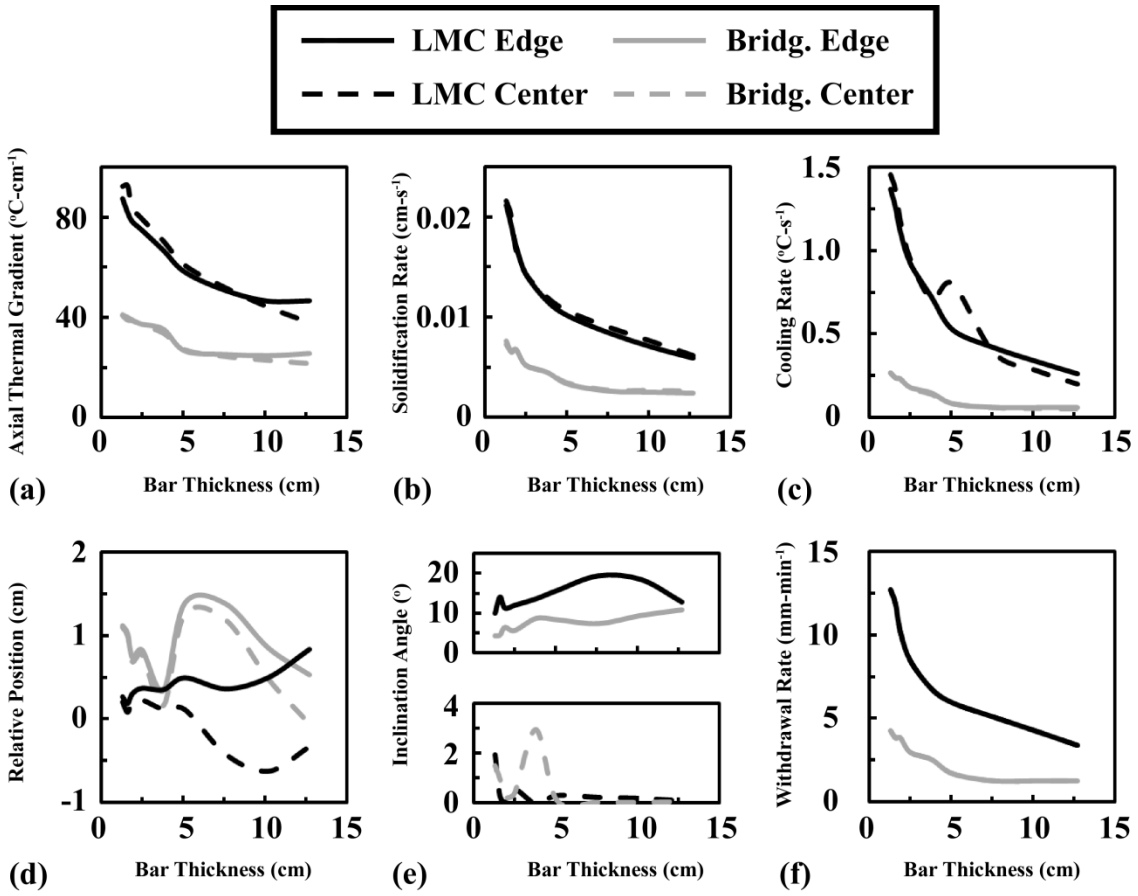

Figure 8.7 – Optimal thermal conditions of a bar mold as related to bar thickness, (a) axial thermal gradient, (b) solidification rate, (c) cooling rate, (d) solidification-front position relative to the top of the baffle, (e) inclination angle and (f) withdrawal rate.

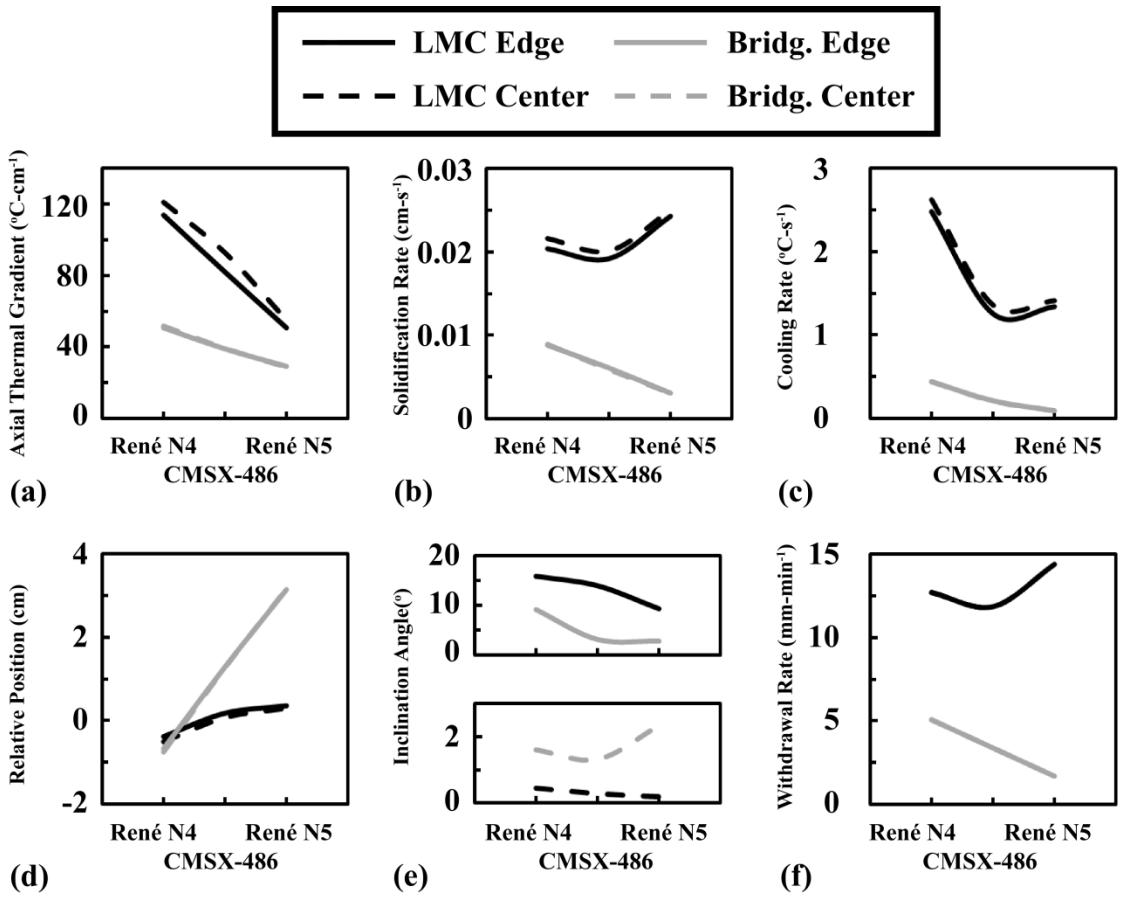

Figure 8.8 – Comparison of optimized thermal conditions for castings with different alloy compositions processed via the Bridgman and LMC conditions, (a) axial thermal gradient, (b) solidification rate, (c) cooling rate, (d) solidification-front position relative to the top of the baffle, (e) inclination angle and (f) withdrawal rate.

These maps can be utilized as a first approximation of the optimal withdrawal rate for casting of a particular thickness and alloy in the absence of solidification models. For example, a casting with a thickness of 2.5 cm and alloy properties similar to CMSX-486 has an optimal withdrawal rate of 3 mm-min^{-1} for the Bridgman process and 8 mm-min^{-1} for the LMC process with a furnace temperature of 1550°C (Figure 8.7f).

Recently, an emphasis on an ICME approach to materials engineering has been proposed [18]. This outlook stresses the importance of considering an integrated, multi-disciplinary approach to the design, manufacturing and life-management of engineering hardware through the insightful utilization of modeling and simulation. The relevance of the ICME goals to this research demonstrates the benefits of solidification modeling: the coupling of solidification modeling with key experimentation for verification and validation, the reduction of pre-production casting trials and the long-term vision of linking processing and performance via microstructure.

This thesis demonstrates an approach wherein significant modeling effort coupled with selective validation experiments could be used to cast a new geometry, determine regimes of dendrite instability, and obtain a deeper understanding of the directional solidification process. Process variables for the single-crystal ring were determined through solidification modeling such that the first experimental trials provided successful castings. In addition, criterion for lateral dendrite growth and breakdown of the solidification front was developed through detailed modeling efforts and selective experimentation. Ultimately, a macroscopic criterion based on inclination angle can now be used to minimize instability of dendrite growth in future casting designs was developed. This would not have been possible with experimentation alone. Therefore, the use of parametric analyses within the simulation space allowed for a fundamental understanding of microstructure evolution and the thermal conditions present during solidification.

A long-term vision for ICME includes the development of modeling tools that unify design, manufacturing and performance of a component into a single design space. In order for this vision to become realizable the microstructure evolution during processing within the casting must be predicted based on the local processing conditions. In turn, the predicted microstructure could then be used as input to mechanical behavior models that incorporate the anticipated environment and predict life. In order to achieve this goal, efforts such as this one are needed to predict microstructure scale - in this case, PDAS and SDAS, but eventually, corresponding precipitate and defect scale. Measurements of PDAS and initiating pore size have been related to high-cycle fatigue life [11]. However, a direct relationship between pore size and PDAS was not identified. Creep has also been associated to the PDAS and thermal conditions during solidification [8]. These relationships do not explicitly consider the mechanisms of creep and fatigue, such as precipitate-rafting or crack-growth kinetics, but instead implicitly utilize the trends of increased precipitate and pore size with increased PDAS. Ultimately, physics-based models are needed to understand the evolution of microstructure in the application environment relative to performance. Overall, the benefits of solidification modeling are invaluable as a base to the future design and manufacturing of cast components.

Microstructure Modeling of Solidification

The primary and secondary dendrite arm spacing can be predicted from dendrite growth equations as discussed previously. The accuracy of these predictions depends on the validity of the model assumptions. The most widely accepted models for predicting

primary dendrite arm spacing assume that the dendrite-growth direction is parallel to the thermal gradient (Equation 8.1) [19,20].

$$\lambda_1 = A_1 {G_z}^{-0.5} V^{-0.25} \tag{8.1}$$

In this equation λ_1 is the PDAS, A_1 is a alloy-dependent parameter, G_z is the axial thermal gradient and V is the solidification rate. Local measurements of dendrite scale have been compared to the predicted thermal conditions at the solidification front and combined with previous results (Figure 8.9) [12]. Different alloys have been observed to have a different sensitivity of dendrtite scale to local thermal conditions (Figure 8.9a). The trend may be associated to combined effects of relative composition of grain-boundary strengthening and solid-solution strengthening elements. Further research is needed to fundamentally explain sensitivity of dendrite scale to the imposed thermal field. Reasonable agreement (within 100 μm) has been achieved with the model proposed by Hunt (Equation 8.1) when the axial thermal gradient is used (Figure 8.9b). If further accuracy is needed, modification to the dendrite-growth model that considers an inclined solidification interface is needed as discussed later in this chapter.

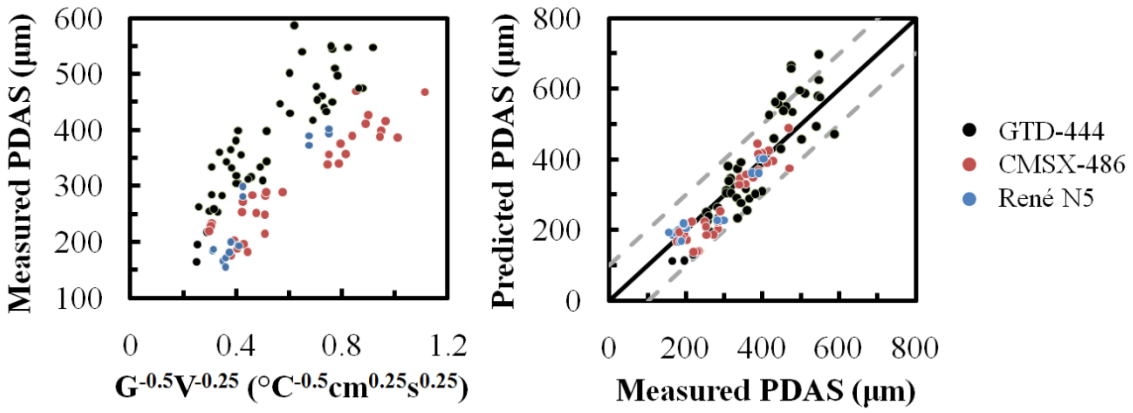

Figure 8.9 – Comparison of PDAS measurements and predictions from this research and from other comparative analyses of the Bridgman and LMC processes [12].

The evolution of microstructure has also been modeled by assuming thermal- or solute-diffusion limited growth. In the case of thermal-diffusion limited growth, the dendrite growth velocity is determined from the undercooling at the dendrite tips [21]. The assumptions of this model break down with abrupt changes in the solute field, which occurs when the dendrite front collides with the casting surface or another dendrite front due to abrupt changes in casting geometry [22,23]. Under these conditions, another model is utilized that predicts dendrite growth according to solute-diffusion-limited growth [24-29]. This model is capable of accurately predicting the dendrite front and its interaction with casting surfaces, but requires significantly more computational expense. A preferred model would operate the thermal-diffusion-limited model and apply a correction factor based on generic growth conditions predicted from the solute-limited-growth model at casting surfaces and collision of dendrite fronts. More research is needed to assess the validity of such a modeling approach.

Models that predict the evolution of dendrite structure typically make assumptions about the alloy composition and associated thermodynamic and kinetic input data. These assumptions have been made (1) for simplification of calculations or (2) in lieu of experimental data of complex material systems. Ideally, the thermodynamic and kinetic input data required for computation are the following: initial alloy composition, partition coefficient, slope of the liquidus line in the phase diagram, diffusion coefficients in the solid and liquid and the melting temperature of the pure metal. For multi-component systems, these input data are required for each alloying element. Thus, it becomes

readily apparent why the multi-component alloy systems are represented as binary alloys within the model framework. More research is needed to obtain the thermodynamic and kinetic data for multi-component alloy systems and develop models that can incorporate the multi-component data. At the same time, a further understanding of the sensitivity of dendrite growth to changes in the binary alloy parameters, such as the work by Lee and coworkers [30], is needed.

In order to improve upon the state-of-the-art modeling tools utilized today, the assumptions of the solute-diffusion-limited-growth model used in this effort were assessed. This model, developed by Lee and coworkers, performs a Monte Carlo calculation for nucleation, a finite difference (FD) approximation to predict the evolution of the solute field and a cellular automaton approach to model the dendrite growth [24-29]. The major approximations of this model are the simplification of the alloy to a binary, the use of a pre-defined thermal field, the presence of a diffuse solid-liquid interface and the corresponding application of a CA growth parameter that prevents growth to the next cell until a specified fraction solid is achieved in the preceding cell.

The first approximation simplifies the calculation of the solute field and alleviates the need for multi-component kinetic input data. With the maturity of kinetic models, the input data required of multi-component dendrite growth models is modeled and could be considered for accurate prediction of engineering alloys. This improvement to the models is possible but limits computational efficiency.

The second approximation assumes that the temperature field is independent of the solute field. This assumption was applied for simplification, such that simultaneous calculation of the thermal and solutal fields was unnecessary. However, because the thermal field is affected by solidification and diffusional processes, improved dendrite-growth models should allow for the interaction.

The other two approximations allow a large grid size that enable the evaluation of large spatial domains but prevent the calculation of the curvature of the solidification front. The curvature of the solidification front contributes to dendrite growth, defines the coarsening behavior of the secondary dendrite arms and thus the SDAS, and predicts freckle formation due to convective instabilities and partial melt-back of the solidification front. Future efforts on dendrite-growth modeling should focus on development of a model that is able to predict the curvature of the dendrite front over large spatial domains without prohibitive computational expense. The model framework that may provide this capability is the level-set modeling approach [31]. More research is needed to evaluate the applicability of this approach to dendrite-growth modeling within alloy systems.

Dendritic Growth during Solidification

The formation of dendrite structure during directional solidification has been evaluated extensively over the past three decades. A drive to predict a unique PDAS for a given set of thermal conditions has been ongoing [12,19,20,32-45]. However, it has been demonstrated that a range of PDAS exists for a given set of thermal conditions [24,46-

48]. Ultimately, the prediction or measurement of microstructure scale could be used to predict the scale of the underlying defect structure, which could then be used to evaluate mechanical performance. With this goal in mind, the variability of microstructure within a given thermal condition must be established to determine a distribution of dendrite scale for a given thermal condition (Figure 8.10) [49]. In order to establish this distribution, the arrangement of primary dendrites and a thermally-stable range of PDAS must be assessed.

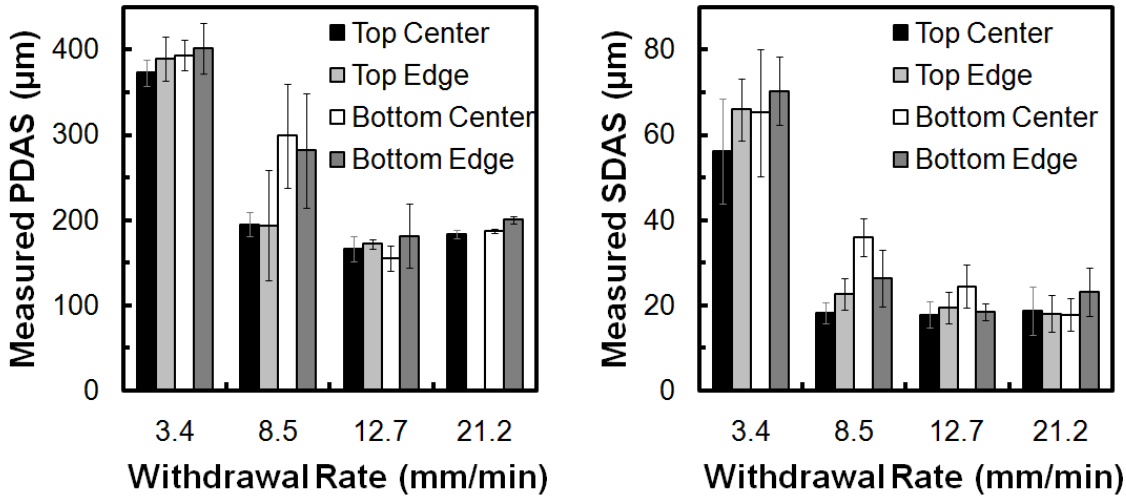

Figure 8.10 – (a) Primary and (b) secondary dendrite arm spacing variability for positions within bar molds with different thermal conditions and for different withdrawal rates.

Measurements of microstructure scale in regions of lateral and axial growth in this effort indicate a strong dependence of dendrite scale on local thermal conditions in both the axial and transverse primary orientations. The secondary dendrite arm spacing in the axial and both radial directions at the same location was within 5 pct (Figure 8.11). The primary dendrite arm spacing (of secondary arms growing into the plane) in the longitudinal plane within a region of lateral growth was 15 pct finer than the primary

dendrite arm spacing in an axial growth region with similar thermal conditions (Figure 8.11). This difference could be (1) associated to the difference in the solidification-front inclination angle relative to the two growth directions as proposed by Grugel [50], (2) an indication of transient growth conditions which may not be sustainable over long distances, or (3) associated to local packing configuration which is unrelated to the thermal field. Additional assessment of these dendrite-growth morphologies is needed to establish the structure differences as well as defect sizes and distributions between axial and lateral growth.

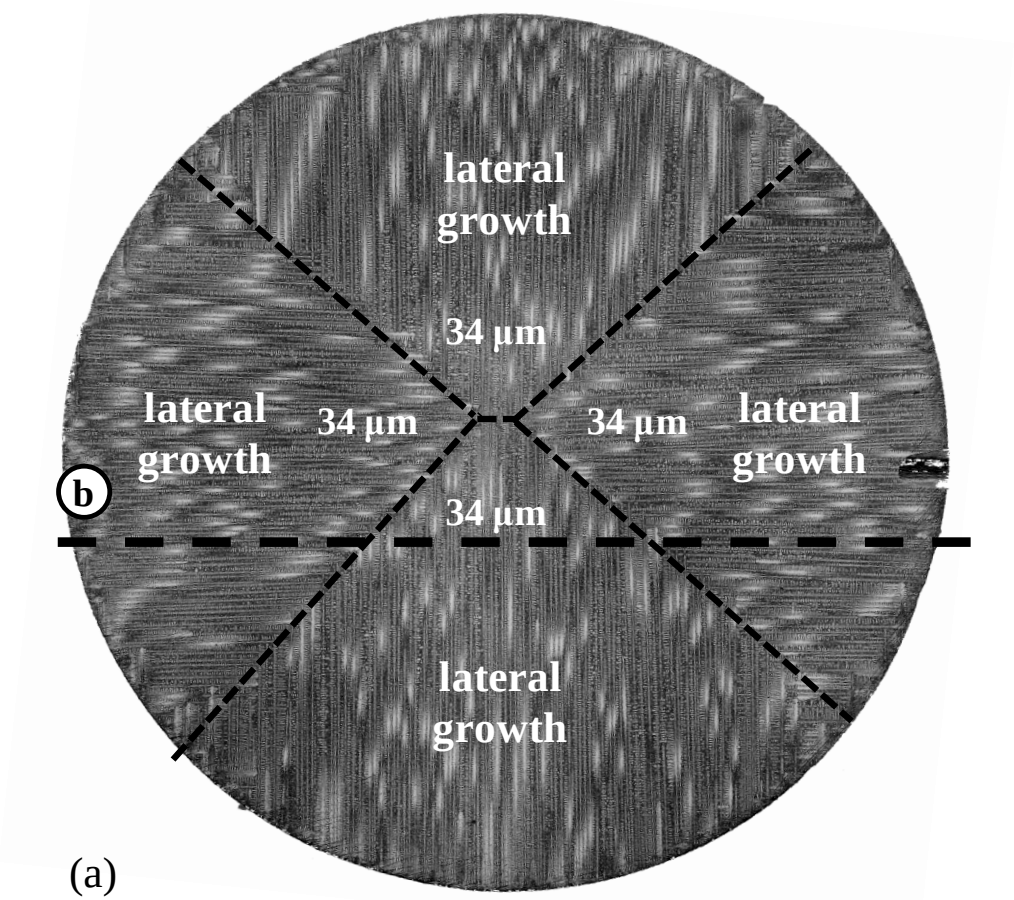
lateral
growth
34 μm
lateral
growth
34 μm
34 μm
lateral
growth
b
34 μm
lateral
growth

(a)

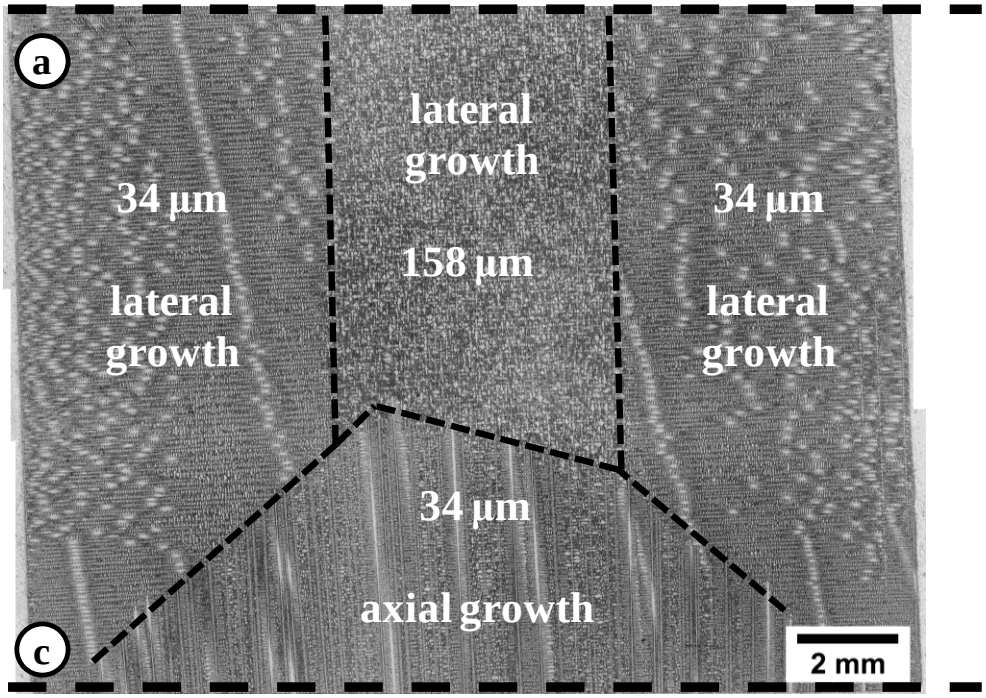
a
lateral
growth
34 μm
34 μm
158 μm
lateral
growth
lateral
growth
34 μm
axial growth
c
2 mm

(b)

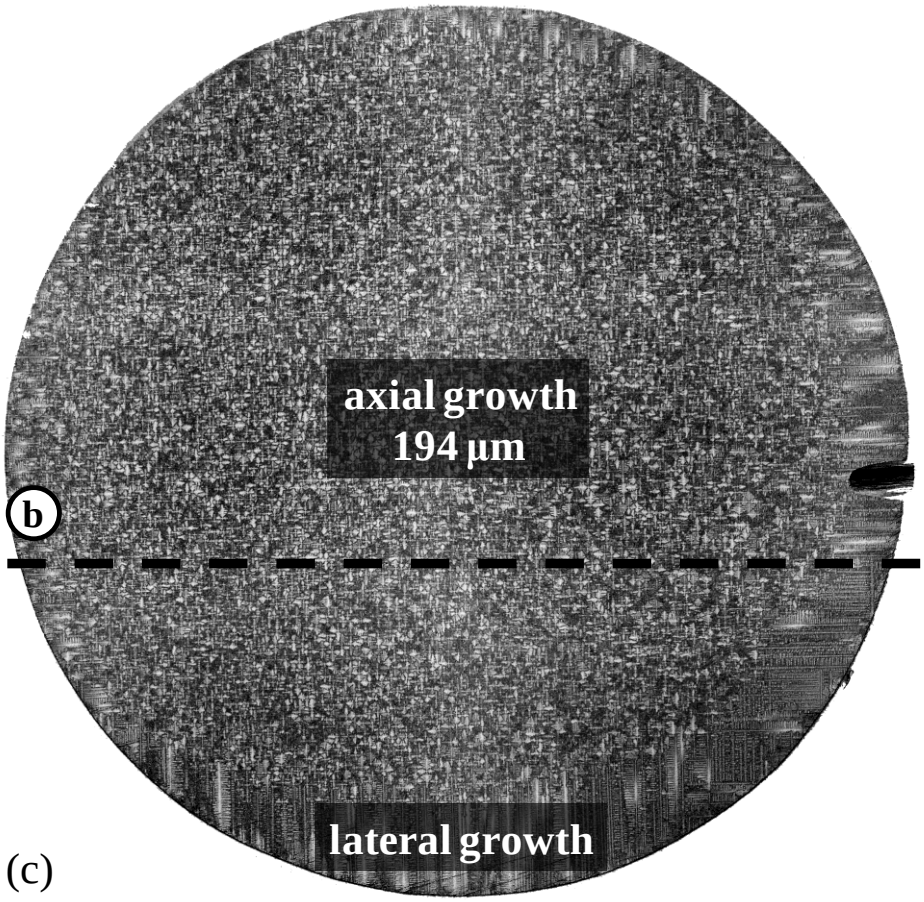

Figure 8.11 – (a) Transverse micrograph within lateral growth region positioned at the top of longitudinal micrograph (b) within transition region. Transverse micrograph (c) corresponds to a transverse section at the bottom of longitudinal micrograph (b). The longitudinal section (b) is marked in (a) and (c) for comparison. Regions of dendrite growth are separated by small dashed lines, and microstructure measurements are shown.

Brundidge has conducted a preliminary local assessment of dendrite scale with Voronoi Tessellations to provide a more detailed description of the dendrite structure (Figure 8.12) [51]. This work has demonstrated the need for a more locally-representative metric for microstructure scale in lieu of PDAS that relates the local dendrite structure to its local defect structure. For instance, a relationship between the size of a pore, the magnitude of the interdendritic region in which it resides and the scale of the neighboring

dendrites could provide the information needed to predict local fatigue behavior based on thermal conditions during solidification.

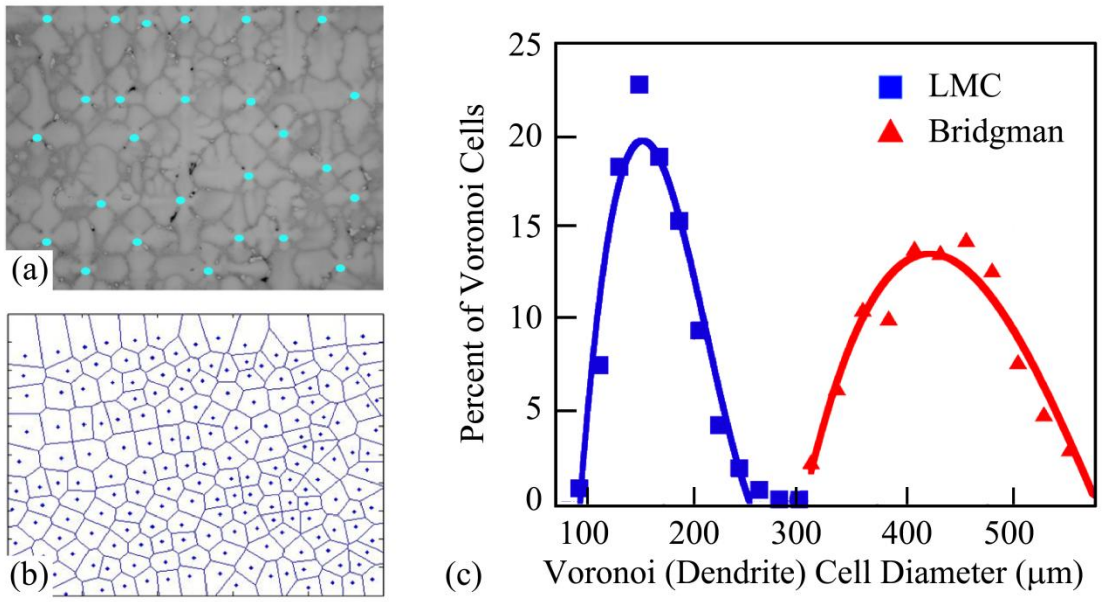

Figure 8.12 – (a) Identification of primary cores for centroids of Voronoi Tessellation, (b) Voronoi Tessellation of dendrite cores from a transverse micrograph and (c) distribution of cell area [51].

Correlation of dendrite scale and pore size has been evaluated using a modified technique of the Voronoi analysis described previously (Figures 8.13). The determination of a relationship requires significant characterization and analysis, including three-dimensional digital reconstruction of local dendrite and defect structure [52]. Research associating the dendrite scale to mechanical performance suggests that a relationship exists [8,10,11]. However, significant research is needed to prove the existence of such a relationship, or whether the stochastic nature of grain nucleation, dendrite branching, and dendrite competition limit the effectiveness of such an ambitious undertaking. Regardless, the benefit of such a relationship warrants further investigation.

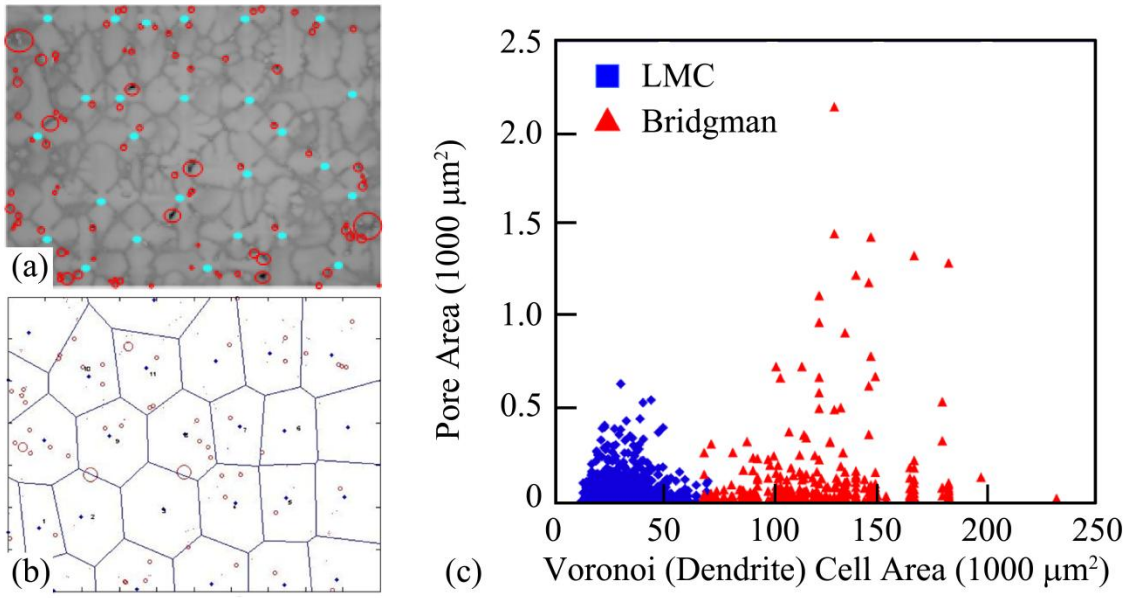

Figure 8.13 – (a) Identification of primary cores for centroids of Voronoi Tessellation with pore areas superimposed into primary core Voronoi cells, (b) Voronoi Tessellation of dendrite cores with superimposed pore areas from a transverse micrograph and (c) relationship between pore area and respective Voronoi cell area [10].

Microstructure Evolution and Non-Axial Thermal Fields

This thesis has demonstrated that minimizing the inclination angle (preferably to less than 25°) of the solidification front during processing, especially with the LMC process, is essential for control of the unidirectional dendritic-growth process. Superposition of experimental data from this thesis onto the solidification map discussed in Figure 1.4 was performed to summarize the effect of inclination angle (Figure 8.14). When the thermal conditions at the solidification interface are considered in this manner, the onset of nucleated grains due to inclination (black points) occurs at a similar thermal condition as the transition from axial to equiaxed growth, defined by the processing map (Figure 8.14). This finding demonstrates that solidification morphology and the formation of

defects are dependent on *axial* thermal gradient and *axial* solidification rate. Experiments and modeling have demonstrated that increased solidification-front inclination angle affects (1) dendrite scale, (2) the formation of lateral growth, and (3) grain nucleation and undesirable competitive grain growth. Each of these points is discussed in turn.

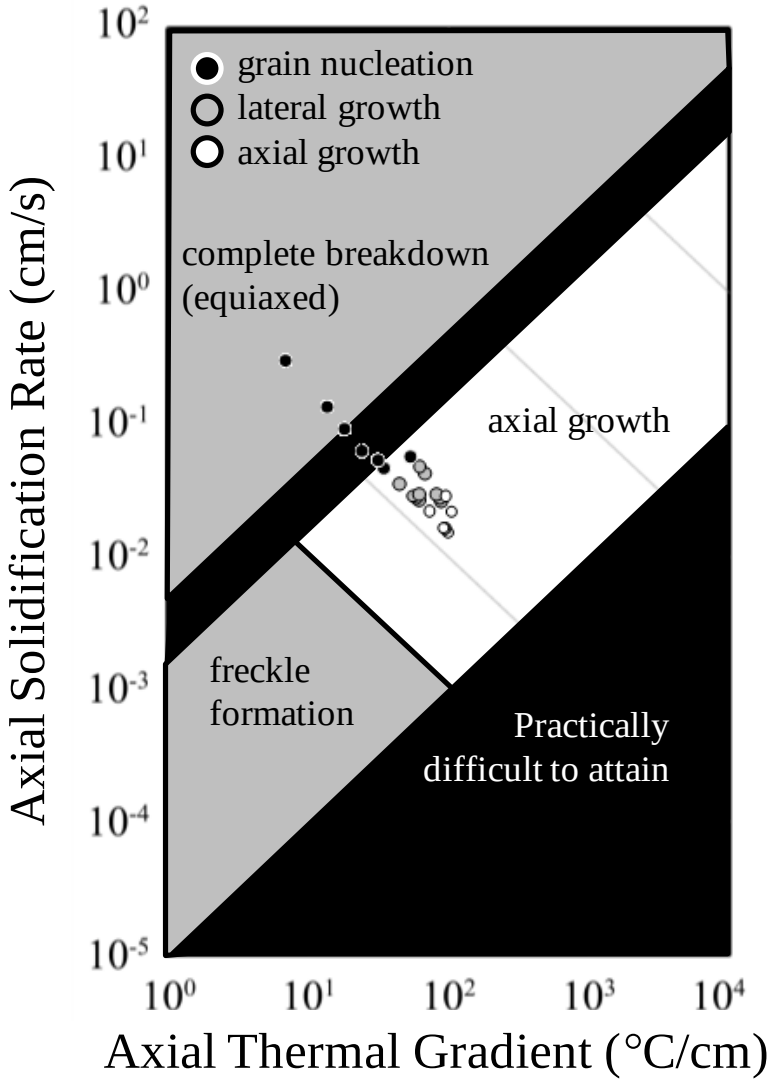

Figure 8.14 – Solidification map identifying dendrite morphology and defect formation based on the thermal conditions at the solidification front with superimposed thermal conditions and observed dendrite morphology from the lateral-growth study of Chapter 6.

Discrepancies between experimental measurements and predicted PDAS for Bridgman and LMC processes indicate a breakdown in the dendrite growth equations with utilization of LMC (Figure 8.9). The measurements of PDAS are coarser than predicted by the dendrite growth equation. This discrepancy can be partially attributed to the increased inclination angle with utilization of the LMC process.

Grugel and Zhou demonstrated an increase in PDAS with increased inclination angle up to 45° for a fixed thermal gradient and solidification rate [50]. The authors observed an increase of PDAS up to 58 pct due to an increase in the inclination angle [50]. These data have been reanalyzed to evaluate the accuracy of the PDAS in the modified dendrite growth model proposed (Equation 8.2).

$$\lambda_1 = \frac{A_1 {G_Z}^{-0.5} V^{-0.25}}{cos(\phi)} \tag{8.2}$$

In this equation G_Z is the thermal gradient in the [001] direction of the single crystal and Φ is the solidification-front inclination angle relative to horizontal. This modification provides improved agreement with the original measurements of Grugel and Zhou for changes in inclination (Figure 8.15) [50]. The disagreement of predicted and measured PDAS for the work of Grugel and Zhou in the absence of inclination, black points of Figure 8.15b, suggests that steady-state solidification was not attained during the expeiriment. In general, Equation 8.2 is more accurate than the original equation proposed by Hunt for prediction of primary dendrite arm spacing in the presence of a non-axial thermal field.

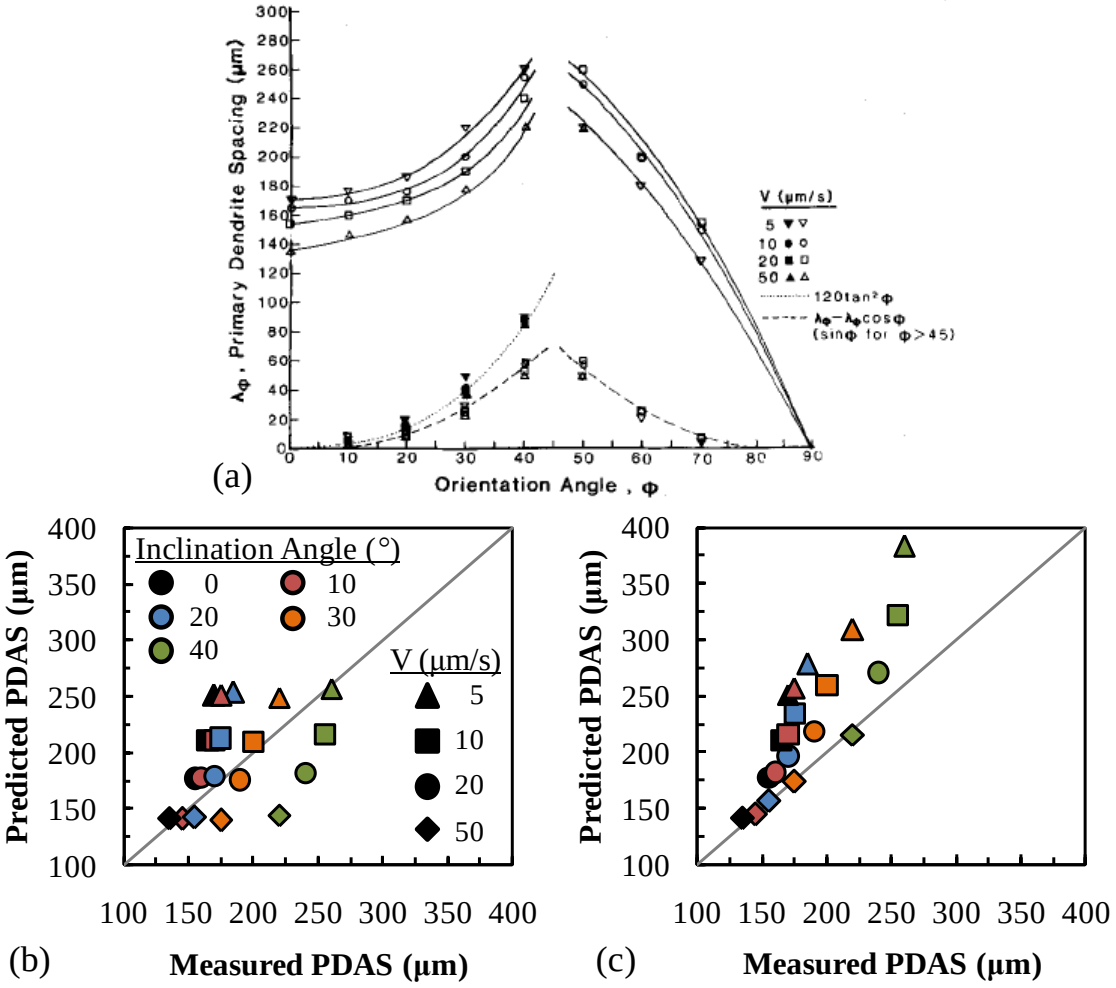

Figure 8.15 – Reanalysis of the (a) sensitivity of PDAS to solidification-front inclination angle (from [50]) and predictions of PDAS using the (b) original and (c) modified dendrite-growth equations as compared to experimental measurement [50].

Stability of single-crystal growth is also affected by an increased solidification-front inclination angle. It has been demonstrated in this effort that an increased inclination angle increases the propensity for lateral growth, with the observed onset of lateral growth occurring as low as 25°, depending on the off-axis misorientation of the single crystal. In addition, experimental observations of nucleated grains indicated an increase in nucleation probability with increasing inclination angle. Grain nucleation has been

observed when the inclination angle exceeds 45°. Grain nucleation occurs when the undercooling of the melt ahead of the solidification front reaches a critical range and a nucleus is present [23]. In general, an increase in pulling velocity increases the propensity for grain nucleation due to an increase in undercooling. Thus, there are two fundamental explanations for increased grain nucleation in the presence of a non-axial thermal field: (1) presence of lateral growth increasing the undercooling at the wall and (2) increased local solidification rate due to increased pulling velocity.

As the inclination angle increases under transient conditions, the magnitude of the solidification rate normal to the solidification front is higher than the pulling velocity due to an increasing inclination angle, Figures 6.14 and 6.15. Therefore, there is an apparent solidification rate increase in regions of high inclination angle. This is important because nucleation probability has been associated to local solidification rate [23]. Thus, regions of high inclination angle have an increased propensity for grain nucleation and can be predicted by evaluation of local solidification rate. The wrapped-bar mold utilized in Chapter 6 could be used to determine the onset of nucleation experimentally, which could then be compared to FE-based predictions of the solidification rate and ultimately CAFD predictions of undercooling. This work could provide a means (1) to compare nucleation propensity of different alloys as a screening for alloy development and (2) to determine the critical undercooling for different alloys for use in solidification models. More research is needed to determine if this is feasible.

The presence of lateral growth at the solidification front may increase the propensity to form a nucleated grain. When the dendrites are primarily growing transverse to the pulling direction, there is a delay in the solidification front proceeding upwards that is associated to the development and growth of tertiary arms parallel to the pulling direction (Figure 8.16). This delay in growth may cause an increase in undercooling ahead of the solidification front above the presence of lateral growth. These two fundamental hypotheses of increased undercooling demonstrate how an inclined solidification front can impact the macrostructure of a desired single crystal casting.

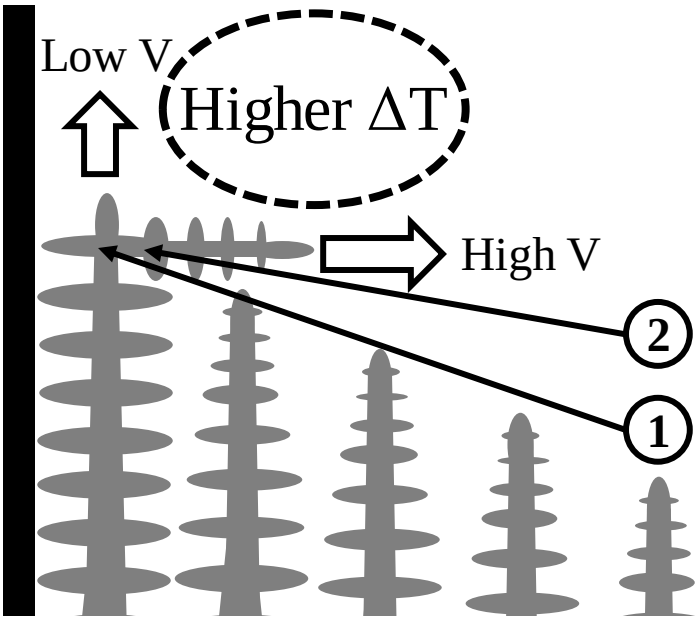

Figure 8.16 – Schematic or dendrite growth in a region comprised of lateral growth, indicating secondary (1) and tertiary (2) nucleation events required to advance dendrite front upwards and the relative growth velocities of the axial and lateral dendrites.

Once a misoriented grain nucleates at the wall according to the above description, competitive growth between the nucleated grain and the single-crystal dendrite front occurs. As was shown previously, the inclined solidification front promotes overgrowth

of the single-crystal dendrite front by the nucleated grain at the wall due to better alignment of the nucleated dendrite with the thermal gradient relative to the primary orientation of the original dendrites (Figure 8.17). For instance, a dendrite whose primary orientation is diverging from the wall has a primary orientation better aligned with the thermal gradient than the dendrites whose primary orientation is parallel to the pulling velocity.

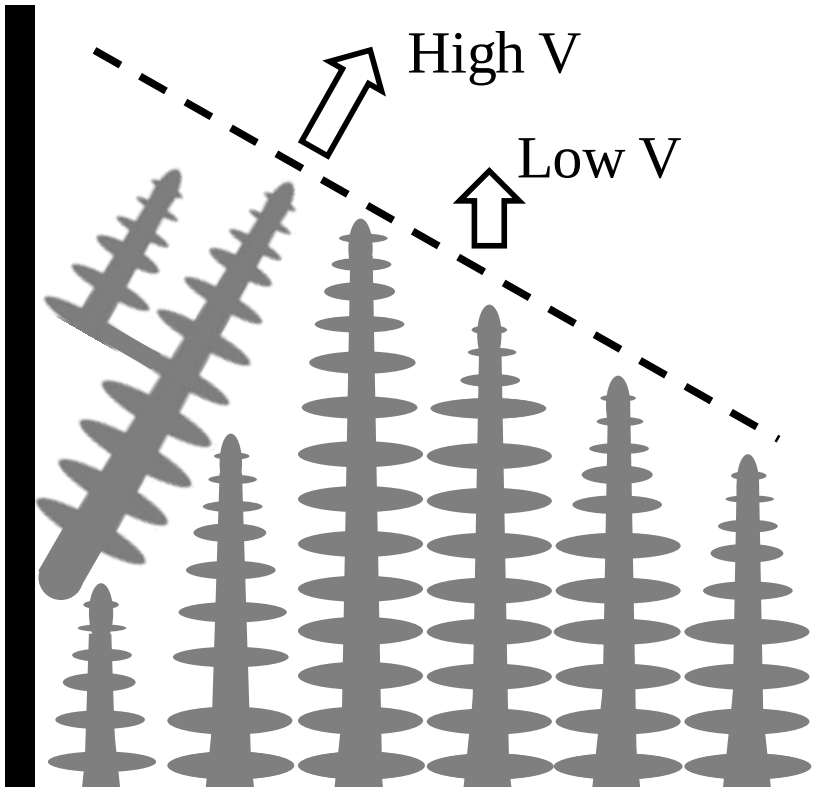

Figure 8.17 – Schematic of dendrite competition between a nucleated dendrite and the original dendrite field in the presence of a non-axial thermal field. The relative magnitude of the growth velocity is depicted by the size of the arrow ahead of the dendrite tips.

Overall, the inclined solidification front decreases the likelihood of having a finely-spaced single-crystal dendritic structure comprised of dendrites which have limited

tertiary growth. Therefore, the curvature of the solidification front should be minimized in order to achieve optimal solidification conditions and the highest yield possible.

Implications of Lateral Growth on Mechanical Response

This research has contributed significant fundamental insights to the problem of lateral growth. A mechanism for the formation of lateral growth has been established, as well as a macroscopic criterion for predicting its formation based on the inclination angle of the solidification front. It has been demonstrated that lateral growth is an indication of process conditions near the threshold of defect formation. As described in the previous section, the presence of lateral growth leads to an increased undercooling ahead of the solidification front that may promote grain nucleation. A further understanding of lateral growth could be obtained by (1) detailed assessment of the defect structure within regions of lateral growth, (2) comparison of the mechanical response in regions of axial and lateral growth, and (3) application of new insights to complex casting geometries.

In spite of morphological disturbances, high-angle boundaries are not necessarily present in regions of lateral growth. However the change in the dendrite structure may have implications for the associated defect structure (porosity, carbides and eutectic). In addition, a higher population of defects may be present at the boundary between axial and lateral growth. A detailed microstructural assessment in regions of axial growth, lateral growth and at the interface could provide insight to the evolution of defects as it relates to the surrounding dendrite structure. Key questions are whether (1) the pore size and

frequency depend on the orientation of the dendrites relative to the growth direction and (2) if there is an increased defect population at the interface between axial and lateral growth despite the absence of a true grain boundary.

The potential difference in defect structure within axial and lateral growth, as well as the interface between the regions motivates the need for mechanical tests dependent on the defect structure. For the alloys investigated in this research, the pore size limits the fatigue resistance at low temperatures for typical single-crystal growth [10]. A direct correlation between pore size at the initiation site and fatigue life has been demonstrated via a fracture-mechanics approach [51]. Thus, differences in fatigue life at low temperature from test specimen excised from regions of axial and lateral growth can identify differences in pore size.

Prior to this research, a method to produce test specimens in which lateral growth was present within the gauge section had not been developed. The mold configuration utilized in Chapter 6 can be modified to induce lateral growth in the center of a bar by axial translation of the mold-wrap location. Various sizes of the lateral growth region could be investigated to evaluate the effect of complete axial growth, complete lateral growth (Figure 8.18) and the presence of an interface between the dendrite growth regimes (Figure 8.19). With the proposed fatigue tests, if the failure mechanism changes, then there is a definitive microstructural difference that requires further examination. On the other hand, if the fatigue resistance is limited by pore size, then examination of the

initiation sites may identify a difference in defect size for the two microstructure regimes [51].

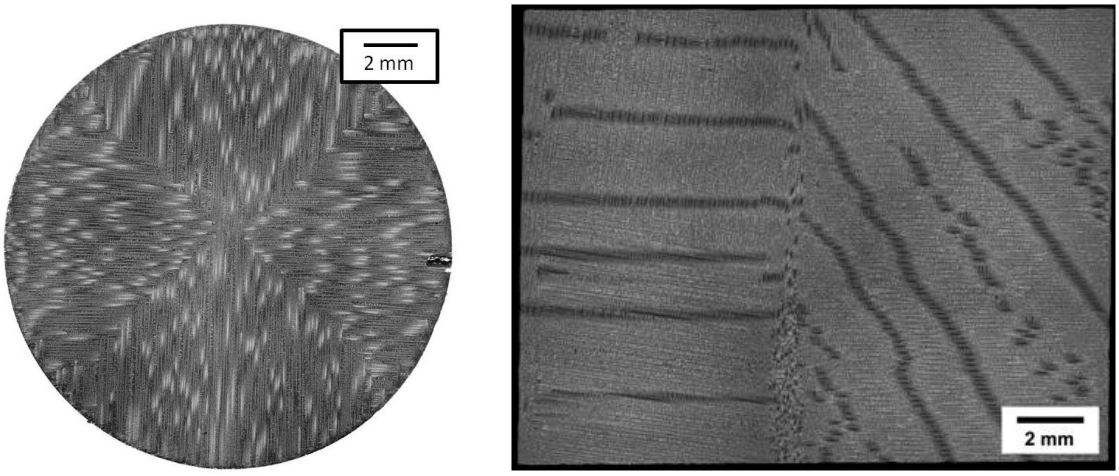

Figure 8.18 – Micrographs of complete lateral growth, (a) transverse and (b) longitudinal to the growth direction.

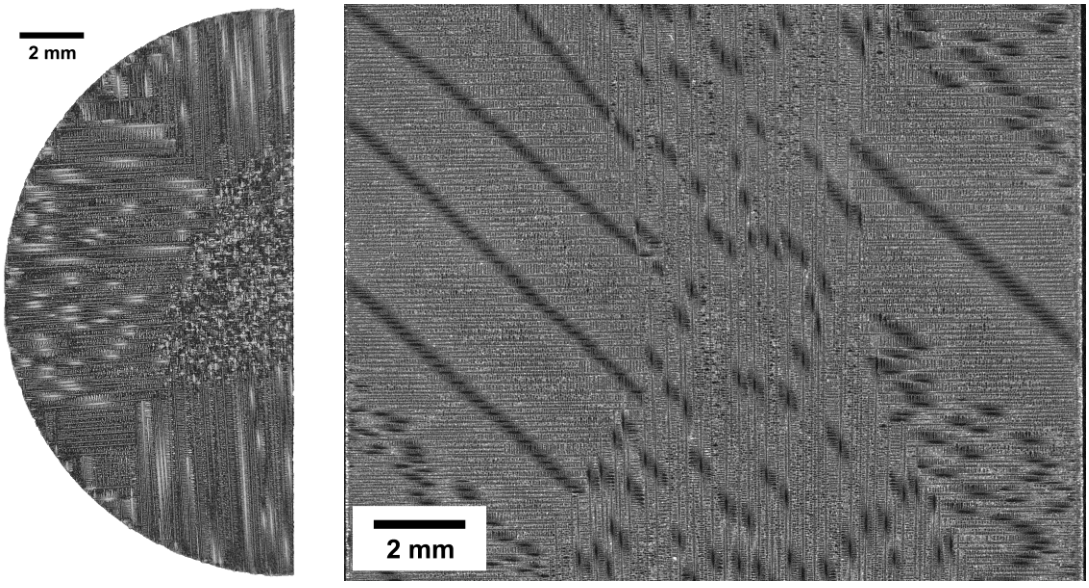

Figure 8.19 – Micrograph of lateral growth at the surface of the casting with axial growth in the center (a) transverse and (b) longitudinal to the growth direction.

Application of the insights of lateral growth obtained in this research to complex geometries is desirable. In this research, lateral growth occurred due to the presence of a non-axial thermal field within a simple geometry. In engineering components, lateral growth has been observed due to abrupt changes in cross-section, such as the platform region of an airfoil [22,53,54]. A potential difference in the formation of lateral growth under these conditions is the formation of two dendrite fronts that ultimately collide above the root of the airfoil internal to the platform (Figure 8.20) [22]. The morphology of this interface is anticipated to be different than the morphology of the interface between the axial and lateral growth regimes investigated in this research. Further research is needed (1) to determine if thermally-induced lateral growth is identical to geometrically-induced lateral growth and (2) to evaluate the applicability of the macroscopic criterion for lateral growth formation to complex geometries. Overall, these proposed assessments in this section can provide the information needed to thoroughly understand the formation *and behavior* of lateral growth due to abrupt thermal *or geometrical* changes during processing.

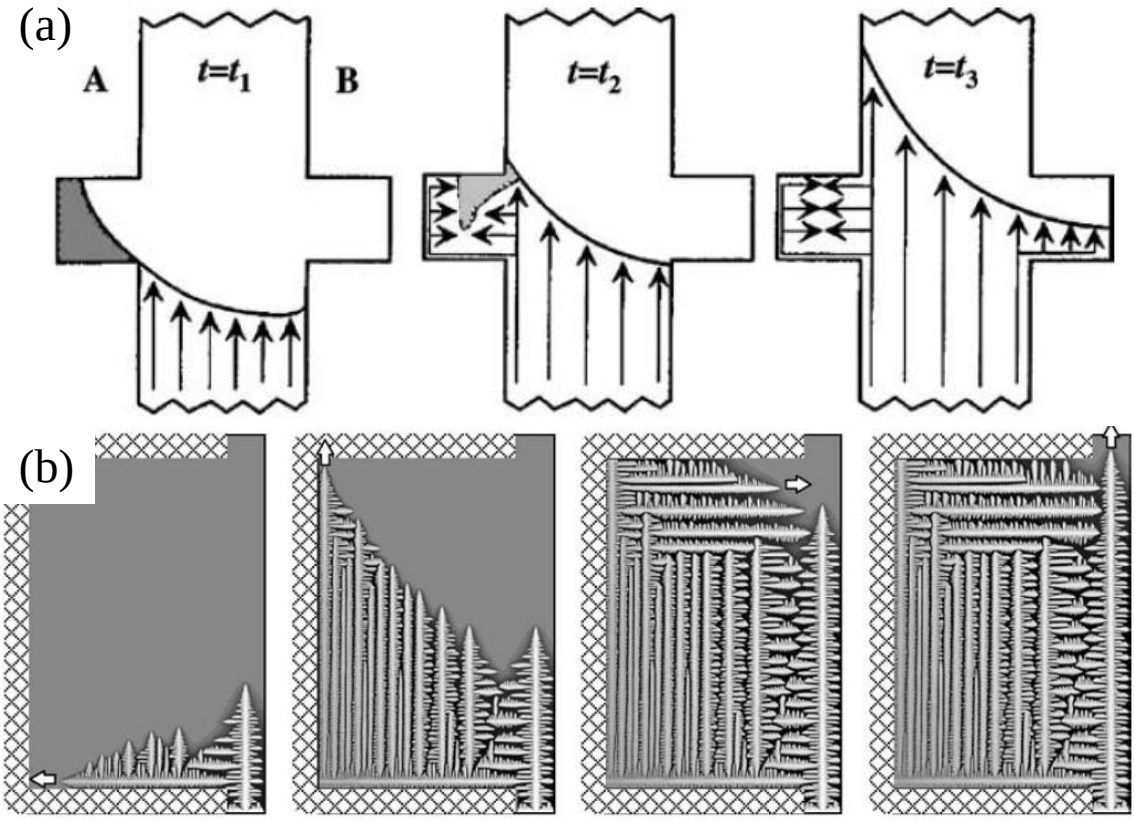

Figure 8.20 – (a) Schematic of solidification of platform region (from [22]) and (b) microstructure prediction indicating collision of dendrite fronts (from [22]).

Summary

Novel processing approaches such as the LMC process provide unique opportunities for revolutionary increases in material performance relative to the conventional processing approaches. Consideration of the fundamental features of the LMC solidification process and the inherent differences compared to conventional processing has permitted physically-realistic process models to be developed. These models can be employed to obtain single-crystal and directionally-solidified materials with improved performance via the LMC process.

In this research, process-simulation and microstructure-modeling tools have been employed to establish a better fundamental knowledge of the LMC process. The relative importance of process variables to the formation of dendrite structure has been assessed, ultimately providing an optimal process configuration for one of the key materials to the success of LMC process, the floating baffle. Solidification models have been validated on multiple geometries and process conditions, resulting in a physically-reliable set of model parameters that appropriately capture the physics of the directional solidification process and are applicable to the modeling of directional solidification in general.

The ability of the LMC process to manufacture single-crystal materials possessing atypical casting geometries has been demonstrated. A viable processing route for the manufacture of a single-crystal ring has been identified. The refinement of microstructure scale through utilization of the LMC process has been demonstrated, resulting in a factor-of-two improvement to the refinement of microstructure. The decreased propensity for formation of convective-type defects such as freckles has also been demonstrated. The microstructure variability observed due to changes in the thermal conditions during solidification, as well as the variability within a unique thermal condition has been quantified and compared to microstructure predictions.

The impact of the increased lateral heat extraction inherent to the LMC process to the thermal conditions during solidification and ultimately the formation of the dendritic structure has been determined. The influence of solidification-front curvature on

microstructure scale has been characterized. Modifications of dendrite growth equations have been developed to account for the inclined solidification front. The propensity for lateral growth and grain nucleation has been related to the increased solidification-front curvature. Experimental observations on dendritic structures in castings exposed to a range of process conditions have been compared to predictions based on thermal conditions present during solidification. A geometrically-independent, macroscopic criterion has been developed for the onset of lateral growth. The mechanisms of lateral overgrowth have been investigated in detail via microstructure models and compared to actual microstructures from experiment. The sensitivity of the onset of lateral growth to thermal conditions and orientation of the single crystal has been established.

The importance of the orientation of the single crystal relative to the withdrawal direction on the ability to produce a single crystal with fine-scale dendritic structure and no high-angle grain boundaries has been demonstrated. The preferential selection of off-[001] misoriented dendrites within the starter region for the LMC process has been related to the inclined solidification front below the starter. A method to optimize tunable process conditions independent of casting thickness has been defined, in which the position of the solid-liquid interface at the surface of the casting relative to the top of the baffle has been used as a metric to determine the process conditions that would provide the maximum axial thermal gradient and minimum solidification-front inclination angle. The dominant heat-transfer mechanism during solidification has been determined, providing a direction for future research to maximize heat extraction.

References

1. A. Kermanpur, N. Varahram, P. Davami and M. Rappaz, *Metall and Mater Trans B*, 31B (2000) 1293-1304.

2. J. Grossmann, J. Preuhs, W. Esser and R.F. Singer, Proceedings of the 1999 International Symposium on Liquid Metal Processing and Casting, eds. A. Mitchell, L. Ridgway and M. Baldwin (The Minerals, Metals & Materials Society, 1999) 31-40.

3. A. Lohmüller, W. Esser, J. Grossman, M. Hördler, J. Preuhs and R.F. Singer, *Superalloys 2000*, ed. T.M. Pollock, R.D. Kissinger, R.R. Bowman, K.A. Green, M. McLean, S.L. Olson, and J.J. Schirra (Warrendale, PA: TMS, 2000) 181-188.

4. L. Liu, T.W. Huang, J. Zhang and H.Z. Fu, *Material Letters*, 61 (2007) 227-230.

5. C. Liu, J. Shen, J. Zhang and L. Lou, *J Mater Sci Technol*, 26 (4) (2010) 306-310.

6. J. Zhang and L.H. Lou, *J Mater Sci Technol*, 23 (2007) 289-300.

7. A. Kermanpur, N. Varahraam, E. Engilehei, M. Mohammadzadeh and P. Davami, *Mat Sci Technol*, 16 (5) (2000) 579-586.

8. P.N. Quested and M. Mclean, "Effect of Variations in Temperature Gradient and Solidification Rate on Microstructure and Creep Behaviour of IN 738LC," *SolidificationTechnology in the Foundry and Cast House* (London: The Metals Society, 1983), 586-591.

9. S. Balsone, G. Feng, L. Peterson and J. Schaeffer, *Solidification Processes and Microstructures: A Symposium in Honor of Wilfried Kurz*, ed. M. Rappaz, C. Beckermann and R. Trivedi (The Minerals, Metals & Materials Society, 2004) 77-83.

10. C. Brundidge, D. VanDrasek, B. Wang and T.M. Pollock, *Proceedings of the 2009 International Symposium on Liquid Metal Processing and Casting*, ed. P.D. Lee, A. Mitchell and R. Williamson (The Minerals, Metals & Materials Society, 2009) 107-117.

11. M. Lamm and R.F. Singer, *Metall and Mater Trans A*, 38 (2007) 1177.

12. A.J. Elliott, "Directional Solidification of Large Cross-Section Ni-Base Superalloy Castings via Liquid Metal Cooling," (Ph.D. thesis, University of Michigan, 2005).

13. T. Strangman, "Integral turbine composed of a cast single crystal blade ring diffusion bonded to a high strength disk," (U.S. Patent No. 6,969,240), 29 Nov 2005.

14. A.J. Elliott and T.M. Pollock, *Metall and Mater Trans A*, 38 (2007) 871-882.

15. T.J. Fitzgerald and R.F. Singer, *Metall Trans A*, 28 (1997) 1377-1383.

16. A.F. Giamei and J.G Tschinkel, *Metall and Mater Trans A*, 7 (1976) 1427-1434.

17. F. Hugo, U. Betz and J. Ren, *Proceedings of the 1999 International Symposium on Liquid Metal Processing and Casting*, eds. A. Mitchell, L. Ridgway and M. Baldwin (The Minerals, Metals and Materials Society, 1999) 16-30.

18. T.M. Pollock, J.E. Allison, D.G. Backman, M. Boyce, M. Gersh, E.A. Holm, R. LeSar, M. Long, A.C. Powell IV, J.J. Schirra, D.D. Whitis and C. Woodward, *Integrated Computational Materials Engineering*, (Washington DC: National Acadamies Press, 2008).

19. J.D. Hunt, *Solidification and Casting of Metals*, ed. J.D. Hunt (London: The Metals Society, 1979), 3-9.

20. W. Kurz and D.J. Fisher, *Acta Metall*, 29 (1) (1981) 11-20.

21. W. Kurz, B. Giovanola and R. Trivedi, *Acta Metall*, 34 (5) (1986) 823-830.

22. W. Wang, A. Kermanpur, P.D. Lee and M. McLean, *J Mater Sci*, 38 (2003) 4385-4391.

23. X.L. Yang, H.B. Dong, W. Wang and P.D. Lee, *Mat Sci Eng A*, 386 (2004) 129-139.

24. W. Wang, P.D. Lee and M. McLean, *Acta Metall*, 51 (2003) 2971-2987.

25. P.D. Lee, A. Chirazi, R.C. Atwood and W. Wang, *Mat Sci Eng A*, 365 (2004) 57-65.

26. R.C. Atwood and P.D. Lee, *Metall and Mater Trans B*, 33B (2002) 209-221.

27. H.B. Dong and P.D. Lee, *Acta Mater*, 53 (2005) 659-668.

28. P.D. Lee and J.D. Hunt, *Acta Mater*, 49 (2001) 1383-1398.

29. P.D. Lee, R.C. Atwood, R.J. Dashwood and H. Nagaumi, *Mat Sci Eng A*, 328 (2002) 213-222.

30. X.L. Yang, P.D. Lee, R.F. Brooks and R. Wunderlich, *Superalloys 2004*, ed. K.A. Green, T.M. Pollock, H. Harada, T.E. Howson, R.C. Reed, J.J. Schirra and S. Walston (The Minerals, Metals & Materials Society, 2004) 951-958.

31. L. Tan and N. Zabaras, *J Computational Physics*, 221 (2007) 9-40.

32. A.J. Elliott et al. *Metall and Mater Trans A*, 35A (2004) 3221-3231.

33. S-C. Huang and M.E. Glicksman, *Acta Metall*, 29 (1981) 717-734.

34. L. Li, R.A. Overfelt, *J Mat Sci*, 37 (2002) 3521-3532.

35. A.F. Giamei and B.H. Kear, *Met Trans*, 1 (1970) 2185.

36. J.D. Hunt and S-Z. Lu, *Metall Trans A*, 27A (3) (1996), 611-623.

37. K. Somboonsuk, J.T. Mason and R. Trivedi, *Metall Trans A*, 15A (6) (1984), 967-975.

38. R. Trivedi, *Metall Trans A*, 15A (6) (1984) 977-982.

39. H. Weidong, G. Xingguo and Z. Yaohe, *J Cryst Growth*, 134 (1993) 105-115.

40. D. Ma and P.R. Sahm, *MetallTrans A*, 29A (3) (1998) 1113-1119.

41. K.A. Jackson, J.D. Hunt, D.R. Uhlmann and T.P. Seward III, *Trans AIME*, 236 (1966) 149.

42. J. Lipton, M.E. Glicksman and W. Kurz, *Mat Sci and Eng*, 65 (1) (1984) 57-63.

43. M.A. Chopra, M.E. Glicksman and N.B. Singh, *Metall and Mater Trans A*, 19 (12) (1988) 3087-3096.

44. S.-Z. Lu and J.D. Hunt, *J Cryst Growth*, 123 (1-2) (1992) 17-34.

45. Ch.-A. Gandin, M. Eshelman and R. Trivedi, *Metall and Mater Trans A*, 27A (9) (1996) 2727-2737.

46. H.B. Dong, W. Wang and P.D. Lee, *Superalloys 2004*, ed. K.A. Green, T.M. Pollock, H. Harada, T.E. Howson, R.C. Reed, J.J. Schirra and S. Walston (The Mineral, Metals & Materials Society, 2004) 925-931.

47. J.A. Warren and J.S. Langer, *Phys Rev A*, 42 (6) (1990) 3518-3525.

48. J.A. Warren and J.S. Langer, *Phys Rev E*, 47 (4) (1993) 2702-2712.

49. C. Brundidge, J.D. Miller and T.M. Pollock, unpublished research, 2010.

50. R.N. Grugel and Y. Zhou, *Metall Mater Trans A*, 20A (1989) 969-973.

51. C. Brundidge, D. VanDrasek, B. Wang and T.M. Pollock, unpublished research, 2010.

52. J. Madison, "Investigating Solidification Defect Formation by Three Dimensional Reconstruction of Dendritic Structure," (Ph.D. thesis, University of Michigan, 2010).

53. R.E. Napolitano and R.J. Schaefer, *J Mat Sci*, 35 (2000) 1641-1659.

54. U. Paul and P.R. Sahm, *Mat Sci Eng A*, 173 (1993) 49-54.